



HAL
open science

Large-Eddy Simulation of constant volume combustion in a ground-breaking new aeronautical engine

Gorka Exilard

► **To cite this version:**

Gorka Exilard. Large-Eddy Simulation of constant volume combustion in a ground-breaking new aeronautical engine. Fluids mechanics [physics.class-ph]. Université Paris Saclay (COMUE), 2018. English. NNT : 2018SACL082 . tel-02100677

HAL Id: tel-02100677

<https://theses.hal.science/tel-02100677>

Submitted on 16 Apr 2019

HAL is a multi-disciplinary open access archive for the deposit and dissemination of scientific research documents, whether they are published or not. The documents may come from teaching and research institutions in France or abroad, or from public or private research centers.

L'archive ouverte pluridisciplinaire **HAL**, est destinée au dépôt et à la diffusion de documents scientifiques de niveau recherche, publiés ou non, émanant des établissements d'enseignement et de recherche français ou étrangers, des laboratoires publics ou privés.

Large-Eddy Simulation of constant volume combustion in a ground-breaking new aeronautical engine

Thèse de doctorat de l'Université Paris-Saclay
préparée à CentraleSupélec

Ecole doctorale n°579 Sciences mécaniques et énergétiques,
matériaux et géosciences (SMEMAG)

Spécialité de doctorat: mécanique des fluides

Thèse présentée et soutenue à Rueil-Malmaison, le 11 octobre 2018, par

GORKA EXILARD

Composition du Jury :

Pr. Benoit FIORINA EM2C, CNRS-CentraleSupélec, Université Paris Saclay	Président
Dr. HDR Florent DUCHAINE CERFACS	Rapporteur
Dr. HDR Vincent ROBIN Institut Pprime CNRS-ENSMA, Université de Poitiers	Rapporteur
Pr. Denis VEYNANTE EM2C, CNRS-CentraleSupélec, Université Paris Saclay	Examineur
Pr. Marc BELLENOUE Institut Pprime CNRS-ENSMA, Université de Poitiers	Examineur
Dr. HDR Olivier COLIN IFP Energies nouvelles	Directeur de thèse
Dr. Vincent MOUREAU CNRS-CORIA-INSA Rouen	Invité
Dr. Stéphane RICHARD Safran Helicopter Engines	Invité
Dr. Karine TRUFFIN IFP Energies nouvelles	Invitée

Titre: Simulation aux Grandes Echelles de la combustion à volume constant dans une architecture de moteur aéronautique en rupture

Mots clés: Combustion à volume constant, SGE, moteur aéronautique en rupture

Résumé: Au cours des dernières années, le transport aérien de passagers connaît un développement sans cesse croissant et continue ainsi d'accroître sa contribution aux émissions mondiale de CO₂. Par conséquent, un effort commun entre les aviateurs est fait pour diminuer les émissions de CO₂ et de polluants. Pour encourager cet effort, les réglementations deviennent de plus en plus drastiques en terme d'émissions et de polluants tels que le CO₂, les NO_x mais aussi le bruit. Ces nouvelles limitations sont à la fois définies à court et moyen-long terme pour inciter les motoristes à travailler sur les technologies de plus en plus efficaces. Pour concevoir des moteurs toujours plus performants tout en respectant ces réglementations à court terme, les motoristes travaillent sur l'optimisation de leurs technologies conventionnelles, en améliorant des leviers bien identifiés comme l'augmentation du taux de compression. Cependant, cette optimisation des turbomachines actuelles a déjà atteint un niveau de maturité très élevé. Il semble ainsi difficile de continuer indéfiniment leurs optimisations. Par conséquent, pour atteindre les objectifs à moyen-long terme, les motoristes sont dès aujourd'hui en train d'étudier des nouveaux systèmes propulsifs avancés comme les chambres de Combustion à Volume Constant (CVC), qui peuvent accroître le rendement thermique. Contrairement aux chambres de combustion traditionnelles, qui fonctionnent à flux continu, les chambres CVC opèrent de façon cyclique afin de créer un volume constant pendant la phase de combustion et libérer les gaz chauds dans les étages de turbines. Pendant cette thèse, une approche numérique permettant d'évaluer ce type de chambres est développée. Tout l'enjeu est de pouvoir étudier des chambres de combustion intégrant des parties

mobiles, qui permettent de créer le volume constant dédié à la combustion tout en évitant les fuites à travers ces systèmes mobiles lors de l'élévation de la pression dans la chambre. Cette modélisation doit aussi prédire correctement les phases transitoires comme l'admission des gaz frais, qui pilote la phase de combustion. Cette étude utilise des objets immergés pour modéliser les parties mobiles. Les objectifs de cette thèse sont de rendre ces objets immergés imperméables et adapter la méthode aux différents modèles utilisés pour étudier les milieux réactifs tels que le modèle de combustion ECFM-LES ou encore l'injection liquide Lagrangienne utilisée pour résoudre l'injection du fuel. Dans cette étude, une nouvelle formulation est développée puis testée sur différents cas tests de plus en plus représentatifs des chambres CVC. Cette approche numérique est ensuite évaluée sur une chambre réelle étudiée expérimentalement au laboratoire Pprime de Poitiers. Dans cette dernière étude, deux cas non réactifs permettent de comparer les évolutions de pression à deux endroits dans le dispositif expérimental, ainsi que les champs de vitesse au sein de la chambre de combustion, aux simulations réalisées. Pour ces cas complexes, l'utilisation des objets immergés permet de prédire les résultats expérimentaux à un coût attractif. Un des cas non réactif est ensuite carburé et allumé pour confronter l'évolution pression et les champs de vitesse dans la chambre de combustion des résultats numériques obtenus aux mesures expérimentales. L'approche numérique développée a permis d'enrichir les données expérimentales, d'analyser les variabilités cycle-à-cycle rencontrées au banc et d'identifier les leviers qui permettraient d'optimiser ce type d'architecture.



Title: Large-Eddy Simulation of constant volume combustion in a ground-breaking new aeronautical engine

Keywords: Constant volume combustion, LES, ground-breaking aeronautical engine

Abstract: Over the past few years, aircrafts have become a common means of transport, thus continuously increasing their contribution to global CO₂ emissions. Consequently, there is a common effort between aircraft manufacturers to reduce CO₂ and pollutant emissions. To encourage this effort, regulations are becoming more and more stringent on the emissions and pollutants like CO₂, NO_x and noise. These regulations are both defined in the short and medium-long terms to urge aircraft manufacturers to work on more and more efficient technologies. In order to design more efficient engines while respecting the short term objectives, engine manufacturers are working on the improvement of conventional architectures by using well-known levers like the increase of the Overall Pressure Ratio (OPR). However, the optimization of the present turbomachinery has already reached a high level of maturity and it seems difficult to continuously enhance their performances. Consequently, to reach the medium-long term objectives, engine manufacturers are working on new advanced propulsion systems such as the Constant Volume Combustion (CVC) chambers, which can increase the thermal efficiency of the system. Contrary to present turbomachinery which are burning fresh gases continuously, CVC chambers operate cyclically so as to create the constant vessel dedicated to the combustion phase and to expand the burnt gases into turbine stages. In this PhD thesis, a numerical approach is developed to allow the evaluation of these kind of combustors. The challenge is to be able to evaluate CVC chambers by taking into account the moving parts which create the constant volume and avoid mass leakages

through these moving parts during the increase of the combustion chamber pressure when the combustion occurs. This approach also has to correctly predict unsteady phases like the intake, which directly controls the combustion process. These moving parts are modeled with a Lagrangian Immersed Boundary (LIB) method. The main goals of this thesis is to make the LIB as airtight as possible and to render this approach compatible with the different models which are adapted to analyse reactive flows such as the ECFM-LES combustion model or Lagrangian liquid injection, used for fuel sprays. In this study, a new formulation is developed and tested on several test cases from very simple ones to cases more representative of CVC chambers. Then, this approach is evaluated on a real chamber experimentally analysed in Pprime laboratory in Poitiers. Two non-reactive operating points are used to compare the experimental pressure at two positions in the apparatus and the experimental velocity fields in the combustion chamber with the numerical results. In this complex configuration, the LIB method allows the prediction of the experimental results with a low CPU cost. As in the experiment, one non-reactive case is carburized and ignited to compare the measured pressure and the velocity fields in the combustion chamber with the simulations. The proposed numerical approach allows the data enhancement of the experiment and then the analysis of the cycle-to-cycle variability encountered during the experimental measurements. Last but not least, this method enables the identification of the different levers that could decrease the variability and then could improve operability of this type of combustors.



Contents

1	Introduction	1
1.1	Industrial context	1
1.1.1	Aviation and environmental objectives	1
1.1.2	Present and future aircraft engine architectures	2
1.1.3	Constant volume combustion chamber working principle	10
1.1.4	Thermal efficiency of combustion at constant pressure and constant volume	11
1.2	Computational approaches	12
1.3	Objectives of this thesis	14
1.4	Organization of the manuscript	15
I	Numerical modeling and realised developments	16
2	Large Eddy Simulation of turbulent combustion	17
2.1	The governing equations	18
2.1.1	The equation of state	19
2.1.2	Conservation of Mass: Species diffusion flux	19
2.1.3	Viscous stress tensor	20
2.1.4	Heat flux vector	20
2.1.5	Transport coefficients	21
2.2	The Governing Equations for LES	22
2.2.1	The filtered viscous terms	23
2.2.2	Subgrid-scale turbulent terms for LES	23
2.3	Subgrid-scale turbulent viscosity modeling	25
2.3.1	Smagorinsky model	25
2.3.2	σ -model	25
2.4	Filtered reaction rate closure: combustion models	26
2.4.1	Premixed turbulent combustion regimes encountered in CVC chambers	26
2.4.2	Combustion model used under flamelet assumption	26
2.4.2.1	Basic principles	27
2.4.2.2	Unburnt and burnt gases properties	28
2.4.2.3	Burnt gas chemistry	30
2.4.2.4	Reaction rate definition	31
2.4.2.5	Computation of the laminar flame speed	32

2.4.2.6	The Flame Surface Density (FSD) transport equation . . .	32
2.4.3	The Imposed Stretch Spark Ignition Model for LES: ISSIM-LES . .	34
2.4.3.1	The spark model	34
2.4.3.2	Initial burnt gases kernel	35
2.4.3.3	Modification of the FSD equation	36
2.4.4	The Wall/Flame interactions Model	37
2.5	Liquid injection modeling	39
2.5.1	Source terms of Lagrangian liquid injection	39
2.5.1.1	Drag of particles	39
2.5.1.2	Evaporation model, mass and heat transferts	40
2.5.2	Spray breakup modeling	44
2.5.3	Distribution of the source terms, the projection operator	46
2.6	Numerical approaches for moving boundaries	47
2.6.1	Arbitrary Lagrangian Eulerian	47
2.6.2	Multi Instance Solver Coupled through Overlapping Grids (MISCOG)	48
2.6.3	Immersed Boundary Method	49
3	Lagrangian Immersed Boundary method	51
3.1	LIB method principle	51
3.2	Modification of the governing equations	53
3.3	Source terms calculation	53
3.3.1	Initial LIB method implemented in AVBP	53
3.3.1.1	The forcing term f_i^n	53
3.3.1.2	The projection operator	54
3.3.1.3	The energy source term \bar{S}_{ELIB}	55
3.3.2	New LIB method developed in this study	55
3.3.2.1	Normalized forcing term $\bar{F}_{LIB,i,j}$ of particles surrounding node j	55
3.3.2.2	The energy source term \bar{S}_{ELIB}	57
3.3.3	Quantitative comparison of the two methods	57
3.4	Improvement and adaptation of the LIB method to model CVC chambers	59
3.4.1	Numerical scheme based on Taylor expansion	60
3.4.2	Special treatment of LIB particles on walls	60
3.4.3	Development of rebound liquid injection on LIB	62
3.4.4	Combustion model adaptation with LIB and liquid injection	64
3.4.4.1	Avoiding combustion inside immersed objects	64
3.4.4.2	Liquid injection taken into account in ECFM-LES	65
4	Evaluation of the implemented LIB method	66
4.1	Static and rotating LIB between two zones at different pressures	67
4.1.1	Conformal wall boundary conditions used	67
4.1.2	2D wall-bounded box	68
4.1.3	2D wall-bounded box with a rotating immersed boundary	70
4.2	Evaluation of the developments on a 3D wall-bounded box with motionless LIB	73
4.2.1	Test case description	73

4.2.2	Evaluation without the second order derivative source terms	73
4.2.3	Evaluation using the second order derivative source terms	74
4.3	LIB isothermal boundary condition evaluation	76
4.3.1	Configuration	76
4.3.2	Computational parameters	76
4.3.3	Results	77
4.4	Acoustic and pressure wave cases	81
4.4.1	Short cavity acoustic eigen-mode 1D case	81
4.4.2	Long cavity acoustic eigen-mode 1D case	83
4.4.3	Pressure wave	86
4.4.4	Conclusion	87
4.5	Steady state flow bench	88
4.5.1	Experimental apparatus	88
4.5.2	Computational parameters	89
4.5.3	Results	89
4.5.3.1	Velocity profiles at 20 mm	90
4.5.3.2	Velocity profiles at 70 mm	91
4.5.3.3	Pressure drop through the expansion	92
4.5.3.4	Conclusion	93
II	Constant volume combustion chamber study	94
5	The CVC chamber apparatus	95
5.1	Intake and exhaust system technologies	95
5.2	Pprime's CVC apparatus	97
5.3	Experimental diagnostics	99
6	Non reactive cases	101
6.1	Operating points	102
6.2	Computational parameters	102
6.3	Preliminary results on non reactive cases	105
6.4	Modification of two parameters: Inlet pressure and mechanical slacks of the intake and the exhaust systems	107
6.5	Improvement of the inlet: extension of the studied domain	109
6.6	O.P.2 final results	111
6.6.1	Pressure evolutions	111
6.6.2	Velocity fields analysis	112
6.6.3	Non-reactive cases conclusion	122
6.7	Complementary study on the inlet pressure: a 0-Dimension model	123
6.7.1	Calibration of the exhaust and inlet section laws with intake pres- sure set to 3 bar	124
6.7.2	Reference 0D response	126
6.7.3	Intake pressure signal modifications	127

7	Reactive case	132
7.1	Operating point	132
7.2	Computational parameters	133
7.3	Results	135
7.3.1	Velocity field analysis	135
7.3.2	Combustion chamber pressure evolution	142
7.4	Cycle-to-cycle variability analysis	146
7.4.1	Slow and fast cycles analysis	146
7.4.2	Peak pressure of consecutive cycles	153
7.4.3	Single regression analysis	154
7.4.3.1	Local and global thermodynamic variables	156
7.4.3.2	Variable averaged on the flame front during the very first moments	162
7.4.4	Multidimensional data analysis	164
7.4.4.1	Maximum pressure	165
7.4.4.2	Angle of the peak pressure	166
7.4.5	Conclusion on the different levers to improve the combustion process	168
7.4.6	Correlation of previous cycle variables with the cycle-to-cycle vari- ability	169
7.4.6.1	Correlation with the mean pressure of the previous cycle .	170
7.4.6.2	Correlation with the pressure difference at the exhaust system at 20 CAD	174
7.4.6.3	Correlation with the pressure difference at the intake sys- tem at 55 CAD	177
7.5	Reactive case conclusion	180
8	Conclusions and perspectives	181
8.1	Conclusions of the present work	181
8.2	Perspectives	183
	Bibliography	185

Chapter 1

Introduction

Contents

1.1 Industrial context	1
1.1.1 Aviation and environmental objectives	1
1.1.2 Present and future aircraft engine architectures	2
1.1.3 Constant volume combustion chamber working principle	10
1.1.4 Thermal efficiency of combustion at constant pressure and constant volume . .	11
1.2 Computational approaches	12
1.3 Objectives of this thesis	14
1.4 Organization of the manuscript	15

1.1 Industrial context

1.1.1 Aviation and environmental objectives

Over the past few years, aircrafts have become a common means of transport, thus continuously increasing their contribution to global CO_2 emissions. Consequently, there is a common effort between aircraft manufacturers, supported by a more and more stringent legislation, to reduce CO_2 and pollutants emissions. The Advisory Council for Aeronautical Research in Europe (ACARE) is helping the air transport industry to pay attention to the environmental issues such as the air pollution, the noise and the climate change. Indeed, the air transport produces today 2% of man-made CO_2 emissions and 12% of all transport sources, i.e. 628 megatons of CO_2 yearly. Due to the continuous and steady growth of air traffic, these levels of pollution are expected to increase continuously up to 3% by the year 2050 .

In 2001 ACARE established targets for 2020 compared to 2000 standards, which are:

- The reduction of the fuel consumption and CO_2 emissions by 50% per passenger per kilometre,
- The reduction of NO_x emissions by 80%,
- The reduction of the perceived noise by 50%,
- The reduction of the environmental impact of the aircraft manufacturing, the maintenance and the disposal of aircraft and related products.

ACARE has identified the main contributors to achieve the above mentioned targets. The predicted contributions to the 50% CO_2 emissions reduction target is divided as follows:

- The efficient of the aircraft: 20-25%,
- The efficient of the engines: 15-20%,
- The improvement of the air traffic management: 5-10%.

Clean Sky, which is the most ambitious aeronautical research programme ever launched in Europe, was born in 2008, to follow the project in reducing aircraft impact on the environment. Indeed, the second version of the project "Clean sky 2" continues to encourage aircraft manufacturers to improve their technologies. In order to keep emissions as low as possible, new restrictions will enter into force by 2050.

These compared with 2000 standards are the following:

- The reduce of the fuel consumption and CO_2 emissions by 75% per passenger kilometre,
- The Reduction of NOx emissions by 90%,
- The Reduction of the perceived noise by 65%,

Aircraft engine manufacturers such as Safran Aircraft Engines are working on several lines to achieve ACARE goals and beyond Clean sky 2 objectives.

One field of study to meet short term goals is to improve the present engine aircraft architectures. Developing new materials in order to reduce the engines weight, is used to increase the power density of propulsion systems. New materials in the combustion chamber and new cooling systems are used to extend the field of operability by raising Turbine Entry Temperature (TET) and hence, improve the thermal efficiency. In the same frame of mind, some gain on thermal efficiency can be achieved by increasing the Overall Pressure Ratio (OPR), defined as the pressure ratio between the inlet of fresh air in front of the fan and the entry of combustion chamber. Moreover, gain on the propulsive efficiency is reached by increasing the ByPass Ratio (BPR), defined as the mass flow rate through the fan which is called the secondary stream, over the mass flow rate through the core engine called the primary stream.

The latest engine based on these lines is the CFM's new LEAP-X engine, which reduces fuel consumption by an additional 15% compared with the best CFM-powered aircraft available at the moment.

1.1.2 Present and future aircraft engine architectures

Airplanes were historically propelled by piston engines. With the growth of high density power demand for military and civil aircrafts, manufacturers began designing gas turbines that deliver much more power per mass unit.

Over the last 50 years, manufacturers have been improving thermodynamic efficiency of gas turbine architecture, which is based on the Brayton cycle. For aircraft engines such as the turbofan (Fig. 1.1, the thermopropulsive efficiency mainly depends on its TET, OPR and BPR. This is why latest generation of aircraft engines such as the LEAP-X

from Safran Aircraft Engine or the GP7200 from Engine Alliance have increased these three design parameters. In larger aircraft engines, TET is above 1800 K, the OPR and the BPR can respectively reach values from 40 up to 50 and 12.

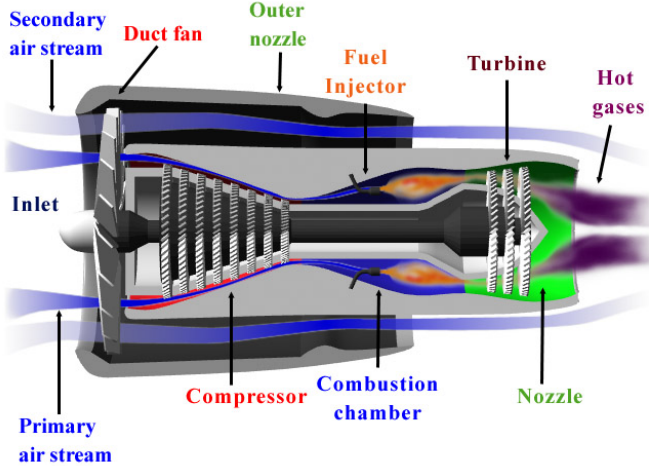


Figure 1.1: Turbofan illustration

After several decades of constant research and development efforts, this kind of architecture has reached an high level of maturity and its global efficiency can not continuously be improved. Consequently, only breakthrough technologies will enable to meet 2050 "Clean Sky 2" objectives. Fig. 1.2 extracted from the International Civil Aviation Organization (ICAO) report shows that some new aircraft engine architectures are studied so as to decrease fuel consumption over coming years.

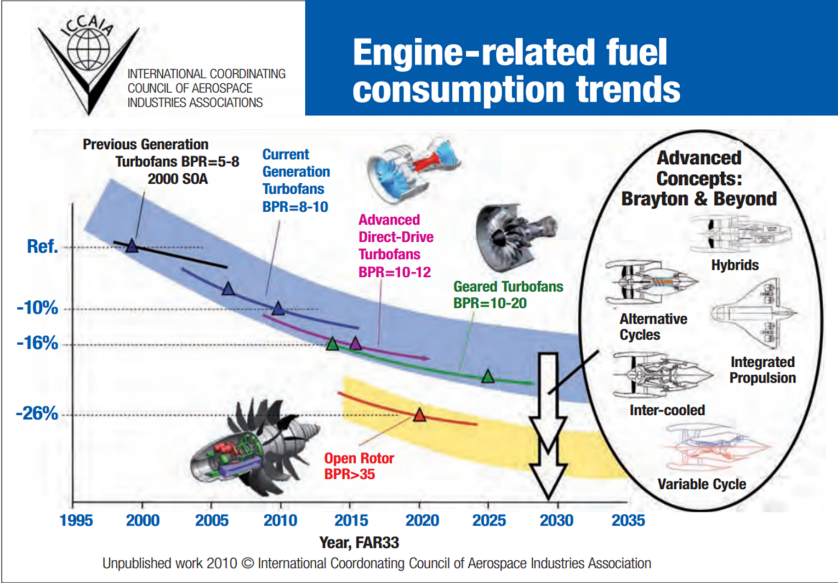


Figure 1.2: History and future of engine fuel consumption trends, extracted from [1]

At the beginning of the 21st century, common aircraft engines have an OPR of 25 up to 30 and a BPR from 5 to 8. Efficiency and emissions of this kind of aircraft engines are chosen as "Clean Sky 2" standards. To meet 2050 "Clean Sky 2" objectives, aircraft manufacturers search for ground-breaking technologies.

Among which, the Open Rotor developed by Safran Aircraft Engine is scheduled to be tested on an Airbus A340 prototype in 2020. The BPR of this engine is increased up to 35 by removing the nacelle surrounding two contra-rotative fans, which will significantly improve the propulsive efficiency. This new aircraft engine will theoretically reduce fuel consumption from 20% down to 30% compared with 2000s engines.

Nevertheless, the enhancement of engine efficiency by 15 – 20% by 2020 is just a first step. 2050 "Clean Sky 2" objectives are more drastic, aircraft engine manufacturers are carrying on their research to develop more efficient architectures, which are based on advanced concepts.

A quick overview of studied architectures is proposed here.

Intercooled cores

Intercooled core designs are concepts studied in the collaborative project NEW Aero engine Core (NEWAC) based on heat management so as to strongly reduce CO_2 and NO_x emissions and improve the thermal efficiency. Several configurations are considered in this project, among which, intercooling cores and intercooling recuperative cores presented in Fig. 1.5. The main effect is to decrease the temperature between two compressor stages which reduces the global compressor work and thus fuel burning.

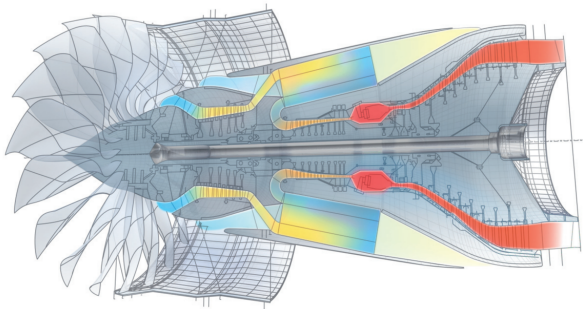


Figure 1.3: Intercooled core

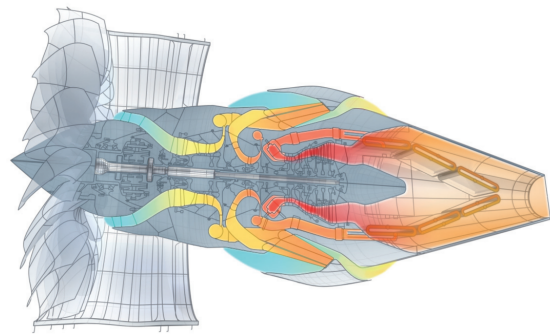


Figure 1.4: Intercooled recuperative core

Figure 1.5: Figures extracted from NEWAC report

On the one hand, intercooled cores can be designed for higher OPR than in conventional core turbofan engines with the same TET, which enhances the thermal efficiency. This temperature is today limited by material technology. On the other hand, intercooled recuperative cores use heat exchangers in the nozzle to heat up the temperature of fresh gases before getting into the combustion chamber and thus reduce the heat supplied by the fuel. Consequently fuel consumption is cut down for the same TET. Therefore, the combination of heat exchangers between the low and the high pressure compressor stages reduces the required compressors work and the heat exchanger between the nozzle and the combustion chamber could improve the fuel consumption. However, the theoretical gain

in thermal efficiency has to compensate the pressure losses through complex geometries and the additional drag introduced by heat exchangers. Hao and Zhan-xue [2] used a quasi one-dimension simulation approach to evaluate the effects of intercooling and recuperation systems on the turbofan engine performances. They found that the use of heat exchangers can improve the thermal efficiency and the net thrust. This technology can decrease the fuel consumption but they highlighted that high effectiveness heat exchangers will deteriorate the gain of the system by introducing too high pressure losses and weight. Kyprianidis et al [3] and Xu et al. [4] used a multidisciplinary aero engines conceptual design tools to emphasis that new core concepts can save 2% up to 5%. Camilleri et al. [5] proposed a new core concept which consists in reversing the flow and mixing the burnt gases into the secondary stream as shown Fig. 1.6. This new core concept can offer 2% of fuel saving comparing with intercooling cores (Fig .1.5). However, the mass increased due to the added parts might reduce block fuel benefit.

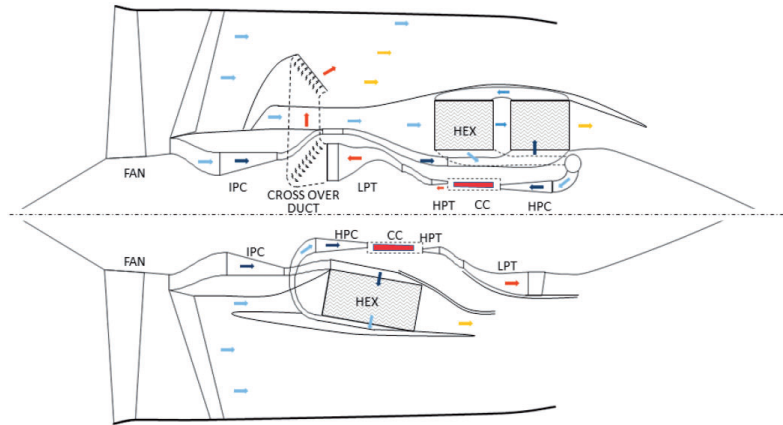


Figure 1.6: Comparison of a Geared Intercooled Reversed Flow Core on the top of the figure with a Geared Intercooled Straight Flow Core on the bottom of the figure, extracted from [5]

Hybridisation technologies

Hybridisation of aero engines seems to be a very attractive solution to reduce CO_2 , NO_x emissions and noise pollution close to airports. Indeed, mission phases such as take off, climbing and approach might be supported by an electrical power. Nowadays, this technology is not yet mature enough to power commercial airliners.

One way to enforce the evolution of the hybridisation of commercial airliners is to develop smaller hybrid or full electric aircrafts. Technologies can deliver the power of light planes such as the all electric E-fan developed by Airbus and its partners (shown in Fig. 1.7). Siemens develops a high performance electric motor which only weights 50 *kg* and delivers an continuous output of about 260 *kW*. This technology powered the Extra 330LE aerobatics airplane, presented in Fig. 1.8, for this maiden flight of 10 minutes on June 24th 2016. Siemens intends to integrate this technology in the development of an airplane with Airbus.



Figure 1.7: E-fan



Figure 1.8: Extra propulsed Siemens

There are currently some technological solutions to reduce the impact of aviation near airports. Another way to save fuel and reduce the noise on tarmacs is to use technologies such as the electric green taxiing system developed by Safran Landing System. The low cost company Easyjet intends to measure this technical solution which could save 4% of its total fuel consumption. This new landing gear is evaluated on several airplanes during 2016 and could be adapted on the whole air fleet.

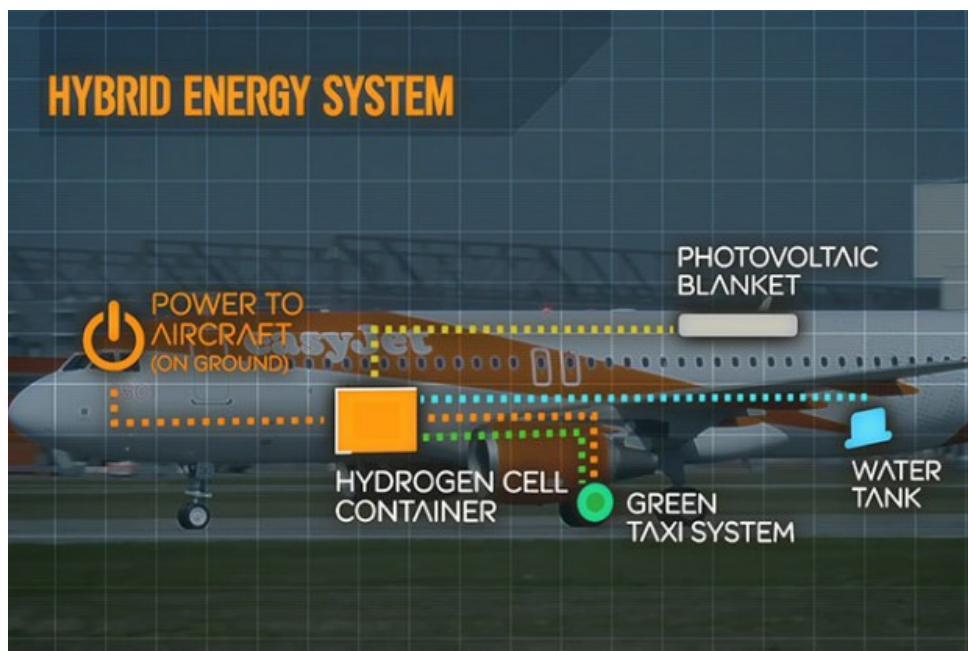


Figure 1.9: Easyjet hybrid aircraft

New aircraft shape designs

In order to improve the global efficiency of aircrafts, some new aerodynamics shapes are evaluated. In these ground-breaking airplane designs, the propulsion is partially or fully embedded in the wing to reduce the drag encountered by the engine nacelles and achieves a maximum noise shielding. NASA is studying these kind of aircraft shapes experimentally and numerically, Figs 1.10 and 1.11 show two new aircraft designs. Moreover, these new airplanes expand the surface exposed to the sun, where solar panels can be installed so as to produce electrical power to supply new power sources.



Figure 1.10: NX-3



Figure 1.11: Double Bubble D8

Alternative Cycles

Two main alternative thermodynamics cycles which improve the thermal efficiency comparing with the usual Brayton cycle, are based on a pressure gain combustion. Indeed, they could lead to a reduction of 20% in specific fuel consumption [6].

The combustion detonation mode described by the detonation cycle proposed by Fickett and Jacob (FJ) is a combustion regime which provides an extremely rapid release of thermal energy. The supersonic combustion wave generates 15 up to 40 times the initial pressure, depending on the considered mixture. There are several ways of implementing detonative combustion in propulsive engines [7].

Standing detonation wave engines operate in supersonic flow where fresh mixture feeds the detonation wave which is stabilized inside the engine by a wedge. The thrust is generated by the expansion of the burnt gases in a nozzle. A schematic diagram of an oblique detonation wave integrated into an hypersonic plane is presented in Fig. 1.12. This type of engine is called "Supersonic Combustion RAMJET" (SCRAMJET). The stability and the performance of such engines have been numerically modelled and results show that the efficiency drastically decreases above 7 Mach. Indeed, the thrust generated by the engine does not counter the aerodynamic forces applied on the engine.

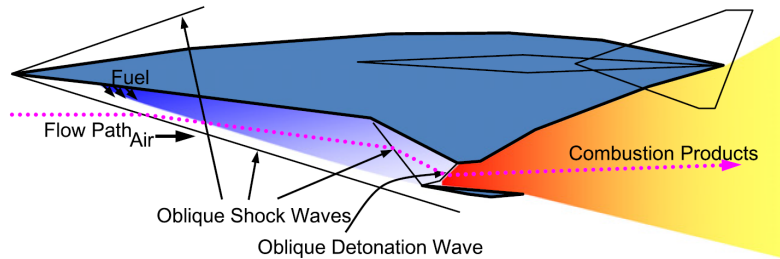


Figure 1.12: Schematic view of a supersonic ramjet with an oblique detonation wave integrated into hypersonic plane

Another way to propel projectile is to use the Ram ACcelerator (RAMAC). The projectile is injected in a tube filled with a reactive mixture, at supersonic velocity. The shape of the injected object can compress and initiate an oblique detonation at the right place to produce pressure increase and then thrust. The RAMAC principle is presented in Fig. 1.13. This technology is more suitable for missiles than aircraft propulsion.

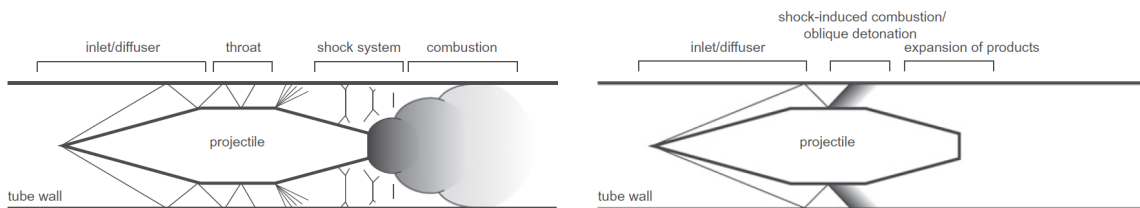


Figure 1.13: Schematic diagram of a Ram Accelerator operating in subsonic (left) and detonation (right) combustion modes

Both Pulsed Detonation Engines (PDE) and Rotating Detonation Engine (RDE) are the class of detonative propulsion systems which receive more attention for aircraft propulsion systems. The PDE consists of filling a tube with fresh fuel-oxidizer mixture, then ignited with a sufficiently strong energy source. The ignited flame front needs some space to gain the speed of a detonation wave in the so-called deflagration-to-detonation transition (DDT). Therefore, a sufficiently long tube is required to reach the detonation combustion mode. Finally, the tube is filled again with new fresh gases, which cool down the chamber walls and avoid the device degradation. Then another detonation can occur. Consequently, the engine operates in pulsed mode which comes with high variability in terms of thrust. This variation can be minimized by installing several combustion chambers. Advantages of PDE are a relatively simple design and high efficiency. The disadvantages are a low frequency, necessity to ignite at each cycle, time variation of thrust, high level of noise and intense vibrations.

In the RDE, the detonation once initiated, propagates continuously in a cylindrical cham-

ber. The engine is more compact and more efficient while smaller variations of thrust than in PDE are generated. This system is schematically described in Fig. 1.14. Experimental and numerical researches have been carried out on this technology, Adamson et al. [8] highlighted the feasibility of this engine through an experimental prototype. Bykovskii et al. [9, 10, 11] reported the results of experimental studies which confirm the feasibility of the kind of combustor. Hishida et al. [12] presented theoretical backgrounds and numerical calculations on this combustion mode. Davidenko et al. [13] also reported attractive results of numerical simulations on a rotating detonation in a rocket engine.

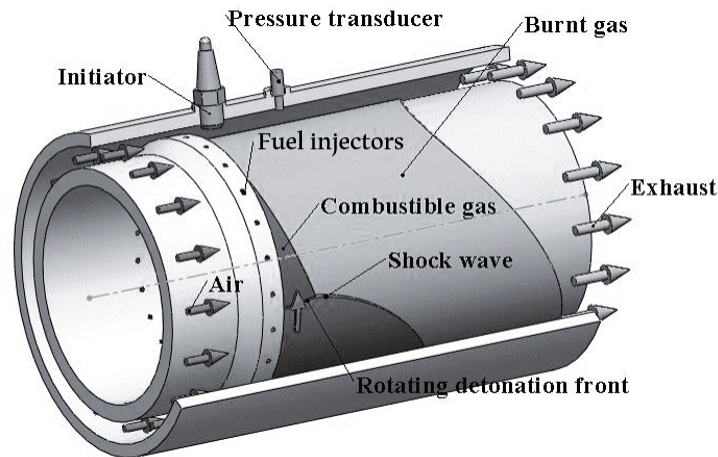


Figure 1.14: Schematic diagram of a Rotating Detonation Engine extracted from [14]

The second main pressure gain combustion mode is the constant volume combustion described by the Humphrey cycle. This combustion process reaches a higher thermodynamic efficiency by achieving a high-speed deflagration in a constant volume chamber. This combustion is not as well-known as the rotating detonation mode. Nevertheless, some studies on this technology have been carried out to motorize aircrafts in the future. Bobusch et al. [15] presented the shockless explosion combustion based on cyclic combustion process like PDE. The proposed system consists of a steady tube without moving parts. The filling of fresh gases and the combustion at constant volume rely on acoustic resonance, the four different phases are presented in Fig. 1.15. This configuration was studied with a simplified one dimensional numerical approach and shown the feasibility of the concept. However, the main difficulty in this architecture is to design the intake system without moving parts which can be handled with Fluidic diodes systems. They are special geometries that have low pressure losses in one direction and high pressure losses in the other and thus counter the backflow from the combustor.

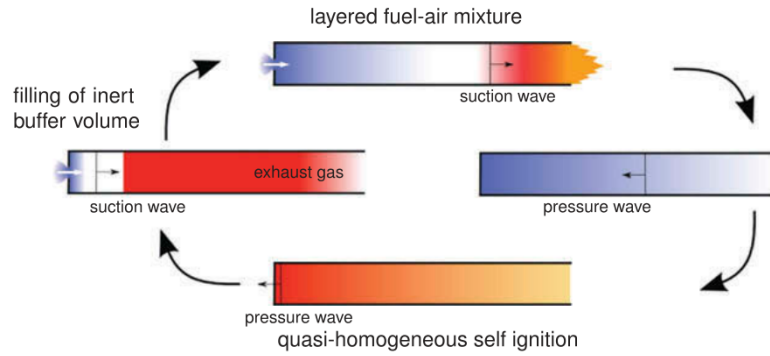


Figure 1.15: Shockless explosion combustion principle extracted from [15]

Devices with moving parts are also investigated. The semi-industrial CVC chamber project created by Safran Helicopter Engines and manufactured by COMAT uses rotating cams as intake and exhaust systems. This combustor was studied experimentally by Bellenoue et al. [16] and Boust et al. [17] to analyse the phenomena and the difficulties met in this kind of architecture, such as misfires and underestimated peak pressure. Labarrere et al. [18] used the LES to study this configuration which emphasizes that misfires were hardly linked to high velocity in the vicinity of the spark plug at the ignition time.

This pressure gain combustor with moving parts is studied in this thesis.

1.1.3 Constant volume combustion chamber working principle

Like the constant pressure combustor, the CVC chamber is supplied with compressed fuel-air mixture and the heat release generated by the combustion process is collected through turbine stages. The moving parts, acting like valves in piston engines, are involved to respectively let air and burnt gases flows inside and outside the chamber. The schematic diagram of this architecture is shown in Fig. 1.16.

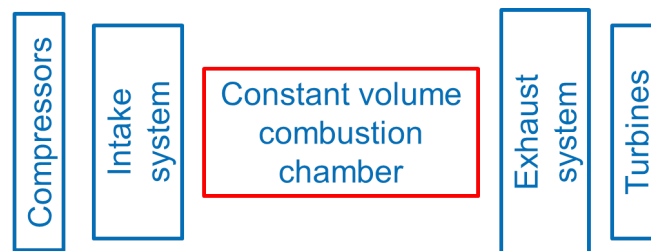


Figure 1.16: CVC architecture

CVC chamber cycle could be described by four main steps: the combustion, the exhaust, the scavenging and the end of intake. During the end of intake and thus while the exhaust system is closed, a direct injection could be realised. These phases are illustrated in Figs. 1.17 to 1.20, where the intake and exhaust systems are filled by grey color when they are closed.



Figure 1.17: Combustion

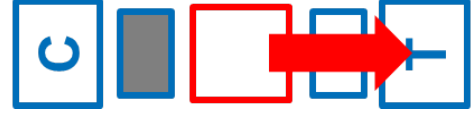


Figure 1.18: Exhaust

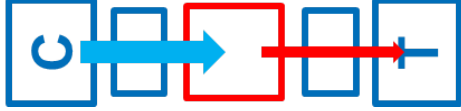


Figure 1.19: Scavenging

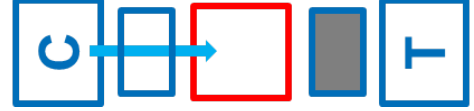


Figure 1.20: End of intake & Injection

1.1.4 Thermal efficiency of combustion at constant pressure and constant volume

The combustion at constant pressure and at constant volume are respectively described by Brayton and Humphrey cycles. In this paragraph, the thermal efficiency of these two combustion modes, on ideal cycle assumption, are analysed. In order to simplify this assessment, the ratio γ of the heat capacity at constant pressure over the heat capacity at constant volume is assumed to be equal equal, in both the fresh and burnt gases of the considered mixture. Moreover, the same amount of energy Q is added in systems through combustion. The two ideal thermodynamic cycles presented in Fig. 1.21 are analysed to find the expression of the efficiency formula, based on entry variables. In order to find this expression, compression and expansion of gases are considered isotropic which allow the use of the Laplace Laws. By using the first principle of thermodynamic applied respectively on an opened or closed system, the thermal efficiency can be in function of variables at the intake and the OPR:

$$\eta_{Brayton} = 1 - \Pi^{\frac{1-\gamma}{\gamma}} \quad (1.1)$$

$$\eta_{Humphrey} = 1 - \gamma \Pi^{\frac{1-\gamma}{\gamma}} \times \frac{(1+q)^{frac{1}{\gamma}} - 1}{q} \quad (1.2)$$

Where Π is the OPR and $q = \frac{Q}{c_v T_2}$ with $T_2 = T_1 \Pi^{\frac{\gamma-1}{\gamma}}$.

In order to illustrate these two thermal efficiencies, the considered mixture is composed of air and methane at the stoichiometric. The Lower Heating Value (LHV) of the methane is $LHV_{methane} = 50 \text{ MJ/kg}$ and thus, the heat release through combustion Q is then equal to 2.75 MJ per kg of fresh mixture. The ratio of heat capacities γ is supposed equal to 1.3 in fresh and burnt gases and specific heat capacities at constant pressure and volume are $c_p = 1267 \text{ J/kg.K}$ and $c_v = 957 \text{ J/kg.K}$. In both cases, intake pressure and temperature are set to respectively 1 bar and 300 K . With these assumptions, thermal efficiencies of both cycles are plotted in Fig. 1.22 as a function of the OPR.

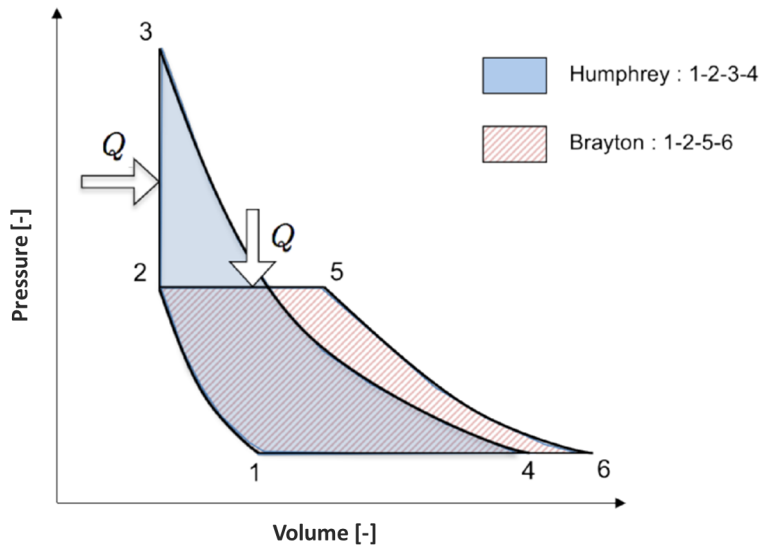


Figure 1.21: Comparison of Brayton and Humphrey cycles

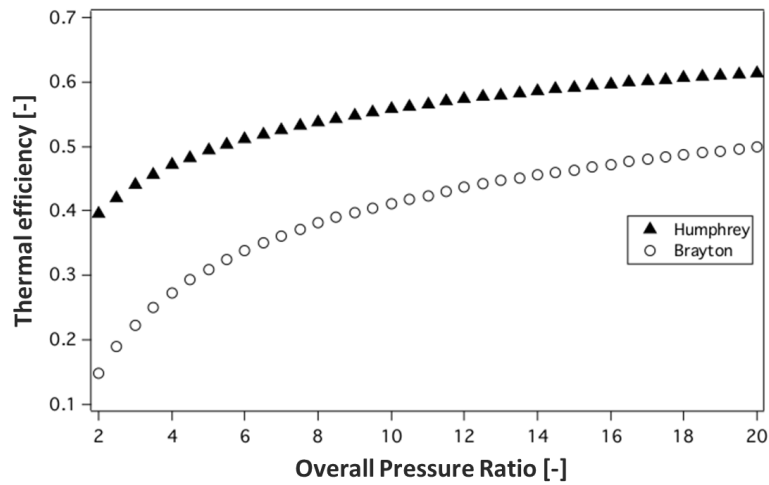


Figure 1.22: Ideal thermal efficiency met for both thermodynamic cycles

1.2 Computational approaches

Computational Fluid Dynamic (CFD) is commonly used to analyse turbulent combustion processes and may be achieved using different resolution levels. The difference between the three methods is the proportion of unresolved and resolved turbulent scales.

On the one hand, Reynolds-averaged Navier-Stokes (RANS) computation gives access to time-averaged fluid flow quantities. The balance equation for Reynolds averaged quantities are obtained by averaging instantaneous balance equations. A turbulence model is required to close these averaged balance equations. This computational approach is

commonly used in commercial codes to design engines for affordable Computer Processor Unit (CPU) cost.

On the other hand, the Direct Numerical Simulation (DNS) is fully instantaneous. Navier-Stokes equations are solved without any model for turbulent motions, all turbulence scales are explicitly determined and their effects on combustion are captured. Consequently, this computational approach requires a high resolution of the computed domain, in order to resolve all turbulent scales. The DNS approach is usually limited to simple academic flows like turbulent channel or combustion in a very small box. Nevertheless, recent improvement in High Performance Computing (HPC) shows that DNS might be applicable to semi-industrial configurations soon.

Between both these approaches, Large-Eddy Simulation (LES) resolves explicitly larger turbulent scales while smaller ones are modelled using sub-grid scale models. Balance equations are obtained by filtering the instantaneous Navier-Stokes equations. LES has become the standard research tool in combustion modelling and is slowly transferred to aeronautical research and development industry.

The turbulence energy spectrum plotted as a function of wave in Fig. 1.23 represent turbulent scales resolved and unresolved for RANS, LES and DNS. As explained above, all turbulent scales are modelled in RANS approach whereas in LES, the turbulent scales above the cut-off wave number k_c are resolved and modeled below this wave number. Finally, DNS resolves all turbulent scales. Fig. 1.24 shows the evolution of the local temperature in a turbulent brush with three approaches.

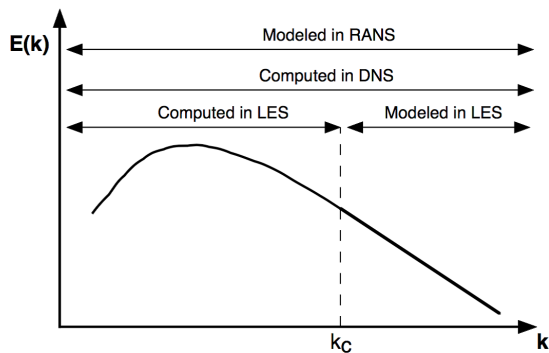


Figure 1.23: Turbulence energy spectrum plotted as a function of wave number for three approaches. k_c is the cut-off wave number used in LES, extracted from [19]

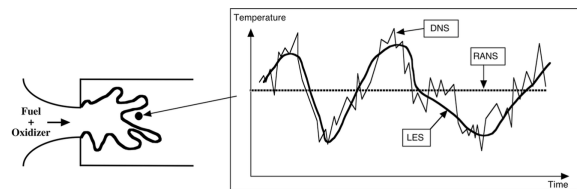


Figure 1.24: Time evolution of local temperature computed with RANS, LES or DNS in a turbulent flame brush, extracted from [19]

1.3 Objectives of this thesis

Some aircraft engine manufacturers used to design their combustors using the numerical simulations to analyse different technical solutions and the experiments to evaluate the chosen one. During the design process, both the simulations and the experiments work together to find the best compromises for the developed engine. This project was created to study ground-breaking new aircraft engine architectures, namely CVC chambers. In fact, these combustors reach theoretically higher thermal efficiency than present turbomachinery, specially for low OPR, and thus might save some fuel consumption. Only the principle of this future technology is known, therefore efficient methods need to be developed to understand the physical phenomenon involved in such combustors. The numerical simulations seem to be an appropriate approach to study different combustor designs in short time periods. Since LES is becoming a reference to study complex reactive flows in aero-engines at Safran Aircraft Engines, the final goal of this PhD thesis is to develop a numerical approach in the LES solver, which allows the studies of CVC chambers.

Consequently, this work is divided into two main objectives: the first one is to develop a numerical method enabling moving boundaries at a reasonable CPU cost. This method must be consistent with models commonly used (LES, combustion, spray, etc.). The second goal is to evaluate this method on a complex configuration already studied experimentally.

The main challenge encountered in this thesis is to model the intake and exhaust systems, which are moving to open and close combustion chamber. These systems can be handled by several numerical methods presented in paragraph 2.6. In this thesis, the intake and exhaust systems are taken into account by using an Immersed Boundary Method (IBM). Immersed boundaries are modeled by a cloud of Lagrangian particles which apply source terms into the Navier-Stokes equations. The first main goal of this thesis is to improve the existing model, by adapting it with moving parts and decreasing the mass flow rates throughout immersed objects, which is realised by working on the application of the different source terms. Furthermore, liquid fuel injection which is commonly modeled with the Lagrangian approach, has to be adapted so as to interact with immersed object walls. Finally, combustion models are adapted to avoid the burning inside objects. All numerical developments are validated through simple test cases and academical configurations. Then, the second main objective of this study is to evaluate all these developments which are used to analyse a semi-industrial CVC configuration, where several operating points are compared with the experimental data. There, both non-reactive and reactive operating point are considered and the LES allows the data enrichment of the experiment which enables to understand the cycle-to-cycle variability better.

1.4 Organization of the manuscript

This manuscript presents the computational approach and the modifications made on the different models so as to study a semi-industrial CVC chamber. Part I of this document deals with the numerical modeling and focuses on all the developments implemented to manage the moving parts and the adaptation of the existing models to study these kind of combustors. Therefore, the LES of turbulent combustion and the models used in this thesis are presented in the chapter 2. The following chapter 3 is dedicated to the Immersed Boundary Method implementation to enable the study of CVC chambers. This chapter emphasises the work made to improve the method to model moving parts, where a new formulation of the source terms calculation is proposed. Additional developments are done on the numerical scheme to increase the capability of the method to hold back some fluid with a high pressure gradient on both sides of immersed objects, which is required in CVC chambers. The lagrangian liquid injection localisation algorithm is modified to take into account the immersed boundaries and an elastic rebound on them is coded. An additional treatment in wall cells to avoid as much as possible the mass flow leakage in these cells. The last development presented is the adaptation of the ECFM-LES combustion model to deal with both the lagrangian liquid injection and the immersed boundaries.

Part II is dedicated to the evaluation of the developed method on a semi-industrial CVC chamber. This part is divided into 3 chapters. The first one is devoted to the presentation of the experimental CVC chamber test bench used to validate the implemented LIB method. Then, the LES solver is evaluated on 2 non reactive operating points where different measurements, like the pressure at different positions and velocity fields inside the chamber, are available. These two test cases show the capability of the method to handle these kind of combustors and present the difficulties met in these complex simulations. Last but not least, the carburation and the combustion is activated in the second operation point like in the experiment. In this test case, the predicted pressure evolution and the velocity fields are compared with the measurements and the analysis of the cycle-to-cycle variability is presented.

Lastly, main conclusions of the project are summarised and outlook actions are suggested.

Part I

Numerical modeling and realised developments

Chapter 2

Large Eddy Simulation of turbulent combustion

Contents

2.1	The governing equations	18
2.1.1	The equation of state	19
2.1.2	Conservation of Mass: Species diffusion flux	19
2.1.3	Viscous stress tensor	20
2.1.4	Heat flux vector	20
2.1.5	Transport coefficients	21
2.2	The Governing Equations for LES	22
2.2.1	The filtered viscous terms	23
2.2.2	Subgrid-scale turbulent terms for LES	23
2.3	Subgrid-scale turbulent viscosity modeling	25
2.3.1	Smagorinsky model	25
2.3.2	σ -model	25
2.4	Filtered reaction rate closure: combustion models	26
2.4.1	Premixed turbulent combustion regimes encountered in CVC chambers	26
2.4.2	Combustion model used under flamelet assumption	26
2.4.3	The Imposed Stretch Spark Ignition Model for LES: ISSIM-LES	34
2.4.4	The Wall/Flame interactions Model	37
2.5	Liquid injection modeling	39
2.5.1	Source terms of Lagrangian liquid injection	39
2.5.2	Spray breakup modeling	44
2.5.3	Distribution of the source terms, the projection operator	46
2.6	Numerical approaches for moving boundaries	47
2.6.1	Arbitrary Lagrangian Eulerian	47
2.6.2	Multi Instance Solver Coupled through Overlapping Grids (MISCOG)	48
2.6.3	Immersed Boundary Method	49

This chapter presents the compressible Navier-Stokes equations and their conservative formulations implemented in the LES solver AVBP. Equations and models shown here are these used in the scope of this thesis, the description is based on the AVBP's handbook.

2.1 The governing equations

Throughout this part, the index notation (Einstein's rule of summation) is adopted for the description of the governing equations, excepted for the index k which refers to the k^{th} species and will not follow the summation rule unless specifically mentioned or implied by the \sum sign.

The set of conservation equations describing the evolution of a compressible flow with chemical reactions of thermodynamically active scalars reads:

$$\frac{\partial}{\partial t}(\rho) + \frac{\partial}{\partial x_j}(\rho u_j) = 0 \quad (2.1)$$

$$\frac{\partial}{\partial t}(\rho u_i) + \frac{\partial}{\partial x_j}(\rho u_i u_j) = - \frac{\partial}{\partial x_j}[P \delta_{ij} - \tau_{ij}] + F_i \quad (2.2)$$

$$\frac{\partial}{\partial t}(\rho E) + \frac{\partial}{\partial x_j}(\rho E u_j) = - \frac{\partial}{\partial x_j}[u_i (P \delta_{ij} - \tau_{ij}) + q_j] + \dot{\omega}_T + Q_r \quad (2.3)$$

$$\frac{\partial}{\partial t}(\rho Y_k) + \frac{\partial}{\partial x_j}(\rho Y_k u_j) = - \frac{\partial}{\partial x_j}[J_{j,k}] + \dot{\omega}_k \quad (2.4)$$

Eqs. (2.2) to (2.4) respectively correspond to the conservation equations for mass, momentum, total non-chemical energy and species. In these equations the following symbols (ρ , u_i , E , Y_k) denote the density, the velocity vector, the non-chemical total energy per unit mass and mass fraction of the chemical species k . Moreover, P denotes the pressure, τ_{ij} the stress tensor, q_i the heat flux vector and $J_{j,k}$ the vector of the diffusive flux of species k . In these equations, there are several source terms: F_i is the vector of momentum source terms and accounts for all external forces such as gravity or drag introduced by liquid droplets. In the energy equation Eq. (2.3), $\dot{\omega}_T$ corresponds to the heat release due to combustion and Q_r the radiative source term. Finally, $\dot{\omega}_k$ in species transport equations Eq. (2.4) is the chemical production or consumption of species k .

The flux tensor can be decomposed into inviscid and viscous terms. They are respectively noted for the four conservation equations:

Inviscid terms:

$$\begin{pmatrix} \rho u_j \\ \rho u_i u_j + P \delta_{ij} \\ (\rho E + P \delta_{ij}) u_i \\ \rho Y_k u_j \end{pmatrix} \quad (2.5)$$

where the pressure P is given by the equation of state for a perfect gas Eq. (2.7).

Viscous terms:

The components of the viscous flux tensor take the form:

$$\begin{pmatrix} 0 \\ -\tau_{ij} \\ -(u_i \tau_{ij}) + q_j \\ J_{j,k} \end{pmatrix} \quad (2.6)$$

where $J_{j,k}$ is the diffusive flux of species k , τ_{ij} is the stress tensor and q_j is the heat flux vector which are respectively presented in sections 2.1.2, 2.1.3 and 2.1.4.

2.1.1 The equation of state

The equation of state for an ideal gas mixture writes:

$$P = \rho r T \quad (2.7)$$

where r is the gas constant of the mixture defined as the ratio of the universal gas constant $R = 8.3143 \text{ J.K}^{-1}.\text{mol}^{-1}$ over the the mean molecular weight of the mixture W .

The gas constant r and the heat capacities at constant pressure C_p and at constant volume C_v of the gas mixture depend on the local gas composition as:

$$r = \frac{R}{W} = \sum_{k=1}^N \frac{Y_k}{W_k} R = \sum_{k=1}^N Y_k r_k \quad (2.8)$$

$$C_p = \sum_{k=1}^N Y_k C_{p,k} \quad (2.9)$$

$$C_v = \sum_{k=1}^N Y_k C_{v,k} \quad (2.10)$$

The adiabatic exponent for the mixture is given by $\gamma = C_p/C_v$. Thus, the gas constant, the heat capacities and the adiabatic exponent are no longer constant. They depend on the local gas composition as expressed by the local mass fractions $Y_k(x, t)$:

$$r = r(x, t), \quad C_p = C_p(x, t), \quad C_v = C_v(x, t), \quad \text{and} \quad \gamma = \gamma(x, t) \quad (2.11)$$

2.1.2 Conservation of Mass: Species diffusion flux

In multi-species flows the total mass conservation implies that:

$$\sum_{k=1}^N Y_k V_i^k = 0 \quad (2.12)$$

where V_i^k is the i^{th} components of the species k diffusion velocity. They are often expressed as a function of the species gradients using the Hirschfelder Curtis approximation:

$$X_k V_i^k = -D_k \frac{\partial X_k}{\partial x_i}, \quad (2.13)$$

where X_k is the molar fraction of species k , $X_k = Y_k W/W_k$. In terms of mass fraction, the approximation of Eq. (2.13) may be expressed by:

$$Y_k V_i^k = -D_k \frac{W_k}{W} \frac{\partial X_k}{\partial x_i}, \quad (2.14)$$

Summing Eq. (2.14) over all species k shows that the approximation of Eq. (2.14) does not necessarily comply with Eq. (2.12) that expresses mass conservation. In order to achieve this mass conservation described by Eq. (2.12), a correction diffusion velocity \vec{V}^c is added to the convection velocity to ensure global mass conservation [19]:

$$V_i^c = \sum_{k=1}^N D_k \frac{W_k}{W} \frac{\partial X_k}{\partial x_i}, \quad (2.15)$$

Computing the diffusive species flux for each species k leads to:

$$J_{i,k} = -\rho \left(D_k \frac{W_k}{W} \frac{\partial X_k}{\partial x_i} - Y_k V_i^c \right), \quad (2.16)$$

Here, D_k are the diffusion coefficients for each species k in the mixture (see section 2.1.5). Using Eq. (2.16) to determine the diffusive species flux implicitly verifies Eq. (2.12).

2.1.3 Viscous stress tensor

The stress tensor τ_{ij} is given by:

$$\tau_{ij} = 2\mu \left(S_{ij} - \frac{1}{3} \delta_{ij} S_{ll} \right) \quad (2.17)$$

where μ is the shear viscosity and S_{ij} the rate of strain tensor defined by:

$$S_{ij} = \frac{1}{2} \left(\frac{\partial u_j}{\partial x_i} + \frac{\partial u_i}{\partial x_j} \right) \quad (2.18)$$

2.1.4 Heat flux vector

In multi-species flows, an additional heat flux term appears in the diffusive heat flux. This term is due to heat transport by species diffusion. The total heat flux vector then takes the form:

$$q_i = \underbrace{-\lambda \frac{\partial T}{\partial x_i}}_{\text{Heat conduction}} + \underbrace{-\rho \sum_{k=1}^N \left(D_k \frac{W_k}{W} \frac{\partial X_k}{\partial x_i} - Y_k V_i^c \right) h_{s,k}}_{\text{Heat flux through species diffusion}} = -\lambda \frac{\partial T}{\partial x_i} + \sum_{k=1}^N J_{i,k} h_{s,k} \quad (2.19)$$

where i is the i^{th} component, λ the heat conduction coefficient of the mixture (see section 2.1.5) and $h_{s,k}$ the sensible enthalpy of the species k .

2.1.5 Transport coefficients

In multi-species flows CFD codes, the molecular viscosity μ is often assumed to be independent of the gas composition and close to that of air, thus the classical Sutherland law can be used. This assumption for a multi-species gas yields to:

$$\mu = c_1 \frac{T^{3/2}}{T + c_2} \frac{T_{ref} + c_2}{T_{ref}^{3/2}} \quad (2.20)$$

where c_1 and c_2 must be determined so as to fit the real viscosity of the mixture. According to White *et al.* [20] the constants can be chosen by $c_1 = 1.71 \cdot 10^{-5} \text{ kg/m.s}$ and $c_2 = 110.4 \text{ K}$ for air at $T_{ref} = 273 \text{ K}$

A second law is available, called Power law:

$$\mu = c_1 \left(\frac{T}{T_{ref}} \right)^b \quad (2.21)$$

with b typically ranging between 0.5 and 1.0. For example, $b = 0.76$ for air.

The heat conduction coefficient of the gas mixture can then be computed by introducing the molecular Prandtl number of the mixture P_r as:

$$\lambda = \frac{\mu C_p}{P_r} \quad (2.22)$$

where P_r supposed as constant in time and space.

The computation of the species diffusion coefficients D_k is a specific issue. These coefficients should be expressed as a function of the binary coefficients D_{ij} obtained from Hirschfelder *et al.* kinetic theory [21]. The mixture diffusion coefficient D_k of species k , is computed as proposed by Bird *et al.* [22]:

$$D_k = \frac{1 - Y_k}{\sum_{j \neq k}^N X_j / D_{jk}} \quad (2.23)$$

The D_{ij} are complex functions of collision integrals and thermodynamic variables. In a simulation that might take into account differential diffusion and full transport, Eq. (2.23) makes sense. However, when a simplified chemical scheme is used, modeling diffusivity in a precise way is not useful due to the assumptions made on the chemical scheme, that is why this approach is much less interesting. In this case, the mixture diffusion coefficient of each species is computed using the Schmidt numbers $S_{c,k}$ of the species and is supposed constant:

$$D_k = \frac{\mu}{\rho S_{c,k}} \quad (2.24)$$

2.2 The Governing Equations for LES

The filtered quantity \bar{f} is resolved in numerical simulations whereas $f' = f - \bar{f}$ is the subgrid-scale part or called the unresolved motion of the flow. For variable density ρ , a mass-weighted Favre filtering is introduced:

$$\bar{\rho}\tilde{f} = \overline{\rho f} \quad (2.25)$$

Conservation equations for Large Eddy Simulations (LES) are obtained by filtering the instantaneous equations (2.1) to (2.4), where the radiation source term Q_r in Eq.(2.3) is neglected:

$$\frac{\partial}{\partial t}(\bar{\rho}) + \frac{\partial}{\partial x_j}(\bar{\rho} \tilde{u}_j) = 0 \quad (2.26)$$

$$\frac{\partial}{\partial t}(\bar{\rho} \tilde{u}_i) + \frac{\partial}{\partial x_j}(\bar{\rho} \tilde{u}_i \tilde{u}_j) = - \frac{\partial}{\partial x_j}[\overline{P} \delta_{ij} - \overline{\tau_{ij}} - \overline{\tau_{ij}^{sgs}}] + \overline{F}_i \quad (2.27)$$

$$\frac{\partial}{\partial t}(\bar{\rho} \tilde{E}) + \frac{\partial}{\partial x_j}(\bar{\rho} \tilde{E} \tilde{u}_j) = - \frac{\partial}{\partial x_j}[\overline{u_i (P \delta_{ij} - \tau_{ij})} + \overline{q_j} + \overline{q_j^{sgs}}] + \bar{\rho}\tilde{\omega}_T \quad (2.28)$$

$$\frac{\partial}{\partial t}(\bar{\rho} \tilde{Y}_k) + \frac{\partial}{\partial x_j}(\bar{\rho} \tilde{Y}_k \tilde{u}_j) = - \frac{\partial}{\partial x_j}[\overline{J_{j,k}} + \overline{J_{j,k}^{sgs}}] + \bar{\rho}\tilde{\omega}_k \quad (2.29)$$

In Eqs. (2.27), (2.28) and (2.29), there are now three types of terms to be distinguished: the inviscid terms, the viscous terms and the subgrid-scale (sgs) terms.

Inviscid terms:

These terms are equivalent to the unfiltered equations except that they now contain filtered quantities:

$$\begin{pmatrix} \bar{\rho} \tilde{u}_j \\ \bar{\rho} \tilde{u}_i \tilde{u}_j + \overline{P} \delta_{ij} \\ \bar{\rho} \tilde{E} \tilde{u}_i + \overline{P} u_i \delta_{ij} \\ \bar{\rho} \tilde{Y}_k \tilde{u}_j \end{pmatrix} \quad (2.30)$$

Viscous terms:

Viscous terms take the form:

$$\begin{pmatrix} 0 \\ -\overline{\tau_{ij}} \\ -(\overline{u_i \tau_{ij}}) + \overline{q_j} \\ \overline{J_{j,k}} \end{pmatrix} \quad (2.31)$$

Filtering the balance equations leads to unclosed quantities, which need to be modeled. Different models are presented in the following sections 2.2.1 and (2.2.2).

Subgrid-scale turbulent terms:

The subgrid-scale terms are:

$$\begin{pmatrix} -\overline{\tau_{ij}^{sgs}} \\ \overline{q_j^{sgs}} \\ \overline{J_{j,k}^{sgs}} \end{pmatrix} \quad (2.32)$$

2.2.1 The filtered viscous terms

The filtered diffusion terms are:

- The laminar filtered stress tensor $\overline{\tau_{ij}}$, which is given by the following relations [19]:

$$\begin{aligned} \overline{\tau_{ij}} &= \overline{2\mu(S_{ij} - \frac{1}{3}\delta_{ij}S_u)}, \\ &\approx 2\overline{\mu}(\tilde{S}_{ij} - \frac{1}{3}\delta_{ij}\tilde{S}_u), \end{aligned} \quad (2.33)$$

and,

$$\tilde{S}_{ij} = \frac{1}{2} \left(\frac{\partial \tilde{u}_j}{\partial x_i} + \frac{\partial \tilde{u}_i}{\partial x_j} \right), \quad (2.34)$$

- The filtered diffusive species flux vector for non-reactive flows is:

$$\begin{aligned} \overline{J_{i,k}} &= -\overline{\rho \left(D_k \frac{W_k}{W} \frac{\partial X_k}{\partial x_i} - Y_k V_i^c \right)} \\ &\approx -\overline{\rho} \left(\overline{D}_k \frac{W_k}{W} \frac{\partial \tilde{X}_k}{\partial x_i} - \tilde{Y}_k \tilde{V}_i^c \right), \end{aligned} \quad (2.35)$$

where high order correlations between the different variables of the expression are assumed negligible.

- The filtered heat flux is:

$$\begin{aligned} \overline{q_i} &= -\overline{\lambda \frac{\partial T}{\partial x_i}} + \sum_{k=1}^N \overline{J_{i,k} h_{s,k}} \\ &\approx -\overline{\lambda} \frac{\partial T}{\partial x_i} + \sum_{k=1}^N \overline{J_{i,k}} \tilde{h}_{s,k} \end{aligned} \quad (2.36)$$

These forms assume that the spatial variations of molecular diffusion fluxes are negligible and can be modeled through simple gradient assumptions.

2.2.2 Subgrid-scale turbulent terms for LES

As highlighted above, filtering the transport equations yields a closure problem evidenced by the so called subgrid-scale (sgs) turbulent fluxes. To solve the system numerically, closures need to be supplied.

- Firstly, the Reynolds tensor defined by:

$$\overline{\tau_{ij}^{sgs}} = -\overline{\rho} (\widetilde{u_i u_j} - \tilde{u}_i \tilde{u}_j) \quad (2.37)$$

$\overline{\tau_{ij}^{sgs}}$ is modeled as:

$$\overline{\tau_{ij}^{sgs}} = 2 \bar{\rho} \nu_{sgs} \left(\tilde{S}_{ij} - \frac{1}{3} \delta_{ij} \tilde{S}_{ll} \right), \quad (2.38)$$

This relation is known as the Boussinesq approximation. It relates the subgrid stresses to a quantity that takes the form of a viscosity. This subgrid-scale turbulent viscosity is called ν_{sgs} and needs to be modeled. Different approaches for this term are explained in section 2.3.

- Secondly, the subgrid-scale diffusive species flux vector $\overline{J_{i,k}^{sgs}}$ expressed as:

$$\overline{J_{i,k}^{sgs}} = \bar{\rho} \left(\widetilde{u_i Y_k} - \tilde{u}_i \tilde{Y}_k \right), \quad (2.39)$$

$\overline{J_{i,k}^{sgs}}$ is modeled following:

$$\overline{J_{i,k}^{sgs}} = -\bar{\rho} \left(D_k^{sgs} \frac{W_k}{W} \frac{\partial \tilde{X}_k}{\partial x_i} - \tilde{Y}_k \tilde{V}_i^{c,sgs} \right), \quad (2.40)$$

where,

$$D_k^{sgs} = \frac{\nu_{sgs}}{S_{c,k}^{sgs}} \quad (2.41)$$

The turbulent Schmidt number is set to $S_{c,k}^{sgs} = 0.6$ for all species. Note also that having one turbulent Schmidt number for all the species does not imply, $\tilde{V}^{c,sgs} = 0$ because of the W_k/W term in Eq. (2.40).

- Finally, the subgrid-scale heat flux vector is:

$$\overline{q_i^{sgs}} = \bar{\rho} (\widetilde{u_i E} - \tilde{u}_i \tilde{E}), \quad (2.42)$$

where E is the non-chemical total energy. The modelisation for $\overline{q_i^{sgs}}$ is written:

$$\overline{q_i^{sgs}} = -\lambda_{sgs} \frac{\partial \tilde{T}}{\partial x_i} + \sum_{k=1}^N \overline{J_{i,k}^{sgs}} \tilde{h}_{s,k}, \quad (2.43)$$

where,

$$\lambda_{sgs} = \frac{\mu_t \overline{C_p}}{P_r^{sgs}}. \quad (2.44)$$

The turbulent Prandtl number is here fixed at $P_r^{sgs} = 0.6$. The correction diffusion velocities are then obtained using Eqs. (2.24) and (2.41):

$$\tilde{V}_i^c + \tilde{V}_i^{c,sgs} = \sum_{k=1}^N \left(\frac{\bar{\mu}}{\bar{\rho}S_{c,k}} + \frac{\mu_{sgs}}{\bar{\rho}S_{c,k}^{sgs}} \right) \frac{W_k}{W} \frac{\partial \tilde{X}_k}{\partial x_i} \quad (2.45)$$

2.3 Subgrid-scale turbulent viscosity modeling

Modeling the subgrid-scale turbulent viscosity ν_{sgs} is an essential part of LES. Subgrid-scale turbulence models are derived on the theoretical ground that the LES filter is spatially and temporally invariant.

2.3.1 Smagorinsky model

In the Smagorinsky model, the subgrid-scale viscosity ν_{sgs} is obtained from:

$$\nu_{sgs} = (C_S \Delta)^2 \sqrt{2 \tilde{S}_{ij} \tilde{S}_{ij}} \quad (2.46)$$

where Δ denotes the characteristic filter width (cube-root of the cell volume), C_S is the model constant is generally set to 0.18. However, it can vary between 0.1 and 0.18 depending on the flow configuration. The Smagorinsky model [23] was developed in the 1960s and heavily tested for multiple flow configurations. This closure is characterized by its globally correct prediction of kinetic energy dissipation in homogeneous isotropic turbulence. However, it predicts non-zero turbulent viscosity levels in flow regions of pure shear, which makes it unsuitable for many wall-bounded flows [24]. This also means that its behaviour is too dissipative in transitioning flows [25].

2.3.2 σ -model

The σ -model developed by Baya Toda *et al.* [26] uses a differential operator based on the singular values of the velocity gradient tensor, which improves the subgrid-scale viscosity prediction. In this model, this viscosity ν_{sgs} is defined by:

$$\nu_{sgs} = (C_m \Delta)^2 D_\sigma \quad (2.47)$$

where the differential operator D_σ is calculated as:

$$D_\sigma = \frac{\sigma_3 (\sigma_1 - \sigma_2) (\sigma_2 - \sigma_3)}{\sigma_1^2} \quad (2.48)$$

where σ_1 , σ_2 and σ_3 are the singular values of the velocity gradient tensor.

2.4 Filtered reaction rate closure: combustion models

The objective of this section is to describe the combustion models used in this study to simulate the spark ignition and the flame propagation in CVC configurations.

2.4.1 Premixed turbulent combustion regimes encountered in CVC chambers

A direct approach to model the reaction rate based on the series expansion of the Arrhenius law cannot be selected for all combustion regimes because of the large number of unclosed quantities, such as the correlation between species concentration and temperature fluctuations and the large truncation errors due to high non linearities. Consequently, combustion models need to be derived based on physical analysis and the comparison of various time and length scales involved in combustion phenomena. Through this analysis, several combustion regimes can be identified by introducing dimensionless characteristic numbers. The Karlovitz number K_a compares the chemical time scale τ_c to the Kolmogorov time scale τ_k and the Damköhler number D_a is the ratio between the turbulent integral time scale τ_t and the chemical time scale τ_c .

These various regimes are generally displayed on a logarithmic diagram ($u'/S_L; l_t/\delta_l$) proposed by Peters in 1999 [27], presented on Fig. 2.1.

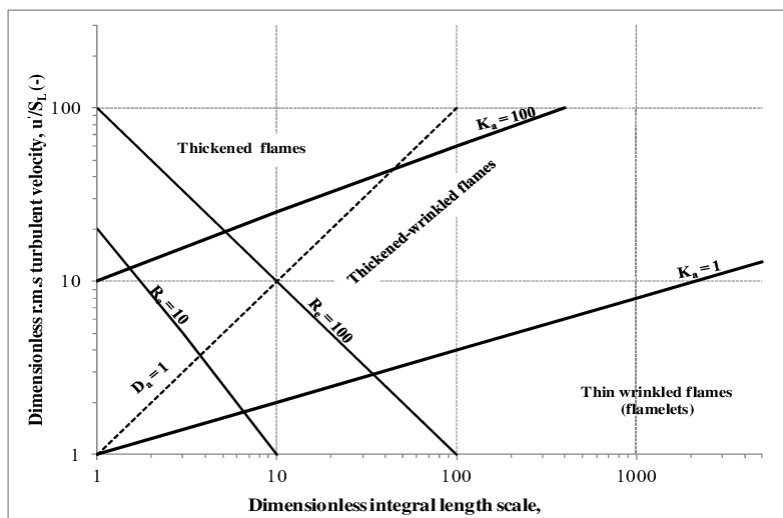


Figure 2.1: Turbulent premixed combustion diagram

2.4.2 Combustion model used under flamelet assumption

A combustion model is used to close the source term $\bar{\omega}_k$ in Eq. (2.29). To this purpose, several models valid under the flamelet assumption are available, such as the G-equation written by Kerstein *et al.* [28], the Thickened Flame-LES (TF-LES) model proposed by Colin *et al.* [29] and the Extended Coherent Flame Model-LES (ECFM-LES) developed by Richard *et al.* [30].

2.4.2.1 Basic principles

The ECFM-LES model chosen in this study is based on the Flame Surface Density (FSD) approach to compute LES premixed turbulent flame. This model is derived from the ECFM RANS model developed by Colin *et al.* [31], where the FSD is computed through a transport equation. Like for the Thickened Flame-LES model [29], the LES mesh is not refined enough to resolve the flame front of the order of 0.1 mm on several points. The method proposed in the ECFM-LES model is to use a new LES filter $\hat{\Delta}$ to increase the resolution of the flame front. As shown in Fig. 2.2, the combustion filter is typically chosen $\hat{\Delta} = n_{res}\Delta$ where $5 < n_{res} < 10$ and n_{res} is the number of points used to resolve the flame.

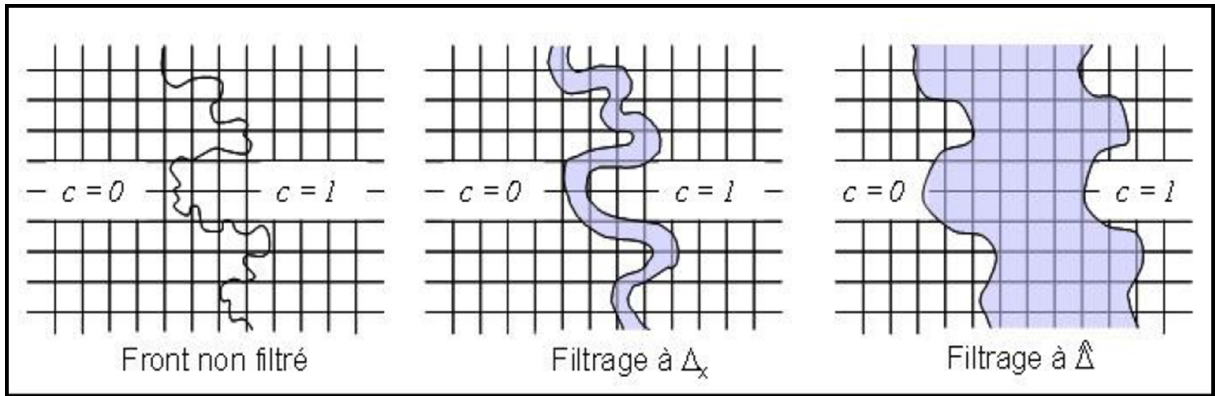


Figure 2.2: Filtering principle at $\hat{\Delta}$ size

By introducing this new filter size, the governing equations have to be written at this scale $\hat{\Delta}$, Eq. (2.29) becomes:

$$\frac{\partial \bar{\rho} \tilde{Y}_k}{\partial t} + \nabla \cdot (\bar{\rho} \tilde{Y}_k \tilde{u}) = -\nabla \cdot \left(\bar{\rho} \left[\frac{\nu}{S_c} + \frac{\hat{\nu}_t}{S_{ct}} \right] \nabla Y_k \right) + \bar{\rho} \tilde{\omega}_k \quad (2.49)$$

where \tilde{u} is the Favre filtered velocity, S_c and S_{ct} the molecular and turbulent Schmidt numbers. The turbulent cinematic viscosity $\hat{\nu}_t$ is defined as following:

$$\hat{\nu}_t = C \hat{u}' \hat{\Delta} \quad (2.50)$$

where C is a fitted constant linked to the turbulence model. As a first approach, \hat{u}' is estimated from the subgrid-scale turbulent intensity u' assuming a Kolmogorov cascade:

$$\hat{u}' = u' \left(\hat{\Delta} / \Delta_x \right)^{1/3} \quad (2.51)$$

where Δ_x and $\hat{\Delta}$ are respectively the length scales of the original mesh and the mesh at the combustion filter. The subgrid-scale turbulent velocity u' is based on the turbulent viscosity ν_t , on a similarity method or a rotational method. In the latter case, the filter size Δ_e corresponds to the largest scale affected by the flame thickening, that is to say δ_t^1 . In practice, $\Delta_e = 10\Delta_x$ with $\Delta_x = \sqrt[3]{\nu_t / u'}$. The subgrid scale turbulent velocity u'_{Δ_e}

is estimated using an operator, based on the rotational of the velocity field to remove the dilatational part of the velocity which must not be counted as "turbulence". A Laplacian operator is directly applied to the velocity:

$$u'_{\Delta_e} = c_2 \Delta_x^3 \left| \frac{\partial^2}{\partial x_j \partial x_j} \left(\epsilon_{lmn} \frac{\partial \bar{u}_n}{\partial x_m} \right) \right| \quad (2.52)$$

with $c_2 \approx 2$ and where ϵ_{lmn} stands for the permutation tensor.

The fuel density is decomposed into unburnt and burnt parts:

$$\bar{\rho}_F = \bar{\rho}_F^u + \bar{\rho}_F^b \quad (2.53)$$

Transport equations similar to that of other species Eq. (2.49) are defined for these fuel densities $\bar{\rho}_F^X = \bar{\rho} \tilde{Y}_F^X$, where X stands for unburnt (u) or burnt (b) state. To account for rich cases, the fuel in the burnt gases Y_F^b must be considered in addition.

Finally, the mean sensible enthalpy is deduced from the total energy $\tilde{h}_s = \tilde{e}_{tot} - \frac{1}{2} \tilde{u}_i \tilde{u}_i + \bar{p}/\bar{\rho}$. As diffusivities in species and energy equations need to be equal in the ECFM-LES approach, $Pr = Sc$ and $Pr_t = Sc_t$.

2.4.2.2 Unburnt and burnt gases properties

The fuel oxidation in ECFM-LES contains three equations, the system of which depends on whether the post-oxidation in the burnt gases is considered ($\alpha_{bg} = 1$) or not ($\alpha_{bg} = 0$) (see section 2.4.2.3:

$$\begin{aligned} & \beta \alpha (1 - \alpha_{CO}) \left[C_x H_y O_z + \left(x + \frac{y}{4} - \frac{z}{2} \right) O_2 \rightarrow x CO_2 + \frac{y}{2} H_2 O \right] \\ & \alpha_{bg} \beta \left[(1 - \alpha) + \alpha \alpha_{CO} \right] \left[C_x H_y O_z + \left(\frac{x}{2} + \frac{y}{4} - \frac{z}{2} \right) O_2 \rightarrow x CO + \frac{y}{2} H_2 O \right] \\ & (1 - \alpha_{bg}) \beta (1 - \alpha) \left[C_x H_y O_z + \left(\frac{x}{2} - \frac{z}{2} \right) O_2 \rightarrow x CO + \frac{y}{2} H_2 \right] \\ & (1 - \beta) \left[C_x H_y O_z^u \rightarrow C_x H_y O_z^b \right] \end{aligned} \quad (2.54)$$

The α and β coefficients depend on the local equivalence ratio $\bar{\Phi}$:

$$\begin{aligned} & \text{If } \bar{\Phi} < 1 : \alpha = 1, \beta = 1 \\ & \text{If } \bar{\Phi} > \bar{\Phi}_{crit} : \alpha = 0, \beta = \frac{\bar{\Phi}_{crit}}{\bar{\Phi}} \\ & \text{If } 1 \leq \bar{\Phi} \leq \bar{\Phi}_{crit} : \alpha = \frac{(4x+y+2z)-2\bar{\Phi}(x-z)}{\bar{\Phi}(2x+y)}, \beta = 1 \end{aligned} \quad (2.55)$$

with the critical equivalence ratio $\bar{\Phi}_{crit}$ is defined as:

$$\begin{aligned} & \text{If } \alpha_{bg} = 0 : \bar{\Phi}_{crit} = \frac{2}{x-z} \left(x + \frac{y}{4} - \frac{z}{2} \right) \\ & \text{If } \alpha_{bg} = 1 : \bar{\Phi}_{crit} = 2 \frac{\left(x + \frac{y}{4} - \frac{z}{2} \right)}{x + \frac{y}{2} - z} \end{aligned} \quad (2.56)$$

The parameter α_{CO} represents the molar fraction of produced CO with respect to CO₂. A constant value $\alpha_{CO} = 0.05$ is imposed when $\alpha_{bg} = 1$ and 0 otherwise. The oxidation of CO into CO₂ is performed following an additional step (see section 2.4.2.3). In the ECFM-LES approach, the flame thickness is supposed infinitely small, then the gases can be present only in two possible states: unburnt and burnt. In order to define correctly the species mass fractions in the unburnt state for variable equivalence ratio and dilution flows, transport equations for the species tracers \tilde{Y}_{T_k} are introduced [32]. \tilde{Y}_{T_k} represents the species mass fraction conditioned in the fresh gases $\tilde{Y}_k|^u$:

$$\tilde{Y}_{T_k} = \tilde{Y}_k|^u = \bar{\rho}_k^u / \bar{\rho}^u \quad (2.57)$$

where $\bar{\rho}_k^u$ is the mass density of species present in the fresh gases and $\bar{\rho}^u$ is the mass density of fresh gases. This transport equation is identical to the mean species transport Eq. (2.49) except that the reaction source term due to combustion is not included. This equation reads:

$$\frac{\partial \bar{\rho} \tilde{Y}_k|^u}{\partial t} + \frac{\partial \bar{\rho} \tilde{u}_i \tilde{Y}_k|^u}{\partial x_i} = \frac{\partial}{\partial x_i} \left(\bar{\rho} \left(\frac{\nu}{Sc} + \frac{\hat{\nu}_t}{Sc_t} \right) \frac{\partial \tilde{Y}_k|^u}{\partial x_i} \right) \quad (2.58)$$

Unburnt, burnt and mean densities are related following:

$$\bar{\rho}_k = \bar{\rho}_k^u + \bar{\rho}_k^b \quad (2.59)$$

$$\bar{\rho} = \bar{\rho}^u + \bar{\rho}^b \quad (2.60)$$

The filtered progress variable \tilde{c} can now be defined using the burnt gas density: $\bar{\rho}^b = \tilde{c} \bar{\rho}$. This relation is equivalent to $\bar{\rho}^u = (1 - \tilde{c}) \bar{\rho}$. In practice \tilde{c} is defined using the unburnt and tracer fuel mass fractions:

$$\tilde{c} = 1 - \frac{\tilde{Y}_F^u}{\tilde{Y}_{TF}} \quad (2.61)$$

Using these relations and Eq. (2.59) leads to:

$$\tilde{Y}_k = (1 - \tilde{c}) \tilde{Y}_k|^u + \tilde{c} \tilde{Y}_k|^b \quad (2.62)$$

In CVC chamber engines, the unburnt gases temperature T^u evolves during the variation of pressure, and also varies due to the equivalence ratio and dilution stratification when the fuel and air are not perfectly premixed. For this reason, a transport equation for the unburnt gases enthalpy \tilde{h}_s^u is introduced. Knowing \tilde{h}_s^u and $\tilde{Y}_k|^u$ allows to compute T^u and the burnt gases enthalpy can be deduced from:

$$\tilde{h}_s = (1 - \tilde{c}) \tilde{h}_s^u + \tilde{c} \tilde{h}_s^b \quad (2.63)$$

For small values of \tilde{c} , Eq. (2.63) leads to numerical problems. For this reason, the burnt gas enthalpy is calculated as follows:

$$\tilde{h}_s^b = \tilde{h}_s + \Delta h_{reac} \quad (2.64)$$

In this equation, the burnt gases enthalpy is assumed to be the result of a complete combustion at constant pressure.

This time, knowing \tilde{h}_s^b and $\tilde{Y}_i|b$ allows to compute T^b . The conditional densities in unburnt and burnt mixtures can be computed as follows:

$$\bar{\rho}|^u = \frac{\bar{p}W^u}{RT^u} \quad (2.65)$$

$$\bar{\rho}|^b = \frac{\bar{p}W^b}{RT^b} \quad (2.66)$$

2.4.2.3 Burnt gas chemistry

If CO₂ dissociation is neglected, the burnt gases temperature can be significantly over-estimated in engine cases. For this reason, a reduced chemistry in the burnt gases is introduced to take into account the effect of temperature on CO production rate. In this case, the post-oxidation of the fuel in the burnt gases can also be computed. The oxidation of CO into CO₂ is computed by considering the same kinetic mechanism as in TF-LES, in addition to the former reactions (2.54):



The use of this chemistry allows more physical functioning: the molar concentration of CO₂ produced by the fuel oxidation depends on the rate of the reaction and on the burnt gas temperature. The reaction rate $\tilde{\omega}_k^{bg}$ of species k is computed using an Arrhenius law and is written:

$$\tilde{\omega}_k^{bg} = W_k \nu_k \mathcal{Q}_1 \quad (2.68)$$

where $\nu_k = \nu_k'' - \nu_k'$ and \mathcal{Q}_1 is the rate progress of reaction which is written:

$$\mathcal{Q}_1 = K_f \prod_{k=1}^N \left(\frac{\bar{\rho} \tilde{Y}_k|b}{W_k} \right)^{\nu_k'} - K_r \prod_{k=1}^N \left(\frac{\rho \tilde{Y}_k|b}{W_k} \right)^{\nu_k''} \quad (2.69)$$

K_f and K_r are respectively the forward and reverse rates of reaction defined by:

$$K_f = A_f \exp\left(-\frac{E_a}{RT}\right) \quad (2.70)$$

$$K_r = \frac{K_f}{K_{eq}}$$

Where A_f and E_a are the pre-exponential factor and the activation energy and K_{eq} is the equilibrium constant defined by Kuo [33] for a reaction j :

$$K_{eq} = \left(\frac{P_0}{RT} \right)^{\sum_{k=1}^N \nu_{kj}} \exp\left(\frac{\Delta S_j^0}{R} - \frac{\Delta H_j^0}{RT} \right) \quad (2.71)$$

Here, $P_0 = 1$ bar, ΔH_j^0 and ΔS_j^0 are respectively the enthalpy (sensible + chemical) and the entropy changes for reaction j defined as follows:

$$\begin{aligned} \Delta H_j^0 &= h_j(T) + h_j(0) = \sum_{k=1}^N \nu_{kj} W_k (h_{s,k}(T) + \Delta h_{f,k}^0) \\ \Delta S_j^0 &= \sum_{k=1}^N \nu_{kj} W_k s_k(T) \end{aligned} \quad (2.72)$$

where $\Delta h_{f,k}^0$ is the mass enthalpy of formation of species k at temperature $T^0 = 0$ K.

The equilibrium computation allows the adjustment of the species mass fractions in the burnt gases and consequently the mean mass fractions and mean sensible enthalpy.

2.4.2.4 Reaction rate definition

The terms $\tilde{\omega}_k$, $\tilde{\omega}_F^u$ and $\tilde{\omega}_{h_s}$ appearing in the species, unburnt fuel and sensible enthalpy transport equations represent the mean reaction rate of the premixed turbulent flame. In the FSD approach they are modeled following:

$$\begin{aligned}\bar{\rho}\tilde{\omega}_k &= -\tilde{Y}_{T,i}\frac{W_k}{W_F}C_{r,k}\left(\tilde{\omega}_c^\Sigma + \tilde{\omega}_c^{ign}\right) + \tilde{c}\tilde{\omega}_i^{bg} \\ \bar{\rho}\tilde{\omega}_F^u &= \bar{\rho}^u\tilde{Y}_F|^u S_L \bar{\Sigma}_{\tilde{c}} \\ \bar{\rho}\tilde{\omega}_{h_s} &= \sum_k h_k^0 \bar{\rho}\tilde{\omega}_k\end{aligned}\tag{2.73}$$

with,

$$C_{r,k} = \alpha\beta(1-\alpha_{CO})\nu'_{k1} + \alpha_{bg}\beta[(1-\alpha) + \alpha\alpha_{CO}]\nu'_{k2} + (1-\alpha_{bg})\beta(1-\alpha)\nu'_{k3} + (1-\beta)\nu'_{k4}\tag{2.74}$$

The coefficients ν'_{k1} to ν'_{k4} are the stoichiometric coefficients in Eq. (2.54). $\tilde{\omega}_c^{bg}$ is the reaction rate due to burnt gas chemistry explained in section 2.4.2.3 and the standard ECFM-LES source term $\tilde{\omega}_c^\Sigma$, the ISSIM-LES spark ignition source term $\bar{\omega}_c^{ign}$ presented in section 2.4.3 are computed as follows:

$$\begin{aligned}\tilde{\omega}_c^\Sigma &= \bar{\rho}^u S_L \bar{\Sigma}_{\tilde{c}} \\ \bar{\omega}_c^{ign} &= \max\left(\bar{\rho}^u S_L \bar{\Sigma}_{\tilde{c}}, \bar{\rho}^b \frac{(\bar{c}_{ign} - \bar{c})}{dt}\right)\end{aligned}\tag{2.75}$$

Then, the remaining unknowns of the problem are the laminar flame speed S_L and the flame surface density $\bar{\Sigma}_{\tilde{c}}$, which are respectively presented in sections 2.4.2.5 and 2.4.2.6.

2.4.2.5 Computation of the laminar flame speed

The laminar flame speed S_L in the CVC chamber simulations is computed using one of the correlations proposed in solver AVBP. For C_xH_y with $x = 2$ to 8, the correlation of Metghalchi and Keck [34] can be used:

$$\begin{aligned}
 S_L &= S_L^0 \left(\frac{\tilde{T}^u}{T_0} \right)^\alpha \left(\frac{\bar{P}}{P_0} \right)^\beta (1 - 2.1\tilde{X}_{dil}) \\
 S_L^0 &= B_m + B_\Phi (\bar{\Phi} - \Phi_m)^2 \\
 \alpha &= 2.18 - 0.8 (\bar{\Phi} - 1) \\
 \beta &= -0.16 + 0.22 (\bar{\Phi} - 1) \\
 P_0 &= 0.1 \text{ MPa} , T_0 = 298 \text{ K}
 \end{aligned} \tag{2.76}$$

Φ is the local fuel/air equivalence ratio. Coefficients B_m , B_Φ and Φ_m are only known for propane and iso-octane and are presented in Tab. 2.1. A linear interpolation is used to compute these constants for a fuel C_xH_y .

Fuel	$B_m(m/s)$	$B_\Phi(m/s)$	ϕ_m
Propane	0.342	-1.387	1.08
Iso-octane	0.263	-0.847	1.13

Table 2.1: Parameter of the laminar flame speed correlation

2.4.2.6 The Flame Surface Density (FSD) transport equation

This section presents the FSD transport equation developed at IFP by S. Richard and O. Colin [30]. In a ECFM-LES approach, the FSD is computed through a transport equation. An exact unclosed equation for the local FSD has first been proposed by Candel and Poinso [35] and filtered by Veynante and Poinso [19] leading to the following equation for the filtered FSD $\bar{\Sigma} = |\nabla \tilde{c}|$:

$$\frac{\partial \bar{\Sigma}}{\partial t} + \nabla \cdot (\langle \mathbf{u} \rangle_s \bar{\Sigma}) = \langle \nabla \cdot \mathbf{u} - \mathbf{nn} : \nabla \mathbf{u} \rangle_s \bar{\Sigma} - \nabla \cdot (\langle S_d \mathbf{n} \rangle_s \bar{\Sigma}) + \langle S_d \nabla \cdot \mathbf{n} \rangle_s \bar{\Sigma} \tag{2.77}$$

where $\bar{\Sigma}$ is the FSD resolved at the LES filter, S_d the local displacement speed of the flame front relative to the gas and \mathbf{n} is the local normal to the flame front pointing towards the fresh gases on the iso-surface of the progress variable \tilde{c} defined in Eq. (2.78):

$$\mathbf{n} = - \frac{\nabla \tilde{c}}{|\nabla \tilde{c}|} \tag{2.78}$$

The first term on the right-hand side corresponds to the straining of the flame by the flow. The second and third terms represent respectively the planar propagation of the flame at speed S_d and the production or destruction of flame surface by the flame front curvature. These terms have to be modeled.

Compared to RANS approaches, the main difference relies on the fact that LES takes into account the effects of the resolved flow on the flame front. For this purpose, the FSD transport equation terms are split into resolved and unresolved parts. The transport equation of the modified FSD $\overline{\Sigma_{\tilde{c}}}$ is used instead of $\overline{\Sigma}$ because it enables to incorporate the unresolved transport of the progress variable [30]. The modified FSD $\overline{\Sigma_{\tilde{c}}}$ is defined as function of $\overline{\Sigma}$:

$$\overline{\Sigma_{\tilde{c}}} = \overline{\Sigma} + \nabla \cdot ((\bar{c} - \tilde{c})\mathbf{n}) \quad (2.79)$$

Where \tilde{c} is the filtered progress variable defined in Eq. (2.61) and \bar{c} is the resolve progress variable defined as a function of \tilde{c} :

$$\bar{c} = \frac{(1 + \tau)\tilde{c}}{1 + \tau\tilde{c}} \quad (2.80)$$

where $\tau\tilde{c} = \frac{\rho^u}{\rho^b} - 1$, with ρ^u and ρ^b are the unburnt and burnt gases densities and τ is the thermal expansion through the flame front.

The transport equation used in ECFM-LES is:

$$\frac{\partial \overline{\Sigma_{\tilde{c}}}}{\partial t} + T_{res} = T_{sgs} + S_{res} + S_{sgs} + C_{res} + C_{sgs} + P \quad (2.81)$$

where these terms are written as follows:

Resolved terms:

- The resolved transport term is defined by:

$$T_{res} = \nabla \cdot (\tilde{u}\overline{\Sigma_{\tilde{c}}}) \quad (2.82)$$

Where \tilde{u} is the velocity resolved at the combustion filter,

- The resolved strain:

$$S_{res} = (\nabla\tilde{u} - \mathbf{nn} : \tilde{u})\overline{\Sigma_{\tilde{c}}} \quad (2.83)$$

- The displacement of the flame is realised at the resolved scale with the propagation and the resolved curvature defined with:

$$P = \nabla \cdot (S_d \mathbf{n} \overline{\Sigma_{\tilde{c}}}) \quad (2.84)$$

$$C_{res} = S_d (\nabla \cdot \mathbf{n}) \overline{\Sigma_{\tilde{c}}} \quad (2.85)$$

where S_d is the relative propagation velocity to the average velocity the \tilde{c} iso-surface defined by:

$$S_d = (1 + \tau\tilde{c}) S_L \quad (2.86)$$

with S_L the laminar flame speed modeled in this thesis with the correlation of Metghalchi and Keck presented in paragraph 2.4.2.5.

Unresolved terms:

- The unresolved transport:

$$T_{sgs} = -\nabla \cdot \left(\sigma_c \frac{\widehat{\nu}_{sgs}}{S_{c_{sgs}}} \nabla \overline{\Sigma_{\tilde{c}}} \right) \quad (2.87)$$

where σ_c is a constant fixed at 1.0, $\widehat{\nu}_{sgs}$ is the turbulent kinematic viscosity at the combustion filter and $S_{c_{sgs}}$ the turbulent Schmidt number.

- The unresolved strain:

$$S_{sgs} = \alpha_{cfm} \Gamma \left(\frac{\widehat{u}'}{S_L}, \frac{\widehat{\Delta}}{\delta_l} \right) \frac{\widehat{u}'}{\sigma_c \widehat{\Delta}} \overline{\Sigma_{\tilde{c}}} \quad (2.88)$$

where Γ is an efficiency function proposed by Charlette *et al.* [36] and modified by Richard [37], δ_l is the laminar flame thickness estimated from Blints correlation [38] and α_{cfm} is a constant of the model, set to 1.0 in the present study.

- The unresolved curvature:

$$C_{sgs} = -\beta_0 S_L \frac{(\overline{\Sigma_{\tilde{c}}} - \overline{\Sigma}^{lam}) \overline{\Sigma_{\tilde{c}}}}{1 - \tilde{c}} + \beta_c S_L \frac{1 + \tau}{\tilde{c}} (\overline{\Sigma_{\tilde{c}}} - \overline{\Sigma}^{lam}) \overline{\Sigma_{\tilde{c}}} \quad (2.89)$$

where β_0 and β_c are the modeling constants respectively equal to 1 and $\frac{4}{3}$. $\overline{\Sigma}^{lam}$ is the laminar part of the FSD, which is defined as:

$$\overline{\Sigma}^{lam} = |\nabla \tilde{c}| + (\bar{c} - \tilde{c}) \nabla \cdot \mathbf{n} \quad (2.90)$$

2.4.3 The Imposed Stretch Spark Ignition Model for LES: ISSIM-LES

The Imposed Stretch Spark Ignition Model ISSIM-LES is based on the same electrical circuit description and flame kernel initialisation as the spark ignition model AKTIM developed at IFP-En [32]. This spark ignition model resides in the description of the flame kernel growth modelled thanks the modified flame surface density of ECFM-LES.

2.4.3.1 The spark model

At breakdown, the spark length is equal to the spark gap between the two electrodes. Then, the spark is stretched by convection and by the turbulent motion of the flow. The total length of the spark reads:

$$l_{spk} = \Xi_{spk} l_{spk}^{mean} \quad (2.91)$$

The curve wrinkling factor corresponds to the wringing of the spark by the turbulent eddies greater than the arc thickness l_c and lower than the half length of the spark ($l_M = 0.5 l_{spk}$). l_c is estimated following:

$$l_c = 2 \sqrt{\frac{i_s}{\pi D_s}} \quad (2.92)$$

where D_s is the current density at the electrode surface, which is on the order of 100 A/cm² during glow mode. The arc wringing equation is written:

$$\frac{1}{\Xi_{spk}} \frac{d\Xi_{spk}}{dt} = a_T \quad (2.93)$$

The computation of the turbulent strain a_T is similar to the ITNFS function in the equation of the flame surface density equation:

$$a_T = \Gamma \frac{u'_\Delta}{\Delta} \quad (2.94)$$

where Δ is the filtering length scale ($\Delta = 2\Delta_x$) and u'_Δ is the fluctuation velocity at the filtering length scale.

$$\Gamma = \frac{0.28}{\log(2)} \frac{3}{2} \left(\left(\frac{\Delta}{\max(l_c, \eta)} \right)^{3/2} - \left(\frac{\Delta}{\min(l_M, \Delta)} \right)^{3/2} \right) \quad (2.95)$$

The mean length of the spark l_{spk}^{mean} can be affected by the flow convection. The lack of experimental data does not allow the precise estimation of it and thus it is assumed to have an elliptical shape:

$$\frac{dl_{spk}^{mean}}{dt} = \frac{\pi}{\sqrt{2}} \frac{|\tilde{u}|^2 t}{(d_{ie}^2 + |\tilde{u}|^2 t^2)^{1/2}} \quad (2.96)$$

2.4.3.2 Initial burnt gases kernel

For $t > t_{bd}$, where t_{bd} is the duration of the breakdown, a critical ignition energy $E_c(t)$ is calculated [39]:

$$E_c = \frac{\gamma}{\gamma - 1} l_{spk} \pi p \delta_l^2 \quad (2.97)$$

where γ represents the ratio of specific heat capacities and δ_l the laminar flame thickness. As soon as the relation $E_{ign}(t_{ign}) > E_c(t_{ign})$ is satisfied, the ignition timing is considered reached, then an initial burnt gases mass m_{bg}^{ign} is deposited. Its volume corresponds to the critical energy of a cylinder of radius $2\delta_l$ and length l_{spk} :

$$m_{bg}^{ign} = \langle \rho^u l_{spk} 4\pi \delta_l^2 \rangle \quad (2.98)$$

where the brackets $\langle \rangle$ designate an average in the spark plug vicinity. This burnt gases volume being much smaller than the actual cell volume used today in LES, it needs to be filtered on the eulerian field at the combustion filter size $\hat{\Delta}$ in the vicinity of the spark. For this purpose, an arbitrary profile of the initial burnt gases volume fraction \bar{c}_{ign} needs to be defined. Here a gaussian function is chosen:

$$\bar{c}_{ign}(x, t_{ign}) = c_0 \exp \left(- \left(\frac{|x - x_{spk}|}{0.5\hat{\Delta}} \right)^2 \right) \quad (2.99)$$

where constant c_0 satisfies:

$$\int \rho^b \bar{c}_{ign} dV = m_{bg}^{ign} \quad (2.100)$$

ρ^b is the burnt gases density and x_{spk} the spark plug position. In order to impose the value $\bar{c}_{ign}(x, t_{ign})$ on the 3D computational domain, the reaction rate of the progress variable is modified, using the relation $\bar{\rho}\tilde{c} = \rho^b\bar{c}$:

$$\bar{\omega}_c^{ign} = \max \left(\rho^u S_L \bar{\Sigma}_{\tilde{c}}, \rho^b \frac{(\bar{c}_{ign} - \bar{c})}{dt} \right) \quad (2.101)$$

where dt is the computational time-step. In expression (2.101), the reaction rate induced by a possible pre-existing flame is also taken into account. This allows the consideration of the interaction of flames coming from different ignitions. The limitations of AKTImeuler comes from its "0D" model approach. The main idea of ISSIM-LES is therefore to model the reaction rate thanks to the FSD equation from the very beginning of ignition. Consequently, a FSD source term due to ignition must be introduced. As suggested by experiments, the initial flame kernel is assumed spherical, therefore its radius can be defined as:

$$r_b^{ign} = \left(\frac{3}{4\pi} \int \bar{c}_{ign} dV \right)^{1/3} \quad (2.102)$$

Defining $\Sigma_{ign} = 3\bar{c}/r_b^{ign}$ allows to recover the surface $4\pi (r_b^{ign})^2$ of the initial sphere [39]. This finally allows to define the ignition FSD source term:

$$\bar{\omega}_\Sigma^{ign} = \max \left(0, \frac{(\Sigma_{ign} - \bar{\Sigma}_{\tilde{c}})}{dt} \right) \quad (2.103)$$

The ignition phase, is extremely fast in real engines, which makes it exist only for several iterations in the computation. The later ignition is governed by different equations, which is presented in the following paragraph.

2.4.3.3 Modification of the FSD equation

For a few milliseconds after the kernel creation, the flame radius r_b remains smaller than the combustion filter size $\hat{\Delta}$ with actual mesh resolutions. For this reason, the flame kernel is described at the subgrid-scale level, which leads to a maximum value of \tilde{c} much smaller than one unity which started typically at t_{ign} close to 0.001 for a cell size $\Delta_x = 1$ mm. The subgrid-scale contributions ($C_{sgs} + S_{sgs}$) in Eq. (2.81) represent the FSD creation by turbulent stretch, while the resolved contributions. ($C_{res} + S_{res}$) represent the FSD creation by resolved curvature and strain. Therefore, the FSD creation by the subgrid scale curvature $2/r_b$ of the early flame kernel is not accounted for and needs to be introduced. For this purpose, the flame kernel is assumed locally as a sphere of radius r_b and surface $S_{tot} = 4\pi(r_b)^2\Xi$. At constant pressure, the radius time derivative reads:

$$\frac{dr_b}{dt} = (1 + \tau) \Xi S_L \quad (2.104)$$

where the expansion ratio τ is defined as $\tau\tilde{c} = \rho^u/\rho^b - 1$. The FSD source term reads in this case:

$$\frac{1}{\Sigma} \frac{d\Sigma}{dt} \Big|_{sphere} = \frac{1}{S_{tot}} \frac{dS_{tot}}{dt} = \frac{1}{\Xi} \frac{d\Xi}{dt} + \frac{2}{r_b} (1 + \tau) \Xi S_L \quad (2.105)$$

The first RHS term represents the turbulent stretch and is already modeled by term $C_{sgs} + S_{sgs}$ in Eq. (2.81). The second term represents the stretch induced by the curvature $2/r_b$ and therefore needs to be introduced in a modified FSD equation:

$$\frac{\partial \bar{\Sigma}_{\tilde{c}}}{\partial t} + T_{res} = T_{sgs} + \alpha_{ign} (S_{res} + C_{res}) - \nabla \cdot (S_d \mathbf{n} \bar{\Sigma}_{\tilde{c}}) + S_{sgs} + \alpha_{ign} C_{sgs} + (1 - \alpha_{ign}) S_{ign} + \bar{\omega}_{\Sigma}^{ign} \quad (2.106)$$

And,

$$S_{ign} = \frac{2(1+\tau)}{3} \frac{S_L}{\tilde{c}} \left(\bar{\Sigma}_{\tilde{c}} - \bar{\Sigma}^{lam} \right) \bar{\Sigma}_{\tilde{c}} \quad (2.107)$$

where transition coefficient $\alpha_{ign}(x, t)$ should remain close to zero during ignition and equal to one when ignition is over. This way, the resolved contribution $(-\nabla \cdot (S_d \mathbf{n} \bar{\Sigma}_{\tilde{c}}) + S_{res} + C_{res})$ is suppressed during ignition and replaced by the S_{ign} . This transition coefficient α_{ign} is defined as:

$$\alpha_{ign} = 0.5 \left(1 + \tanh \left(\frac{r_b^+ - 0.75}{0.15} \right) \right) \text{ with } r_b^+ = r_b / \hat{\Delta} \quad (2.108)$$

To compute multi-spark ignitions, r_b must be modeled through a transport equation. The quantity Ψ is used here:

$$\bar{\rho} \Psi = \bar{\rho} \tilde{c} \frac{2}{r_b} = \frac{2}{3} \bar{c} \Sigma_{ign} \quad (2.109)$$

Assuming Ψ is convected and diffused as a passive scalar, its reaction rate is easily deduced [39]:

$$\bar{\rho} \frac{\partial \Psi}{\partial t} \nabla \cdot (\bar{\rho} \tilde{\mathbf{u}} \Psi) = \nabla \cdot \left(\frac{\hat{\mu}_{sgs}}{S C_{sgs}} \nabla \Psi \right) - \frac{(1+\tau)}{r_b} \Xi S_L \bar{\rho} \Psi + \frac{2}{r_b} \bar{\omega}_c + \bar{\omega}_{\Psi}^{ign} \quad (2.110)$$

As a first approximation, Ξ is set to one. Note this approximation is not very prejudicial to the model because it only leads to a slower increase of r_b in time, which in turn leads to delaying the transition from S_{ign} to $C_{res} + S_{res} + P$ in the FSD equation. As $C_{res} + S_{res}$ and S_{ign} become identical for a spherical flame when \tilde{c} reaches unity, the flame surface growth rate should not be very much affected by this delayed transition. Like for $\hat{\Sigma}$, a source term for Ψ needs to be added at the instant of flame kernel creation. It consistently reads:

$$\bar{\omega}_{\Psi}^{ign} = \max \left(\frac{(2/3) \rho^b \Sigma_{ign} - \bar{\rho} \Psi}{dt}, 0 \right) \quad (2.111)$$

2.4.4 The Wall/Flame interactions Model

In internal combustion engines, heat losses near the walls strongly influence the combustion processes and can lead to flame extinction. Hence, in a ECFM-LES model, it is necessary to take the wall effects on the flame surface density into account. The proposed model considers that the laminar flame speed is affected by enthalpy losses to the wall and that the flame wrinkling is modified near the wall.

For non-adiabatic flames, it is convenient to introduce a classical enthalpy loss parameter \tilde{L}_h :

$$\tilde{L}_h = \tilde{c} + \frac{\tilde{h}^u - \tilde{h}^m}{\Delta H} \quad (2.112)$$

where ΔH is the reaction heat release and \tilde{h}^m is the mean enthalpy defined by:

$$\tilde{h}^m = (1 - \tilde{c})\tilde{h}^u + \tilde{c}\tilde{h}^b \quad (2.113)$$

with \tilde{h}^u is the fresh gases enthalpy and \tilde{h}^b is the burnt gases enthalpy.

In an adiabatic premixed flame with unit Lewis number, \tilde{L}_h is zero everywhere. When the flame is non-adiabatic for example, near walls, \tilde{L}_h increases, indicating that quenching is possible. By extending analytical results from laminar to turbulent flames, the speed S_L of a flame submitted to heat losses is linked to the "adiabatic" flame speed S_L^0 by:

$$S_L = S_L^0 \exp\left(-\gamma_{hl}\beta\tilde{L}_h\right) \quad (2.114)$$

where γ_{hl} is a parameter fitted with DNS to 2, and β is the reduced activation energy:

$$\beta = \frac{\left(\tilde{T}_{ad}^b - \tilde{T}^u\right) T_a}{\left(\tilde{T}_{ad}^b\right)^2} \quad (2.115)$$

where \tilde{T}^u , \tilde{T}_{ad}^b , T_a correspond respectively to the fresh gases, the adiabatic flame and the activation temperatures. In addition, it is important to note that the flame speed S_L^0 depends on the fresh gases temperature. This temperature can be obtained by inverting the fresh gases enthalpy \tilde{h}^u . This enthalpy is, as the mean enthalpy \tilde{h}^m , submitted to heat transfer near the wall, so that \tilde{T}^u and consequently S_L^0 are modified. This heat flux Q_{h^u} is written, as for the mean enthalpy, by a wall law-of-the-wall the type:

$$Q_{h^u} = K \left(\tilde{T}^u - T^{wall}\right) \quad (2.116)$$

where K is a heat transfer coefficient and T^{wall} the temperature of the wall.

The focus is now on the wall effect, namely on the flame wrinkling. It is directly taken into account for many terms of Eq. (2.73) (P , C_{res} , C_{sgs}) as S_L is modified by the laminar flame speed correction of Eq. (2.114) and by the heat flux of fresh gases enthalpy near the wall. The production terms S_{sgs} and S_{res} involved in Eq. (2.73) are then corrected by assuming that flame surface density can not be created at the wall, so that:

$$S_{sgs}^{wall} = 0 \text{ and } S_{res}^{wall} = 0 \quad (2.117)$$

2.5 Liquid injection modeling

The liquid injection model chosen in this present work is the Lagrangian approach where each droplet is considered individually. This method was implemented in the LES solver by Garcia [40]. Two different approaches can be used to solve the liquid phases, the first one insists in representing each real droplet with a numerical one. In this case, the approach can be called a DNS. However, the modeling of real sprays with a high number of droplets can significantly increase the CPU cost. That is why, the second approach consists in collecting several real droplets with the same physical properties in the same numerical droplet. The second method is used in the present work.

In this method, each droplet is considered as a material point moving in the fluid domain, this approach relies on several assumptions:

- Surface tension is major which leads to spherical droplets,
- The dispersed phase is diluted, the liquid volume fraction is lower than 10^{-4} [41],
- Droplet-droplet interactions such as collisions are negligible.

2.5.1 Source terms of Lagrangian liquid injection

In order to take into account the liquid phase and phenomena involved by the liquid injection, source terms are added into flow governing equations presented in section 2.2. The source terms applied in the momentum equations Eq. (2.27) result from the drag of each particle. The liquid phase evaporates and transfers some mass of from this liquid phase to the gaseous state, which is taken into account in the transport equation of the fuel mass fraction equation Eq. (2.29). The energy required during the evaporation process, has to be removed from the transport equation of the total energy Eq. (2.28). These source terms are quickly presented in the following paragraphs.

2.5.1.1 Drag of particles

The drag force applied by the gas on an isolated liquid particle and applied into Eq. (2.27) is obtained by the following equation:

$$F_{d,i} = \frac{1}{2} \bar{\rho}_g C_D A_p \|\tilde{u}_g - u_p\| (\tilde{u}_{g,i} - u_{p,i}) \quad (2.118)$$

where $\bar{\rho}_g$ is the density of the gas phase, C_D the drag coefficient, $A_p = 1/4 \times \Pi d_p^2$ with d_p the diameter of the particle, \tilde{u}_g and u_p respectively the fluid and the particle velocities. Several drag coefficient C_D formula can be found in the literature, However, the common formula used is the empirical correlation proposed by Schiller and Naumann [42]:

$$C_D = \frac{24}{Re_p} (1 + 0.15 Re_p^{0.687}) \quad (2.119)$$

which is valid for particle Reynolds number $Re_p < 1000$, which compares the inertial forces with the viscous forces:

$$Re_p = \frac{\rho_p d_p \|\tilde{u}_g - u_p\|}{\mu_p} \quad (2.120)$$

2.5.1.2 Evaporation model, mass and heat transferts

As soon as a droplet is put in a flow without velocity at a higher temperature than itself, mass and heat transfers occur on the droplet surface not at saturation. The evaporation models implemented in the solver AVBP assume the thermodynamic equilibrium law based on the Spalding mass-transfer model [43]. The following assumptions are made:

- A spherical and isolated droplet is considered, interactions between droplets are neglected.
- The thermal conductivity in the liquid phase is infinite, which results in a homogeneous temperature over the droplet volume.
- The droplet is assumed to be at equilibrium with the surrounding gas phase (but diameter and temperature evolve over time).

The derivation of the evaporation model and the notations follow the outlines given by Kuo [33], Sirignano [44] and Boileau [45].

The gaseous field around a given droplet is considered non-convective, i.e. the only non-zero velocity component at any given location points in radial direction. The gas flow is also assumed to be quasi steady, which means that equations are independent of time. Furthermore, the position of the liquid surface is considered constant. This reflects the fact that $\rho_l \gg \rho_g$, which is resulting in a velocity of the receding liquid surface smaller than the evaporated fuel velocity, which is moving away from the surface. The problem is formulated in spherical coordinates (illustrated in Fig. 2.3) for radius between the droplet surface (index ζ) and the far-field (index ∞). The following set of equations of the gaseous flow field for $r > r_\zeta$ is obtained:

$$\text{Mass conservation:} \quad \rho u r^2 = \text{const} = (\rho u r^2)_\zeta = \frac{\dot{m}_F}{4\pi} \quad (2.121)$$

$$\text{Fuel species conservation:} \quad \rho u r^2 \frac{dY_F}{dr} = \frac{d}{dr} \left(r^2 [\rho D_F] \frac{dY_F}{dr} \right) \quad (2.122)$$

$$\text{Enthalpy equation:} \quad \rho u r^2 \frac{dC_P T}{dr} = \frac{d}{dr} \left(\frac{\lambda}{c_P} r^2 \frac{dc_P T}{dr} \right) \quad (2.123)$$

The expression $[\rho D_F]$ in Eq. (2.122) contains the diffusion coefficient of the species representing the fuel, D_F , and the density of the mixture in the gas phase, ρ . It can be expressed as a function of the gas viscosity μ and the Schmidt number of the gaseous fuel Sc_F .

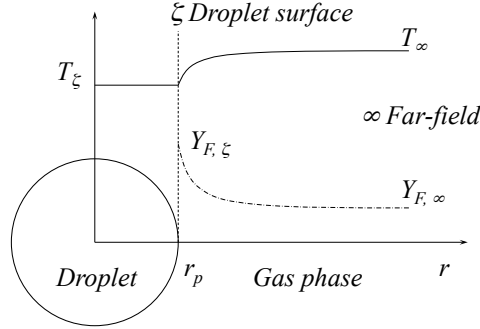


Figure 2.3: Variations of the temperature T and the fuel mass fraction Y_F over the radial distance from a spherical single droplet with constant temperature T_ζ

Mass transfer:

The model for the mass transfer between a single, isolated droplet and the surrounding gas is derived using the equation of species conservation Eq. (2.122). Two boundary conditions intervene, one at the droplet surface (ζ), the other at the far-field (∞).

Eq. (2.122) can be integrated to give:

$$\rho u r^2 Y_F = r^2 [\rho D_F] \frac{dY_F}{dr} + c_1 \quad (2.124)$$

The constant c_1 is determined by observing that $\rho u r^2 Y_F - r^2 [\rho D_F] \frac{dY_F}{dr}$ is the fuel flux. Since only the fuel is moving, this flux is the total flux $\rho u r^2$ so that $c_1 = \rho u r^2 = \dot{m}_F / 4\pi$. The equation for Y_F becomes

$$\rho u r^2 (Y_F - 1) = r^2 [\rho D_F] \frac{dY_F}{dr} \quad (2.125)$$

Assuming that $[\rho D_F]$ is constant allows to integrate Eq. (2.125) between r and ∞ :

$$\frac{\dot{m}_F}{4\pi r [\rho D_F]} = \ln \left(\frac{Y_{F,\infty} - 1}{Y_F - 1} \right) \quad (2.126)$$

Applying the boundary conditions at $r = r_\zeta$ leads to:

$$\dot{m}_F = 4\pi r_\zeta [\rho D_F] \ln(B_M + 1) \quad \text{where} \quad B_M = \frac{Y_{F,\zeta} - Y_{F,\infty}}{1 - Y_{F,\zeta}} \quad (2.127)$$

Heat transfer:

The derivation of a law for the temporal evolution of a droplet's temperature involves the enthalpy conservation equation Eq. (2.123) with boundary conditions at the far-field (∞)

and the droplet surface (ζ). The balance enthalpy equation on the liquid phase leads to:

$$\frac{d}{dt} (m_p h_{s,l}(T_p)) = \Phi_l^c + \Phi_l^{cv} \quad (2.128)$$

where Φ_l^c and Φ_l^{cv} are respectively the conductive and convective fluxes.

Considering the conservation law at the liquid-gas interface, the balance enthalpy fluxes at the interface describe in Fig. 2.4 leads to:

$$\Phi_l^{cv} + \Phi_l^c + \Phi_g^{cv} + \Phi_g^c = 0 \quad (2.129)$$

where Φ_g^{cv} and Φ_g^c are respectively the convective and conductive fluxes which are then applied in the transport equation of the total energy Eq. (2.28).

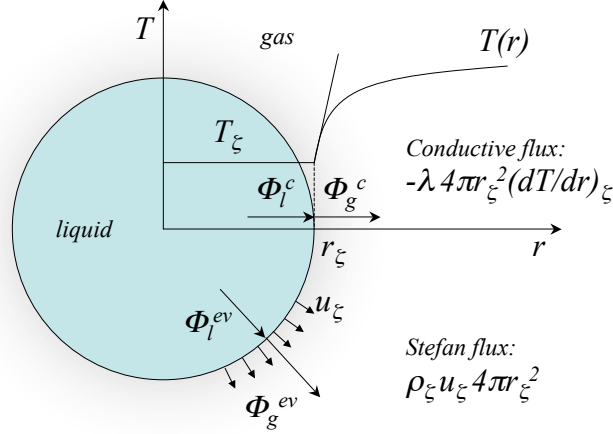


Figure 2.4: Contributions to the enthalpy balance at the liquid-gaseous interface

At the liquid-gas interface, the convective fluxes Φ_{cv} in both phases are defined by:

$$\Phi_g^{cv} = \dot{m}_F h_{s,F}(T_\zeta) \quad (2.130)$$

$$\Phi_l^{cv} = \dot{m}_p h_{s,p}(T_p) \quad (2.131)$$

Using the assumption: $T_\zeta = T_p$ gives:

$$\Phi_g^{cv} + \Phi_l^{cv} = \dot{m}_p [h_{s,p}(T_p) - h_{s,F}(T_p)] \quad (2.132)$$

Using the definition of the latent heat:

$$L_v(T) = h_{s,F}(T) - h_{s,p}(T) \quad (2.133)$$

And the balance fluxes Eq. (2.129) yields the following form:

$$\Phi_l^c + \Phi_g^c - \dot{m}_p L_v(T_p) = 0 \quad (2.134)$$

The conductive heat transfer Φ_g^c of the gaseous phase is proportional to the temperature gradient at the surface.

$$\Phi_g^c = \left(-4\pi r^2 \frac{\lambda}{c_P} \frac{dC_P T}{dr} \right)_\zeta \quad (2.135)$$

Finally, using Eqs. (2.129) and (2.135), the convective liquid flux is:

$$\Phi_l^c = \left(4\pi r^2 \frac{\lambda}{C_P} \frac{dC_P T}{dr} \right)_\zeta + \dot{m}_p L_v(T_p) \quad (2.136)$$

By developing Eq. (2.128) and using Eqs. (2.131) and (2.136) yields to:

$$\frac{d c_{p,l} T_p}{dt} = \frac{1}{m_p} \left[\left(-4\pi r^2 \frac{\lambda}{c_P} \frac{d c_P T}{dr} \right)_\zeta + \dot{m}_p L_v(T_p) \right] \quad (2.137)$$

The radial variation of the conductive flux of the gas phase is determined by integrating Eq. (2.123). Using boundary conditions on the droplet surface gives:

$$\dot{m}_F (c_p(T)T - c_p(T_\zeta)T_\zeta) = 4\pi r^2 \frac{\lambda}{c_p} \left[\frac{d c_p T}{dr} \right] - 4\pi r_\zeta^2 \frac{\lambda}{c_p} \left[\frac{d c_p T}{dr} \right]_\zeta \quad (2.138)$$

where $r_\zeta = r_p$. By doing a second integration and use far-field boundary conditions, Eq. (2.138) becomes:

$$\dot{m}_F = 4\pi r_p \frac{\lambda}{c_p} \ln(B_T + 1) \quad (2.139)$$

where B_T is the heat transfer Spalding number defined by:

$$B_T = \frac{(c_p(T_\infty)T_\infty - c_p(T_\zeta)T_\zeta) \dot{m}_F}{\Phi_g^c} \quad (2.140)$$

The mass flux expression in Eqs. (2.127) and (2.139) are used to obtain:

$$B_T = (1 + B_M)^{\frac{1}{Le_F}} - 1 \quad (2.141)$$

with the *Lewis* number of the fuel species Le_F :

$$Le_F = \lambda / (c_p \rho D_F) \quad (2.142)$$

Finally the convective flux of the gas phase Φ_g^c :

$$\Phi_g^c = 2\pi d_p \frac{\lambda}{c_p} (c_p(T_\zeta)T_\zeta - c_p(T_\infty)T_\infty) \frac{\ln(B_T + 1)}{B_T} \quad (2.143)$$

where the droplet temperature evolution is defined as:

$$\frac{d c_{p,l} T_p}{dt} = \frac{1}{m_p} \left[\dot{m}_p L_v(T_p) - 4\pi d_p \frac{\lambda}{c_p} (c_p(T_p)T_p - c_p(T_\infty)T_\infty) \frac{\ln(B_T + 1)}{B_T} \right] \quad (2.144)$$

2.5.2 Spray breakup modeling

In the studied apparatus presented in chapter (5), the carburation is realised in a chamber upstream of the combustor thanks to 8 automotive injectors, which generates large droplets. The breakup of the larger droplets occurs during the intake phase, where high intensity of the velocity is observed above 200 m/s. Therefore, the secondary breakup has to be taken into account in order to meet a droplet size distribution consistent with the experiment. In this study, the energy Spectrum Analogy Breakup (SAB) model developed at IFP-En [46], is used to capture this phenomenon. The breakup of droplets has been the subject of many experimental, theoretical and numerical studies. Four regimes of breakup are today identified, which are as a function of Weber number We_p and Ohnesorge number Oh_p . These two numbers are defined as follows:

$$We_p = \frac{\rho_g |u_g - u_p| d_p}{\sigma} \quad Oh_p = \frac{\nu_p}{\sqrt{\rho_p d_p \sigma}} \quad (2.145)$$

Where ρ_g and ρ_p are respectively the mass density of the gas and the liquid, u_g and u_p the velocities of the gas and the droplet, d_p the diameter of the particle, σ the surface tension and ν_p the dynamic viscosity of the droplet.

The breakup model is activated as soon as the following criteria are met:

$$We_p > We_c \quad (2.146)$$

And,

$$r_{p,m} > r_{clip} > r_s \quad (2.147)$$

Where We_c is the critical Weber number, which defines the different regimes. $r_{p,m}$ is the radius of the mother droplet, r_{clip} a user-defined radius, below which all the liquid phase is instantaneously evaporating, which is commonly set to 2.5 μm . r_s the maximum stable radius of the child droplet.

The secondary breakup phenomenon is defined by the breakup duration and the maximum stable radius.

Breakup duration

In the SAB secondary breakup model, the duration of the breakup τ_{sab} is calculated as follows:

$$\tau_{sab} = (T_{bu} - T_{init}) \frac{d_{m,p}}{|u_g - u_p|} \sqrt{\frac{\rho_{p,m}}{\rho_g}} \quad (2.148)$$

Where $d_{m,p}$ and $\rho_{p,m}$ are the diameter and the density of the mother droplet, T_{bu} is the dimensionless breakup duration given by Pilch and Erdman [47] correlations:

$$\begin{aligned} T_{bu} &= 6.00(We_p - 12)^{-1/4} & 12 < We_p < 18 \\ T_{bu} &= 2.45(We_p - 12)^{-1/4} & 18 < We_p < 45 \\ T_{bu} &= 14.1(We_p - 12)^{-1/4} & 45 < We_p < 351 \\ T_{bu} &= 0.76(We_p - 12)^{-1/4} & 351 < We_p < 2670 \\ T_{bu} &= 5.5 & 2670 < We_p \end{aligned} \quad (2.149)$$

And T_{init} is the period of initialisation of the breakup, which depends on the breakup regimes:

$$T_{init} = 1.9(We_p - We_c)^{-1/4} (1.0 + 2.2 Oh^{1.6}) \quad (2.150)$$

Maximum stable radius

The maximum stable radius of a child droplet r_s is calculated by the following expressions:

$$r_s = r_{p,m} \left(\frac{We_c}{We_p} \right)^{\alpha_{sab}} \quad (2.151)$$

Where α_{sab} depends on the breakup regimes:

$\alpha_{sab} = 1$	$We_p < 45$	Bag breakup regime,	
$\alpha_{sab} = 3/5$	$45 < We_p < 120$	Multimode breakup regime,	
$\alpha_{sab} = 2/5$	$120 < We_p < 350$	Shear or thinning breakup regime,	(2.152)
$\alpha_{sab} = 1/7$	$350 < We_p$	Catastrophic breakup regime.	

energy Spectrum Analogy Breakup (SAB model)

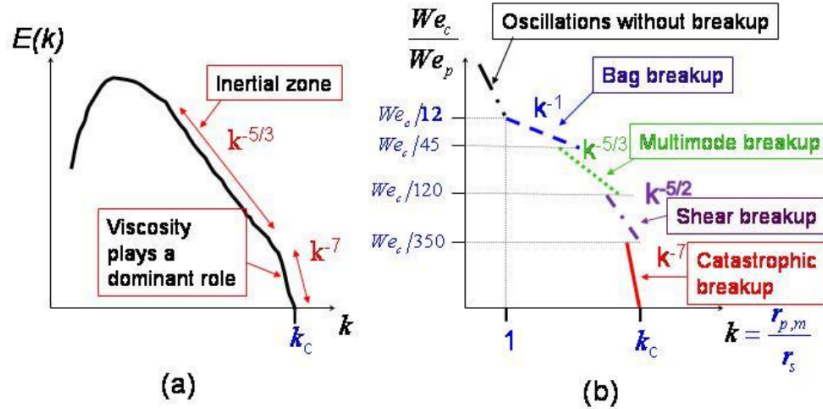


Figure 2.5: Extracted from [46]: Definition of the energy spectrum of breakup (b) by analogy to the turbulent energy spectrum (a)

The Discontinuities in the spectrum of breakup presented in Fig. 2.5, reflect changes in the regime of the breakup. The wave number k decreases at each breakup regime change, while the stable radius r_s increases. For each of the four breakup regimes considered in the SAB model, the exponent α_{sab} has been determined assuming an analogy between the energy spectrum of breakup and the energy spectrum of turbulence. For each breakup regime, the value of α_{sab} specifies the turbulence effects on the size of the produced child droplets.

2.5.3 Distribution of the source terms, the projection operator

The projection operator W is used to scatter the contribution of the source terms S_{Lag}^n of each droplet n at the position x_n , here applied on the node j located at the position x_j . The expression of the global source term \bar{S}_{Lag}^{tot} is added in the momentum Eq. (3.1) or the total energy Eq. (2.28):

$$\bar{S}_{Lag} = \frac{1}{N_p} \sum_{n=1}^{N_p} S_{Lag}^n \quad (2.153)$$

where N_p is the number of droplets surrounding the node j , S_{Lag}^n is the source terms of the liquid phase, namely the mass transfer, the drag or the heat transfer, calculated at the particle n , $W(x_n, x_j)$ is the projection operator from particle n at the position x_n to the grid node j at the position x_j . The projection operator is constructed to be inversely proportional to the distances $d(x_n, x_j)$ between the liquid particle n and the node j :

$$W(x_n, x_j) = \frac{1/d(x_n, x_j)}{\sum_{k=1}^N 1/d(x_n, x_k)} \quad (2.154)$$

where N is the number of vertices of the cell.

Fig. 2.6 sketches resulting drag terms $\vec{F}_d^n \times W(x_n, x_j)$ of one particle n on the node j .

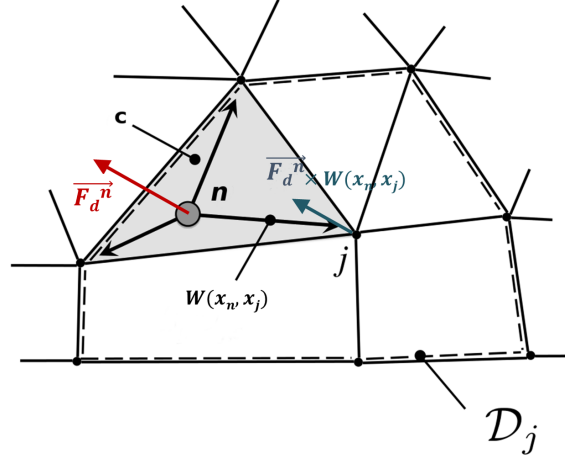


Figure 2.6: Projection weight W of the particle n onto the vertices j

In Fig. 2.6, the red vector \vec{F}_d^n is the drag calculated at the particle n and the blue vector is the terms applied on the node j . Obviously, all vertices of cell c receive the scattered source terms calculated from \vec{F}_d^n and the projection operator $W(x_n, x_j)$.

2.6 Numerical approaches for moving boundaries

As explained in section 1.1.3, constant volume combustion chambers require moving parts as the intake and the exhaust systems to open and close the chamber. These systems have to be modeled in our simulations. Nowadays, several numerical methods exist to incorporate moving parts, among which the following:

- The Arbitrary Lagrangian Eulerian method,
- A coupling method through overlapping grids: the "Multi Instance Solver Coupled through Overlapping Grids" (MISCOG) implemented in the AVBP LES solver,
- An Immersed Boundary Method.

All these methods are implemented in the AVBP-LES solver and are presented hereafter.

2.6.1 Arbitrary Lagrangian Eulerian

The Arbitrary Lagrangian Eulerian description was presented by C. W. Hirt *et al.* [48] and was implemented in the CFD code AVBP by V. Moureau *et al.* [49]. This numerical approach is commonly used to model moving boundaries in linear motions such as the valves and the engine pistons in internal combustion engine simulations. In this kind of simulations, the valves and the engine pistons cover respectively a distance of a few millimetres and few centimetres. To make the simulation feasible, users generate a set of meshes which are deformed during the motion of the parts. These meshes divide the simulation in several phases. For each mesh, the end of the deformation is determined by mesh quality criteria. When the values of the criteria are reached, a new mesh is created at the same crank angle position to start the following new phase. At the end of each phase, the momentum, the energy and the species of the deformed mesh are projected on the new one thanks to an interpolation algorithm. The principle of this process is shown in Fig. 2.7.

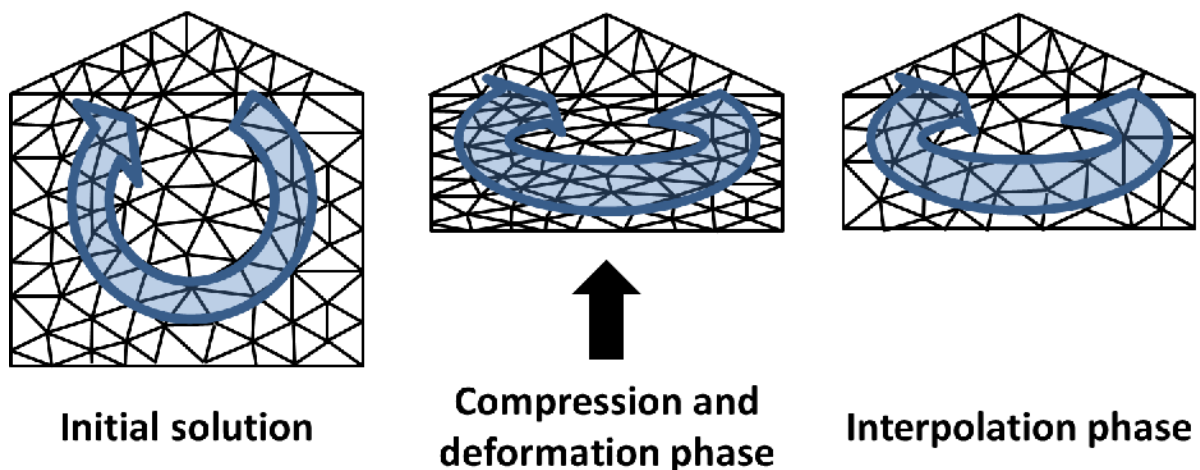


Figure 2.7: Mesh management in internal combustion engine simulation, where the blue arrow sketches the tumble motion

This numerical approach is currently used in spark ignition engine applications and allows the analysis of the physical phenomena involved in these engines. A. Robert *et al.* [50, 51] studied knocking combustion using Extended Coherent Flame Model (ECFM-LES) [30] coupled with the ignition model ISSIM-LES [39], presented in section 2.4, and the Tabulated Kinetics of Ignition (TKI) [52]. These moving boundaries method and these combustion models are used by K. Truffin *et al.* [53] to study the cyclic-to-cycle variability encountered in the SGEmac engine. Moreover, the ALE method and the Thickened Flame model for LES (TFLES) [54] was used by Misdariis *et al.* [55] to analyse the same kind of cycle-to-cycle variability.

2.6.2 Multi Instance Solver Coupled through Overlapping Grids (MISCOG)

The Multi Instance Solver Coupled through Overlapping Grids was developed for turbomachinery applications. Several instances of the LES solver, used for static and rotational parts, are coupled through overlapping zone with the coupler OpenPALM [56]. In this method, both instances are exchanging Dirichlet boundary conditions. Most of flow structures are then resolved and transferred by preserving the flow coherence and the properties of the numerical schemes. It is indeed crucial to transport the information at the right physical speed across the interface, without dissipating the resolved turbulent vortices and the acoustic waves structures.

This numerical approach was firstly developed to study a compressor stage using a RANS solver [57, 58]. J. U. Schlüter *et al.* [59] performed the simulation of the whole gas turbine system with the compressor, the combustion chamber and the turbine. In this simulation, the compressor and the turbine were calculated using a RANS solver whereas the combustion chamber was performed using a LES solver. In fact, CFD for turbomachinery still remaining a challenging subject, because of the high Reynolds and Mach-number flows encountered in compressor and turbine stages.

Fig. 2.8 exhibits this method functioning [60], where the domain is divided into two zones, the AVBP01 is coloured in red, is the static part and the AVBP02 filled in blue, is the rotor. In this study, the conservative variables were exchanged between the two instances and interpolated through the overlapping grid coloured in black, where the exchanges are highlighted with the purple arrows.

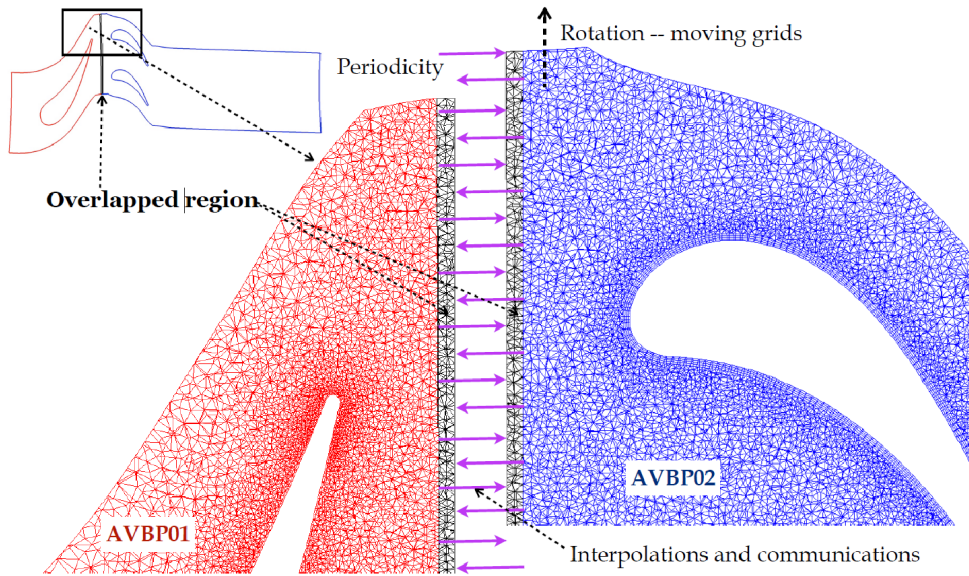
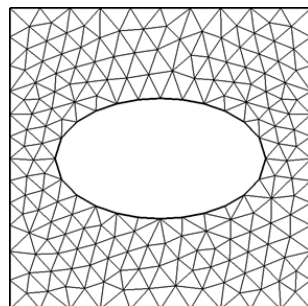


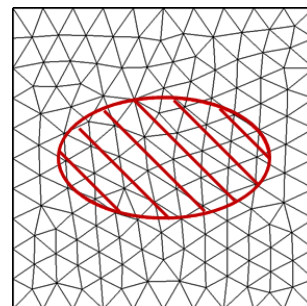
Figure 2.8: Multi Instance Solver Coupled through Overlapping Grids, extracted from [60]

2.6.3 Immersed Boundary Method

In standard CFD, a flow domain is firstly meshed and the boundary conditions are applied on the domain boundaries, such as the inlet, the outlet or the walls. As long as boundaries do not move this approach is very efficient and accurate. But fluid-structure interactions like in piston engines or turbomachinery computations require to deal with moving boundaries. One solution to handle these moving boundaries is the use of an Immersed Boundary Method (IBM). In this approach, the meshes are generated over the whole domain and do not have to match with the shape of moving parts. These moving boundary conditions are then introduced in the governing equations via forcing terms. Fig. 2.9 shows an example of an ellipsoidal wall, on the left of the figure, the object is conventionally meshed and on the right, it is modeled by an immersed boundary.



(a) Standard Body Conformal approach.



(b) Immersed Boundary Method.

Figure 2.9: Comparison of classical meshing and IBM.

This approach consists in decoupling the mesh generation of the fluid domain from the moving parts, which makes the method particularly interesting for complex and moving geometries. Indeed, the mesh neither moves nor deforms and consequently, only one mesh is needed. This is a considerable advantage since higher complex geometries, especially with moving boundaries, consume a higher time to be meshed. This is why, the implementation of an IBM in the AVBP LES solver seems very promising.

The IBM was firstly introduced by Peskin in 1972 [61] to simulate the blood flow in heart valves. Goldstein *et al.* [62] and Saiki and Biringen [63] modeled solid boundaries as a sharp interface. They employed feedback forcing terms added in the incompressible Navier-Stokes equations to take into account the surface of the immersed objects. The feedback forcing terms induced spurious oscillations and restricted computational time step to meet the numerical stability. For example, Goldstein *et al.* [62] used a very small time step equivalent to a Courant Friedrichs Lewy (CFL) number between 10^{-3} and 10^{-2} , when they simulated the start-up flow around a circular cylinder. The order of the CFL in LES varies between 0.7 and 0.9 depending on the numerical scheme used. In 1997, Mohd-Yusof [64] suggested a different approach to evaluate the momentum forcing in a spectral method. His method improved the computational time step compared with previous approaches. Like in previous methods, momentum forcing terms were only applied on the surface of the body. Fadlun *et al.* [65] studied Goldstein [62] and Mohd-Yusof [64] approaches on a staggered grid and showed that the discrete-time forcing method suggested by Mohd-Yusof [64] was more efficient than feedback forcing terms for three-dimensional flow problems. In this study, the discrete-time forcing approach was changed. The velocity at the first grid point external to the body was obtained by a linear interpolation of the second grid point velocity, which was predicted by solving the Navier-Stokes equations, and the body surface velocity. This conceptually corresponds to the application of the momentum forcing terms inside the flow. The direction of the interpolation of the second grid point was arbitrary and it was either stream wise or transverse direction. When a bilinear (2D) interpolation was chosen to avoid the arbitrariness, the use of the approximate factorization scheme combined with a tridiagonal matrix solver might require several numerical iterations, which increased the CPU time, especially for three-dimensional flow. In 2001, Ye *et al.* [66] proposed a different approach on a non-staggered grid called a "Cartesian grid method", which did not use the concept of the additional momentum forcing terms. In this method, a control volume near the immersed object was re-formed into a body-fitted trapezoidal shape, by discarding the solid part of the cell and adding the neighbouring cells. To accurately discretize the governing equations at the cell containing the immersed boundary, they also presented a new interpolation procedure, that preserved the second-order spatial accuracy. However, because the stencil of the trapezoidal boundary cell was different from that of the regular cell, an iteration technique was applied to solve the discretized momentum equations at each computational time step.

Nguyen *et al.* [67, 68] developed an IBM method base on "mirror flow" concept [69] to simulate the moving and stationary boundaries of an internal combustion engine in a LES solver. In their studies, they highlighted the capability of the IBM to predict the pressure evolutions and velocity fields in both aerodynamic and reactive cases.

Chapter 3

Lagrangian Immersed Boundary method

Contents

3.1	LIB method principle	51
3.2	Modification of the governing equations	53
3.3	Source terms calculation	53
3.3.1	Initial LIB method implemented in AVBP	53
3.3.2	New LIB method developed in this study	55
3.3.3	Quantitative comparison of the two methods	57
3.4	Improvement and adaptation of the LIB method to model CVC chambers	59
3.4.1	Numerical scheme based on Taylor expansion	60
3.4.2	Special treatment of LIB particles on walls	60
3.4.3	Development of rebound liquid injection on LIB	62
3.4.4	Combustion model adaptation with LIB and liquid injection	64

This chapter presents the IBM implemented in the LES solver AVBP. In this method, immersed boundaries are made of Lagrangian particles, this approach is then called Lagrangian Immersed Boundary (LIB). In the following approaches, the modifications of Navier-Stokes equations are realised in the vicinity of immersed walls but also inside immersed boundaries since it was found more effective in this solver. Firstly, the initial LIB method is described and a new approach is then presented. Numerical adaptations required to simulate CVC chambers are also explained. All numerical developments are validated on several test cases presented in the following parts.

3.1 LIB method principle

As explained in the introduction of this chapter, the implemented IBM in the AVBP solver requires Lagrangian particles to track the position of immersed boundaries. In order to make immersed objects as airtight as possible, each Eulerian cell inside solid boundaries must have at least one particle. The method used in this study is inspired from Goldstein [62], where a feedback forcing term is added into compressible Navier-Stokes equations.

Fig. 3.1 shows how a solid body is modeled by Lagrangian particles on an Eulerian mesh. The body can be motionless or driven by solid movement, which imposes a velocity u_p on each particle.

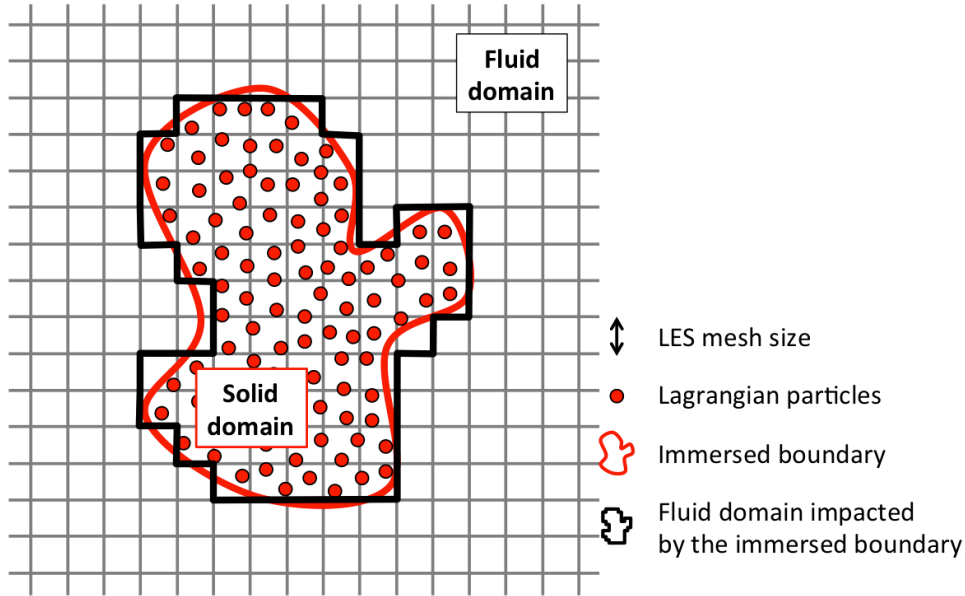


Figure 3.1: Modeling an immersed boundary with Lagrangian particles.

The initial method, detailed in section 3.3.1, interpolates the fluid velocity at the particle position $u_{f@p}$ so as to calculate feedback forcing terms using both the interpolated fluid velocity $u_{f@p}$ and the particle u_p velocity. Then, these source terms are applied on the grid nodes surrounding the considered particle with a "projection operator" described in paragraph 3.3.1.2. However, the initial method is not adapted to hold back efficiently the mass flow rate from a high pressured zone to a lower one, due to its numerical approach. Indeed, some parameters have to be set depending on the flow near immersed boundary walls, which makes the simulation difficult to parameterize, especially in CVC chamber simulations where significant changing flows are encountered during the different phases. Consequently, a new method presented in section 3.3.2 is developed in this thesis so as to avoid the variation of the model parameters during the calculation, in order to make the model as simple as possible to use. Based on the same approach which consists in adding feedback forcing terms into the Navier-Stokes equations, these terms are directly calculated on the Eulerian mesh nodes for each particle. By avoiding the interpolation and the projection realised in the previous method, discrepancies between neighbour particles are eliminated, which leads to a very smooth evolution of the feedback forcing terms throughout the immersed boundary. In order to enhance the differences which are introduced by a different number of particles seen by two neighbour Eulerian nodes, the applied feedback forcing terms are normalised by using all particles surrounding the considered node. This new method is then evaluated on several test cases.

3.2 Modification of the governing equations

As explained above, LIB are taken into account by adding source terms into the Navier-Stokes equations, based on formulation proposed by Goldstein *et al.* [62]. The momentum Eqs (2.27) becomes:

$$\frac{\partial \bar{\rho} \tilde{u}_i}{\partial t} + \frac{\partial}{\partial x_j} (\bar{\rho} \tilde{u}_i \tilde{u}_j) = - \frac{\partial}{\partial x_j} [\bar{P} \delta_{ij} - \bar{\tau}_{ij} - \bar{\tau}_{ij}^{sgs}] + \bar{F}_i + \bar{F}_{LIB,i} \quad (3.1)$$

Where $\bar{F}_{LIB,i}$ is the i^{th} component of the additional LIB source term, which is respectively described in sections 3.3.1 and 3.3.2 for initial approach and the new developed one. Moreover, these additional source terms generate a source term into the energy equation:

$$\frac{\partial \bar{\rho} \tilde{e}_t}{\partial t} + \frac{\partial}{\partial x_j} (\bar{\rho} \tilde{e}_t \tilde{u}_j) = - \frac{\partial}{\partial x_j} [\overline{u_i (P \delta_{ij} - \tau_{ij})} + \bar{q}_j + \bar{q}_j^{sgs}] + \bar{\rho} \tilde{\omega}_T + \bar{S}_{ELIB} \quad (3.2)$$

where \bar{S}_{ELIB} is the energy LIB source term. Like the momentum source terms, the energy source term is described for the two approaches, respectively in sections 3.3.1.3 and 3.3.2.2.

3.3 Source terms calculation

3.3.1 Initial LIB method implemented in AVBP

The global LIB source term $\bar{F}_{LIB,i}$ is a combination of the forcing terms f_i^n calculated on each LIB particle surrounding the Eulerian grid node and a "projection operator". The computation of these terms are presented in the following paragraph.

Firstly, momentum source terms f_i^n of one particle n is presented and then the global contribution is detailed.

3.3.1.1 The forcing term f_i^n

The forcing term f_i^n of a particle n , applied on the fluid node j is calculated following the formulation of Goldstein *et al.* [62] $f_{Gold,i}^n$:

$$f_{Gold,i}^n = M(u_{p,i}^n - u_{f@p,i}) + N \int_0^t (u_{p,i}^n - u_{f@p,i}) dt' \quad (3.3)$$

where $u_{f@p,i}$ is the i^{th} -component of the gas velocity interpolated at the particle position, M and N are two case-dependent parameters. These feedback forcing terms are relaxing the interpolated velocity $u_{f@p,i}$ to the particle velocity u_p . Then, and thanks to a scatter operation called "projection operator" presented in section 3.3.1.2, these feedback source terms are distributed on the surrounding fluid nodes of the cell. In the framework of control systems theory, the Goldtsein's formulation is called a Proportional-Integral (PI) controller. Using concepts from linear control theory in LES can be applied in this case since the flow inside immersed boundary has to behave as a solid motion which is a linear motion.

The determination of the M and N coefficients in Eq. (3.3) might be tricky. Bonhomme [70] proposed to write M and N as a function of relaxation times, which represents the

number of iterations needed to reach the equilibrium $u_{f@p} = u_p$. Finally, the formulation of f_i^n implemented in AVBP is the following:

$$f_i^n = \frac{\bar{\rho}V_j}{\beta\Delta t} (u_{p,i}^n - u_{f@p,i}) + \frac{\bar{\rho}V_j}{\alpha^2\Delta t^2} \int_0^t u_{p,i}^n - u_{f@p,i} dt' \quad (3.4)$$

where α and β are respectively relaxation times for integral and proportional source terms in number of iterations. These two key parameters are still cases dependant and must be chosen with care by the user. The control volume V_j of node j is defined as shown Fig. 3.2, Δt is the timestep and $\bar{\rho}$ the fluid density.

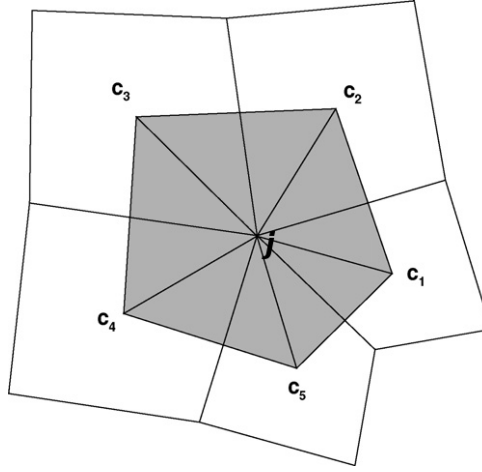


Figure 3.2: Control volume of node j

3.3.1.2 The projection operator

The projection operator W is used to scatter the contribution of each particle f_i^n at the position x_n surrounding the node j located at the position x_j , is the same scatter operator used in liquid evaporation. The expression of the global source term $\bar{F}_{LIB,i}$ added in momentum Eq. (3.1) writes:

$$\bar{F}_{LIB,i} = \frac{1}{N_p} \sum_{n=1}^{N_p} f_i^n \cdot W(x_n, x_j) \quad (3.5)$$

where N_p is the number of particles surrounding the node j , f_i^n is the feedback forcing term calculated at the particle n , $W(x_n, x_j)$ is the projection operator from particle n at the position x_n to the grid node j at the position x_j . The projection operator is constructed to be inversely proportional to the distances $d(x_n, x_j)$ between the particle n and the node j :

$$W(x_n, x_j) = \frac{1/d(x_n, x_j)}{\sum_{k=1}^N 1/d(x_n, x_k)} \quad (3.6)$$

where N is the number of vertices of the cell. Fig. 3.3 sketches resulting feedback forcing terms $\vec{f}^n \times W(x_n, x_j)$ of one particle n on the node j .

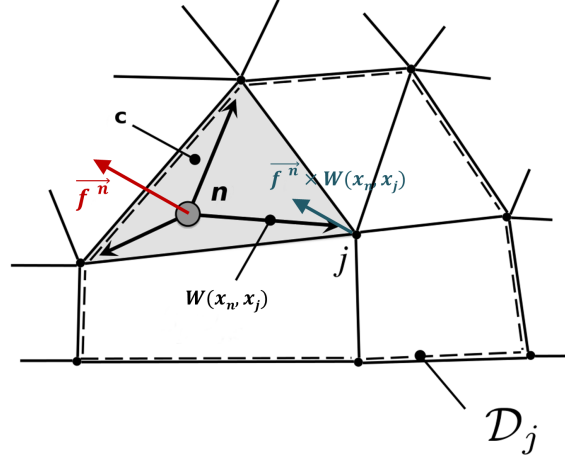


Figure 3.3: Projection weight W of the particle n onto the vertices j

In Fig. 3.3, the red vector \vec{f}^n is the feedback forcing term calculated at the particle n and the blue vector is the feedback forcing terms applied on the node j . Obviously, all vertices of cell c receive the scattered source terms calculated from \vec{f}^n and the projection operator $W(x_n, x_j)$.

3.3.1.3 The energy source term \bar{S}_{ELIB}

The energy source term in Eq. (3.2) is computed using the global momentum LIB source terms and the resolved velocity on the Eulerian grid:

$$\bar{S}_{ELIB} = \sum_{k=1}^{ndim} \bar{F}_{LIB,k} \cdot \tilde{u}_k \quad (3.7)$$

where $ndim$ is the number of dimensions of the simulation, here in 2 or 3 dimensions and \tilde{u}_k the k^{th} component of the resolved fluid velocity.

3.3.2 New LIB method developed in this study

A new method is proposed in this work to substantially simplify the use of this model by making the parametrization independent of the case as shown in section 3.3.3. In this new approach, source terms are directly calculated on the fluid nodes where the details of each source terms are described in the following paragraphs.

3.3.2.1 Normalized forcing term $\bar{F}_{LIB,i,j}$ of particles surrounding node j

Like initial formulation, the feedback forcing terms in momentum equations aim at controlling the fluid velocity inside and in the vicinity of the immersed object. The innovation of the method is to create a source term which is derived from the Goldstein *et al.* [62] formulation, where velocities under consideration are the resolved fluid velocity \tilde{u}_j on

node j and the average velocity $u_p^{ave,j}$ of all particles surrounding node j defined by:

$$u_{p,i}^{ave,j} = \frac{1}{N_p} \sum_{k=1}^{N_p} u_{p,i}^k \quad (3.8)$$

where N_p is the number of particles surrounding node j .

With the Goldstein's formulation, momentum LIB source terms in Eq. (3.1) can be written into two terms:

$$\bar{F}_{LIB,i} = \bar{F}_{LIB,i}^{prop} + \bar{F}_{LIB,i}^{int} \quad (3.9)$$

With proportional source terms defined by:

$$\bar{F}_{LIB,i}^{prop} = \frac{\bar{\rho}V_j}{\beta\Delta t} (u_{p,i}^{ave,j} - \tilde{u}_{j,i}) \quad (3.10)$$

where V_j is the control volume of node j defined in Fig. 3.2, β the relaxation time parameter for proportional source terms in number of iterations and $\tilde{u}_{j,i}$ the i^{th} component of the revolved fluid velocity on node j .

Then integral source terms are written:

$$\bar{F}_{LIB,i}^{int} = \frac{\bar{\rho}V_j}{\alpha\Delta t^2} \int_{t'=0}^t (u_{p,i}^{ave,j} - \tilde{u}_{j,i}) dt' \quad (3.11)$$

Where α is the second relaxation time parameter for integral source terms which is defined in number of iterations.

By developing the expression of both integral and proportional parts, the global can be written as follows:

$$\bar{F}_{LIB,i} = \frac{1}{N_p} \sum_{k=1}^{N_p} \left[\underbrace{\frac{\bar{\rho}V_j}{\alpha\Delta t^2} \int_{t'=0}^t (u_{p,i}^k - \tilde{u}_{j,i}) dt'}_{\bar{f}_{LIB,i}^{int,k}} + \underbrace{\frac{\bar{\rho}V_j}{\beta\Delta t} (u_{p,i}^k - \tilde{u}_{j,i})}_{\bar{f}_{LIB,i}^{prop,k}} \right] \quad (3.12)$$

Where $\bar{f}_{LIB,i}^{int,k}$ and $\bar{f}_{LIB,i}^{prop,k}$ can respectively be interpreted as integral and proportional source terms of the particle k .

Moreover, the operator $\frac{1}{N_p} \sum_{k=1}^{N_p} *$ is an arithmetic average applied on all particles surrounding node j .

This formulation allows the computation of the source terms on each particle and then uses an arithmetic average to obtain the global source term.

3.3.2.2 The energy source term \bar{S}_{ELIB}

In this paragraph, additional source terms in the energy equation Eq. (3.2) are explained. Firstly, in order to be coherent with the forcing terms of the momentum equations, it is necessary to apply a source term presented in Eq.(3.14), which is derived from momentum equations source terms $\bar{F}_{LIB,i}$. In the following paragraph, this source term is called "Standard" energy source term since it is related to the LIB velocity variations and does not take into account thermal heat fluxes.

Secondly, an isothermal source term inspired from conventional isothermal boundary conditions could be added to reach a targeted temperature inside immersed objects.

These sources terms are written:

$$\bar{S}_{ELIB} = \bar{S}_{ELIB}^{st} + \bar{Q}_{ELIB}^{isoT} \quad (3.13)$$

"Standard" source term:

This term is used to be consistent with the forcing terms applied in the momentum equation:

$$\bar{S}_{ELIB}^{st} = \sum_{k=1}^{ndim} \bar{F}_{LIB,k} \cdot \tilde{u}_k \quad (3.14)$$

where $ndim$ is the number of dimensions of the simulation, here in 2 or 3 dimensions and \tilde{u}_k the k^{th} component of the resolved fluid velocity.

Isothermal source term:

Isothermal energy source term could be added to relax the temperature inside immersed boundaries toward a user defined temperature T_{LIB} . This source term modifies the fluid internal energy. The relaxation is achieved through the parameter θ , which is a number of iterations required to meet the targeted temperature. This parameter has to be larger than one.

$$\bar{Q}_{ELIB}^{isoT} = \frac{V_j}{\Delta t} \left[\frac{\bar{\rho} c_v (T_{LIB} - T_j)}{\theta} \right] \quad (3.15)$$

where c_v is the specific constant volume heat capacity and T_j the temperature at the node j .

3.3.3 Quantitative comparison of the two methods

The main difference between these two methods is the way to compute source terms. In the initial method, the velocity is firstly interpolated at the Lagrangian particle and feedback forcing terms are calculated at the particle position. Then, these source terms are projected on the Eulerian mesh weighted by coefficients depending on the distance. To use this method, it is recommended to firstly only turn on the integral controller (which leads to $\beta = \infty$) and then activate the proportional-integral controller with a low contribution of the integral controller and a high contribution of the proportional part, this time β could be set to one unity.

With the new implemented method, the user does not have to care about the parametrization of the LIB model since α and β are set to 2 for all cases.

In this paragraph, these two methods are compared using a configuration close to a CVC chamber with rotating immersed boundary. This circular immersed boundary separates the flow into two main zones where the pressure on the left is set to 30 *bar* and a pressure gradient from 30 to 5 *bar* is initialized on the right, as shown in Fig. 3.4. The temperature is initialized at 1000 *K* throughout the domain (Fig. 3.5) and the velocity is set to zero. In this simulation, the immersed boundary is rotating at 6000 revolutions per minute (RPM). The coefficients α and β used to calculate source terms are set to 2 for both methods, even if it is not advised to activate the proportional-integral controller in the initial method at the beginning of the simulation. Indeed, for very turbulent flows in the vicinity of the boundary, the user, who uses the initial method, will need to adjust coefficients to make the LIB condition as efficient as possible.

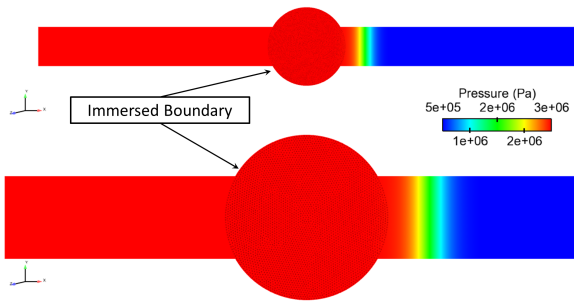


Figure 3.4: Initial pressure

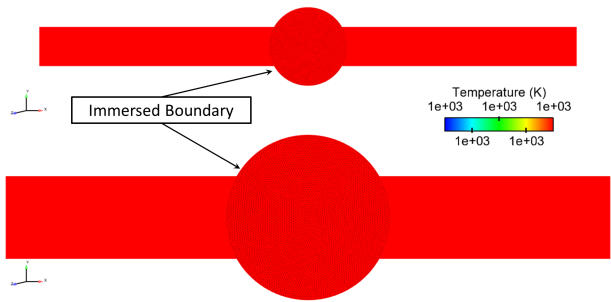


Figure 3.5: Initial temperature

This simulation is very short, but the main goal is to show how the flow performs inside and the vicinity of the immersed boundary during the transient flow. This functioning could be extended to flows near LIB with a high velocity.

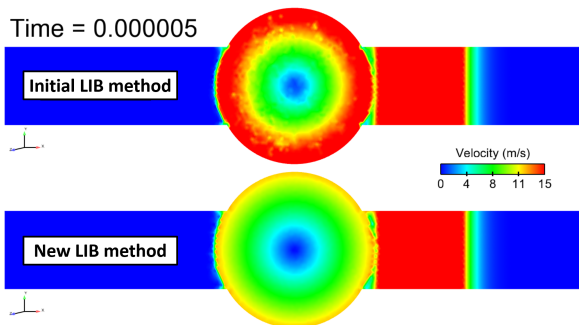


Figure 3.6: Velocity after 1 iteration

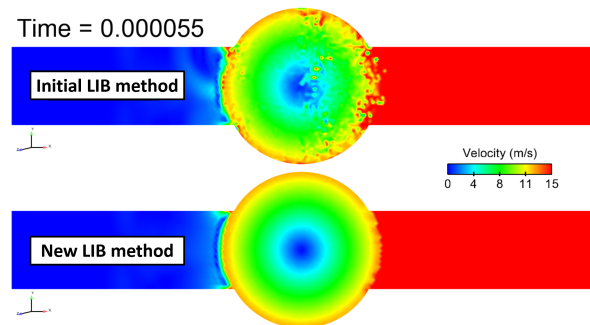


Figure 3.7: Velocity after 10 iterations

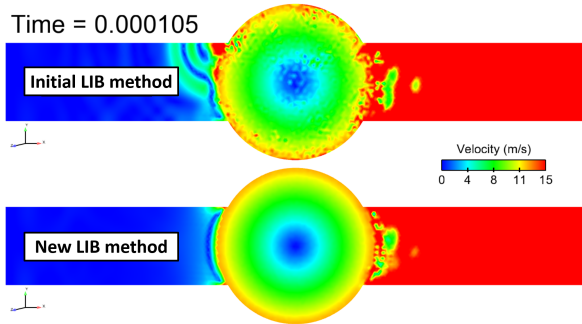


Figure 3.8: Velocity after 20 iterations

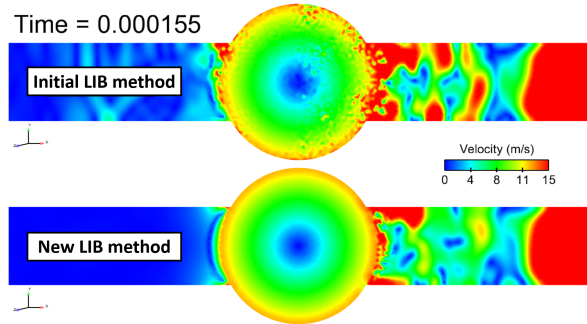


Figure 3.9: Velocity after 30 iterations

Figs 3.6 to 3.9 show respectively on the top and the bottom of the figure, the functioning of the flow in the rotating immersed boundary with the initial and the developed LIB methods. In these figures, the initial method presents several oscillations in the velocity field which is due to the interpolation, calculation and projection processing. The developed method which directly uses the average velocity of the surrounding particles to calculate the feedback forcing terms seems very appropriate in this kind of configuration. Indeed, the velocity inside the immersed boundary behaves like the object where the velocity magnitude is linearly proportional with the distance ($V_R = R \times \omega$, where ω is the rotation speed). With this approach, the fluid in the vicinity of LIB is relaxed to the velocity of the rotating object.

=====
Conclusion:
 =====

A pressure gradient from 30 bar down to 5 bar can be met in CVC configuration at the end of the combustion and thus has to be compatible with the numerical approach. In this test case, the new LIB method does not generate velocity overshoot inside and in the vicinity of the immersed boundary even if α and β coefficients are constant throughout the simulation. On the contrary, the initial formulation creates velocity overshoots, which are significantly visible throughout the immersed rotating object. Consequently, this very simple test case shows that the developed approach seems more appropriate to handle rotating immersed boundary in between flows at different pressures.

3.4 Improvement and adaptation of the LIB method to model CVC chambers

In this section, additional developments needed to simulate CVC chamber are presented. First, the Lax-Wendroff scheme is modified to take into account LIB source terms at the second order derivative. This modification significantly enhances the capability to hold back fluid especially when a LIB is used as a wall between two zones at different pressures. Secondly, some numerical adaptations in the vicinity of conform walls are presented. Here, the aim is to avoid applying LIB source terms on no-slip walls. Third, the interactions with the liquid spray, especially the rebound on LIB walls are detailed. Last, the flame quenching on LIB walls are presented.

3.4.1 Numerical scheme based on Taylor expansion

The use of the LIB presented above in section 3.3.2 as a wall between high and low pressure fluids, needs to be robust and efficient to hold back the fluid. At this time, the robustness of the method was validated in paragraph 3.3.3, but an important mass flow rate is observed through the wall. The chosen way to improve the numerical effectiveness is to work on the numerical scheme, namely the Lax-Wendroff numerical scheme. As proposed by Zhang in 1999 [71], in order to be fully consistent with additional source terms into Navier-Stokes equations, the source terms which are added at the first order derivative, have to be taken into account in the flux divergence. To explain the method, a simplified momentum equation is considered:

$$\frac{\partial \rho u}{\partial t} = -\nabla \cdot F + \bar{F}_{LIB} \quad (3.16)$$

Where $\nabla \cdot F$ is the flux divergence.

Using a second order Taylor development, the left terms of Eq. (3.16) could be written:

$$\rho u(t + dt) = \rho u(t) + \Delta t \frac{\partial \rho u}{\partial t} + \frac{\Delta t^2}{2} \frac{\partial^2 \rho u}{\partial t^2} \quad (3.17)$$

Developing the right terms of Eq. (3.17), the second order difference becomes:

$$\frac{\partial^2 \rho u}{\partial t^2} = \frac{\partial}{\partial t} \left(\frac{\partial \rho u}{\partial t} \right) = \frac{\partial}{\partial t} (-\nabla \cdot F + \bar{F}_{LIB}) = \frac{\partial(-\nabla \cdot F)}{\partial t} + \frac{\partial}{\partial t} (\bar{F}_{LIB}) \quad (3.18)$$

There, the temporal derivative of F_{LIB} , $\frac{\partial}{\partial t} (\bar{F}_{LIB})$ could be neglected.

Time derivative term $\frac{\partial(\nabla \cdot F)}{\partial t}$ is then replaced by spatial derivatives:

$$\frac{\partial(\nabla \cdot F)}{\partial t} = \frac{\partial(\nabla \cdot F)}{\partial \rho u} \frac{\partial \rho u}{\partial t} = \frac{\partial(\nabla \cdot F)}{\partial \rho u} (-\nabla \cdot F + \bar{F}_{LIB}) \quad (3.19)$$

As shown Eq. (3.19), the term \bar{F}_{LIB} must be in addition to the flux divergence $\nabla \cdot F$ so as to be consistent with the momentum source terms and it is called "second order derivative" source terms in this manuscript. The space discretization selected in AVBP solver is the Galerkin finite element method and convective source terms relied on Cell-Vertex Finite-Volume method. All source terms are then calculated in cells and then scattered on nodes linked to cells. This numerical method is detailed in the AVBP handbook.

These additional LIB source terms are evaluated in the paragraph 4.2.

3.4.2 Special treatment of LIB particles on walls

The purpose of the LIB method is to drive the fluid velocity towards the particles velocity. However, this method could be faced with an issue when moving objects are near conforming walls, especially when velocity is set to zero on these walls (no-slip conditions). Consequently, a special treatment of particles and LIB sources terms have to be implemented in these wall cells. The selected method is to deactivate LIB particles in these no-slip wall cells so as to respect the no-slip boundary condition, which is shown on the right of Fig. 3.10, and to modify the computation of the second order derivative source

terms in these cells. In this figure, the red circles in the center of cells sketch Lagrangian particles of the LIB and a cross on LIB particles in wall cells is added to highlight that these LIB particles are deactivated.

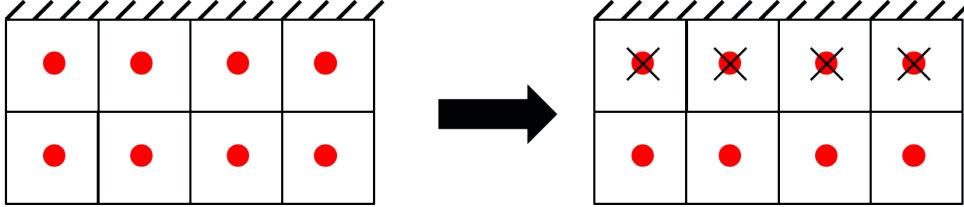


Figure 3.10: Deactivating particles in no-slip wall cells

LIB source terms in momentum and energy equations are applied on fluid nodes, they are highlighted in blue circles in Fig. 3.11.

For the sake of clarity, the considered LIB first order source term applied is supposed equal to S_{LIB} on all fluid nodes.

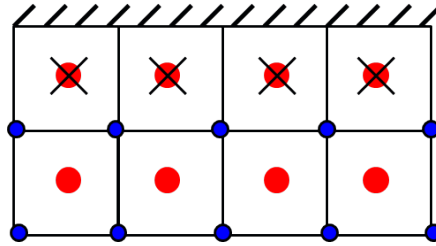


Figure 3.11: LIB source terms application on nodes

Since the capacity to reduce LIB mass leakage through immersed walls is highly related to the momentum source terms and their application of the second order derivative source terms in the numerical scheme, it is necessary to compute accurately these second order source terms and apply it only on fluid nodes highlighted with blue circle in Fig. 3.11.

The numerical scheme calculates the second order derivative source terms by averaging the first order derivative source terms of the nodes of the cell and then, scattering these averaged values from the cell to the nodes. Fig. 3.12, shows on the left how the average source terms were calculated with the original routine “average”. In this case, the cell average source term is calculated with the equation:

$$S_{ave} = \frac{\sum_{n=1}^{N_{nodes}} S_{LIB}(n)}{N_{nodes}} \quad (3.20)$$

Where N_{nodes} is the number of nodes of the considered cell. In the following description, S_{ave} is the “value” of the averaged LIB source terms in cells and it is supposed equal in all cells with a LIB source terms on each fluid nodes.

By disabling LIB particles in wall cells, LIB source terms on wall nodes are equal to zero. Consequently, the averaged source terms in wall cells are two times lower than inside the fluid. Fig.3.12 schematics this calculation on the left. The difference between the

averaged source terms in the wall cells and the first fluid cells are responsible for the mass loss through wall cells.

Therefore, the average calculation of the source terms in wall cells is modified to only take into account nodes with non zero LIB source terms. The computation of these source terms becomes:

$$S_{ave} = \frac{\sum_{n=1}^{N_{nodes}} S_{LIB}(n)}{N_{nodes_{LIB}}} \quad (3.21)$$

Where N_{nodes} is the number of node of the considered cell and $N_{nodes_{LIB}}$ is the number of nodes where LIB source terms are different from zero. With this method, source terms scattered by the numerical scheme on fluid nodes is consistent to that applied at the first order derivative. The right part of Fig. 3.12 highlights how averaged source terms are now homogeneous in all cells instead of being divided by the ratio $N_{nodes_{LIB}}/N_n$.

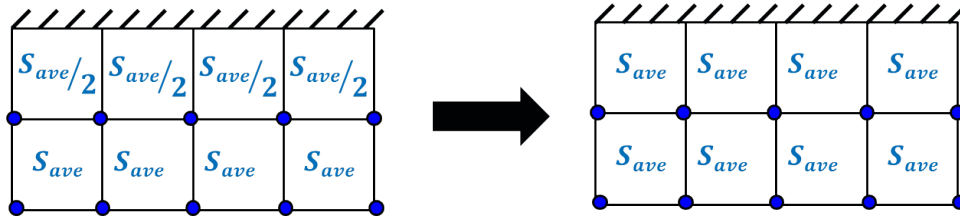


Figure 3.12: New method to compute second order derivative source terms

3.4.3 Development of rebound liquid injection on LIB

The Lagrangian approach tends to be used in SI and aeronautical applications to simulate the liquid phase. That is why Lagrangian liquid injection has to be compatible with LIB.

The numerical approach is to keep the Lagrangian particles used to simulate the spray by creating a new set of Lagrangian particles to model immersed objects. Then both Lagrangian particles used to model spray and immersed boundaries need to interact. As a first approach only the rebound on LIB is implemented. In order to explain the developed method, a simple inclined LIB is placed in a Cartesian grid as shown in Fig. 3.13.

The first step is to identify Eulerian cells which contain LIB particles. This operation is highlighted by the cells filled with the red color on the last right image of Fig. 3.13. Then the normal vectors of the LIB in black are projected on the Eulerian mesh, here presented in white vectors in Fig. 3.14.

The spray particles will then rebound on this fictive surface using both the flag and the projected vectors.

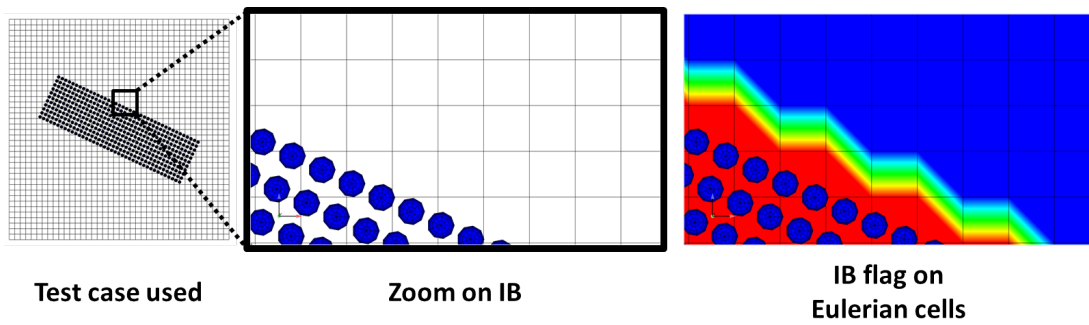


Figure 3.13: Test case and immersed boundary flag

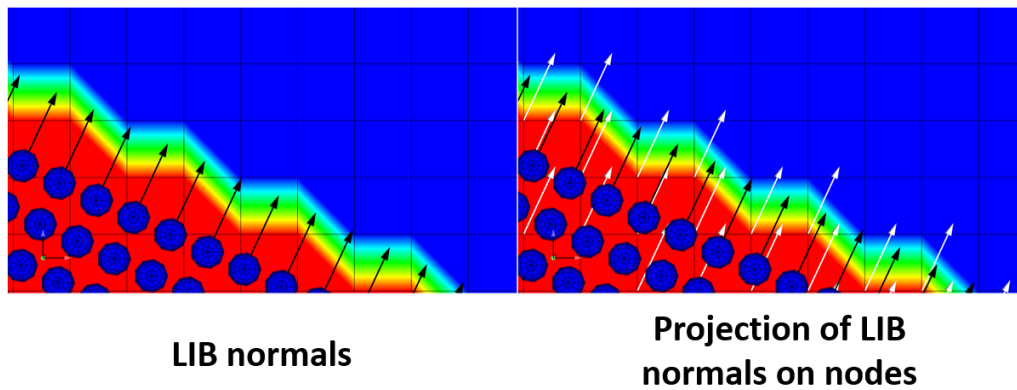


Figure 3.14: Normal LIB projection on Eulerian mesh

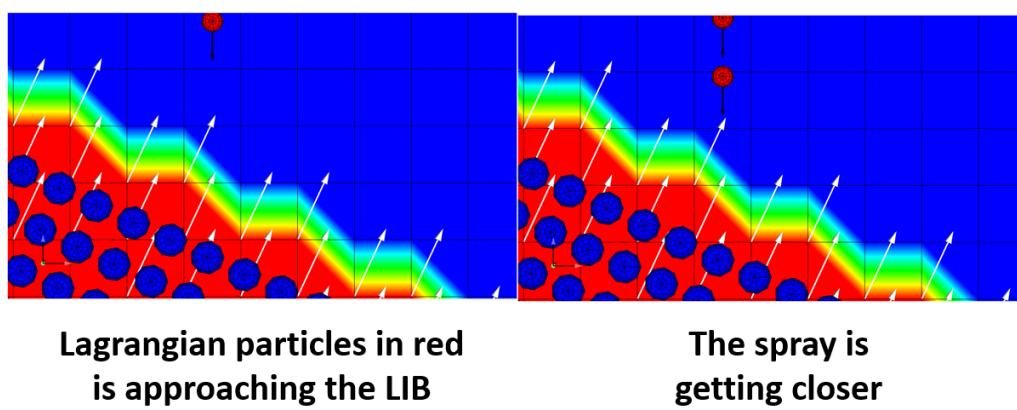


Figure 3.15: Spray coming closer to the LIB

In this case, the liquid injection is generated by a point so as to spread in a line direction. In Fig. 3.15 the spray modeled by Lagrangian particles, which are coloured in red. In this figure, the particles are getting closer to the LIB.

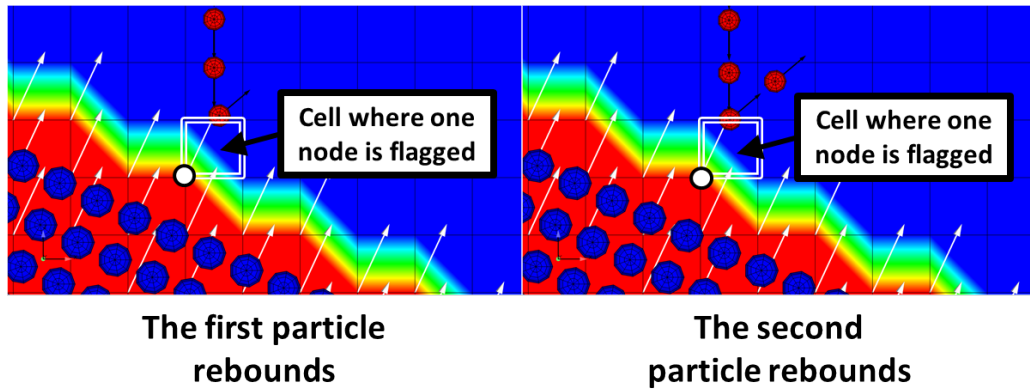


Figure 3.16: First and second rebound on the LIB

As soon as one Lagrangian particle of the spray is getting into a cell where one node is flagged, the particle rebounds on the cells using the projected immersed boundary normal. In Fig.3.16, this cell is surrounded by the white square and the flagged node is highlighted by a white circle. With this method, even if the immersed boundary is moving, spray particles can not get into the object.

To summarise, the algorithm of the liquid phase rebound on LIB is composed of the following steps:

1. Cells including LIB particles are flagged,
2. Normals of the object are projected on the mesh,
3. When Lagrangian spray particle is getting into a new cell, the nodes of this cell are tested in order to know if one node is flagged,
4. In the case where one flagged node is identified and if the spray Lagrangian particle is going in the direction of the object like in Fig. 3.16, the rebound on this cell is activated.

=====
Conclusion:
 =====

The implemented rebound model is a pragmatic approach that allows the interaction between the spray and the LIB. More sophisticated models could be developed in the future.

3.4.4 Combustion model adaptation with LIB and liquid injection

3.4.4.1 Avoiding combustion inside immersed objects

As explained above, LIB method consists in modifying LES governing equations so as to control the fluid inside immersed boundary. However, all physical models are still applied inside immersed objects. The simple manner to avoid combustion in moving parts is to disconnect chemical reactions by setting species reaction rates to zero like in TF-LES [29].

In ECFM-LES, the flame surface density source term is also set to zero. Moreover when the isothermal boundary condition is used inside immersed objects, the enthalpy variation introduced by the temperature relaxation in immersed boundary must be added into the unburnt gases enthalpy transport equation. This source term $\overline{Q}_{h_{LIB}^u}^{isoT}$ is similar to that of the energy Eq. (3.15):

$$\overline{Q}_{h_{LIB}^u}^{isoT} = \frac{V_j}{\Delta t} \left[\frac{\rho c_p (T_{LIB} - T_j^u)}{\theta} \right] \quad (3.22)$$

Where c_p is the constant pressure heat capacity, T_j^u is the temperature of fresh gases.

3.4.4.2 Liquid injection taken into account in ECFM-LES

ECFM-LES is a combustion model dedicated to premixed flame combustion. However, liquid droplets may not have enough time to evaporate in the fresh gases before the combustion process. That is why, the evaporation in the burnt gases phase has to be taken into account and it is necessary to activate the burnt chemistry. Therefore, additional source terms are introduced in the fuel species transport equation and in the burnt gases fuel mass fraction using the fuel mass transfer $d\overline{m}_F^k/dt$ from liquid to gases phase by:

$$\overline{S}_{f,j}^u = \frac{1}{V_j} \sum_{k=1}^{N_p} W(x_p, x_j) \frac{d\overline{m}_F^k}{dt} \times (1 - \tilde{c}) \quad (3.23)$$

$$\overline{S}_{f,j}^b = -\frac{1}{V_j} \sum_{k=1}^{N_p} W(x_p, x_j) \frac{d\overline{m}_F^k}{dt} \times \tilde{c} \quad (3.24)$$

Where V_j is the control volume of node j , N_p the number of liquid particles surrounding the node j , $W(x_p, x_j)$ the liquid scatter operator, \overline{m}_F^k the fuel mass transfer from the droplet k to gas and \tilde{c} is the progress variable defined in EFCM-LES.

Moreover, the energy variation due to liquid droplets evaporation has to be considered. This source term derived from [32] is added into the unburnt enthalpy transport equation:

$$\overline{S}_{h^u,j}^{lig} = \frac{1}{V_j} \sum_{k=1}^{N_p} W(x_p^k, x_j) \left[\left(\overline{\Phi}_g^{cv,k} + \overline{\Phi}_g^{c,k} \right) + \left(\tilde{h}_{m,j} - \tilde{h}_j^u \right) \frac{d\overline{m}_F^k}{dt} \right] \quad (3.25)$$

Where $W(x_p^k, x_j)$ is the projection operator defined in section 3.3.1.2, here applied on the evaporation source terms, $\overline{\Phi}_g^{cv,k}$ and $\overline{\Phi}_g^{c,k}$ are respectively the convective and the conductive heat fluxes of the liquid droplet k defined in the section 2.5.1.2 and $d\overline{m}_F^k/dt$ is the mass transfer of the droplet k to the gas phase.

Chapter 4

Evaluation of the implemented LIB method

Contents

4.1	Static and rotating LIB between two zones at different pressures	67
4.1.1	Conformal wall boundary conditions used	67
4.1.2	2D wall-bounded box	68
4.1.3	2D wall-bounded box with a rotating immersed boundary . . .	70
4.2	Evaluation of the developments on a 3D wall-bounded box with motionless LIB	73
4.2.1	Test case description	73
4.2.2	Evaluation without the second order derivative source terms	73
4.2.3	Evaluation using the second order derivative source terms	74
4.3	LIB isothermal boundary condition evaluation	76
4.3.1	Configuration	76
4.3.2	Computational parameters	76
4.3.3	Results	77
4.4	Acoustic and pressure wave cases	81
4.4.1	Short cavity acoustic eigen-mode 1D case	81
4.4.2	Long cavity acoustic eigen-mode 1D case	83
4.4.3	Pressure wave	86
4.4.4	Conclusion	87
4.5	Steady state flow bench	88
4.5.1	Experimental apparatus	88
4.5.2	Computational parameters	89
4.5.3	Results	89

The aim of this chapter is to evaluate the developments made on the LIB method from simple test cases to an experimental steady state flow bench study.

4.1 Static and rotating LIB between two zones at different pressures

Two test cases representative of a CVC chamber at the end of the combustion phase, namely with a significant pressure gradient on both sides of the immersed boundary, are used to evaluate fluid tightness efficiency of the LIB method. In these cases, the two main families of conformal walls which use a zero velocity at the wall or a law of the wall are analysed. In this part, only the new implemented method is analysed without the isothermal condition in the immersed boundary and both parameters α and β are set to 2 as presented above.

4.1.1 Conformal wall boundary conditions used

In this paragraph, two conformal wall boundary conditions are used to evaluate the LIB method, namely the mass leakage in wall cells. These two boundary conditions are a no-slip adiabatic and an adiabatic wall law-of-the-wall boundary conditions, which are defined as followed:

Adiabatic no-slip wall boundary condition:

Adiabatic no-slip boundary condition consists in setting both wall velocities and wall heat fluxes to zero.

$$u_c = 0.0 \quad v_c = 0.0 \quad w_c = 0.0 \quad Q_w = 0.0 \quad (4.1)$$

Adiabatic wall law-of-the-wall boundary condition:

Adiabatic wall law-of-the-wall condition uses the logarithmic law to impose wall shear stress $\tau_{wall} = \rho u_\tau^2$ [72]. Non-dimensional variables for wall-distance and velocity in the boundary layer are defined as:

$$y^+ = \frac{y_{wall} u_\tau}{\nu_{wall}} \quad u^+ = \frac{u_f}{u_\tau} \quad (4.2)$$

Where:

- y_{wall} is the cell height perpendicular to the wall
- u_f is the mean velocity of all cell-vertices not connected to the wall
- ν_{wall} is the viscosity on the wall-face

The friction velocity τ_{wall} is now calculated depending on y_{wall} either by a linear relation or the logarithmic law of the wall:

$$y^+ < 11.445 : u^+ = y^+ \quad (4.3)$$

$$y^+ > 11.445 : u^+ = k^{-1} \ln(E y^+) \quad \text{where } k = 0.41 \text{ and } E = 9.2 \quad (4.4)$$

4.1.2 2D wall-bounded box

The first 2D test case is separated in two main zones delimited by an immersed object. The initialization imposes a pressure of 50 *bar* in the left zone and a pressure gradient down to 5 *bar* in the other immersed boundary side as shown in Fig. 4.1. The temperature is homogeneous through the whole domain and is set to 1000 *K*.

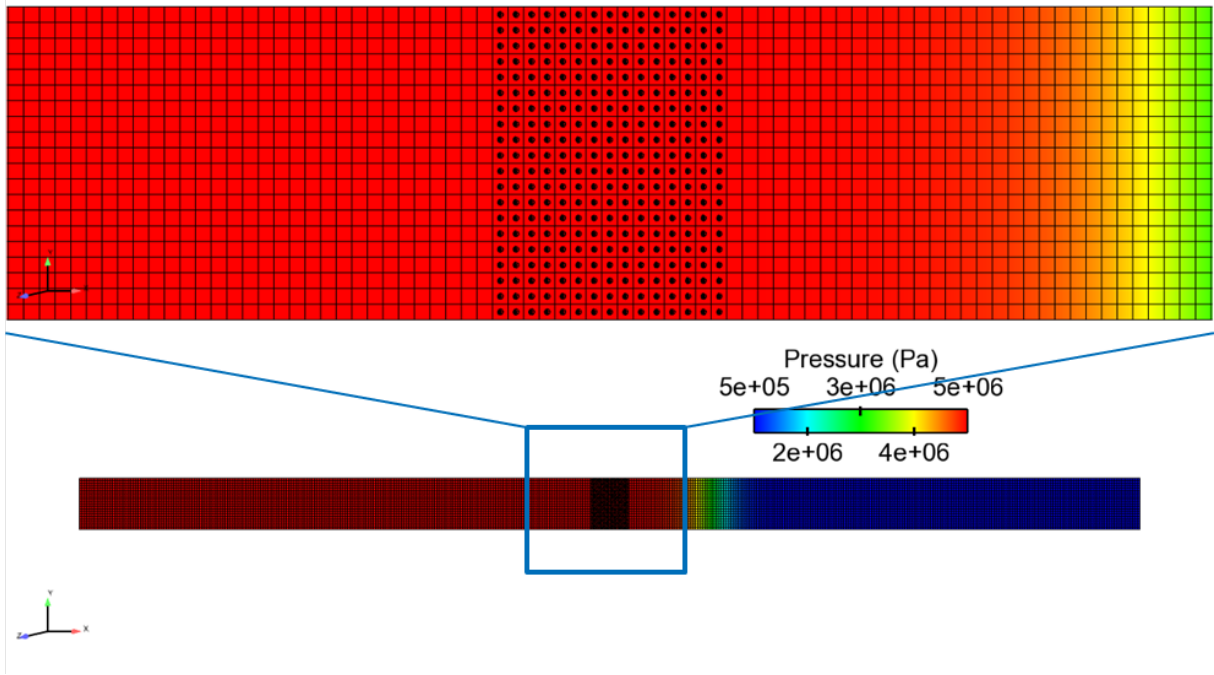


Figure 4.1: Initial condition for the 2D case

Computational parameters

LES is performed on this non reactive case to evaluate the LIB method proposed in this study, where the gas is only composed of one species, here O_2 . The Lax-Wendroff numerical scheme is chosen here and the Smagorinsky SGS model [73] is used. Moreover, no artificial viscosity is used to avoid the increase of diffusion in the vicinity of immersed boundary.

The Cartesian mesh has 24218 nodes and the characteristic length cell is 0.5 mm. The domain is 207.5 mm long and 10 mm high, where the immersed boundary is added in the middle of the flow. In this configuration, the object covers 15 cells.

The new LIB method is evaluated on this test case, where the two conform boundary conditions presented above are compared with each other. The aim is to analyse which conform boundary condition is the most efficient to hold back the high pressure fluid.

Results

In order to quantify the leakage from high to low pressure zones, the temporal evolution of the HP mass evolution function of time is plotted in fig. 4.2.

Mass evolution

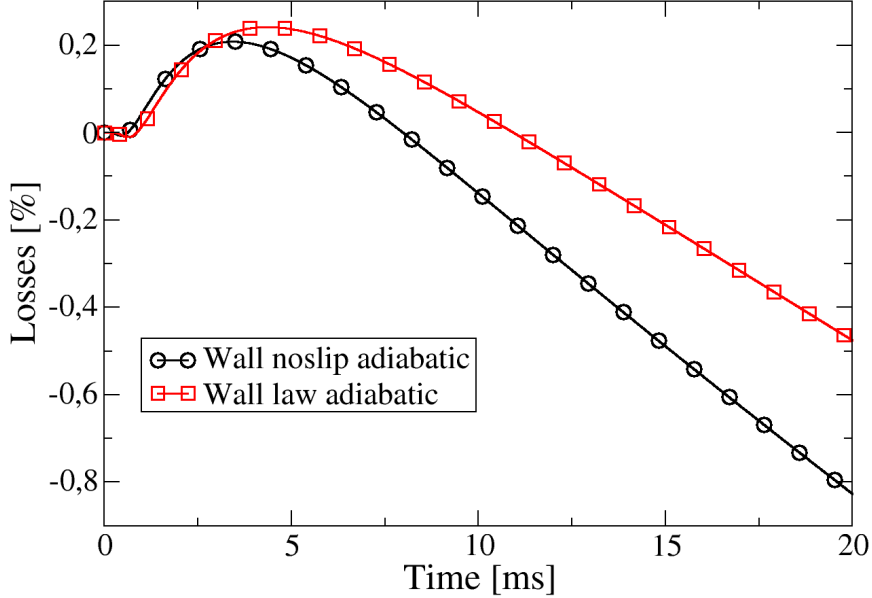


Figure 4.2: Mass losses in percentage

For both conform boundary conditions, 3 phases are identified. Firstly, from 0 to around 0.1 ms , the HP zone mass slightly decreases by $1 \cdot 10^{-4}\%$ which is almost invisible. During the first iteration, the simulation predicts a high velocity due to the high pressure gradient and the lack of LIB source terms which causes the emptying the HP zone. The second phase, from 0.6 to 0.21 ms the mass inside the HP zone increases. This is the result of both a motionless LIB and the initial solution which generates a high feedback forcing term at the second iteration. This kind of overshooting feedback requires several iterations to attain a stabilized value. Finally, a steady state seems to be reached while the HP mass progressively empties through the immersed boundary. At the end of the simulation, less than 1% of HP zone mass is lost after a typical CVC cycle duration, namely 20 ms .

These test cases are the reason for the work proposed on source terms in walls cell presented in section 3.4.2. Indeed, the discrepancies appear between two conformal wall boundary conditions.

The main difference between these cases is that with a wall law-of-the-wall applied on conformal walls leads to the wall velocity different from zero. This generates LIB source terms different from zero on wall nodes, which then creates second order source terms in wall cells of the order of fluid cells. Consequently, the source terms in wall cells are slightly different and introduce different mass leakages in these cells.

=====
Test case conclusion:
=====

The first evaluation of the capability of an immersed boundary to hold back the mass from a high pressure fluid to a lower one is very promising. With both wall boundary conditions, the leakage is lower than 1 % of the initial mass which makes it quite acceptable to apply this method on CVC chamber configurations.

Moreover, this evaluation shows the improvement of the LIB method in wall cells.

4.1.3 2D wall-bounded box with a rotating immersed boundary

LIB flow airtightness efficiency is now examined with a 2D circular immersed object rotating at 6000 RPM. It is placed in a fluid with an initial zero velocity, where a constant pressure of 30 bar and a pressure gradient down to 5 bar are initialised respectively on the left and the right of the rotating immersed boundary.

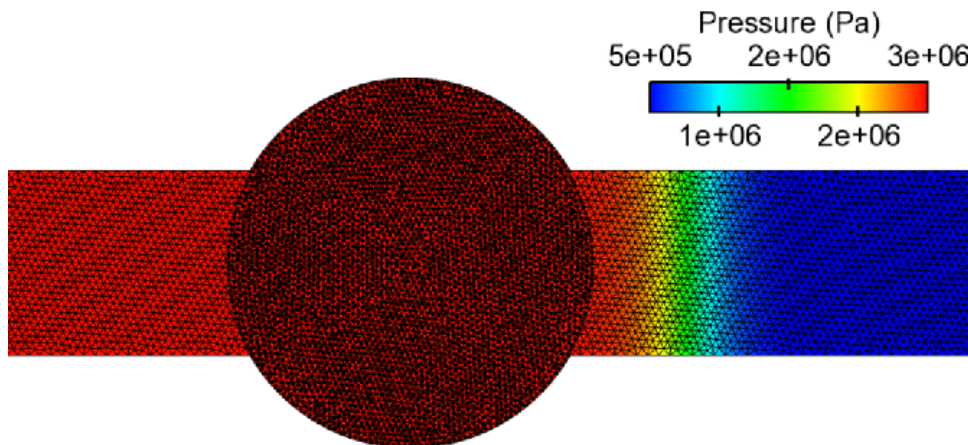


Figure 4.3: Initial condition of the 2D rotation case

Computational parameters

The numerical setup is exactly the same as the previous static case. Indeed, the LES is performed using the Law-Wendrorff numerical scheme and the Smagorinsky SGS model [73]. Also only one species is used, namely O_2 .

This 2D mesh is made of 10998 nodes and the elements used are triangles of 1 mm size. The simulated domain is 280 mm long and 10 mm high and the circular immersed boundary placed in the middle. Since the object is rotating, the density of Lagrangian particles is higher than the Eulerian mesh density in the recovering zone so as to avoid cells without any LIB particles. Typically, the size of the particle mesh is 0,8 mm. Like the previous case, adiabatic no-slip and adiabatic wall law-of-the-wall boundary conditions are evaluated.

Results

As presented in paragraph 3.3.3, the new implemented LIB method can handle this kind of configuration. The first analysis made is to verify that the fluid inside the object has a circular motion. Fig. 4.4 shows velocity fields and iso-velocity contours inside the object.

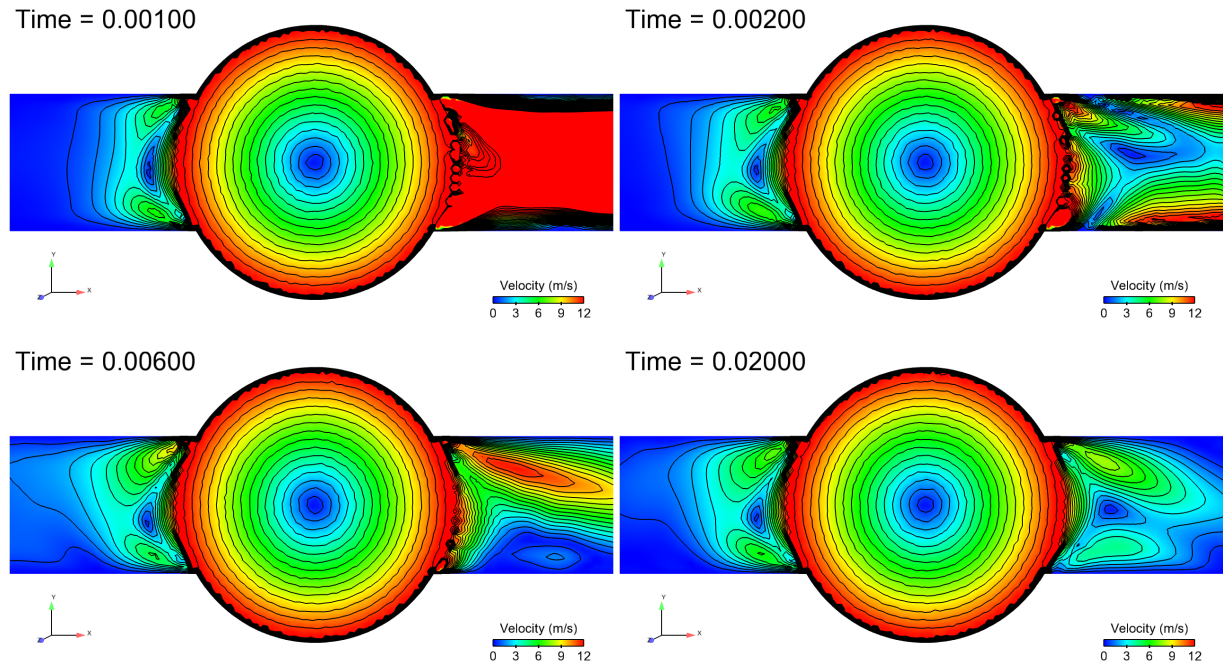


Figure 4.4: Instantaneous snapshots showing velocity field and velocity contours

Fig. 4.4 highlights that the velocity inside and in the vicinity of the rotating object has a solid motion performance. Mass flow rate through the object is now evaluated. In this case, the LIB is rotating at 6000 RPM, therefore the object makes 2 rotations in 20 ms, i.e. 720 degrees. The temporal evolution of the mass losses obtained with the two boundary conditions are compared with each other and results are presented in both Fig. 4.5 and Table 4.1.

Crank angle degrees	Mass losses No-slip wall (%)	Mass losses Wall law (%)
90	-0.179	-0.0667
180	-0.51	-0.58
270	-1.63	-1.81
360	-2.90	-2.96
540	-5.22	-5.127
720	-7.32	-7.23

Table 4.1: Comparison of mass losses with two different wall boundary conditions

In this case, mass losses through the rotating object rise dramatically after 200 degrees and then reach a constant mass flow rate from the high to the low pressure zones. Indeed, a pressure gradient through the object is established after one half rotation.

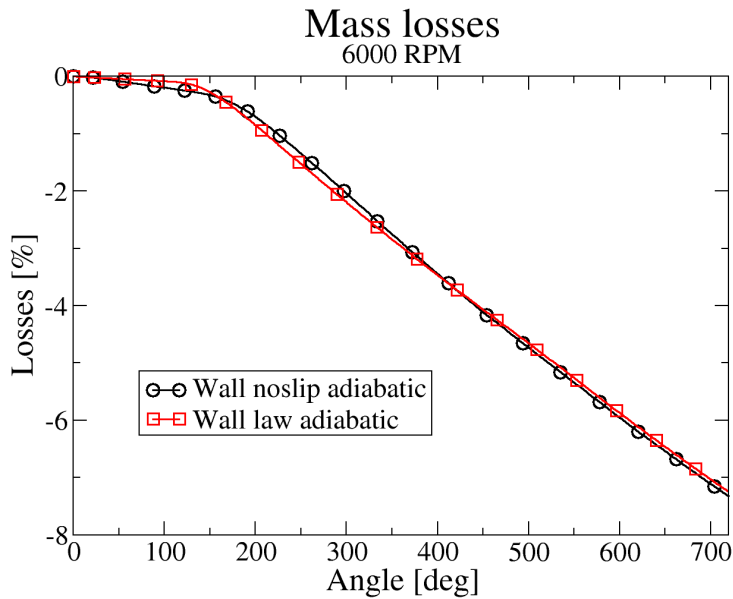


Figure 4.5: Mass losses

However, in a CVC simulation, the chamber does not stay closed during the whole cycle and thus stays closed for less than 180 degrees. That is why, the flow action which has to be considered for CVC chambers is during the first 180 degrees. With a rotating object, both boundary conditions perform the same way and the mass losses are lower than 1 % for a rotation of 180 degrees. Then, mass flow rate increases up to 7.3% after 2 completed rotations.

=====
Test case conclusion:
 =====

With a rotating immersed boundary, the mass losses are higher than through a static object. For a rotation smaller than 180 crank angle degrees, the mass losses in percentage are of the order of 0.5%–0.6%. These results remain very promising for using this method on CVC chamber simulations.

=====
Static and rotating test cases conclusion:
 =====

In these two cases, the LIB used as a wall between high and low pressure flows shows its capacity to hold back the fluid in the HP zone. In the static case, the mass losses are still lower than 1% after a duration of the order of a CVC chamber cycle. The mass losses with a rotating object rise after a half rotation but less than 1% of the mass of the HP zone empties into the LP zone. These two cases demonstrate that this method is suitable to simulate CVC chambers without significant overestimated mass losses.

4.2 Evaluation of the developments on a 3D wall-bounded box with motionless LIB

4.2.1 Test case description

In this paragraph, the fluid airtightness of the developed LIB method is tested in a 3D static case, where an immersed wall is placed between two zones at 50 and 5 bar as shown in fig 4.6. Initial pressure gradient is realised on one cell in front of the immersed boundary in the HP zone. For this case, the cell length scale is of the order of 1 *mm* and 10 cells are covered with Lagrangian particles. All boundary conditions are adiabatic no-slip walls and parameters α and β are set to a value of 2. The numerical scheme is the Lax-Wendroff numerical scheme [74] and the turbulent model is the Smagorinsky model presented in paragraph 2.3.1.

To analyse the new implemented LIB method, pressure evolution over time is plotted in the high pressure zone, firstly without the second order derivative source terms and then with these source terms.

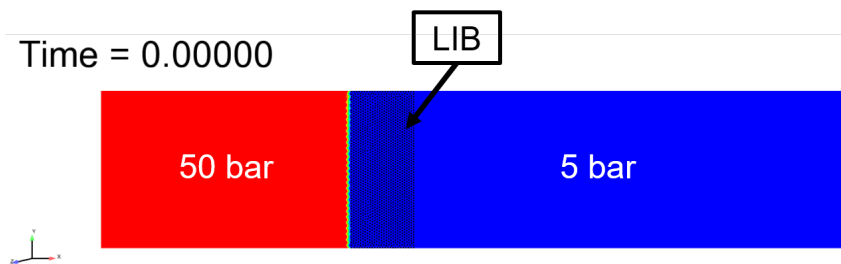


Figure 4.6: Initial solution to evaluate the developed LIB method

4.2.2 Evaluation without the second order derivative source terms

Figure 4.7 highlights that the high pressure zone progressively emptied into the low pressure zone. At the first iteration, the pressure drops by around 1.5 *bar* since LIB source terms are not yet calculated nor applied. After 10 millisecond, the HP pressure drops from 50 bar down to 27 bar, which corresponds to a 46% loss. This result is far from being acceptable to simulate a CVC chamber where the phase at constant volume may last 2 up to 10 *ms* depending on the rotation speed.

This test case demonstrates that the model handles this kind of configuration with high pressure gradient on both sides of the immersed boundary. However, the mass flow rate through this object is far too high which leads to a non acceptable pressure loss in the high pressure zone. That is why the second order derivative source terms were developed and are evaluated in the following paragraph.

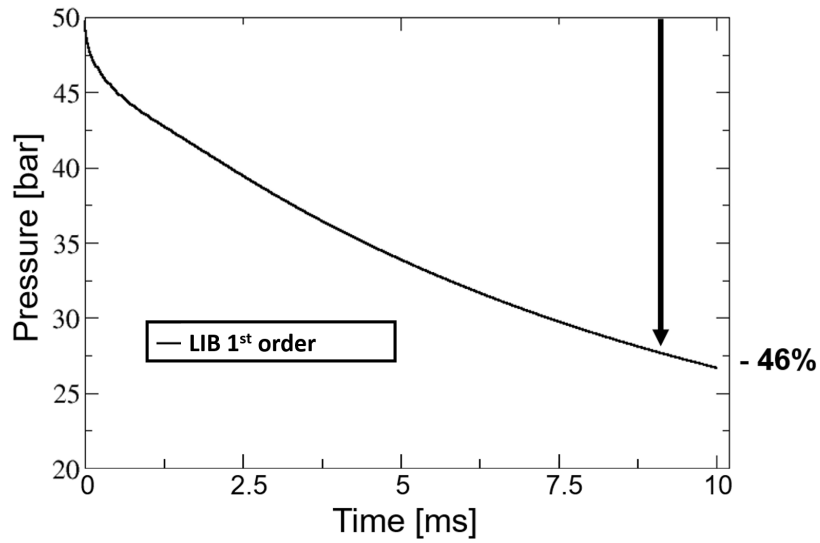


Figure 4.7: Pressure evolution in high pressure zone

4.2.3 Evaluation using the second order derivative source terms

The additional source terms is now evaluated on this case. The same initial solution, presented in Fig. 4.6, is used and the influence of the second order derivative source terms on the pressure loss is analysed.

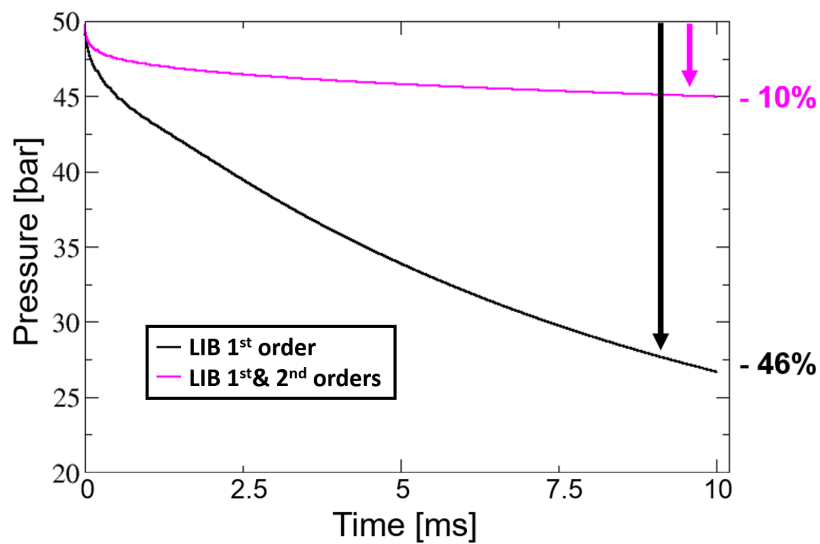


Figure 4.8: Pressure evolution in high pressure zone with additional second order derivative source terms

With this additional sources terms, the pressure drop is of the order of 10% after 10 *ms*. Therefore, the method is improved by a factor of 4.6.

The same simulation is performed on a refined mesh with a cell size of 0.3 mm, so that 30 cells are covered with immersed boundary. The result of this is presented in Fig. 4.9.

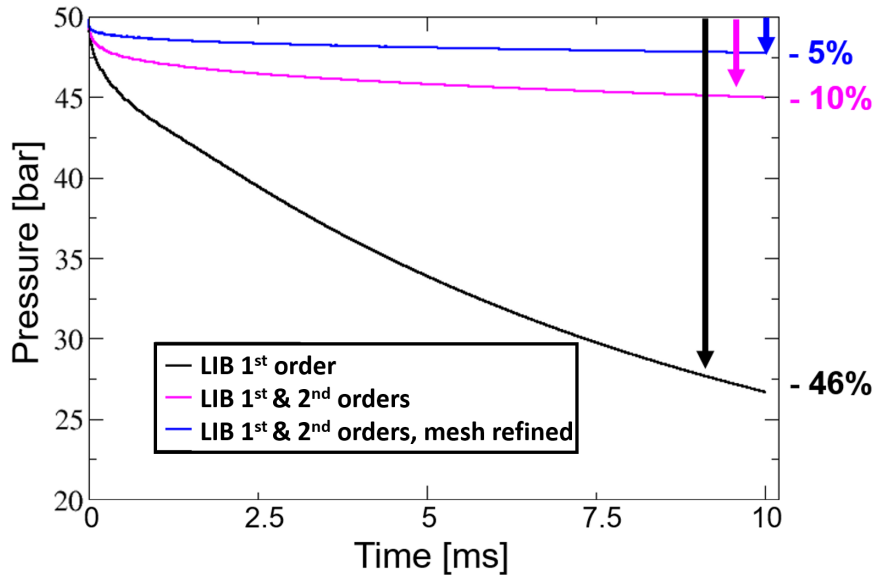


Figure 4.9: Pressure evolution in high pressure zone with additional second order derivative sources term and mesh refinement

Increase the number of covered cells can improve the fluid tightness of the object. This time, the pressure loss in the high pressure zone reaches a value of 5% which is now acceptable.

=====
Conclusion:
 =====

The additional source terms, in the second order derivative of the Lax-Wendroff numerical scheme, clearly improve the flow airtightness of the immersed boundary. By considering the initial pressure in the high pressure zone at 50 bar, the pressure drops by 10 % after 10 *ms*. The initial condition can not be met in CVC chamber since the pressure increases progressively during the combustion. Therefore, the pressure drop during the very first iterations may not be considered, and the real initial pressure which could be taken into account is 48.5 bar. With this initial pressure, the pressure loss through the immersed wall is of 44% when the second order derivative source terms are not activated. With the activation of these terms, the pressure drop is measured at 7.2 % and around 3 % for the refined mesh. By assuming that the initial pressure is close to 48.5 bar instead of 50 bar, the modification of the numerical scheme significantly enhances the method, where a loss of less than 4 % could be acceptable to simulate CVC chambers.

4.3 LIB isothermal boundary condition evaluation

In this paragraph, the additional immersed boundary isothermal boundary condition is compared with an isothermal boundary condition commonly used for conform walls. To this purpose, both the temperature and the temperature gradient through the fluid domain are analysed. The body conform test case is used as the reference for the temperature and the temperature gradient inside the studied domain. In this case, boundary conditions on the left and the right of the domain are realised, on the one hand, with a heat loss thermal boundary condition where the heat surface resistance is set at $R_w = 10^{-4} \text{ m}^2.K/W$ (Eq. 4.5) and, on the other hand, with immersed boundaries which impose the isothermal boundary condition presented in Eq. (3.15). In both cases, the Lax-Wendroff [74] and the TTGC [29] numerical schemes are compared with each other.

$$q = -\frac{T_{wall} - T_{ref}}{R_w} \quad (4.5)$$

4.3.1 Configuration

In order to evaluate the LIB isothermal boundary condition, conform walls and immersed boundary cases are initialized with the same temperature gradient inside the studied domain as shown in Fig. 4.10. As explained above, the isothermal conditions of the LIB case are applied on the same fluid node as the conform walls. Indeed, the domain of the LIB case is extended by 2 cells on each sides, where the Lagrangian particles of the immersed walls are placed. This extension is presented in Fig. 4.10.

Fig. 4.10 shows the initial temperature gradient with the conform case on the top of the figure and the LIB case on the bottom. This figure also presents the two cartesian grid used. For both the conform and the LIB test cases, temperatures on the left and on the right are respectively set at 600 K and 610 K .

The aim of this case is to see the thermal diffusion inside the fluid. where the temperature will reach the linear function from 610 K to 600 K in 2 mm and thus follows the expression :

$$T(x) = 610 - \nabla T \times x \quad (4.6)$$

Where x is the abscissa and ∇T the steady state temperature gradient in the fluid domain, which equals 5000 K/m .

4.3.2 Computational parameters

The LES is performed using both the Lax-Wendroff and TTGC numerical schemes. Since thermal diffusion is the studied phenomena, no SGS and artificial viscosity models are chosen for these simulations. Moreover, only one species is used, namely O_2 .

The Cartesian conform mesh has 441 nodes where quadrilateral size is of 0.1 mm . The computational domain is 2.0 mm long and 2.0 mm high. The two walls on the top and on the bottom have an adiabatic no-slip boundary condition. However, the walls on the left and on the right have a no-slip heat loss boundary condition to relax the temperature. The thermal resistance on these walls are set at $10^{-4} \text{ m}^2.K/W$.

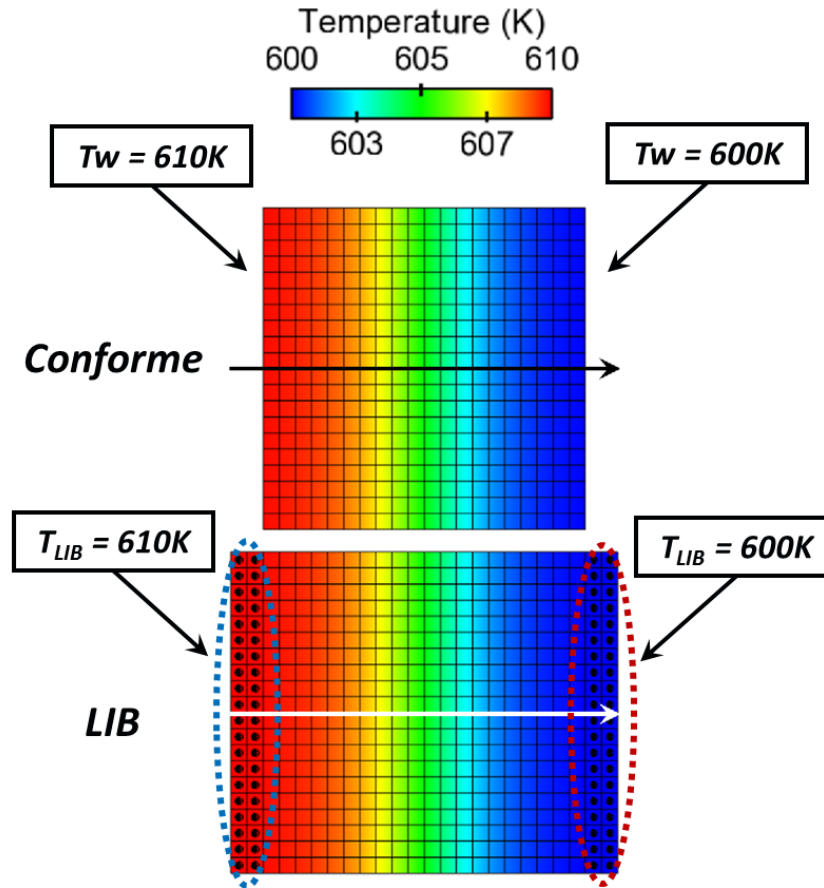


Figure 4.10: Initial temperature in the conform and the LIB test cases

The LIB case mesh has exactly the same topology. However, 0.2 mm are added on each side to place the isothermal immersed boundary walls. Consequently, LIB mesh has 525 nodes, it is 2.4 mm long and 2.0 mm high.

4.3.3 Results

Spatial temperatures and temperature gradient profiles are plotted in the middle of the domain (arrows Fig. 4.10). The following figures from 4.11 to 4.18 show the evolution of these two variables at different times for the three following cases :

- The conform walls case simulated with Lax-Wendroff numerical scheme,
- The LIB case simulated with Lax-Wendroff numerical scheme,
- The LIB case simulated with TTGC numerical scheme.

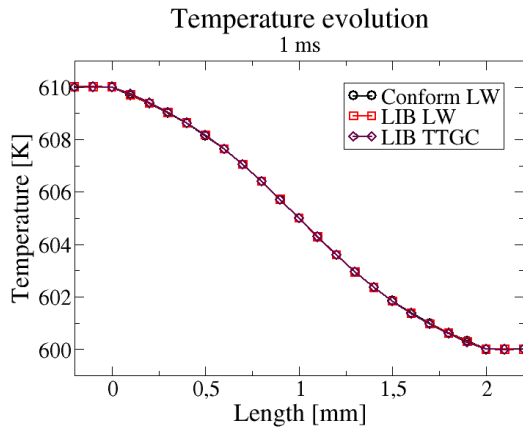


Figure 4.11: Temperature at 1ms

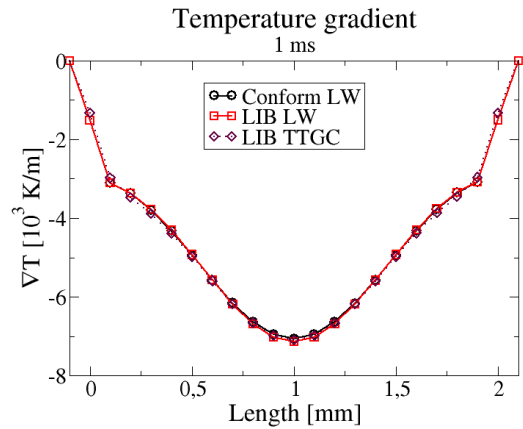


Figure 4.12: Temperature gradient at 1ms

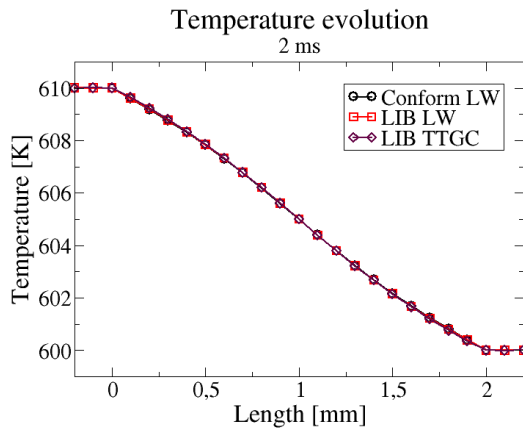


Figure 4.13: Temperature at 2ms

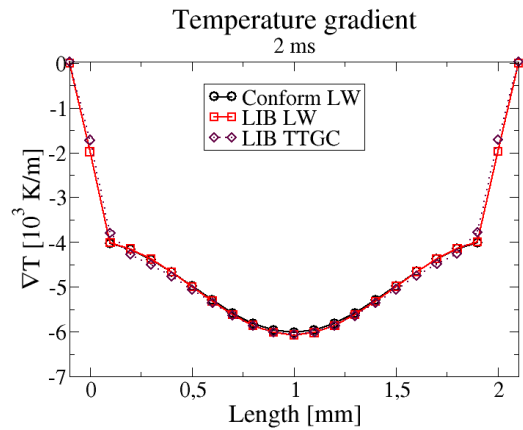


Figure 4.14: Temperature gradient at 2ms

At 1 *ms* three cases behave similarly but small discrepancies are visible on temperature gradients. Body conform and LIB cases which both use Lax-Wendroff numerical scheme predict the same temperature and the same temperature gradient near walls. However, the TTGC LIB case slightly underestimate temperature gradients near walls. During the second millisecond, the same discrepancies can be seen.

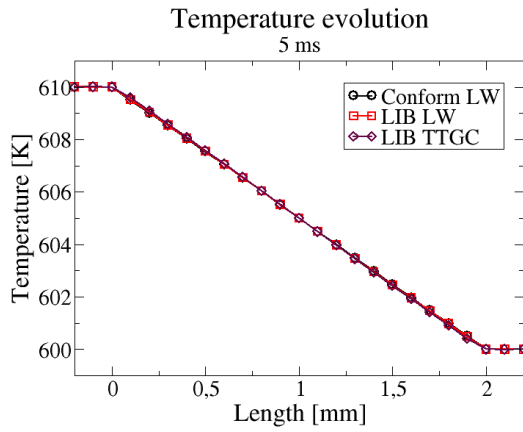


Figure 4.15: Temperature at 5 ms

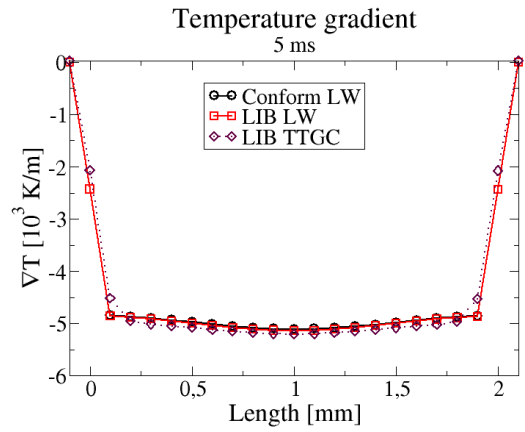


Figure 4.16: Temperature gradient at 5 ms

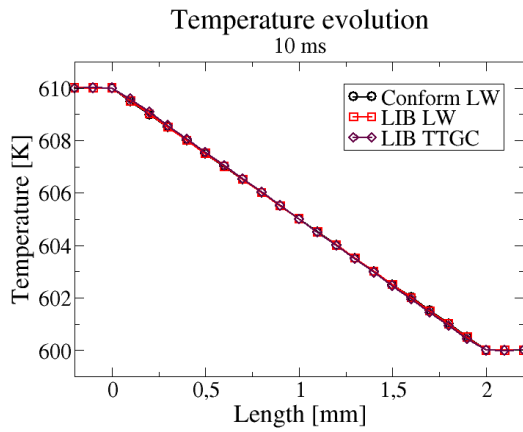


Figure 4.17: Temperature at 10 ms

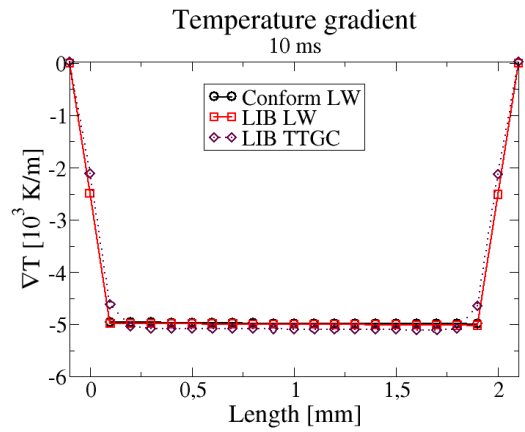


Figure 4.18: Temperature gradient at 10 ms

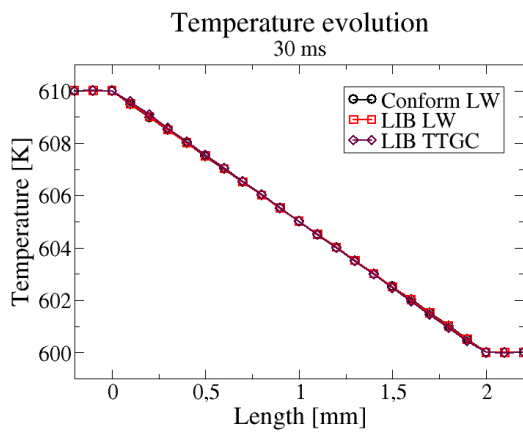


Figure 4.19: Temperature at 30 ms

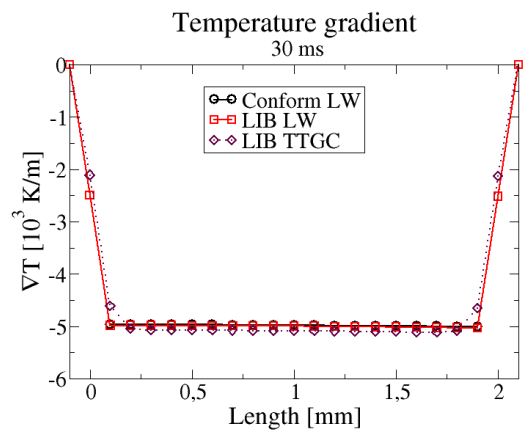


Figure 4.20: Temperature gradient at 30 ms

From 10 ms, the steady state is reached since no differences in the temperature and the temperature gradient are observed between Figs. 4.17 and 4.19 and also between 4.18 and 4.20.

As expected, the temperature reaches the linear evolution through the fluid domain and the pressure gradient meets the targeted value of 5000 K/m.

Final results highlight that the LIB cases which use the Lax-Wendroff and the TTGC numerical schemes respectively predict temperature errors of lower than 0.02% and 0.03% on first fluid nodes and temperature gradient errors of 0.2% and 2.0% throughout the whole domain by comparing to the conform case.

=====
Conclusion:
=====

As shown in all graphics, discrepancies between all cases are far from being significant, which allows the use of this boundary condition on the intake and the exhaust systems of CVC chambers.

4.4 Acoustic and pressure wave cases

In this paragraph, two eigen-modes with different cavity lengths and one pressure wave propagation are performed using both body conformal and immersed boundary walls to evaluate the discrepancies introduced by the model. These test cases are proposed here because the following CVC configuration in chapter 5 required simple cases to evaluate the functioning of immersed boundary walls with acoustic and pressure waves.

4.4.1 Short cavity acoustic eigen-mode 1D case

The objective of this test case is to compare the first acoustic eigen-mode in a 1D closed cavity using a case where all walls are conformally meshed with another one where the right wall is made of an immersed boundary. These cases are used to measure discrepancies and dissipation introduced by LIB method. As shown in Fig 4.21, the studied domain of 10 mm long is delimited by a conform wall on the left and either a conform wall or a LIB on the right. In the LIB case, the mesh is enlarged to place LIB particles into several cells. On both top and bottom walls, the boundary condition are realised with a conform approach.

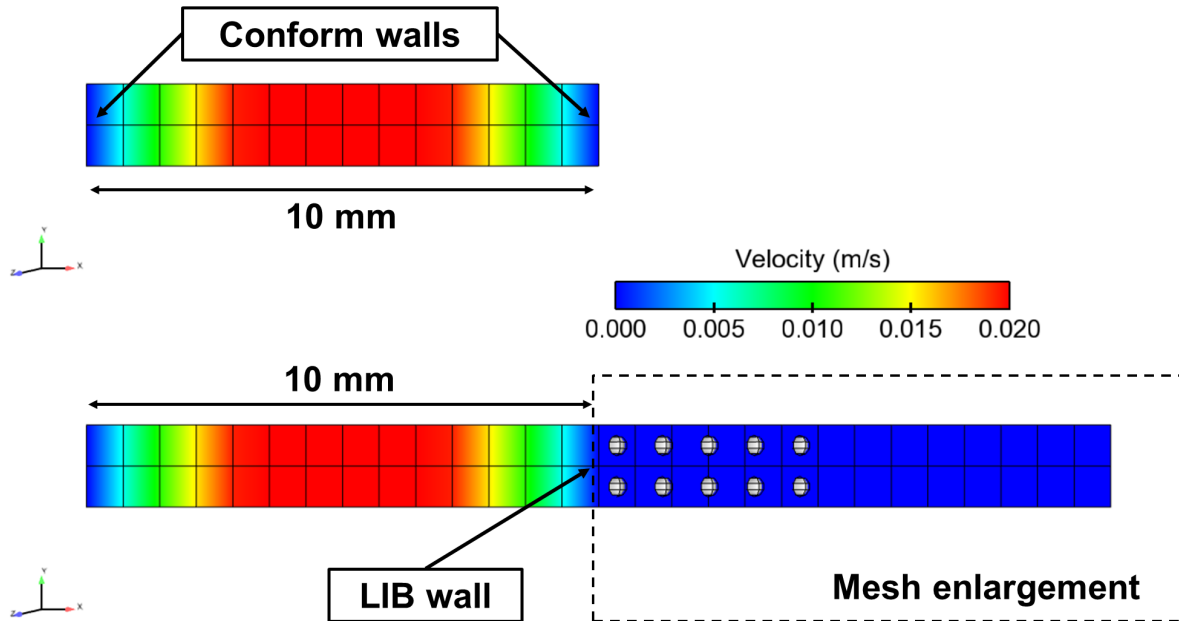


Figure 4.21: Initialization of the first acoustic mode in the cavity

Initial values of pressure and velocity correspond to the first mode of the cavity. The analytical form of the initial solution is given in Eq. (4.7).

$$u(x) = \frac{p'}{\rho c} \sin\left(\frac{\pi x}{l}\right) \quad p = 101300 \text{ Pa} \quad (4.7)$$

where $p' = 10 \text{ Pa}$ is the equivalent pressure fluctuation, $l = 10 \text{ mm}$ is the length of the

cavity, ρ is the density and c the sound speed. Fig. 4.22 shows the initial profiles of the axial velocity and the pressure.

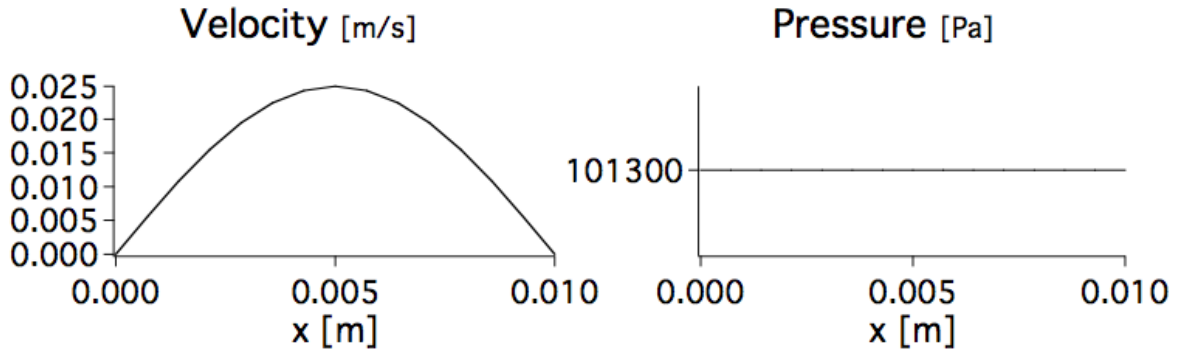


Figure 4.22: Velocity and pressure initialization of the 1D cavity test

The pressure evolution is measured with a probe positioned on the left wall. Simulations are performed using Lax-Wendroff [74] and TTGC [75] numerical schemes.

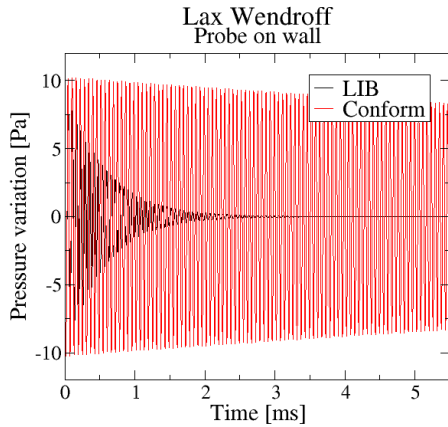


Figure 4.23: Hundreds of cycles

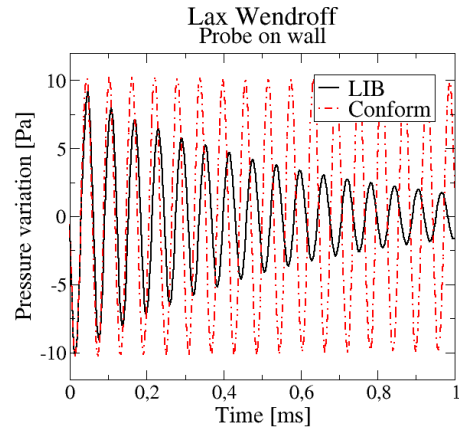


Figure 4.24: Zoom on the very first acoustic cycles

Fig 4.23 highlights that the two cases are dissipative with Lax-Wendroff numerical scheme and the absorption rate introduced by the LIB wall is more significant since after 2.5 ms almost all the pressure fluctuations disappear, while the conform case lowers to only 9 % of pressure amplitude. Moreover, Fig.4.24 shows that the LIB wall also introduces a time lag compared with body conformal case. With a studying zone of 10 mm the LIB pressure signal is in phase opposition after 0.75 ms or 13 cycles.

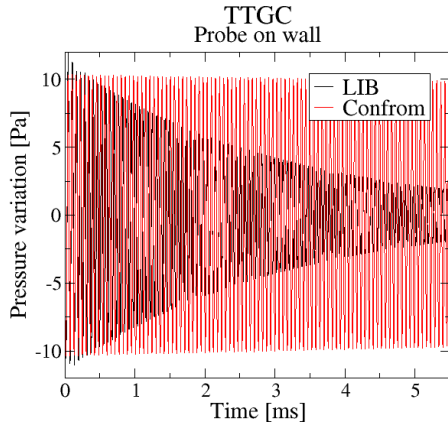


Figure 4.25: Hundreds of cycles

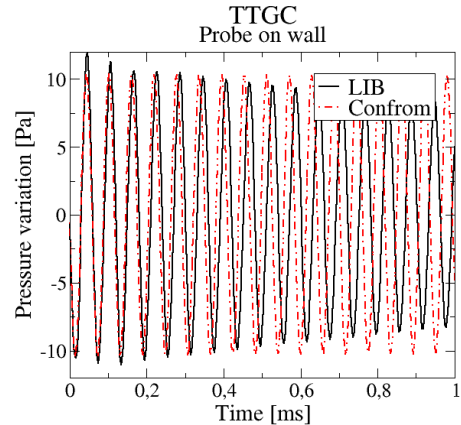


Figure 4.26: Zoom on very the first acoustic cycles

As expected, Fig. 4.25 shows that TTGC numerical scheme is less dissipative than Lax-Wendroff numerical scheme and the LIB wall is still more diffusive than the conform wall. Like the dissipation rate, the time shift between the conform and the LIB wall appears later than with Lax-Wendroff numerical scheme. Indeed, Fig. 4.4.1 shows that two pressure signals are in phase opposition after 0.95 ms or after 17 cycles.

=====
Conclusion:
 =====

The study of the acoustic eigen mode in the case of 10 mm length highlights that LIB walls are significantly more dissipative than conform walls and introduce a time delay which leads to phase opposition after one or two tens of cycles depending on the numerical scheme.

4.4.2 Long cavity acoustic eigen-mode 1D case

This case is similar to the previous one except that the length of the closed cavity is expanded to 600 mm which is the intake pipe length of the studied CVC chamber. The aim of this study is to identify whether or not a significant time shift can be observed between conform and LIB walls. With exactly the same methodology, the pressure and the velocity are initialized according to the first mode of this cavity. Fig. 4.27 shows the studied domain and the mesh enlargement used in the LIB case.

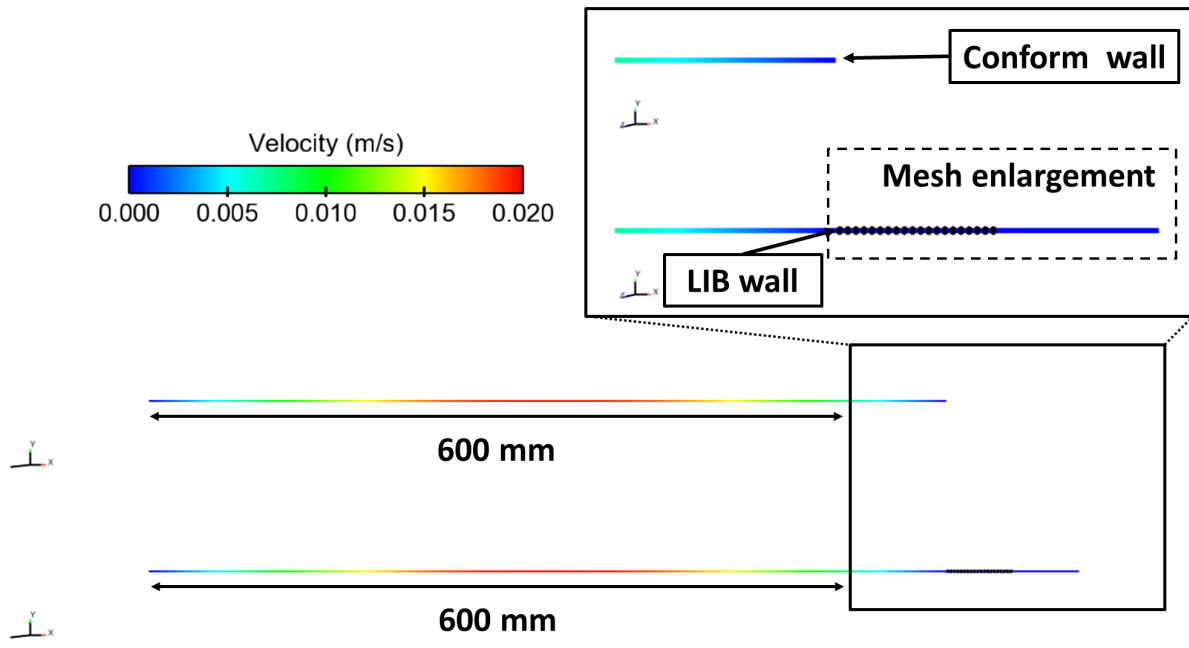


Figure 4.27: Initialization of the first acoustic mode in the cavity of 600 mm

Pressure evolution is measured on left wall and the velocity is plotted at the center of the cavity.

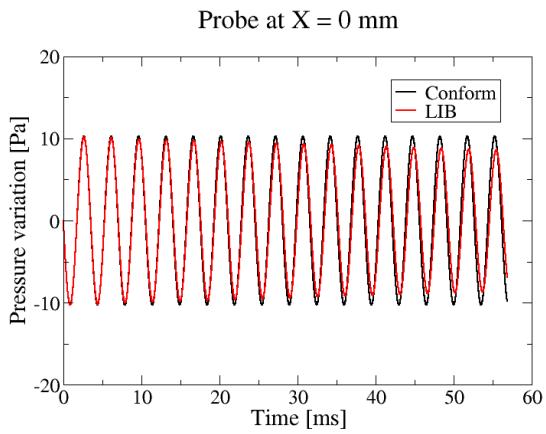


Figure 4.28: Pressure evolution on the left wall

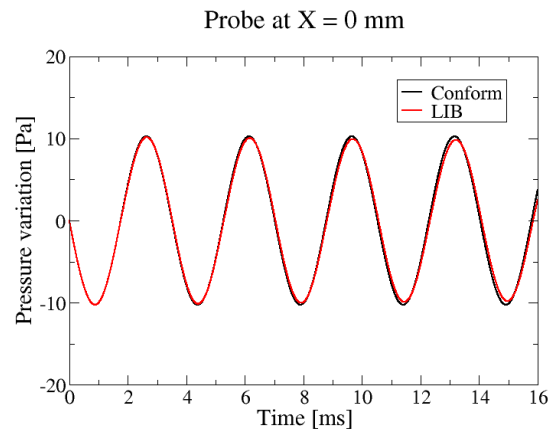


Figure 4.29: Focus on the pressure evolution of the first cycles on the left wall

Like in the previous acoustic study, Figs. 4.28 and 4.29 highlight that the LIB wall quickly dissipates the pressure fluctuation. After 16 cycles the pressure loses 15% of its initial amplitude whereas the conform case does not lose any pressure amplitude. Moreover, Figs. 4.29 and 4.29 shows that the time shift is nearly imperceptible.

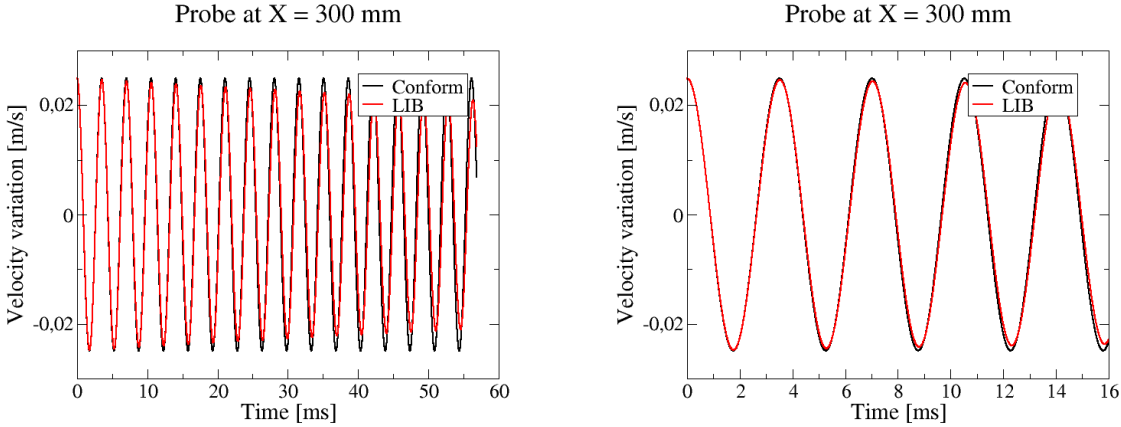


Figure 4.30: Velocity evolution in the center of the cavity
 Figure 4.31: Focus on the velocity evolution of the first cycles

The velocity performs the same as the pressure evolution but is dephased by 1/2 of phase.

=====
Conclusion:
 =====

The study of the first eigen acoustic mode in a cavity with the same length of the intake pipe of studied CVC chamber yields the following conclusions. Modelling moving boundary with LIB can slightly decrease the pressure amplitude and introduce time shift if a large amount of acoustic mode cycle can occur. However, this can not explain the observed discrepancies between experimental and LES pressure signals presented in part II.

4.4.3 Pressure wave

The final test case is chosen to evaluate the performance of LIB walls in front of a propagating pressure wave. In this particular case, a pressure wave is created by initializing a pressure gradient from 30 down to 1 *bar*. The aim of this paragraph is to analyse whether or not the LIB wall acts in the same way as a conform wall. The considered domain is 200 mm long and 20 mm high. Fig 4.32 presents how the pressure wave is initialized on the left and how LIB wall is introduced. Pressure evolutions are analysed with a probe put in the middle of the studied domain.

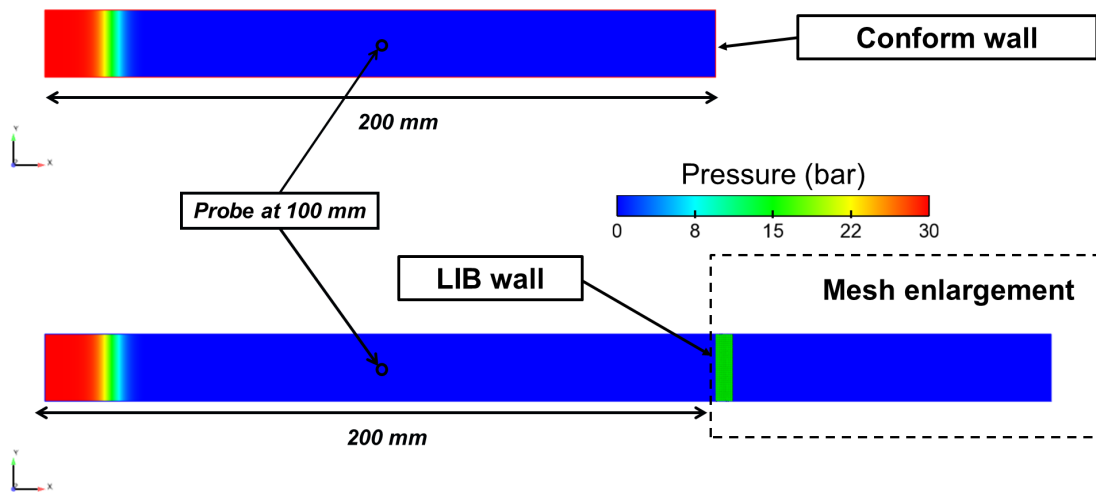


Figure 4.32: Pressure wave initialization

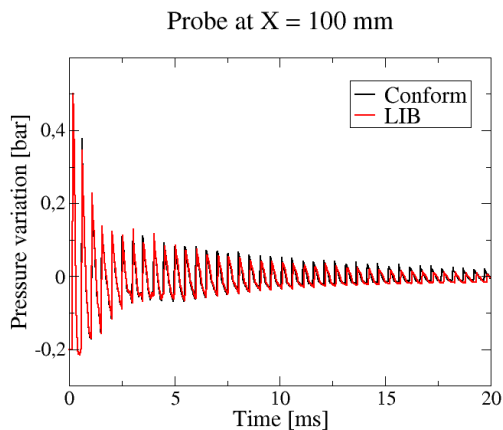


Figure 4.33: Pressure Evolution

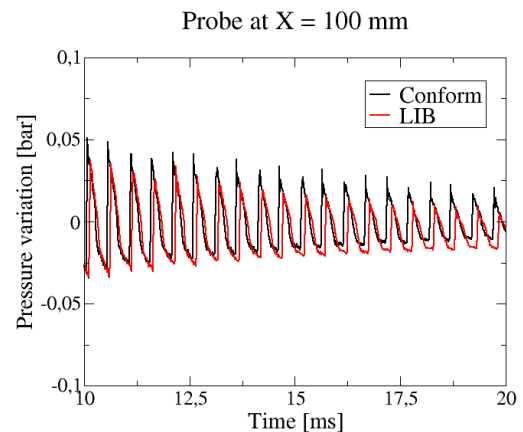


Figure 4.34: Focus on 10 to 20 *ms*

Fig. 4.33 shows that pressure evolutions in the middle of the studied domain behave similarly. However, Fig. 4.34 emphasizes that small discrepancies are noticeable from 5 *ms*. Like in the previous acoustic test cases, the LIB wall lightly dissipates the pressure wave compared with the conform wall.

=====
Conclusion:
=====

LIB walls behave like conform walls when pressure wave rebounds on them even if the dissipation rate is higher when LIB walls are used. The discrepancy between the conform and the LIB cases are acceptable, which demonstrates that the wall boundary condition is correctly reproduced with LIB walls.

4.4.4 Conclusion

All these three acoustic test cases highlight that the flow and the acoustics perform properly near immersed boundary walls. However, this study also shows that LIB walls are more dissipative than conform walls and can introduce a time delay depending on the acoustic of the studied domain.

4.5 Steady state flow bench

The objective of this configuration is to evaluate the flow around a spark ignition engine valve modeled by immersed boundary.

4.5.1 Experimental apparatus

The steady state flow bench consists of a sudden pipe expansion of a factor of 3.53 where a valve similar to these used in SI engines is positioned with a constant 10 mm lift so as to let the air go through the configuration. Experimentally, the flow inside the test bench is driven by a pressure difference between the inlet and the outlet generated by a fan downstream of the apparatus. The targeted inlet bulk velocity is of 65 m/s which is used as inlet boundary condition in the LES. As soon as the steady state is established, Particle Image Velocimetry (PIV) and Laser Doppler Anemometry (LDA) measurements provide velocity fields on two planes downstream of the valve. Fig 4.35 presents all dimensions of the studied zone and the two planes positions. Moreover, pressure sensors are disposed among the intake and exhaust pipes to give access to the pressure drop through the expansion. Experimentally, the valve axis is vertical so as to avoid gravity effects. Finally the pressure loss through the flow bench is measured with several static pressure sensors along the walls upstream and downstream of the valve. This configuration is studied by Thobois *et al.* [76] and more recently by Piscaglia *et al.* [77, 78] where more details on the configuration can be found.

In the present study the valve is modelled with both a body fitted mesh and a immersed boundary and results are compared with experimental data. The aim of this test case is to evaluate valve jet generated with immersed boundary and analyse whether or not this turbulent flow is correctly captured with the LIB approach.

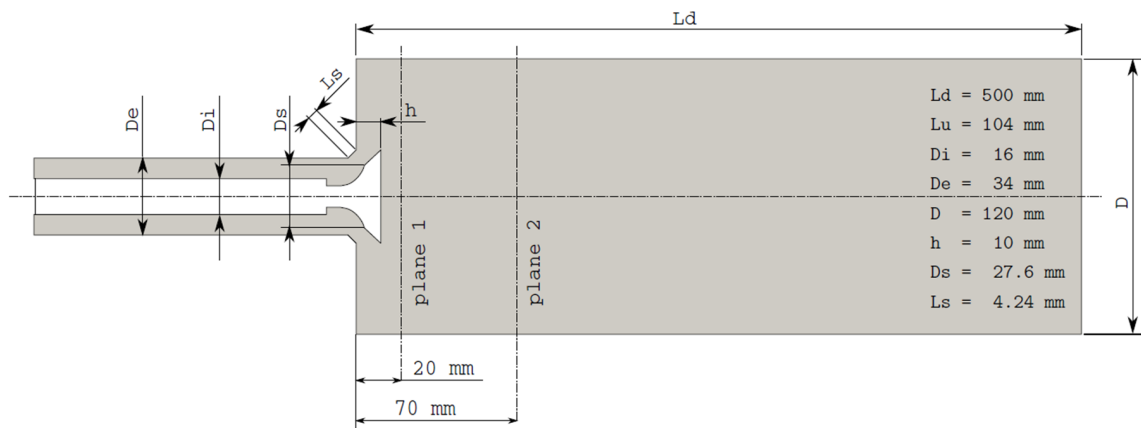


Figure 4.35: Apparatus geometry dimensions

4.5.2 Computational parameters

To study this apparatus, LES is performed with Lax-Wendroff numerical scheme [74] with Simga SGS model [26] as prescribed in SI engine simulations. Indeed, this SGS model is known to predict viscosity on high shears stress zone like in valve jets better. Conform and immersed boundary meshes used in LES simulations are respectively presented in Figs. 4.36 and 4.37. They are both made of tetrahedral elements and are refined down to 0.4 mm in the jet of the valve in order to reproduce flow detachments better. Adiabatic no-slip law of the wall developed by Nicoud [79] is imposed on all conform walls. The inlet boundary condition imposes an inlet bulk velocity at 65 m/s and the pressure at the outlet of the domain is relaxed to the atmospheric pressure.

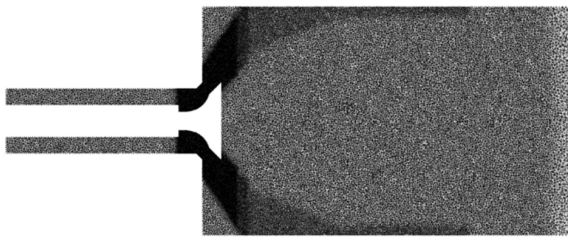


Figure 4.36: Body-fitted mesh

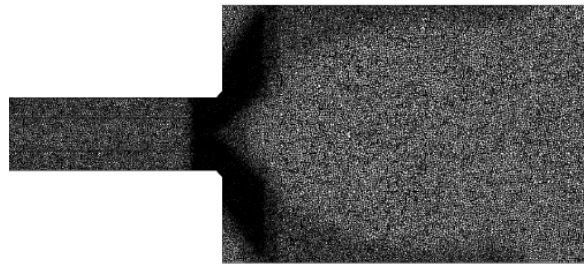


Figure 4.37: IB mesh

4.5.3 Results

Velocity field is averaged on 15 convective times and velocity profiles are plotted on two planes presented above. Fig. 4.38 shows the solution used to extract velocity profiles at 2 positions, namely at 20 mm and 70 mm from the expansion. Moreover, Fig. 4.39 allows the visualisation of the two planes used to realise the spatial averaging on axial and tangential velocities.

Finally the pressure drop through the expansion is analysed.

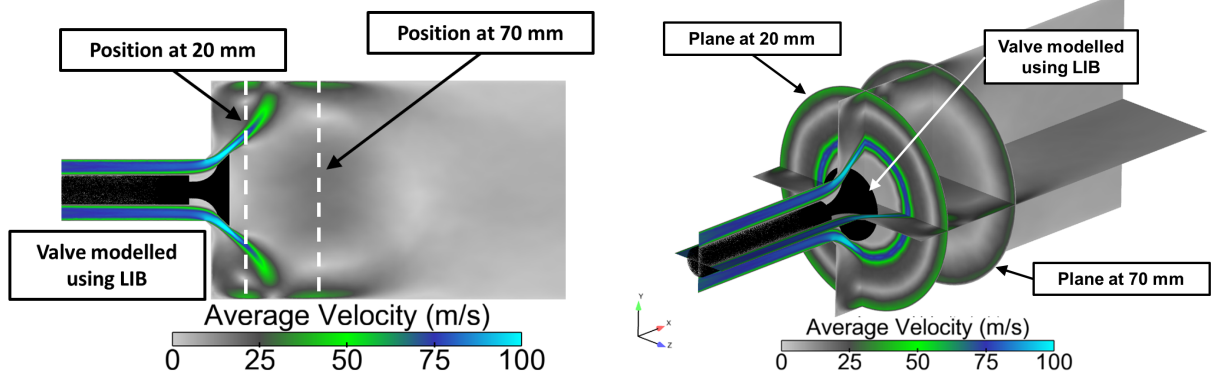


Figure 4.38: Studying zone around the valve jet Figure 4.39: Planes where velocity profile are plotted

Firstly the computed mass flow rate is checked to be consistent to the targeted bulk velocity of 65 m/s . In this configuration, the mass flow rate equals 55 m/s as shown in 4.40.

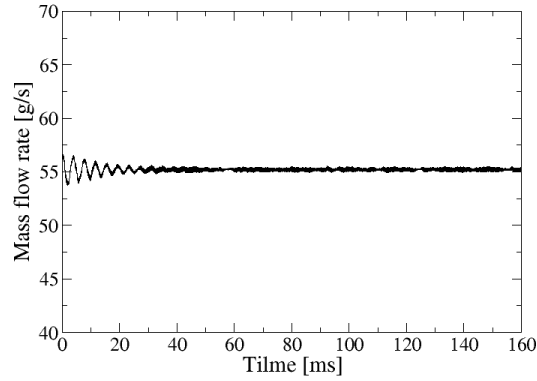


Figure 4.40: Inlet mass flow rate

4.5.3.1 Velocity profiles at 20 mm

The first plane considered in this paragraph is positioned at 20 mm from the expansion. At this position, the flow downstream of the edge of the valve is highly turbulent. The following graphs present the axial, the tangential velocities and the RMS velocities which are normalized by the bulk velocity of the experiment, of the conform simulation, the LIB case and the experiment. In these graphs, the profiles are plotted as function of r/R where R the the radius of the cylinder downstream of the expansion.

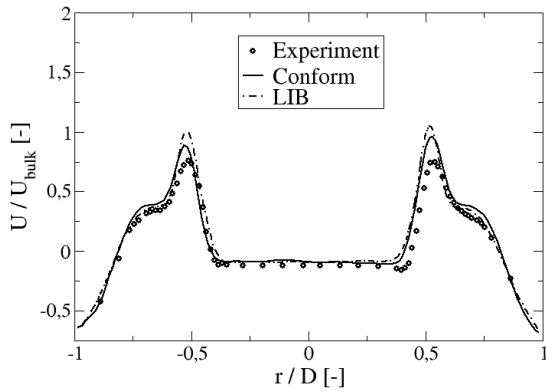


Figure 4.41: Axial velocity profiles at 20 mm

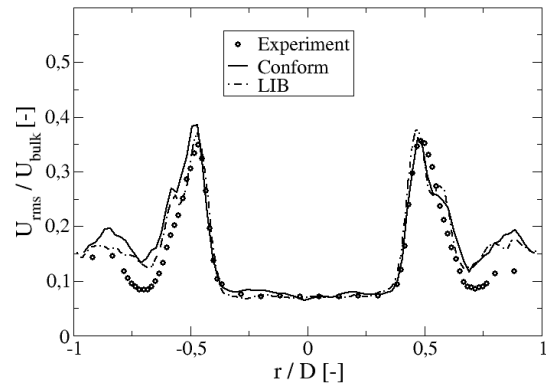


Figure 4.42: RMS axial velocity profiles at 20 mm

Fig. 4.41 shows the axial velocity where all cases perform the same way. However, both simulations seem to overestimate the axial velocity where the LIB method and the conform simulation respectively predict 99% and 90% of the bulk velocity while the experimental velocity equals 78% the bulk velocity, all being at r/R equals to 0.5 and -0.5 .

The RMS axial velocity is also accurately predicted even if both simulations overestimate the RMS axial velocity in zone close to walls as shown in Fig. 4.42.

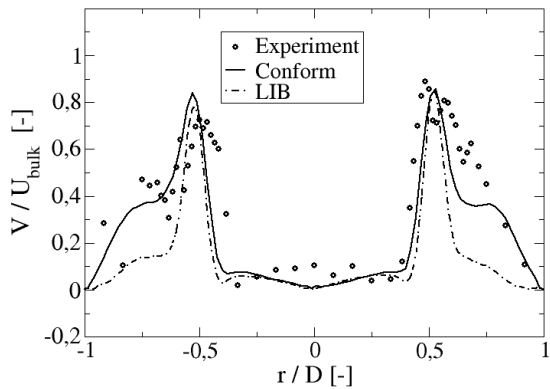


Figure 4.43: Tangential velocity profiles at 20 mm

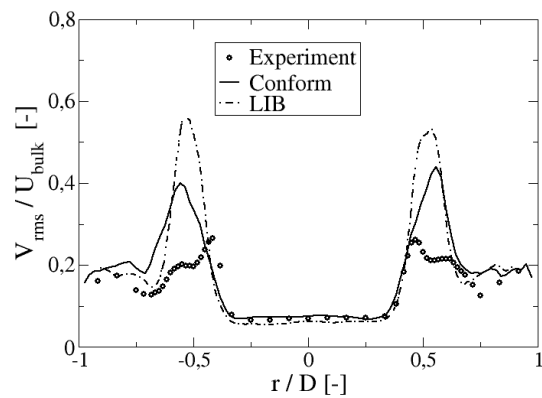


Figure 4.44: RMS tangential velocity profiles at 20 mm

The tangential velocity presented in Fig. 4.43 shows some discrepancies between all cases. The global trend is captured by both simulations and the maximum tangential velocity magnitude is predicted but the velocity near the walls is not accurately obtained. The results on the RMS tangential velocity also show very different trends and both simulations, which significantly overestimate the RMS tangential velocity.

4.5.3.2 Velocity profiles at 70 mm

The second position at 70 mm emphasises on the recirculation zone close to the apparatus axis, generated by the valve jet.

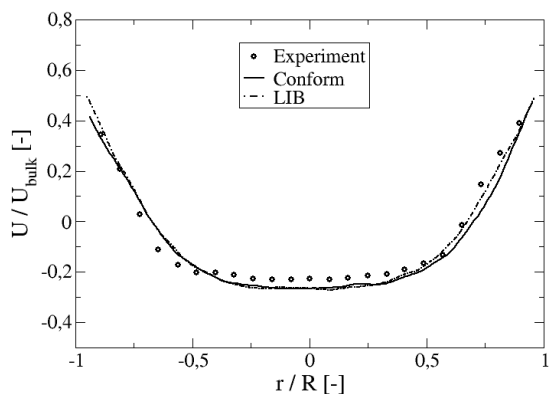


Figure 4.45: Axial velocity profiles at 70 mm

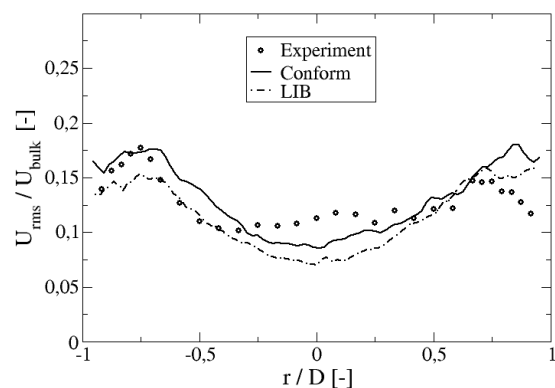


Figure 4.46: RMS axial velocity profiles at 70 mm

The axial velocity on the plane at 70 mm is accurately reproduced by both simulations as shown Fig. 4.45. In this graph, the recirculation zone is captured between normalized radius -0.5 and 0.5 . In Fig. 4.46, the trend of the RMS axial velocity is correctly predicted.

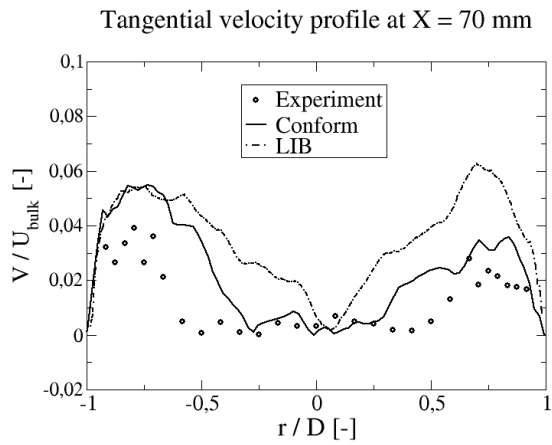


Figure 4.47: Tangential velocity profiles at 70 mm

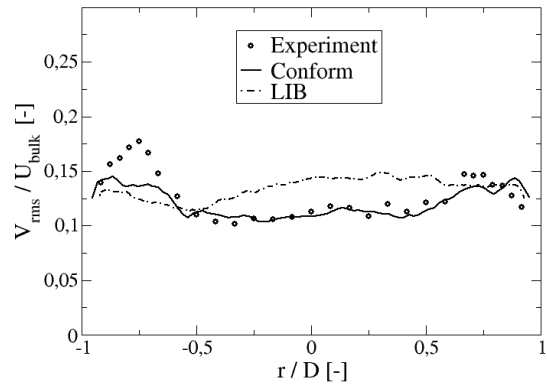


Figure 4.48: RMS tangential velocity profiles at 70 mm

At this position, the tangential velocity and the RMS axial velocity presented in Figs. 4.47 and 4.48 have a low magnitude compared with previous profiles. Therefore, the performance captured here is quite satisfactory.

4.5.3.3 Pressure drop through the expansion

In this paragraph, the attention is focused on the pressure drop generated by both the expansion and the valve. To measure this pressure loss, the pressure evolution is plotted along walls upstream and downstream of the valve.

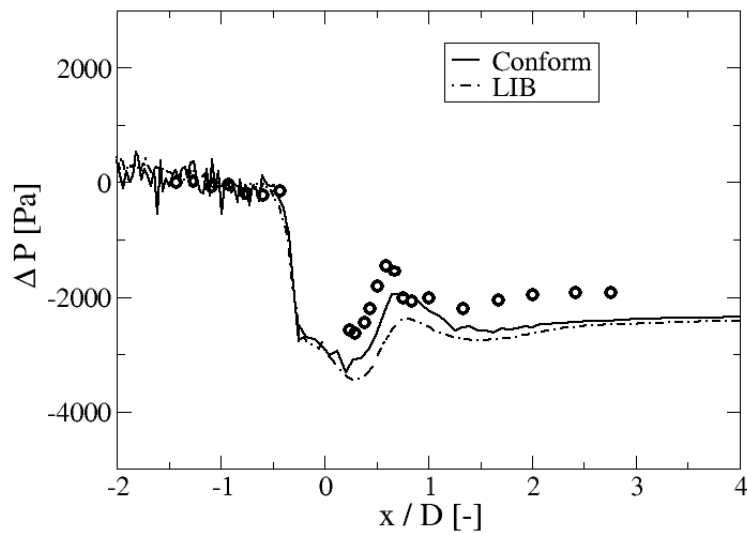


Figure 4.49: Pressure loss through the expansion

The axial profile of static pressure obtained experimentally indicates the complexity of such a configuration. Nevertheless both LES predict the global behaviour of the static pressure even if the pressure drop is overestimated by 25 %. The pressure drop might be improved by refining the mesh inside the valve gap.

4.5.3.4 Conclusion

The simulation of the steady state flow bench around a valve modelled by the LIB method gives satisfactory results in the prediction of the velocity field downstream of the valve and the pressure drop through the expansion.

Part II

Constant volume combustion chamber study

Chapter 5

The CVC chamber apparatus

Contents

5.1	Intake and exhaust system technologies	95
5.2	Pprime’s CVC apparatus	97
5.3	Experimental diagnostics	99

The previous part was dedicated to the evaluation of the new LIB formulation upon basic test cases. The aim of the following chapters is to measure its capability to simulate a semi-industrial CVC chamber. The analysis proposed here evaluates the performance of the LIB method in modeling the intake and exhaust cams and its effect on the fluid flow. Moreover, the efficiency in terms of permeability of these systems will be quantified when the chamber is closed.

5.1 Intake and exhaust system technologies

As presented in section 1.1.3, the constant combustion chambers require intake and exhaust systems to create the constant volume combustor. Several technical solutions may be considered to open and close this type of chambers.

Commonly used in SI engines, valves can be used to perform this role. Nevertheless, this technology requires camshaft or a very complex system to control the valves, which may add too much weight on the whole propulsive system and thus significantly decreases the power density.

Safran Aircraft Engines proposes new spherical contra-rotative cams as intake and exhaust systems on both part of a cylindrical combustion chamber. This combustor was designed to propel aircraft [80]. Fig. 5.1 shows an image of the concept extracted from the patent.

Moreover, Safran Helicopter Engines and Safran Tech propose the intake and the exhaust systems designed to fit in present aeronautical engines. The corresponding systems are made of cylinders coaxial to the turbine shaft, where ports open and close several chambers in a barrel shape. Both companies patented these technologies [81] and [82] and are

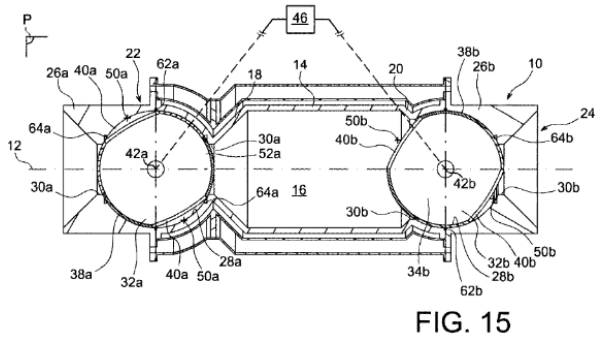


Figure 5.1: Safran Aircraft Engines CVC patent, extracted from [80]

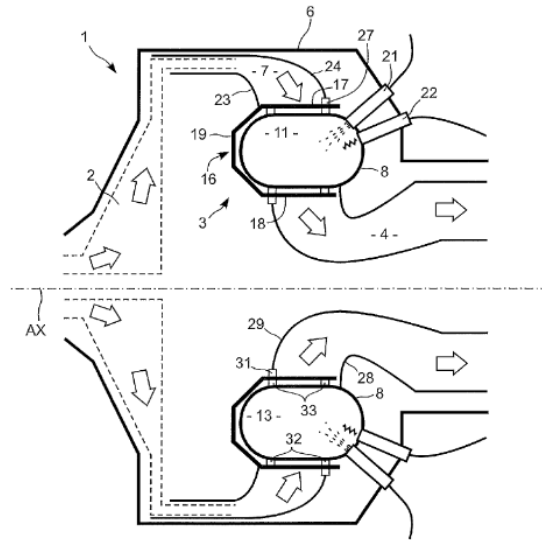


Figure 5.2: Safran Helicopter Engines CVC patent, extracted from [81]

respectively presented in Figs 5.2 and 5.3.

In this study, the CVC chamber called the "Thermo-reacteur" was designed by M. Aguilar [83] and is shown in Fig. 5.4 to motorise the Xplorair presented in Fig. 5.5.

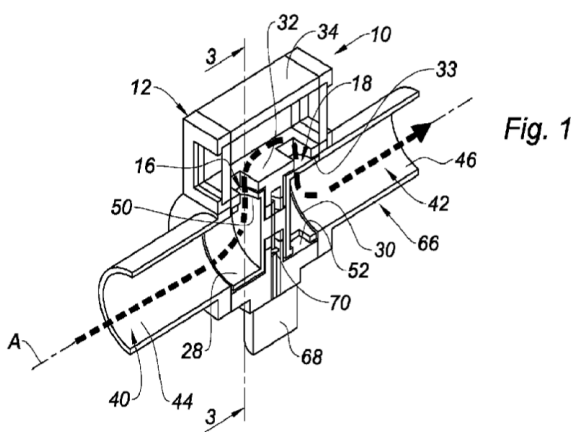


Figure 5.3: Safran Tech CVC patent, extracted from [82]

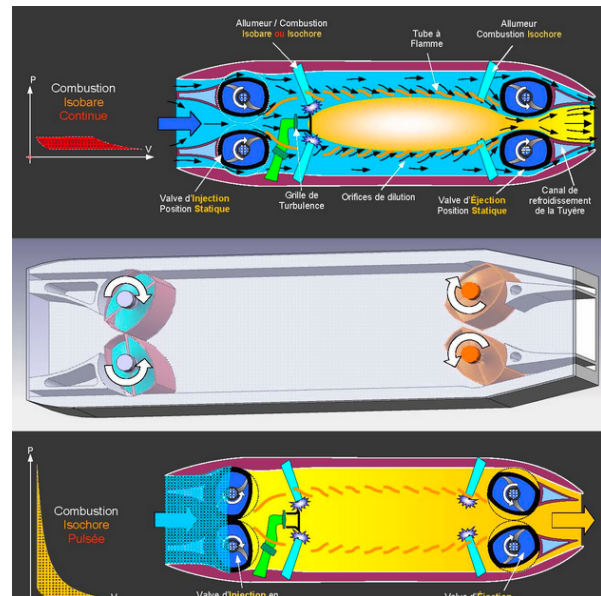


Figure 5.4: "Thermo-reacteur" concept extracted from the website : http://www.xplorair.com/concept_xplorair.html

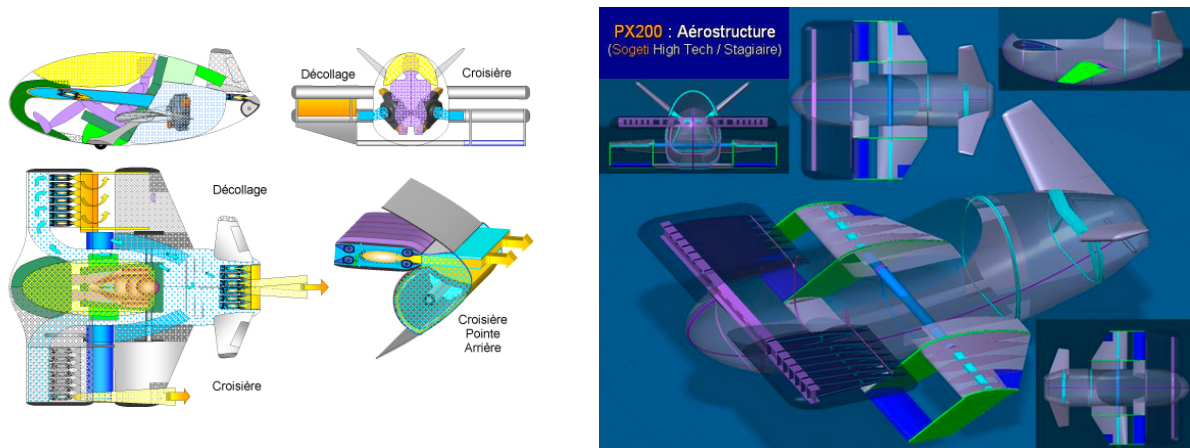


Figure 5.5: Xplorair concept, images extracted from the website : http://www.xplorair.com/concept_xplorair.html

5.2 Pprime's CVC apparatus

The semi-industrial CVC chamber simulated in this study was designed by COMAT and the experiments on this apparatus were set-up at the PPRIME laboratory in Poitiers. This test bench, shown in Figs. 5.6 and 5.7, was designed to analyse experimentally main physical phenomena involved in such an innovative technology.

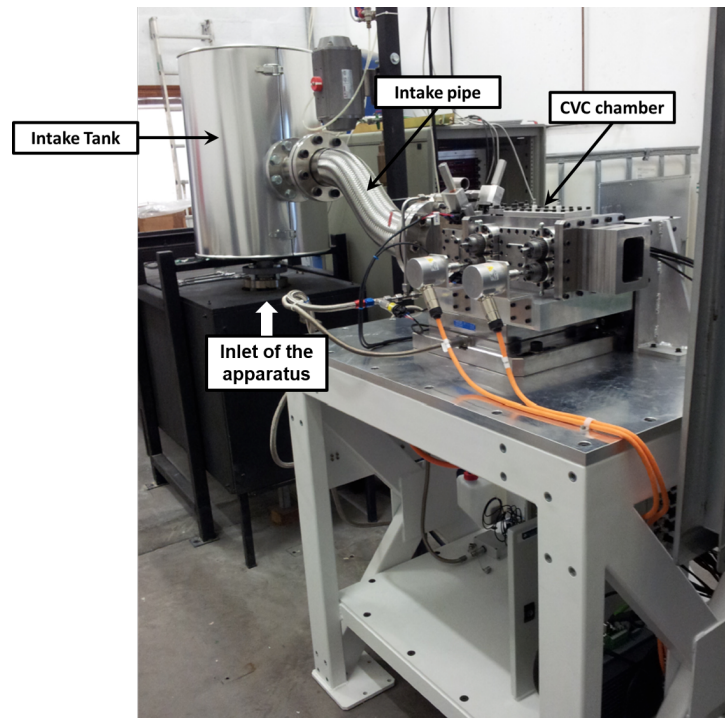


Figure 5.6: Pprime's CVC test bench

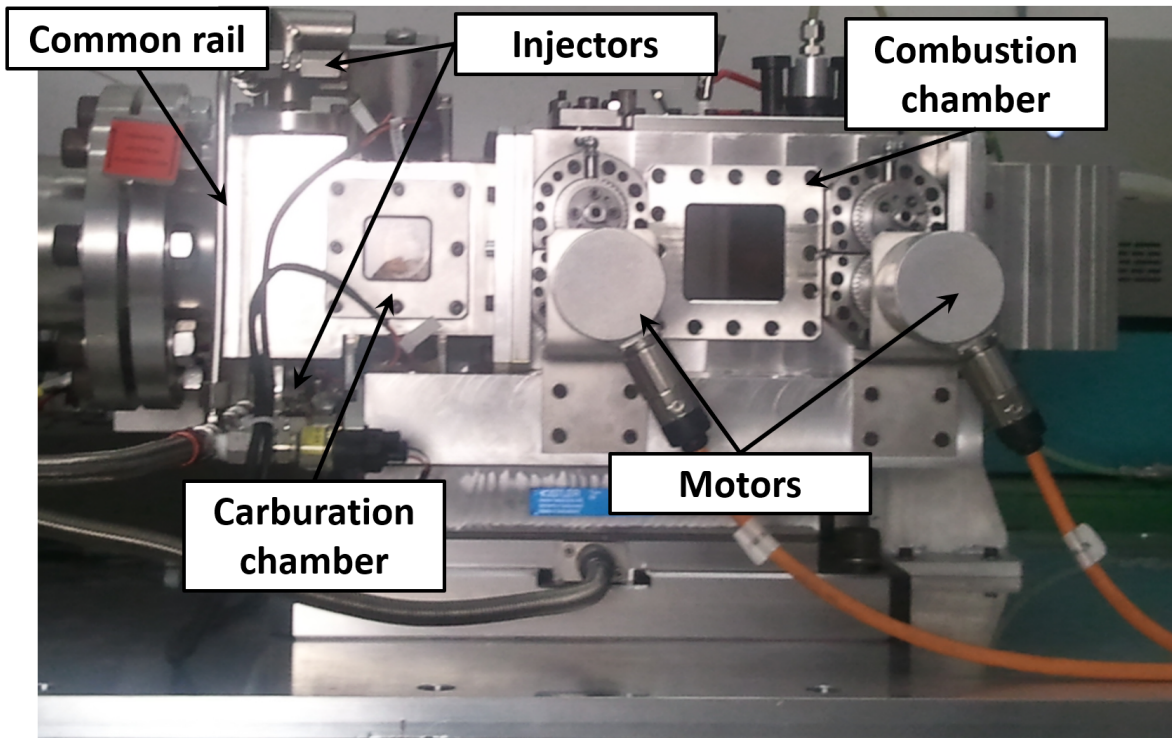


Figure 5.7: Pprime's CVC chamber, side view

This experimental apparatus is made of the following different parts :

- One intake tank of 65 L fed from underneath by a larger tank filled with compressed and heated air, presented in Fig. 5.6,
- One curved intake pipe between the tank and the studied system, shown in Fig. 5.6,
- The carburation chamber downstream of the intake pipe where the mixture is realised by 4 pairs of Bosh automotive injectors, where the positions are presented in Fig. 5.7,
- The CVC chamber where the intake and the exhaust systems are both made of 2 cams, driven one motor each. Fig. 5.7 presents the side view of the experiment and Fig. 5.8 shows the inside of the simulated chamber, where the shape of the different cams and their rotation directions are highlighted,
- The exhaust pipe used to evacuate the burnt gases outside the experimental room.

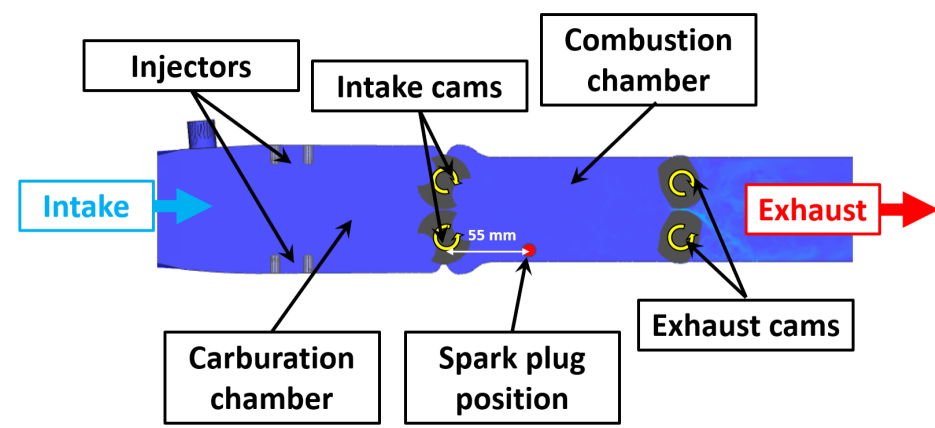


Figure 5.8: Preview of the simulated domain, used to show the shapes of intake and exhaust systems

This chamber is designed to work downstream a compressor with an OPR of 3, therefore this chamber is fed with air at 3 bar and 400 K.

The fuel-air mixture is realised in the carburator chamber just upstream of the intake cams by 4 pairs of automotive injectors. In this experiment, pairs shown in Fig. 5.7 are phased-shifted by 10 crank angle degrees each. The fuel used in this experiment is isoctane.

5.3 Experimental diagnostics

The combustion process in this CVC chamber is examined using several diagnostics. The two main measurements used, in the present study, to evaluate the LIB method are the pressure evolutions and the velocity fields. The pressure evolution is measured every 0.1 degrees by sensors positioned in both the carburator chamber and the combustion chamber. The pressure in the combustion chamber is used to evaluate the combustion in this combustor. Last but not least, the velocity fields are recorded using the Particle Image Velocimetry (PIV). This method consists in introducing very tiny oil particles smaller than $10 \mu m$ in the intake tank and tracking their trajectories with an high speed camera. Fig. 5.9 shows the position of the camera on the side of the chamber while this measurement is done. The results are treated to extract the mean velocity on tens of cycles by averaging the velocity fields of the considered cycles at the same crank angle. The zone where the velocity fields are available is highlighted in Fig. 5.10 by the white squares. Other diagnostics such as, the temperature on walls or the thrust generated by the exhaust of the burnt gases were measured, but they are not used in the present study. In this apparatus, the walls can be disassembled so as to replace them with other equipped walls with the different sensors or with the visualisation window. Therefore, all measurements can not be used in every test, depending on the different walls mounted.

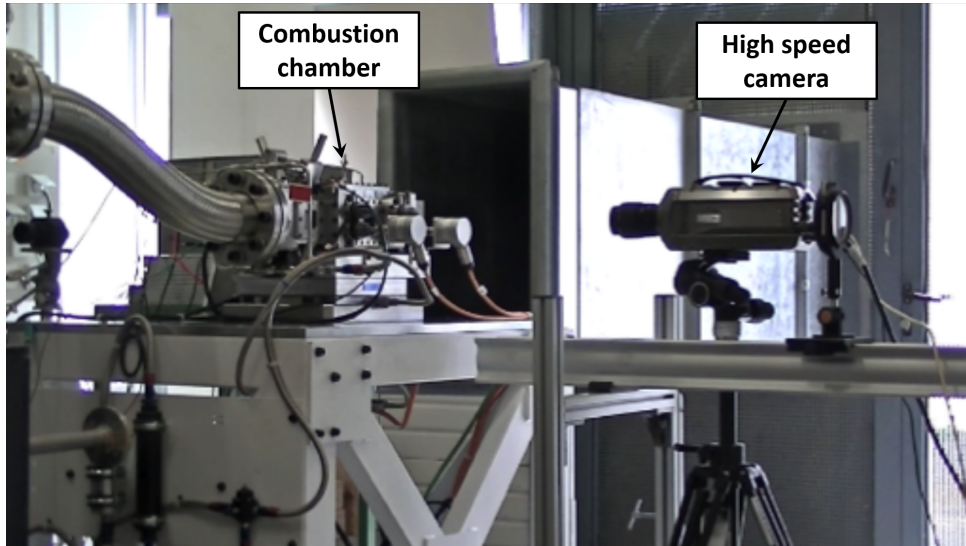


Figure 5.9: Position of the high speed camera to measure velocity field

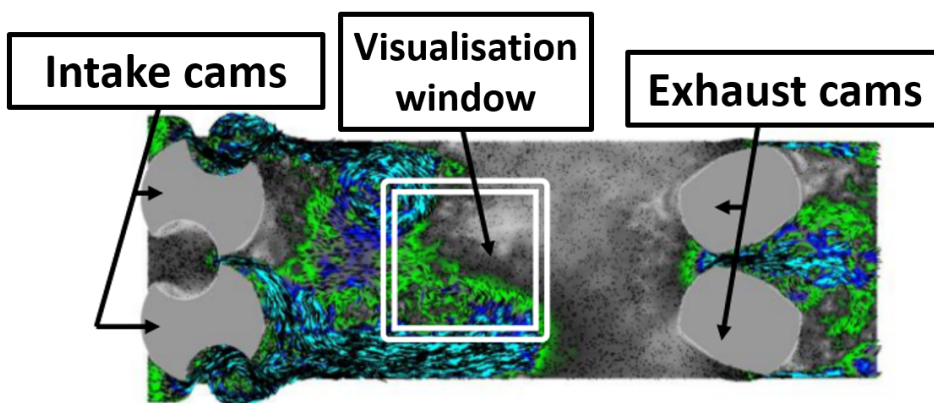


Figure 5.10: Position of the visualisation window in the combustion chamber

Chapter 6

Non reactive cases

Contents

6.1	Operating points	102
6.2	Computational parameters	102
6.3	Preliminary results on non reactive cases	105
6.4	Modification of two parameters: Inlet pressure and mechanical slacks of the intake and the exhaust systems	107
6.5	Improvement of the inlet: extension of the studied domain	109
6.6	O.P.2 final results	111
6.6.1	Pressure evolutions	111
6.6.2	Velocity fields analysis	112
6.6.3	Non-reactive cases conclusion	122
6.7	Complementary study on the inlet pressure: a 0-Dimension model	123
6.7.1	Calibration of the exhaust and inlet section laws with intake pressure set to 3 bar	124
6.7.2	Reference 0D response	126
6.7.3	Intake pressure signal modifications	127

The aim of this chapter is to evaluate the LIB method on non reactive cases. The two diagnostics of the experiment used here are the pressure in both the carburation and the combustion chambers and also the velocity fields in the combustion chamber. First of all, one operating point is used, where both pressure evolutions are available. The second operating point studied in this chapter uses the pressure evolution in the combustion chamber and the velocity fields available on the medium plane of the chamber through an analysis window to evaluate the simulations. This chapter firstly presents the results obtained with the new implemented LIB method set up to avoid as much as possible the low mass flow rate through gaps in both systems, which occurs in the contact zones between cams and walls and between cams. Secondly, the immersed boundaries made of particles are adjusted to allow some mass flow rate throughout these gaps to fit the experiment better. Finally, the LES velocity fields are compared with experimental data.

6.1 Operating points

The analysis proposed here is based on two complementary operating points used to evaluate the capability of the method to model the intake and the exhaust systems. These two cases are simulated in parallel with the same LIB set up, which is improved to fit the experiment. The different phases made on the LIB set up are described in the following sections 6.3, 6.4 and 6.5.

The first operating point, called in this chapter the "O.P.1", is used to evaluate if the LES is able to capture both the pressure evolution of the carburation and the combustion chambers.

The second operating point, called in the following paragraphs the "O.P.2", is used to compare the pressure in the combustion chamber and the phase averaged velocity fields with the experiment. Tab. 6.1 summarises the operating conditions and the diagnostics available. Both cases are fed with air pressurised at 3 bar, the fluid is heated at different temperatures, namely 390 and 420 K respectively for the O.P.1 and O.P.2. Moreover, the crank shift between the intake and the exhaust systems are respectively set to 27.6 and 45.5 degree.

Operating points	Inlet pressure [bar]	Inlet temperature [k]	Shift crank angle [deg]	Diagnostics
O.P.1	3.0	390	27.6	Carb and CC pressure
O.P.2	3.0	420	45.5	CC pressure and velocity fields

Table 6.1: The two operating points main parameters and diagnostics

6.2 Computational parameters

To study this apparatus, LES is performed with Lax-Wendroff numerical scheme [74] and the Sigma SGS model [26] as prescribed in SI engine simulations. The conform walls in the chamber are modeled with an isothermal wall law-of-the-wall boundary conditions. The temperature of the walls depends on the operating point simulated, and is set to the temperature of the inlet. The inlet boundary condition is relaxing the values of the pressure and the temperature presented in Tab. 6.1, which are the experimental measured values of a large tank upstream of the buffer tank of 65 L, presented in Fig. 5.6. Therefore, the total pressure and the total temperature are used in the LES. The inlet boundary condition is also relaxing the mass fraction of the air composed of 23.3 % of O_2 and 76.7 % of N_2 in mass. The last boundary condition used in this simulation is the outlet which relaxes the static pressure to the atmosphere at 1.013 bar. The LIB developed in this thesis is used to simulate the intake and the exhaust systems rotating at 1200 RPM. Here, the temperature of both walls and inside immersed boundaries are relaxed to the inlet temperature. Indeed, this temperature is used since the experimental device is heated up with some pressurized and heated air which goes through the device. Then, less than 3 seconds are analysed experimentally, which hardly changes the temperature

of the apparatus. Fig. 6.1 presents the positions of the different boundary conditions applied on the studied domain.

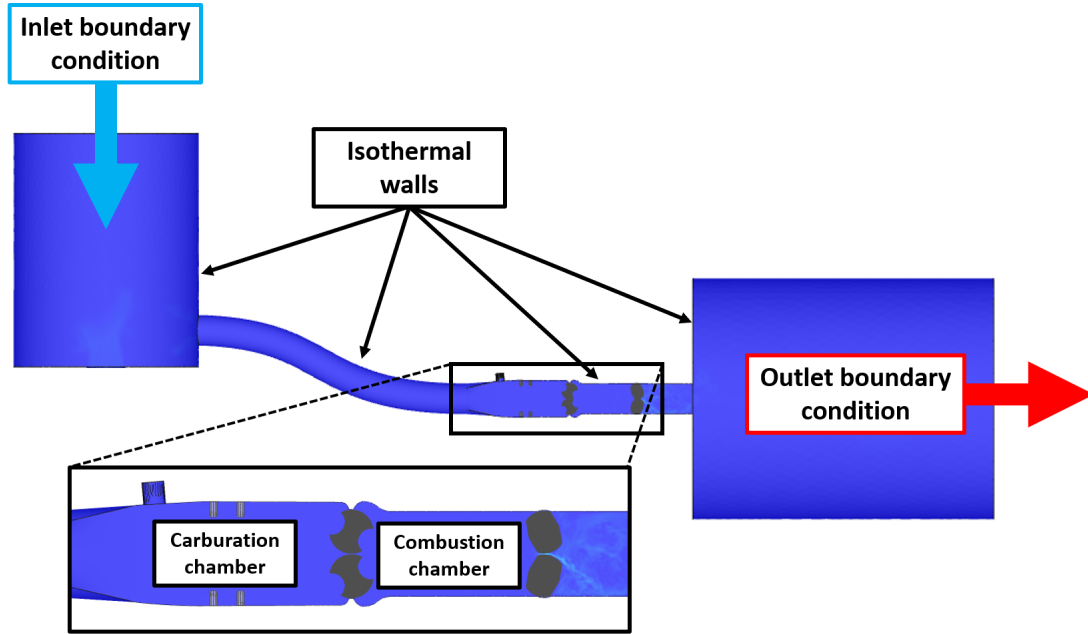


Figure 6.1: Definition of the boundary conditions of the simulation

During the scavenging and the intake phases, the shear stress in the flow meets its higher value due to the intense jets throughout the intake system. Therefore, to correctly capture the velocity fields and the flow during these phases, different mesh refinements are analysed at the opening of the intake system so as to evaluate the part of the turbulence model. Tab. 6.2 presents the main characteristics of the three meshes used to find out the best compromise between precision and CPU cost. In this table, the different lengths from Δ_0 to Δ_3 , which respectively correspond to the characteristic length of the cells in the carburation chamber, in gaps between statics and rotating parts, in the jet zone near walls downstream of the intake system and in the combustion chamber. These lengths are also shown in Fig 6.2. Last but not least, this table gives the CPU cost required to simulate one cycle which varies from one to ten.

Characteristics	Coarse mesh	Medium mesh	Refined mesh
Number of cells	18 367 865	55 154 448	91 167 108
Smallest cell volume [mm ³]	$1.1 \cdot 10^{-2}$	$2.5 \cdot 10^{-3}$	$6.5 \cdot 10^{-4}$
Δ_0 [mm]	3.0	2.0	2.0
Δ_1 [mm]	0.6	0.35	0.25
Δ_2 [mm]	0.7	0.55	0.35
Δ_3 [mm]	1.0	0.65	0.55
CPU cost / cycle [h]	2 048	6 656	19 080

Table 6.2: Experimental diagnostics

One of the mesh convergence criteria is the ratio of the turbulent viscosity to the laminar viscosity. In practice, a mesh with this ratio of the order of several tens is reasonable. Fig. 6.2 presents the ratio of the turbulent viscosity over the laminar viscosity on the three meshes right after the opening of the intake system. In the coarse mesh, this ratio is higher than 40 in some zones like in the vicinity of the immersed boundary and near the walls downstream of the intake system. In the medium mesh, these zones are significantly refined to curb this effect. There, this ratio is divided by more than 2 which is clearly acceptable. Finally, the refined mesh provides the best result in terms of flow resolution, however the simulation is ten times more expensive than the coarse case and three times more expensive than the medium case. Consequently, the medium mesh is chosen to realise all the simulations.

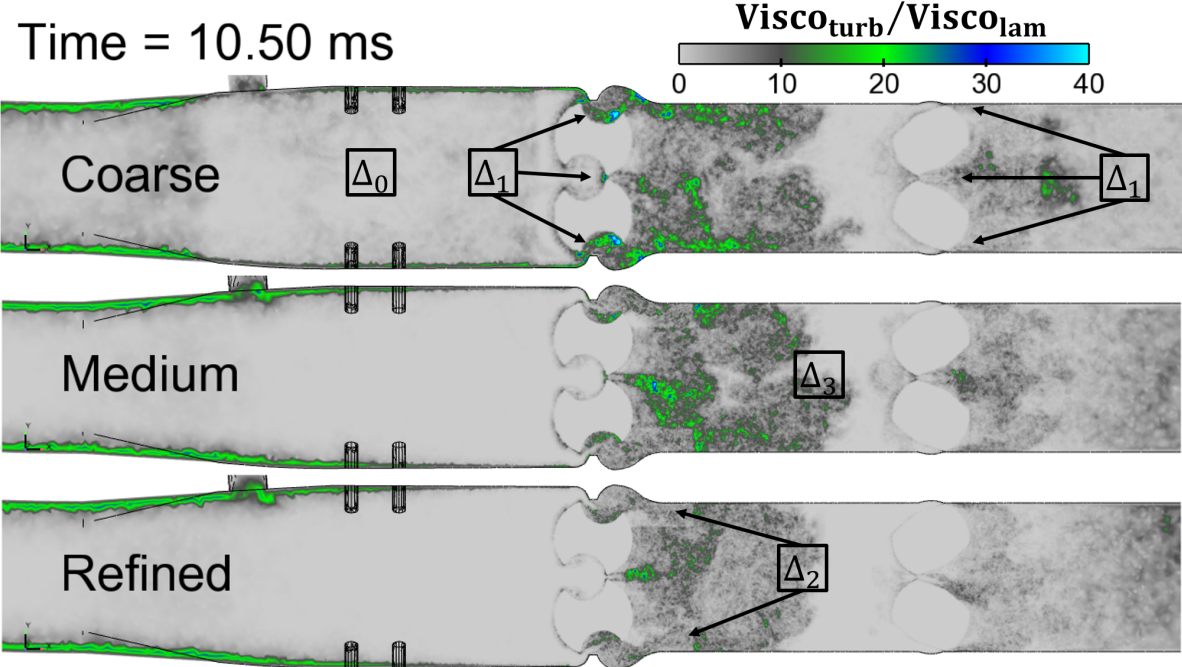


Figure 6.2: Ratio of the turbulent over the laminar viscosities at the opening of the intake system

6.3 Preliminary results on non reactive cases

This paragraph presents the very first results on the O.P.1 and the O.P.2. In these two simulations, the intake and the exhaust systems are created to avoid as much as possible the mechanical slacks in both systems. Thanks to the developments made, especially the special treatment of LIB particles on wall cells presented in section 3.4.2, LIB are set to be as close as possible to walls and between each other.

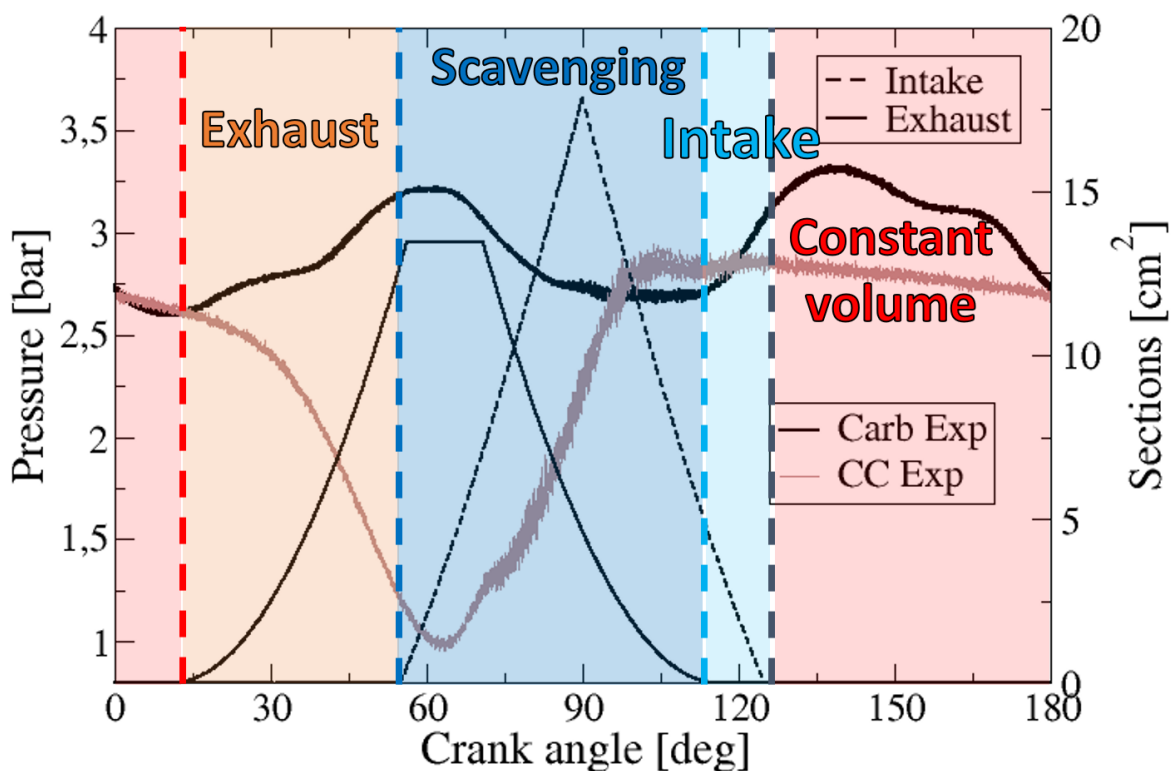


Figure 6.3: Different phases of the cycle are presented along with experimental carburation (Carb) and combustion chamber (CC)

Fig 6.3 highlights the different phases encountered in this kind of combustor, here the experimental pressure evolution during one cycle of the O.P.1 is used. In this figure, the experimental carburation and combustion chambers pressures are respectively plotted in a large black line and in a large grey line. The values of these pressures are specified on the left y-axis. Moreover, this figure gives the section area of the intake and the exhaust systems which are respectively plotted in dashed and continuous black lines. Their values are defined on the right y-axis. Both the pressure evolutions and the section areas allow the identification of the different phases of the cycle which is here presented on 180 degrees. The constant volume phase starts as soon as both systems are closed, namely at 125 CAD and finishes at 191 CAD, or here on the left part of the graph, at 11 CAD.

This phase is identified by the red color on the graph. The following phase is the exhaust which begins when the exhaust system is opening, here at 11 CAD. This phase ends at 55 CAD when the intake system is opening. It is represented here with the orange color. The third step of this cycle is the scavenging phase, which takes place while both systems are opened, it ends at 116 CAD and is coloured in blue. The last phase is the intake which consists in filling the chamber with fresh gases by delaying the intake system closing time from the exhaust system closing time. This phase is here identified with light blue color. All the following figures of this paragraph present the result on this type of graph.

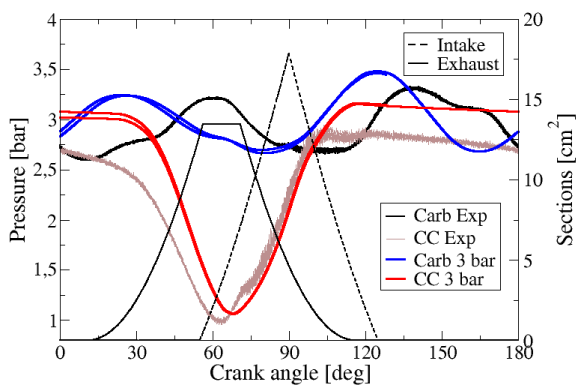


Figure 6.4: First pressure evolution of O.P.1

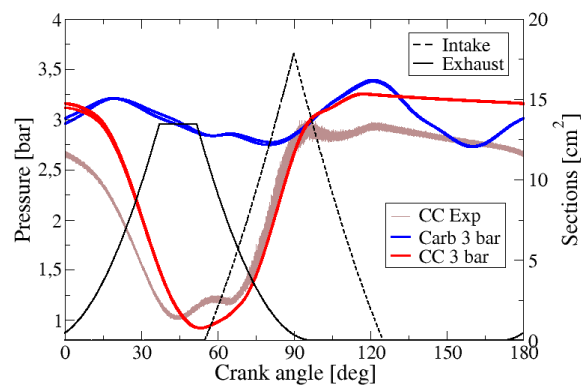


Figure 6.5: First pressure evolution of O.P.2

Figs 6.4 and 6.5 show the pressure evolutions on these two operating points using the initial set of LIB. In O.P.1, the measurements give the pressure in the carburation chamber and in the combustion chamber while in O.P.2 only the experimental combustion pressure is available. Like in Fig. 6.3, the experimental combustion pressure is plotted in grey for both operating points and the experimental carburation chamber pressure is plotted in black for the O.P.1. The LES pressure evolutions in the carburation and in the combustion chambers, are respectively plotted in blue and in red line. In both figures, the pressure in the combustion chamber is significantly overestimated by 0.25 – 0.30 bar after the intake system closing at 125 CAD. The main assumption for this deviation from the experiment is that the carburation chamber pressure is not correctly predicted as shown in Fig. 6.4. Indeed, the LES carburation chamber pressure of the O.P.1 reproduces globally the evolution of the experimental signal but it is shifted by approximately 30 degrees, which corresponds to around 4.2 ms. Moreover, during the constant volume phase which starts in both cases at 125 CAD and finishes at 13 CAD and 175 CAD for the O.P.1 and O.P.2, the pressure loss and thus the mass flow rates are underestimated. Consequently, some modeling adjustments are required so as to better predict the maximum pressure and the pressure loss while both systems are closed.

6.4 Modification of two parameters: Inlet pressure and mechanical slacks of the intake and the exhaust systems

As presented in section 6.3, the pressures at the closing time of the combustion chamber are significantly overestimated and the simulated pressure leakages during the constant volume phase are underestimated. Therefore, to fit the experimental pressure evolution, the two following parameters can be adjusted:

- The cam dimensions are slightly scaled to create some numerical mechanical slacks between walls and cams at the exhaust system, so as to reach the right level of pressure loss during the constant volume phase.
- The inlet pressures are decreased from 3 down to 2.75 bar to meet the experimental pressure at the end of the intake phase. Indeed, several tests were realised and shown that the use of both the LIB method with this mesh refinement and these simulated mechanical slacks, could slightly change the acoustic effects through the apparatus. Consequently, the method found to meet the pressure at the beginning of the constant phase was to decrease the inlet pressure.

As shown in previous Figs. 6.4 and 6.5 the pressure at the end of the intake is overestimated by approximately 8 – 10%. Consequently, the method used is to decrease the inlet pressure imposed on the top wall of the inlet tank. The best compromise found was to diminish the inlet pressure from 3.0 bar down to 2.75 bar. In order to explain this inlet pressure decrease, a study is proposed in section 6.7, where the 0-Dimension commercial software AMESim is used to analyse the impact of the variation of the carburation chamber pressure on the combustion chamber pressure. Moreover, the real mechanical slacks between walls and cams or between both cams of the intake / exhaust system evolve between 10 and 150 μm . These gaps cannot be solved in our simulations since the required mesh refinement will surge the CPU cost. Therefore, these gaps on both systems are slightly widened in order to increase the simulated pressure loss while both systems are closed. The cams are scaled by a factor of 0.985 in order to leave some fluid nodes in wall cells without LIB feedback source terms and thus, lets the flow go through numerical mechanical slacks, which unfortunately depend on the mesh size.

Figs. 6.6 and 6.7 present the results where the inlet pressure is decreased down to 2.75 bar and the intake and exhaust systems dimensions are reduced by 1.5%. In these figures, the carburation chamber and the combustion chamber pressure evolutions obtained with the new LIB set up, are added to the two previous Figs. 6.4 and 6.5 in order to evaluate the improvement. These additional curves are plotted in blue and red lines with circles.

Fig. 6.6 shows the improvement made on the combustion chamber pressure which correctly fits the experiment. During the constant volume phase, from 125 CAD to 210 or 30 CAD in the graph, the combustion chamber pressure matches the experimental combustion chamber in terms of pressure level and pressure loss. However, during the end of the scavenging phase, between 90 and 120 CAD, the combustion chamber filling rate decreases compared with the experiment since the pressure gradient in both sides of the intake systems decreases. The modification of the inlet pressure and the exhaust system

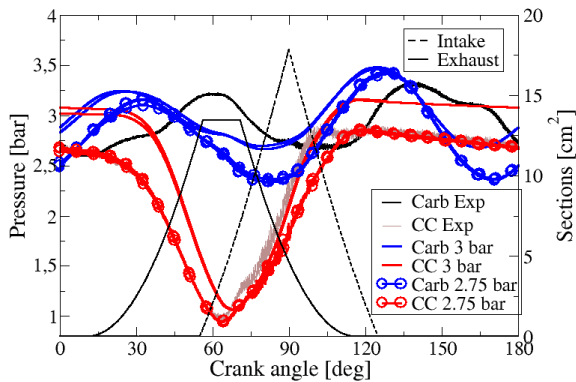


Figure 6.6: O.P.1's new setup

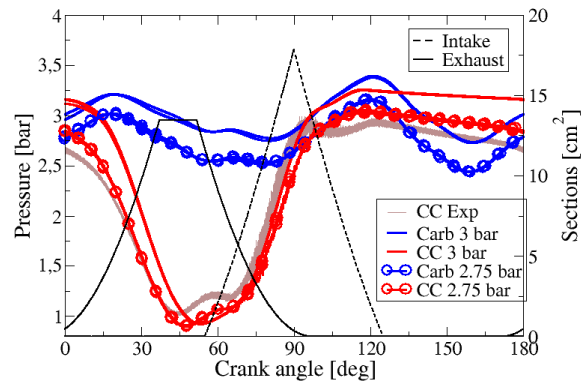


Figure 6.7: O.P.2's new setup

dimensions also changes the carburation chamber pressure evolution. As presented in Fig. 6.6, the two peak pressure values reached at around 30 and 120 CAD are decreased by 0.1 and 0.05 bar. They are also shifted by +8 and +5 CAD. The two minimum pressure values are also modified. With this new set up, the previous minimum pressure values reached at around 90 and 170 CAD, are decreased by 0.3 and 0.32 bar and are shifted by +5 CAD.

Fig. 6.7 also shows some improvements, even if they are less visible. As expected, the carburation chamber pressure evolution is shifted down by 0.25 bar.

The additional mass flow rate enables to predict the right order of pressure loss in the combustion chamber during the constant volume phase but the pressure remains overestimated by around 0.1 bar. Like in the O.P.1 the diminution of the pressure gradient between the carburation and the combustion chamber implies a lower filling rate during the end of the scavenging phase. Consequently, the pressure increase at the end of the scavenging phase is underestimated. However, the bump between 45 and 75 CAD which corresponds to a back flow from the exhaust to the combustion chamber is now captured. This back flow was not predicted by the first simulation plotted in the yellow curve in Fig. 6.7 since the emptying rate does not permit to reach a pressure in the combustion chamber lower than the exhaust one, before the opening of the intake system.

In both cases, decreasing the pressure intake and additional mass flow rate through the exhaust system tend to improve combustion chamber pressure evolutions, but some enhancements may still be done.

The next step analysed here is to extend the simulated domain and feed the buffer tank by the bottom so as to be more representative of the experiment and to account for the acoustic effects better.

6.5 Improvement of the inlet: extension of the studied domain

Most experiments use a buffer tank to supply the experimental apparatus by a fluid at constant properties. Fig. 5.6 shows that the studied experimental bench uses this kind of buffer tank. The first simulated domain only takes into account the buffer tank where the inlet boundary condition is located on the top tank as shown in Fig. 6.8. However, the experiment inlet feeds the tank buffer through a smaller pipe on the bottom of the tank as presented in Fig. 5.6. Therefore, one lever to improve the simulation is to extend the simulated domain which mainly consists in simulating the inlet through the bottom inlet pipe. The final simulated domain which accurately represents the experimental inlet is shown in Fig. 6.9.

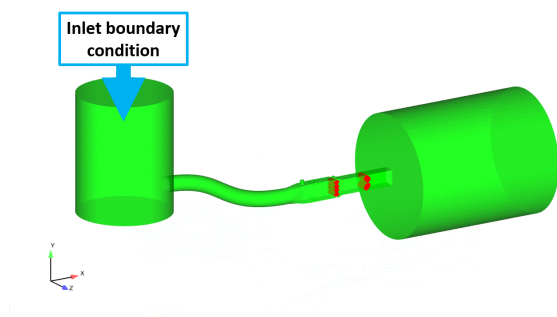


Figure 6.8: Inlet at the top of the intake tank

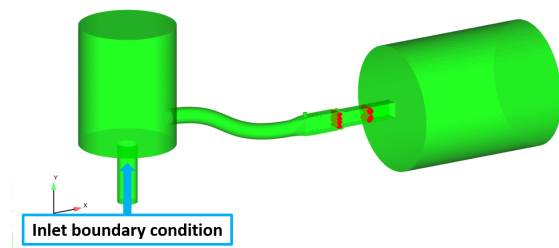


Figure 6.9: Inlet at the bottom pipe of the intake tank

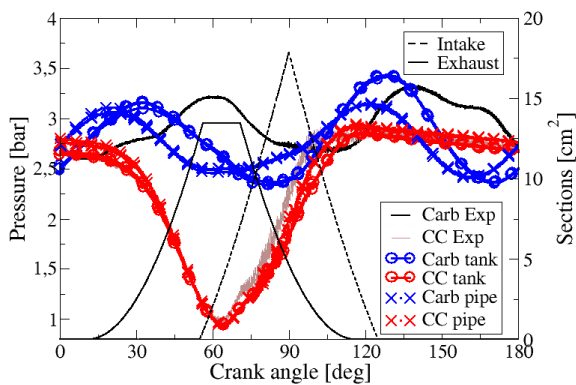


Figure 6.10: O.P.1's inlet comparison

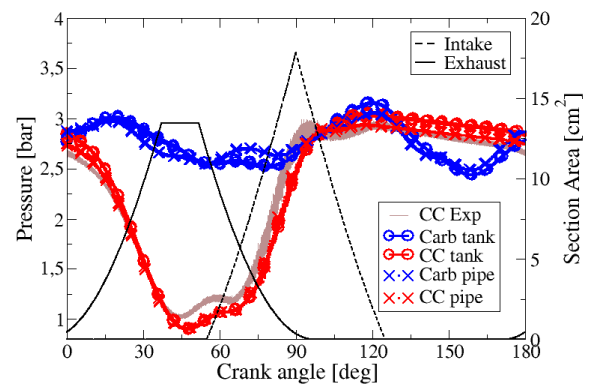


Figure 6.11: O.P.2's inlet comparison

In Figs. 6.10 and 6.11, the previous results presented in section 6.4 are compared with the extended domain. The previous results are plotted with the same color code and respectively named "Carb tank" and "CC tank". The carburation chamber and combustion chamber pressure evolutions obtained on the new simulated domain are respectively plotted in blue and red dotted lines with crosses and called "Carb pipe" and "CC pipe". According to Fig. 6.10, the modification of the inlet boundary condition significantly changes the carburation chamber pressure evolution predicted by the simulation in O.P.1

where the scavenging lasts 60 CAD. In O.P.2 presented in Fig. 6.11, the new inlet boundary condition has less effect on the carburation chamber pressure evolution than in O.P.1, where the scavenging phase only lasts 48 CAD.

In Fig. 6.10, the maximum amplitude goes from 1.1 bar for the previous studied domain down to 0.7 bar and pressure extrema are respectively shifted by -12 , -22 , -8 and -15 degrees. Moreover, during the scavenging phase, the carburation chamber pressure of the new studied domain is lowered by around 0.25 bar, which decreases the pressure gradient on both sides of the intake system, and thus diminishes the filling rate of the combustion chamber. The carburation chamber pressure evolution of the new studied domain plotted in red is still significantly different from the experiment. In the experiment, the carburation chamber pressure has two bumps at 25 and 165 CAD which are not captured by the LES. Moreover, the pressure seems stabilized between 90 and 120 CAD and starts to rise again as soon as the exhaust system is fully closed, namely around 116 CAD. In the LES, the same kind of stabilized zone is observed between 55 and 75 CAD and starts to rise progressively near 90 CAD. This time-shifting might be explained by an anticipated exhaust system closure due to the LIB approach.

At the end of the intake between 110 and 125 CAD, the combustion chamber pressure is overestimated by 0.05 bar. This discrepancy between the experiment and the simulations raises up to 0.14 bar at the opening of the exhaust system which highlights that the mechanical slack should be slightly extended.

In Fig. 6.11, the LES carburation chamber pressure of the extended domain is also plotted in red. This pressure presents more fluctuations especially near 105 CAD which directly impacts the filling of the combustor just after the exhaust system closing. With this domain modification, the dump of combustion chamber pressure near 60 CAD is still captured. In O.P.2, the pressure at the beginning of the constant volume phase is correctly predicted but the pressure at the opening of the exhaust system is 0.15 bar higher than the experiment. Like in the O.P.1, the mass flow rate through the exhaust system seems slightly underestimated which confirms that the mechanical slack should be slightly extended.

The addition of the intake pipe at the bottom of the buffer tank allows the correct prediction of the combustion chamber pressures. These results might be improved by slightly widening the gaps at the exhaust system. Finally, the pressure delay might be the consequence of an anticipated closing of the exhaust system due to the LIB model. Indeed, the LIB source terms are applied in the Navier-Stokes equations inside the immersed objects but also on first nodes outside the immersed walls since LIB source terms are applied on all nodes of cells which contains at least one LIB particle. Consequently, the LIB impacts the fluid on the first node ahead of the immersed walls and thus can anticipate the closing or delay the opening of both systems by at least one cell size. Therefore, to decrease this functioning, the meshing size of the gaps between both systems and walls might be refined but the method will be expensive, and thus will lose its interest.

6.6 O.P.2 final results

The previous section shows that the addition of the intake pipe upstream of the buffer improved the prediction of the combustion chamber pressure. The following paragraphs present the final pressure evolution in the combustion chamber and the comparison of the velocity fields with the experiment where the following adjustments are used:

- The cams of the exhaust system are scaled by the factor 0.98, which represents a 2.0 % decrease of the size of the cams,
- The inlet pressure is set at 2.75 bar,
- The upper and the lower cams of the intake system are angularly shifted so as to create a non symmetrical flow, as observed in the experiment. This adjustment is presented in section 6.6.2.

6.6.1 Pressure evolutions

In this section, the combustion chamber pressure evolution of the O.P.2 is plotted for 8 cycles. As explained above, the intake tank pressure is set to 2.75 bar and the intake and exhaust systems gaps are adjusted to reach the right mass flow rate during the constant volume phase.

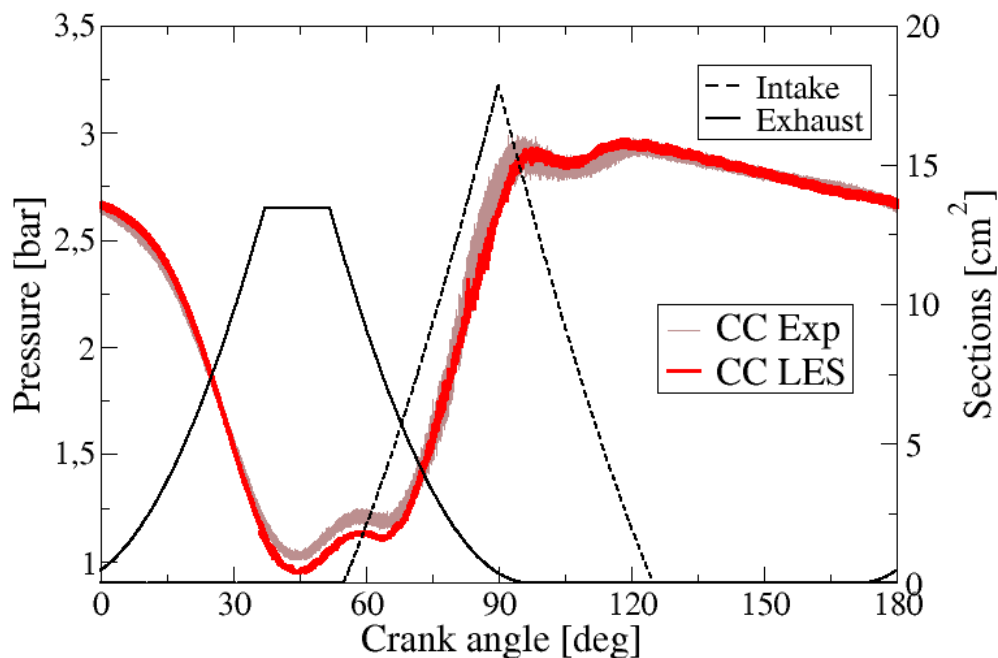


Figure 6.12: O.P.2 pressure evolution

Fig. 6.12 presents the pressure evolution on 180 CAD like in Fig. 6.3. The 8 LES combustion chamber pressure evolutions are plotted in black lines and are compared with experimental measurements in grey lines. In this case, the pressure evolution is accurately predicted by the simulation. The back flow from the exhaust to the combustion chamber before the intake system opening at 55.5 CAD is correctly captured, although the pressure is underestimated by 0.05 bar. This can be improved by raising the exhaust pressure by 0.05 bar. Moreover, the back flow from the combustion chamber to the carburation chamber between 95 and 120 CAD is also properly described by LES.

The experimental combustion chamber mass flow rate is progressively increasing near 175 degrees, while the exhaust system is opening. At this time, the LES mass flow rate seems to be slightly delayed. This might be the consequence of an under-refinement of gaps in this configuration.

6.6.2 Velocity fields analysis

The second experimental diagnostic available on this operating point, is the time averaged velocity fields. In the experiment, phase average velocity fields are performed on 80 cycles whereas LES velocity fields are averaged on 8 cycles. In order to analyse different velocity fields, three CAD are chosen after the opening of the intake system, while the air flow is entering into the chamber. During this phase, the velocity fields created through gaps between the walls and the intake cams is highly sheared. In the experiment, the vortices visualised through the analysis window are not symmetrical, whereas the preliminary simulations give a symmetrical flow fields. Consequently, the opening time of the upper and the lower cams of the intake system are time delayed. To introduce this non symmetrical air flow, a crank angle shift is added to open the lower cross section between the lower cam and the wall earlier than the upper cross section between the upper cam and the wall. As explained before, the simulated gaps are more than 10 times larger than the real mechanical slacks of the order of 10 up to 150 μm , therefore the introduced shift is far from being representative of the experiment. In these simulations, this shift between upper and lower intake cams is set to 2.0 degrees, which theoretically correspond to a time delay of 0.28 ms. This crank angle shift between both intake cams and its impact on the flow fields are illustrated in Figs. 6.13, 6.14 and 6.15.

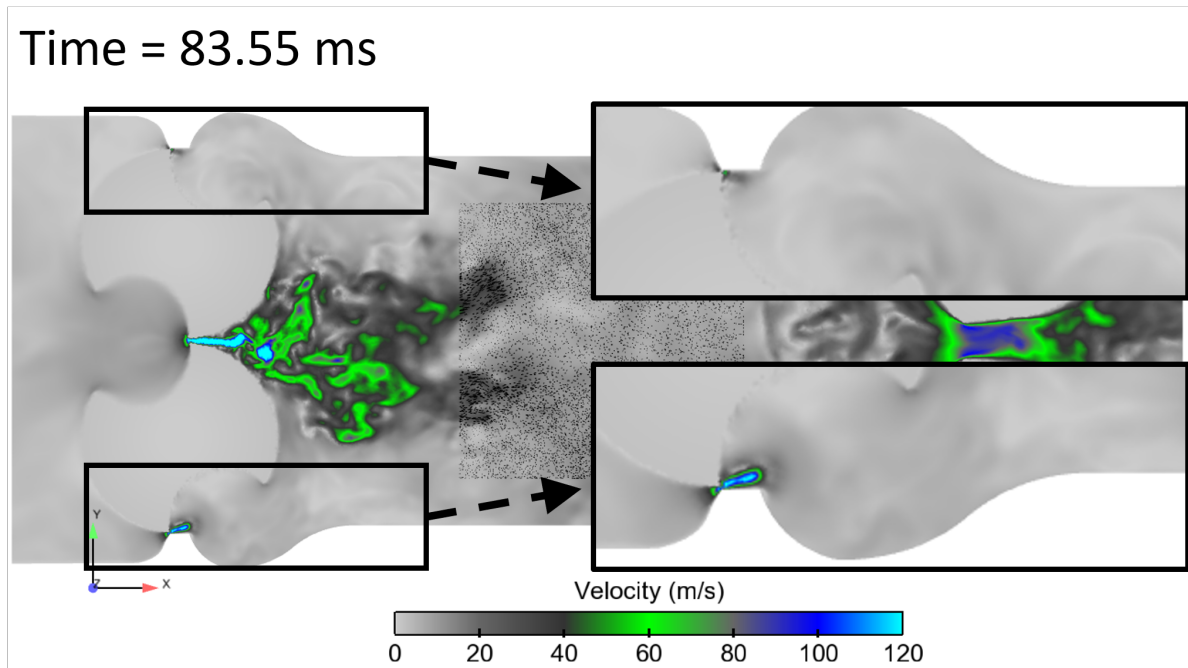


Figure 6.13: Opening of the lower cam of the intake system

Fig. 6.13 presents the instantaneous velocity field of the third cycle at the opening time of the intake system. This Figure focuses on the opening cross sections of the lower and upper cams and walls which are enlarged to be easily analysed. As expected, the air flow starts to generate a strong jet through the lower cam cross section where the velocity reaches a magnitude higher than 120 m/s. At the same time, the air flow starts to pass through the mechanical gap between the upper cam and the wall since the velocity starts to increase up to values close to 20 m/s.

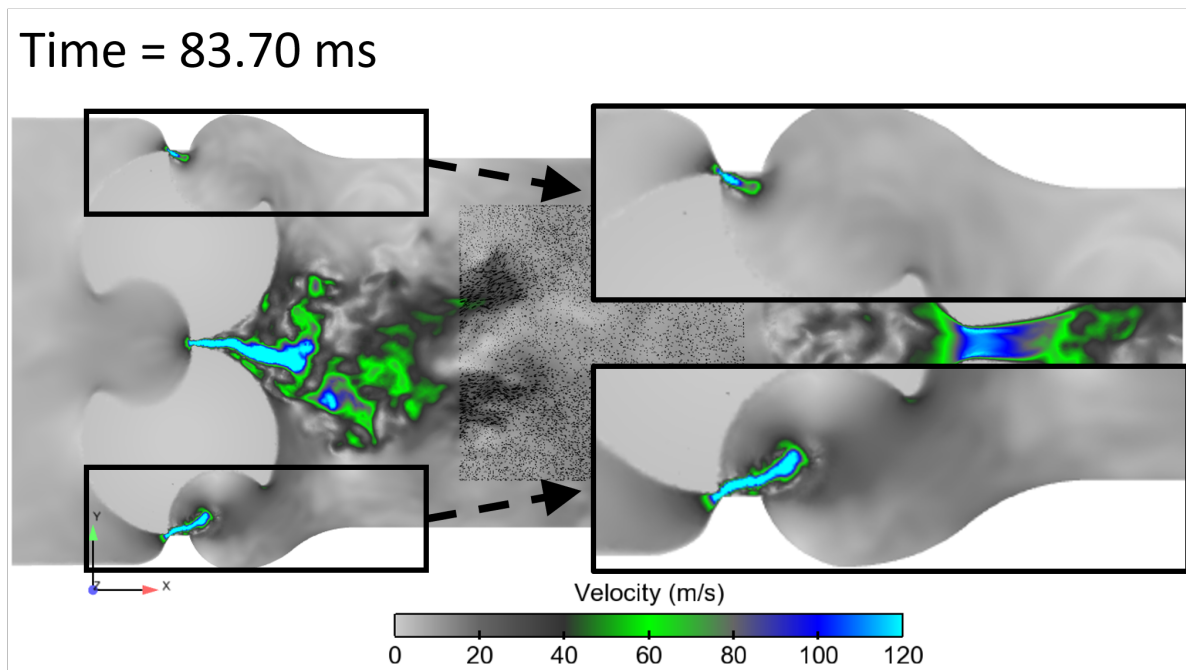


Figure 6.14: Time delay of 1.5 ms between the intake system cams opening

Fig. 6.14 shows that 0.15 ms after the opening of the lower cross section between the lower cam and the wall, the air flow starts to be significantly visible through the cross section of the upper cam and the wall. The jet on the bottom of the intake system seems three times longer than the upper one. The crank angle shift and the gaps between cams and walls generates the non symmetrical flow at the opening of the intake system.

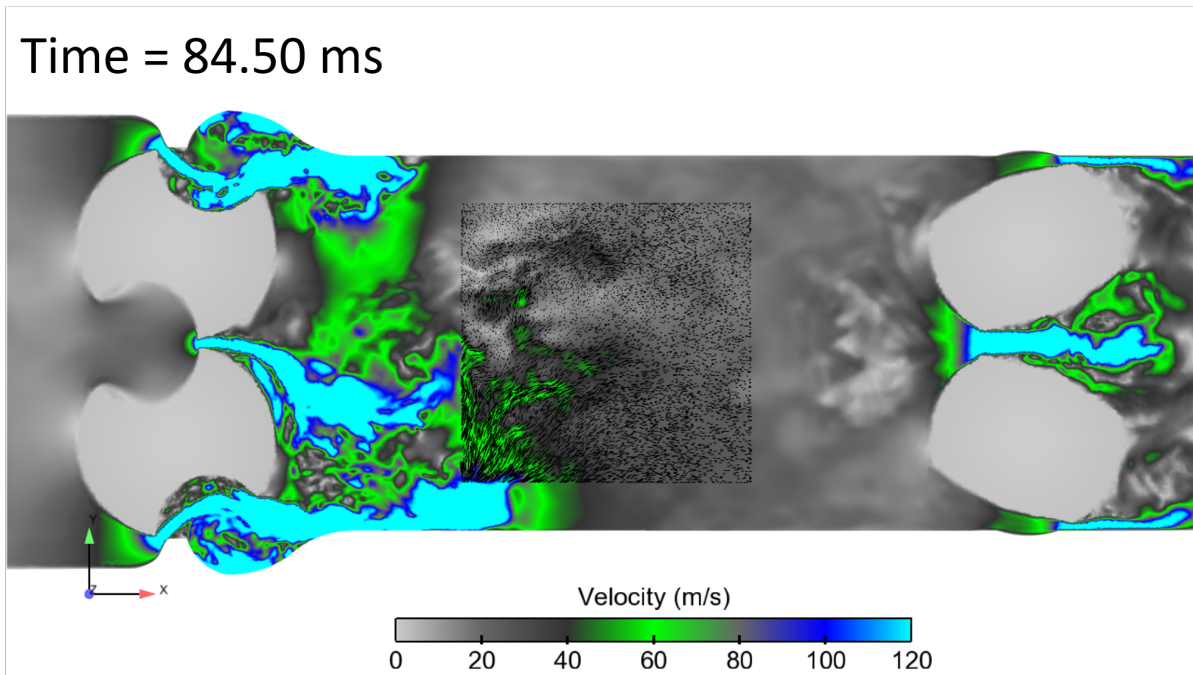


Figure 6.15: Observation of the required non symmetrical velocity field

Finally, Fig. 6.15 shows the instantaneous velocity fields 0.8 ms after the intake system opening time, which clearly becomes non symmetrical. Therefore, the shift crank angle of 2 degrees seems sufficient to generate the non symmetrical flow field measured in the experiment through the analysis window. In this figure, the tiny black arrows represent the velocity vectors inside this visualisation window.

The measured velocity flow fields are compared with the LES ones, through the visualisation window presented Fig. 5.10. Three times during the intake phase are chosen where the vortices are visible, namely at 72.00, 75.60 and 79.20 CAD.

Fig. 6.16 and the following figures present the experimental velocity fields on the left and LES ones on the right. Like in Fig. 6.15, the intake system is on the left of the analysis window and the exhaust system is on the right. Therefore the flow is coming from left to right.

At each analysed CAD, axial and tangential velocity profiles are plotted at 6 positions from 5 mm up to 55 mm separated by a spatial step of 10 mm. They are highlighted by white vertical dashed lines on the different velocity fields.

Velocity fields at 72.00 CAD:

Fig. 6.16 presents the velocity fields visualized through the analysis window at 72.00 CAD and Fig. 6.17 the corresponding axial and tangential velocity profiles at the different positions. Fig. 6.16 corroborates the fact that the shift crank angle of 2 degrees between the upper and the lower cams of the intake system enables to capture the non symmetrical flow of the experiment. The lower vortex spinning counter-clockwise is flattened

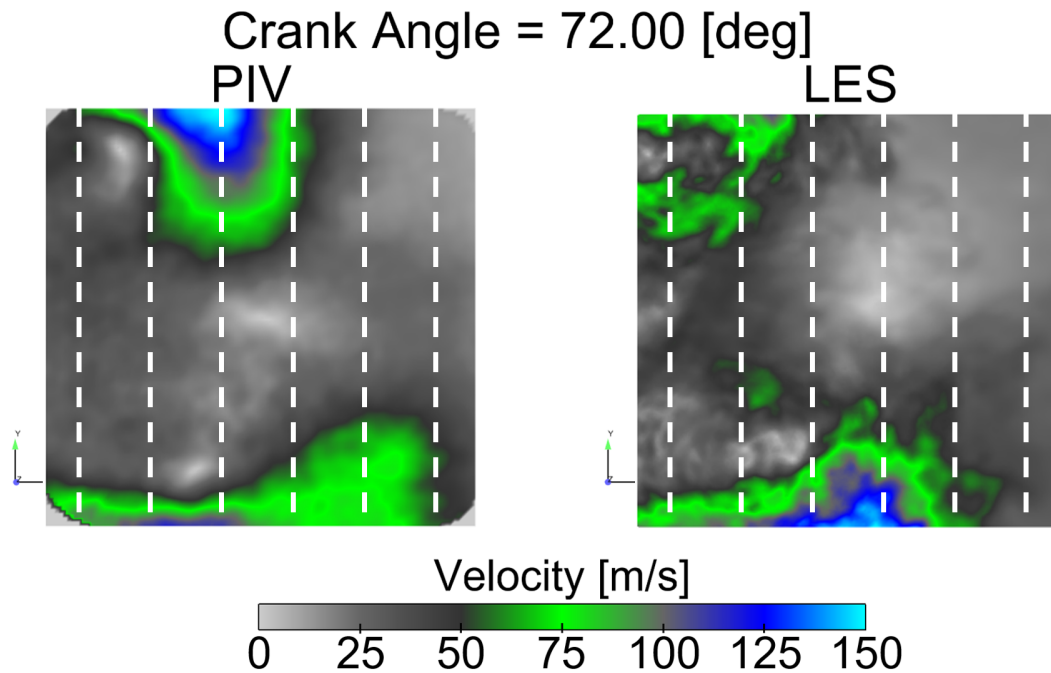


Figure 6.16: Impact of time delay opening between both cams of the intake system on the generated velocity flow fields

compared with the upper vortex, which turns in the other direction. The lower vortex generated by an earlier opening tends to vacuum the upper vortex and thus bends the upper vortex. Both vortices are moving from the intake to the exhaust and their rotation center axial motions are slowing down while the exhaust system is closing. The restriction of the exhaust cross section tends to intensify the recirculation motion of both vortices. At this crank angle, the global trend of the experiment is correctly predicted by the LES. The lower vortex shape is correctly predicted but the velocity magnitude around 125 m/s visible on the bottom of the visualisation window in the experiment between 15 and 25 mm is observed between 20 and 40 mm in the LES. These observations are confirmed with velocity profiles presented in Fig. 6.17. The discrepancies are notable especially between the 2nd and the 4th positions namely at 15, 25 and 35 mm. The vertical position of the lower vortex centre in the simulation is slightly closer to the centre of the visualisation window. As a result, this yields both an higher axial and tangential velocity.

The global behaviour of the upper vortex is also captured but this vortex is more bent than in the experiment and is slowly spinning clockwise. Moreover, the centre of this vortex has a lower axial displacement. These observations are visible in Fig. 6.17 on the upper part of each graphics. At 5 mm, the experiment and the LES have opposite tangential velocity signs, since the rotation centre are respectively at 10 and 3 mm. At both 25 and 35 mm, the trend is predicted but the discrepancies in the centre position and in the velocity magnitudes lead to an underestimation of velocity extrema.

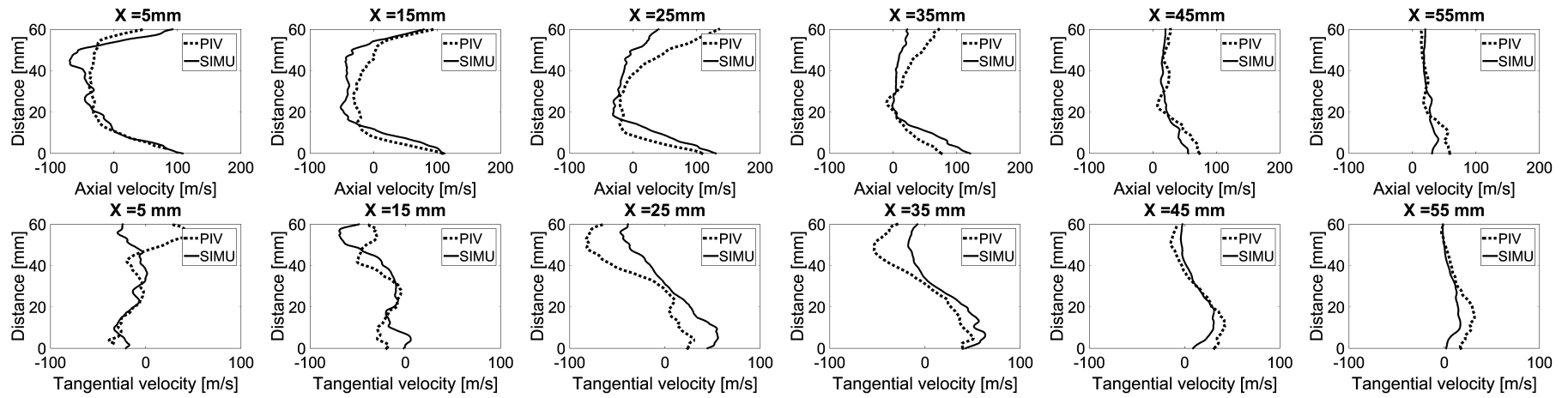


Figure 6.17: Axial (on top) and tangential (on bottom) velocity profiles at 72.00 CAD

Velocity fields at 75.60 CAD:

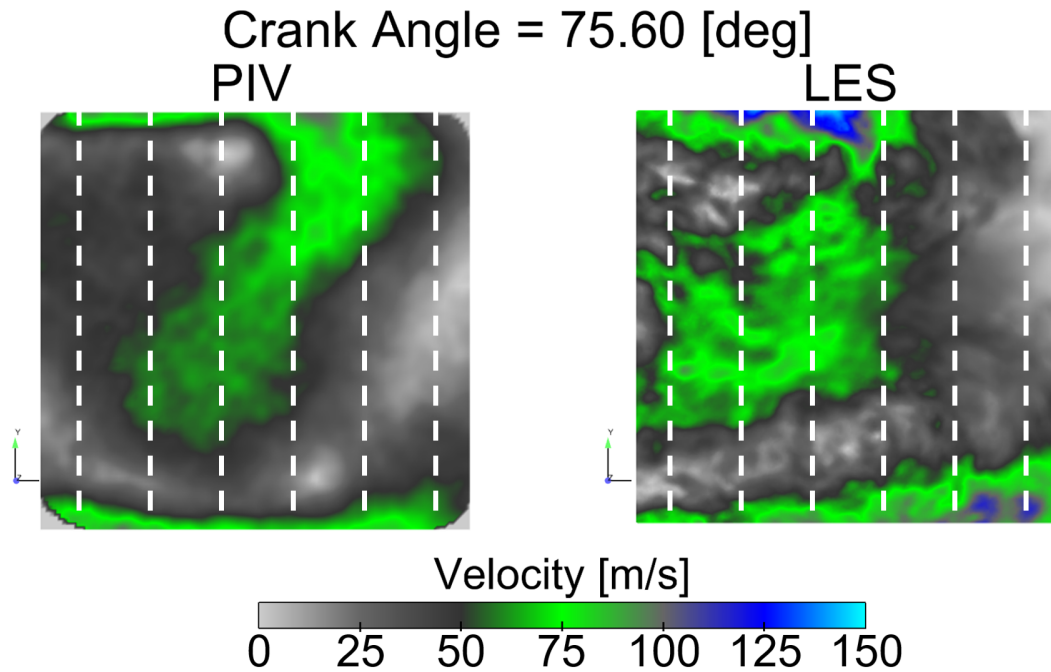


Figure 6.18: PIV and LES average velocity fields at 75.60 CAD

The second considered time is at 75.6 CAD, Fig. 6.18 shows the displacement of the two vortices. In this figure, both global shape vortices are well captured by the LES. However, LES centre vortices move slowly towards the exhaust system.

The LES axial centre position of the lower vortex is at 30 mm instead of 37 mm and its vertical position is almost the same as in the experiment. In Fig. 6.19 the different centre position is clearly identified at 35 mm where the tangential velocity has opposite signs, positive in the LES while it is negative in the experiment. This involves that the rotation centre is located more downstream in the experiment than in the LES. Like in previous CAD, the LES velocity at the bottom and the right of the analysis window is overestimated. This is visible on the axial velocity at positions from 25 to 55 mm.

The upper vortex is also convected slower further downstream of the chamber than in the experiment. The rotation of the LES centre is located at 25 mm instead of 35 mm. This is identified in tangential velocity profiles at 15 and 25 mm. Moreover, the LES velocity magnitude is slightly overestimated in the upper part of the vortex and also in the centre of the window. This is visible in the axial velocity at 15 and 25 mm.

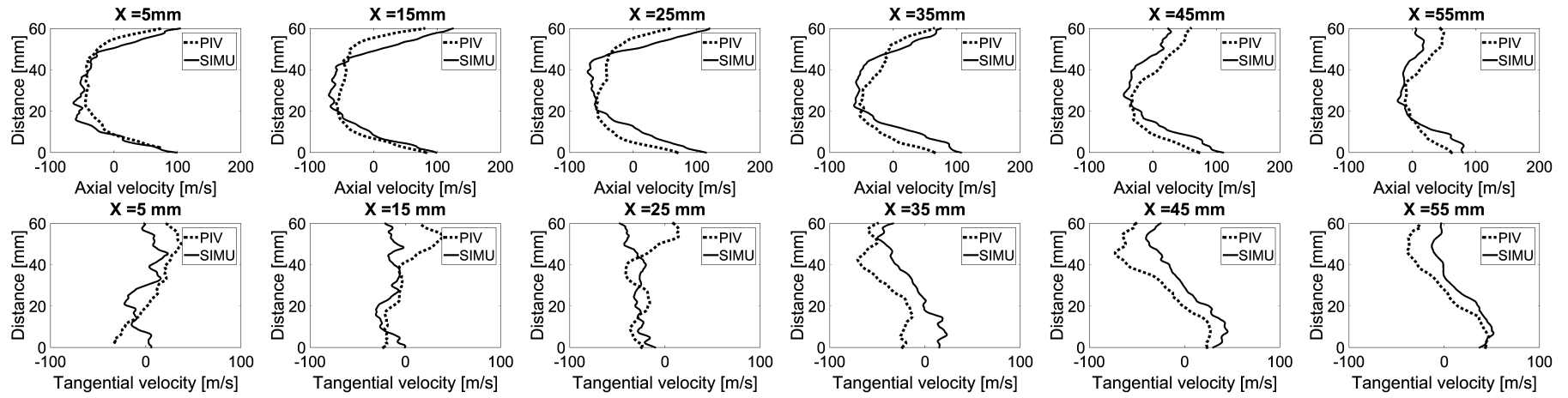


Figure 6.19: Axial (on top) and tangential (on bottom) velocity profiles at 75.60 CAD

Velocity fields at 79.20 CAD:

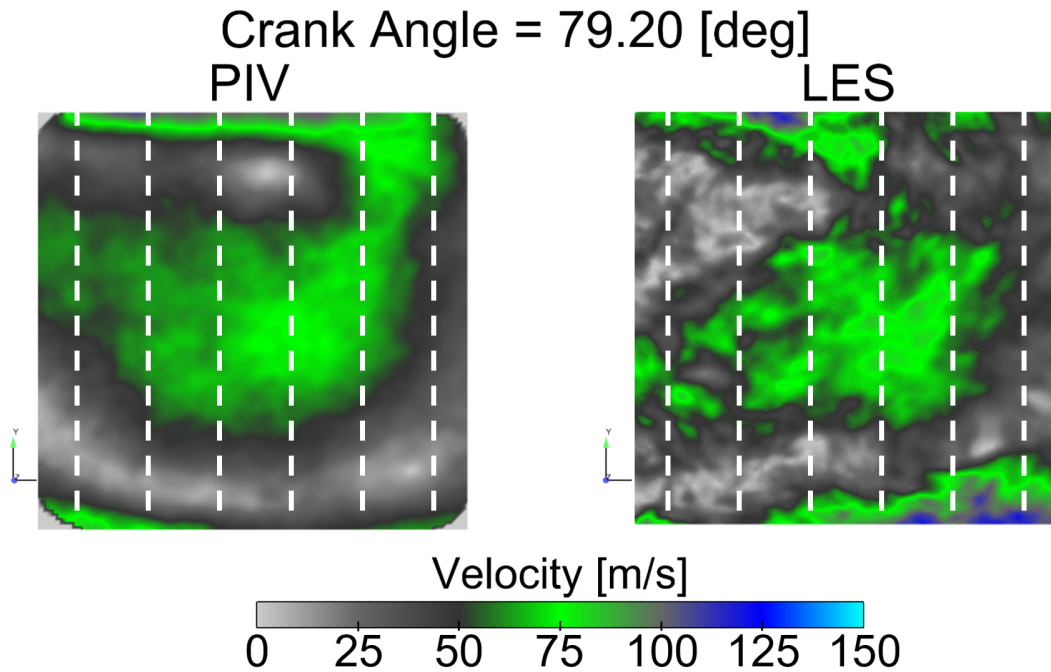


Figure 6.20: PIV and LES average velocity fields at 79.20 CAD

The last velocity field analysed here is at 79.2 CAD. In Fig. 6.20, both vortices are well captured by the LES, even if the simulation seems to lack cycles to converge correctly the velocity fields.

As well as in the experiment, the lower vortex is completely flattened but the velocity is still overestimated on the bottom of the window. This is easily visible in the lower part of graphs in Fig. 6.21 from 25 to 55 mm.

The upper vortex generates a large recirculation zone which is well reproduced in the simulation. Like in previous CAD, the position of the rotation centre and thus the convection speed of the vortex are underestimated. The position of the rotation centre is located 22 mm instead of 31 mm and moves slightly down. As shown in Fig. 6.21, these discrepancies involve different tangential velocities at all positions except at 55 mm.

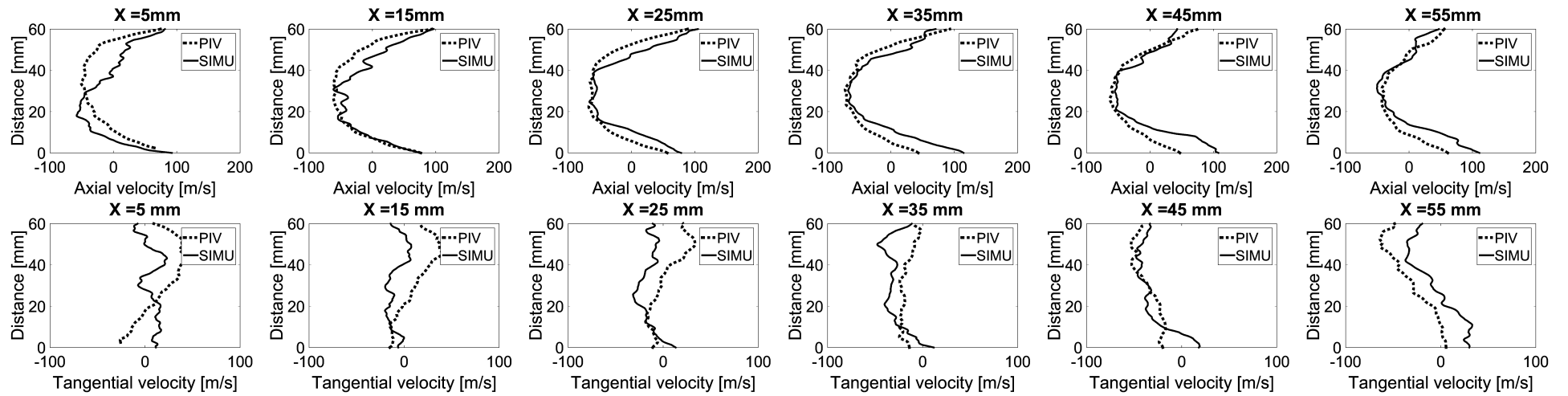


Figure 6.21: Axial (on top) and tangential (on bottom) velocity profiles at 79.20 CAD

6.6.3 Non-reactive cases conclusion

To fit the mass flow rate during the constant volume phase, the dimensions of cams are adjusted to generate gaps between cams and walls. The acoustic does not seem correctly predicted by using immersed boundaries, therefore to reach the correct pressure in the combustion chamber at the closing time, the intake tank pressure is reduced from 3 bar down to 2.75 bar. Finally, an angular shift is used to predict the experimental non symmetrical velocity fields during the intake phase.

With these settings, the combustion chamber pressure evolution is correctly predicted but the minimum pressure met at the end of the exhaust phase might be improved by slightly increasing the exhaust pressure. On both systems, the mesh might be refined to be perfectly phased with the experimental opening and closing times. This will significantly increase the CPU cost and diminish the interest of this method. A better approach could be to slightly modify the geometry of cams so as to open and close the systems like in the experiment. Here, this approach should consist in reducing the angular coverage of the cams depending on the size of the mesh in gaps. Globally, the simulations of these non reactive cases highlight the capability of the approach to analyse this kind of configuration even if some drawbacks are found.

This method might be considered to analyse the main characteristics and the global efficiency of a configuration with an affordable CPU cost.

6.7 Complementary study on the inlet pressure: a 0-Dimension model

The first aim of this paragraph is to analyse why the pressure in the buffer tank was decreased from 3 to 2.75 bar so as to meet the right pressure at the closing of the intake system. Then, the second goal is to identify how this pressure might be set to 3 bar, by using a 0-dimension (0D) simulation.

The 0D simulations are performed by using the commercial software AMESim to evaluate the carburation chamber pressure role on the combustion chamber pressure results, namely the filling-emptying rates and the maximum pressure at the end of the intake.

To do this study, the 0D CVC model is evaluated on the two non reactive operation points. For this approach, the combustion chamber, the intake and the exhaust systems are considered and the exhaust pressure is set to the atmosphere, namely 1.013 bar. The carburation chamber pressure is the input, on which some variations are studied. The section laws are extracted from the geometry of both systems, which are supplied by the manufacturer COMAT. In order to generate some mass flow rate during the constant volume phase, some residual sections are added. The aim is to calibrate the section laws of both systems and then use this set of section laws to study the influence of an intake pressure variation on the pressure in the combustion chamber.

First, the carburation chamber pressure is set to a constant pressure of 3 bar and the section laws are calibrated to reach the right filling-emptying rates and the pressure loss rate during the constant volume phase. These simulations are presented in the paragraph 6.7.1.

These adjusted sections laws are used to study the influence of the intake pressure variation on the pressure in the combustion chamber using the AMESim model. With these section laws, the 0D model is fed with the experimental pressure for the O.P.1 and with the LES carburation chamber pressure for the O.P.2. The two combustion chamber pressures obtained are used to define the reference combustion chamber pressures, which will be researched during the variations realised on the carburation chamber pressure. These results are presented in section 6.7.2

Finally, by assuming that an increase of the pressure in the buffer tank only involves an increase of the carburation chamber pressure, and does not change the acoustic through the intake pipe, the LES carburation chamber pressure signals are increased by 0.25 bar in order to reach the experimental pressure in the buffer tank. Then, these two modified LES carburation chamber pressure signals are shifted by 15 and 25 CAD and the pressures met in the combustion chamber are compared with the two reference combustion chamber pressures defined in section 6.7.2. These results are presented in section 6.7.3.

Tab. 6.3 summarizes the 3 different section laws of the intake and the exhaust systems used in the following parts. The maximum and the residual sections are defined with their maximum values measured in cm^2 and in percentage of the reference section supplied by COMAT. For example, the "Set 3" has a maximum intake section of $8.88 cm^2$, which corresponds to a section 2 times smaller than the section supplied by COMAT (50 %). The exhaust section law is also defined with a maximum section of $8.74 cm^2$, namely 65 % of the section supplied by COMAT. In order to generates some mass flow rate through the

Set of sections	$S_{I_{max}}$ [cm ²]/[% of $S_{I_{COM}}$]	$S_{I_{res}}$ [cm ²]/[% of $S_{I_{max}}$]	$S_{E_{max}}$ [cm ²]/[% of $S_{E_{COM}}$]	$S_{E_{res}}$ [cm ²]/[% of $S_{E_{max}}$]
Set 1	17.76 cm ² / 100.0 %	0.0 cm ² / 0.0 %	13.45 cm ² / 100.0 %	0.0 cm ² / 0.0 %
Set 2	17.76 cm ² / 100.0 %	0.0 cm ² / 0.0 %	13.45 cm ² / 100.0 %	0.27 cm ² / 2.0 %
Set 3	8.88 cm ² / 50%	0.0 cm ² / 0.0 %	8.74 cm ² / 65%	0.22 cm ² / 2.5 %

Table 6.3: Maximum and maximum residual sections where $S_{I_{max}}$, $S_{I_{res}}$, $S_{E_{max}}$ and $S_{E_{res}}$ respectively correspond to the maximum intake section, the intake residual section, the maximum exhaust section and the exhaust residual section. $S_{X_{COM}}$ are the section laws supplied by the designer COMAT where X corresponds to the intake I of the exhaust E .

exhaust system, a residual section of 2.5 % of the maximum section supplied by COMAT is added. The evolution of the sections are plotted on Fig. 6.22.

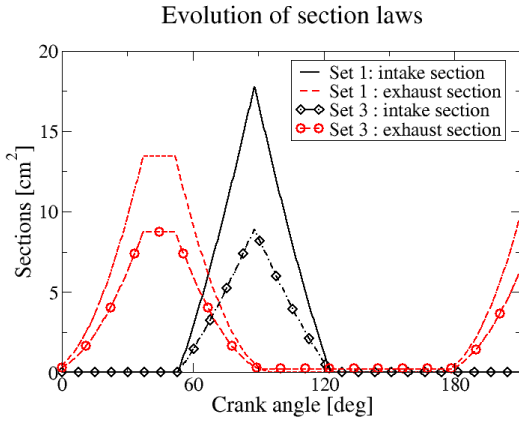


Figure 6.22: Evolution of the intake and the exhaust systems section laws between Set 1 and Set 3

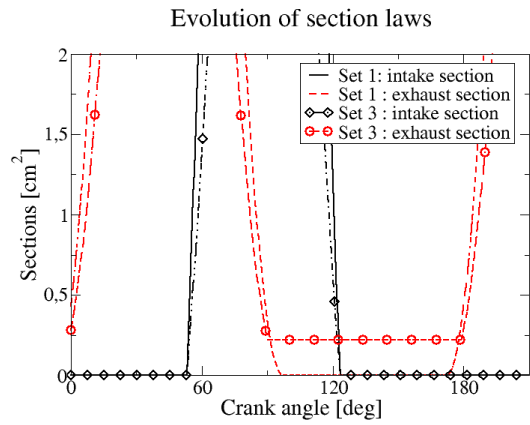


Figure 6.23: Focus on the exhaust residual section of Set 3

As presented in Fig. 6.22, the final section laws calibrated on the filling and emptying rates, maximum pressure at the end of the intake and pressure loss are significantly modified. Moreover Fig. 6.23 focuses on the additional residual section of the exhaust system.

6.7.1 Calibration of the exhaust and inlet section laws with intake pressure set to 3 bar

As explained above, the first step is to calibrate the 0D CVC model with a very simple inlet boundary condition, namely an inlet at a constant pressure and an inlet temperature which depends on the studied case.

In the following figures, the carburation chamber pressure used as an input of the 0D model is plotted in blue and the output of the 0D model, namely the combustion chamber pressure, is plotted in red. This output pressure is compared with the experimental combustion chamber pressure plotted in black line. The intake and exhaust section laws are respectively in black and red dashed lines.

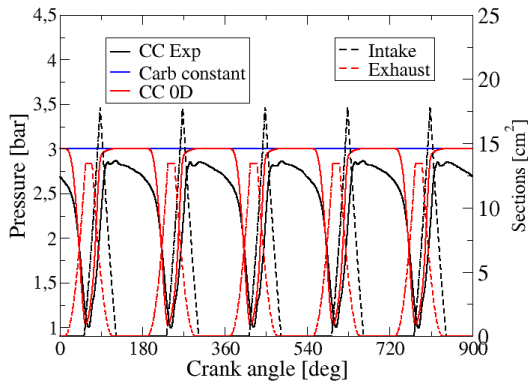


Figure 6.24: O.P.1 with section law's set 1

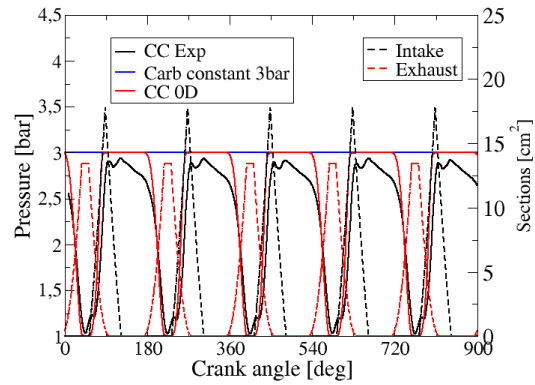


Figure 6.25: O.P.2 with section law's set 1

Figs 6.24 and 6.25 show the 0D results using Set 1 (Tab. 6.3). The constant inlet pressure leads to an overestimation of the combustion chamber pressure at the closing time. Moreover, the pressure in the combustion chamber remains constant since the model is perfectly airtight. Consequently, the predicted combustion chamber pressure at the exhaust system opening time is significantly overestimated. In order to introduce some mass flow rate during the constant volume phase, a residual section is added to the exhaust system which leads to the new section laws Set 2 (Tab. 6.3).

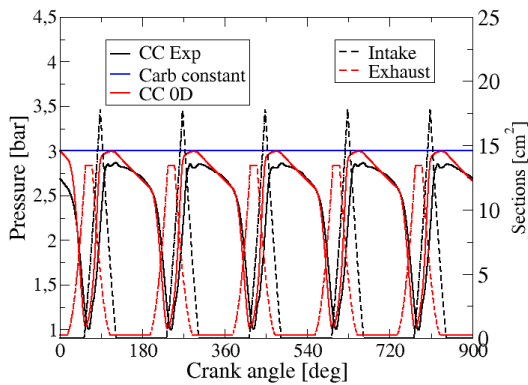


Figure 6.26: O.P.1 with section law's set 2

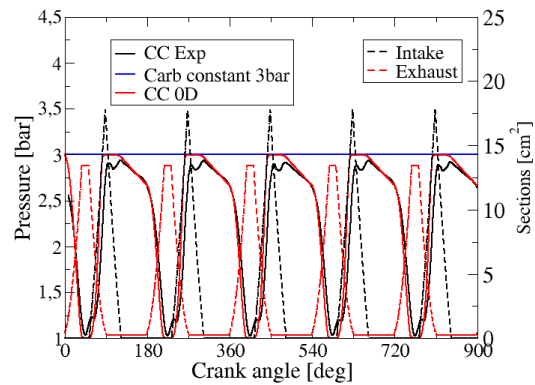


Figure 6.27: O.P.2 with section law's set 2

Figs 6.26 and 6.27 present the results using the new Set 2 (Tab. 6.3), where the exhaust section law is modified. A mechanical slack is added by creating a residual section of 2 % of the maximum exhaust free cross section of 13.45 cm^2 . This modification leads to a residual section of 0.27 cm^2 . The introduced leakage significantly improves the pressure loss rate during the constant volume phase even if this loss, represented by the slope of the pressure evolution during the constant volume phase, is overestimated by 7.3 %. In the model, the filling and emptying rates are overestimated, the section laws are then scaled to decrease these filling and emptying rates. In Set 3 Tab. (6.3), the intake and the exhaust section laws are respectively scaled by 50 % and 65 % and the exhaust residual

section is set to 2.5 % of the maximum exhaust free cross section.

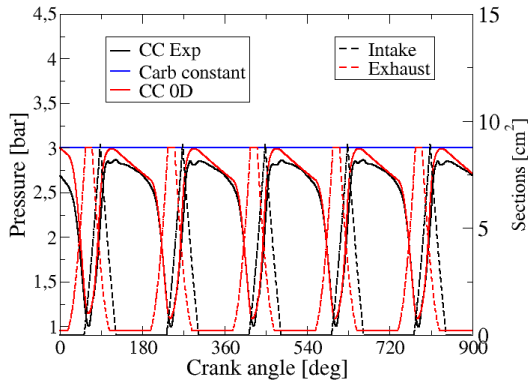


Figure 6.28: O.P.1 with section law's set 3

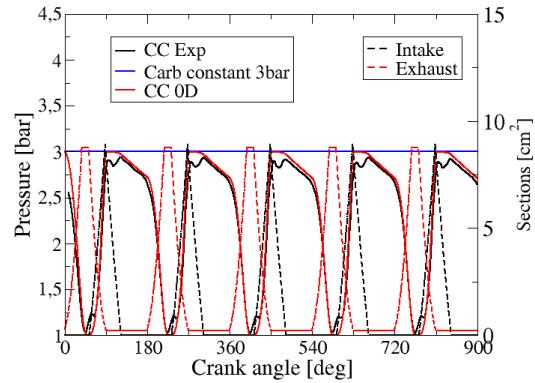


Figure 6.29: O.P.2 with section law's set 3

The third set of section laws presented in Figs. 6.28 and 6.29 gives a satisfactory prediction of both filling-emptying rates and a good order of pressure loss during the constant volume phase.

This set of section laws is used to study the influence of the intake pressure variation on the pressure in the combustion chamber.

6.7.2 Reference 0D response

The aim of the paragraph is to define the reference combustion chamber pressure with the intake and the exhaust section laws Set 3 (Tab. 6.3) defined above. To determine these reference pressures, two approaches are proposed. On the one hand, the O.P.1 reference pressure is generated using the experimental carburation chamber. On the other hand, the O.P.2 reference pressure is defined by using the LES carburation chamber pressure, previously set to 2.75 bar to fit the experiment, which is presented in section 6.5. The responses of the 0D model are presented in Figs. 6.30 and 6.31.

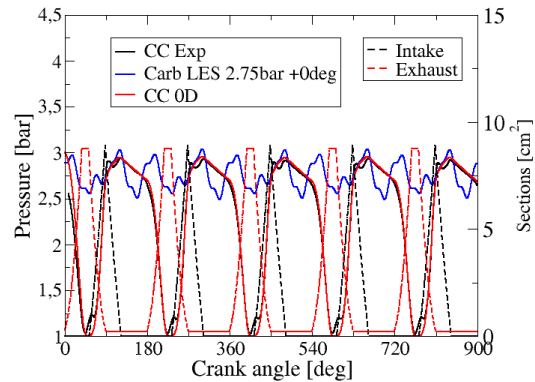
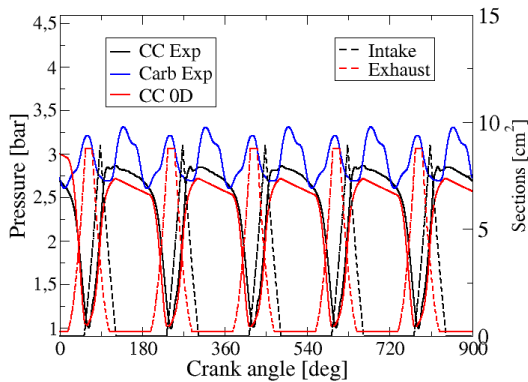


Figure 6.30: O.P.1 with experimental intake signal Figure 6.31: O.P.2 with fitted LES intake signal

Fig. 6.30 shows that the 0D model response of O.P.1 does not predict the experimental combustion chamber pressure while using the experimental carburation chamber pressure as an input. This is due to the model of the valve used, which only takes into account the pressure difference to let the air go through the valves and does not take into account the dynamics of the fluid which can counter the pressure difference. Despite this deviation, his combustion chamber pressure plotted in red is chosen as the targeted pressure in the following tests.

Fig. 6.31 highlights that using the LES carburation chamber pressure set to 2.75 bar as an input of the 0D model, gives a good correspondence of the combustion chamber with the experimental measurements. This pressure is also used as the targeted pressure in the following tests.

6.7.3 Intake pressure signal modifications

The aim of this paragraph is to find the angular shift needed on the LES carburation combustion pressures, previous increased by 0.25 bar and so set to 3 bar, to meet the reference 0D combustion chamber pressures defined in section 6.7.2. The LES carburation chamber pressures of both operating points are increased from 2.75 bar to 3 bar, and are time shifted so as to analyse this effect on the combustion chambers.

In both Figs. 6.32 and 6.33, the combustion chamber pressures clearly overestimate the experimental pressures and the targeted pressures. Indeed, the increase of the LES carburation chamber pressures raises the maximum intake pressure and the pressure gradient on both sides of the intake system during the intake phase. Consequently, a higher pressure is reached in the combustion chamber at the intake system closing time. This carburation chamber pressure elevation, to the experimental value of 3 bar, leads to a significant over-estimation of the combustion chamber pressure, functioning which was already analysed in preliminarily LES results presented in section 6.3. The hypothesis made here is that the acoustic through the intake pipe is modified by the LIB method. That is why, a shift of +15 degrees is tested to decrease the pressure gradient on both sides of the intake system and the carburation chamber pressure at the chamber closing time.

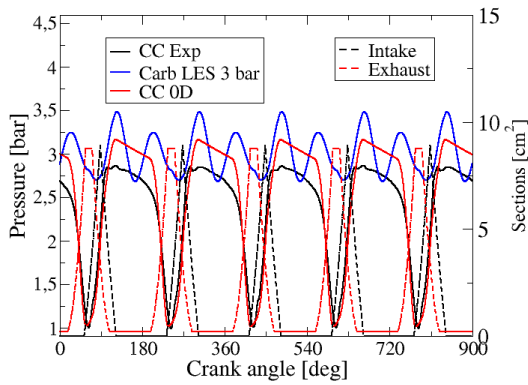


Figure 6.32: O.P.1 with LES 3 bar intake signal

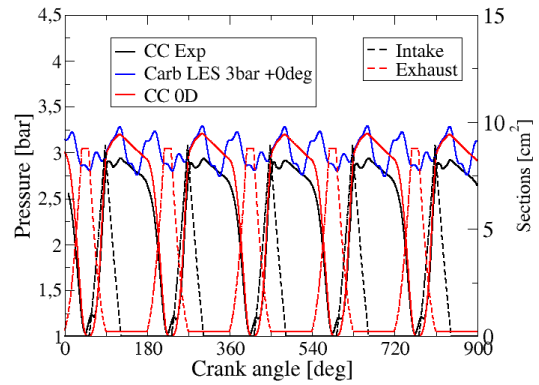


Figure 6.33: O.P.2 with LES 3 bar intake signal

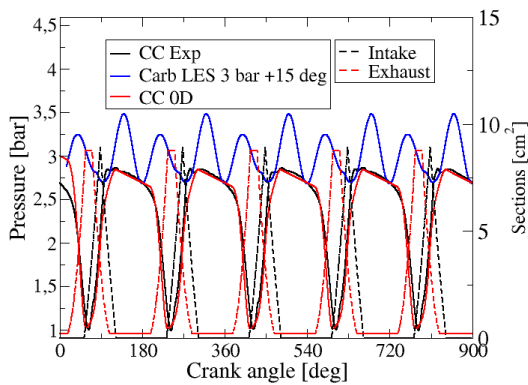


Figure 6.34: O.P.1 with LES 3 bar intake signal shifted by 15 degrees

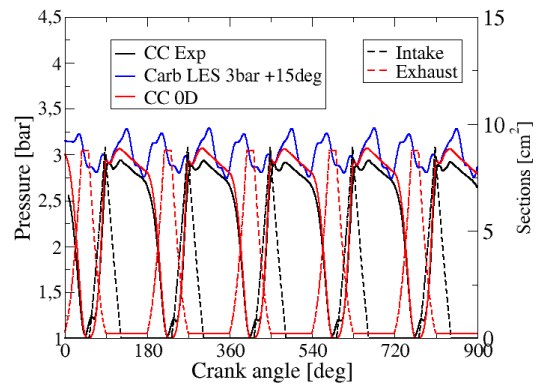


Figure 6.35: O.P.2 with LES 3 bar intake signal shifted by 15 degrees

Shifting the carburation chamber pressure by + 15 degrees improves the combustion chamber pressure at the closing time. As shown in Figs 6.34 and 6.35 the 0D responses fit the experimental pressure better, but do not match the targeted pressures defined in section 6.7.1. That is why the shifting of the carburation chamber pressure is increased from + 15 to + 25 degrees.

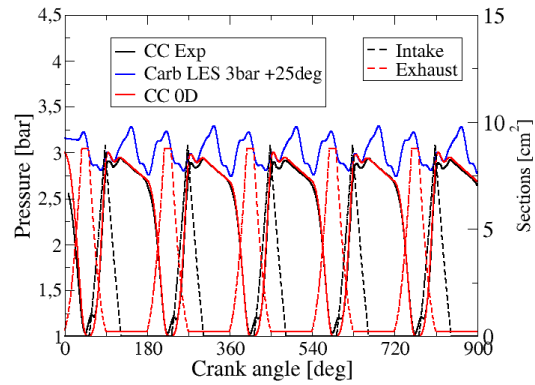
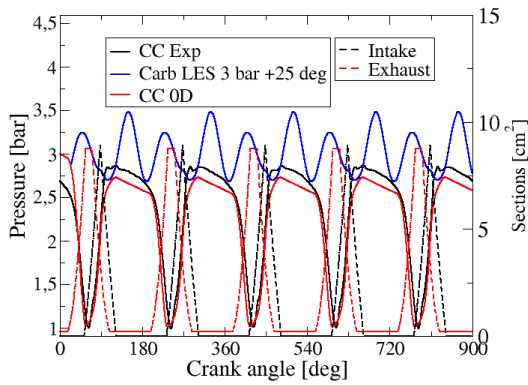


Figure 6.36: O.P.1 with LES 3 bar intake signal shifted by 25 degrees

Figure 6.37: O.P.2 with LES 3 bar intake signal shifted by 25 degrees

With a shift of + 25 degrees, the combustion chamber pressure evolutions predicted by the 0D model gives a very good accordance with the targeted pressures previously defined in Figs 6.30 and 6.31.

The final results of the targeted pressure and the results obtained by increasing the pressure by 0.25 bar and shifting them by + 25 degrees are presented in Figs 6.38 and 6.39.

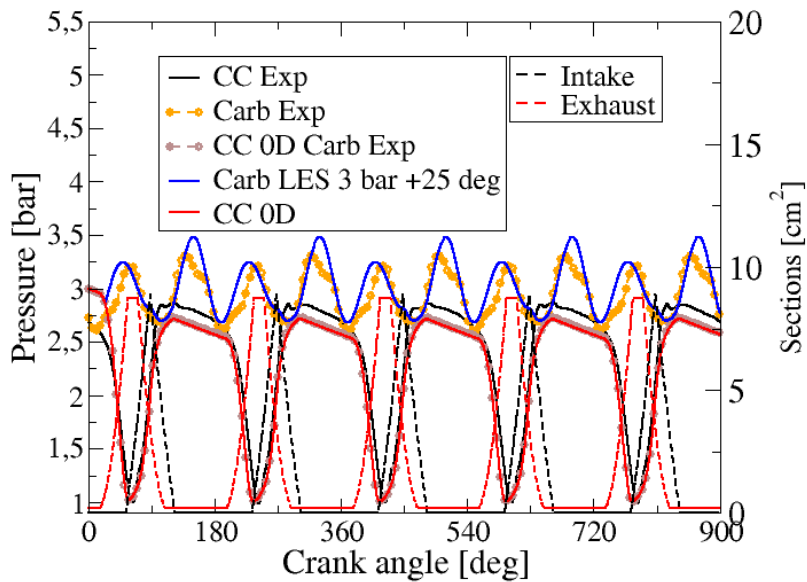


Figure 6.38: O.P.1 targeted pressure and final LES carburation chamber pressure adaptation

Fig 6.38 presents the results generated with the carburation chamber pressure increased to 3 bar and time shifted by +25 CAD. In this graph, the reference pressure, namely the experimental carburation chamber pressure, and the combustion chamber pressure

obtained with this input pressure are respectively plotted in yellow and grey lines with circles. Last but not least, the last modified LES carburation and the combustion chamber predicted by the 0D model with the last input pressure are respectively plotted in the blue and red lines.

According to this figure, the last LES carburation chamber pressure fits the experimental one where extrema are time-phased. Moreover, with these modifications, the minimum and maximum values of this pressure are consistent with the experimental ones. However, the simulated pressure does not fluctuate like in the experiment which might emphasize that the acoustic is not correctly resolved in the LES.

With this inlet carburation pressure, the combustion chamber pressure obtained with the 0D model fits the reference pressure. Therefore, the LES should be shifted by + 25 degrees to correctly predicts the experiment with a pressure of 3 bar at the inlet.

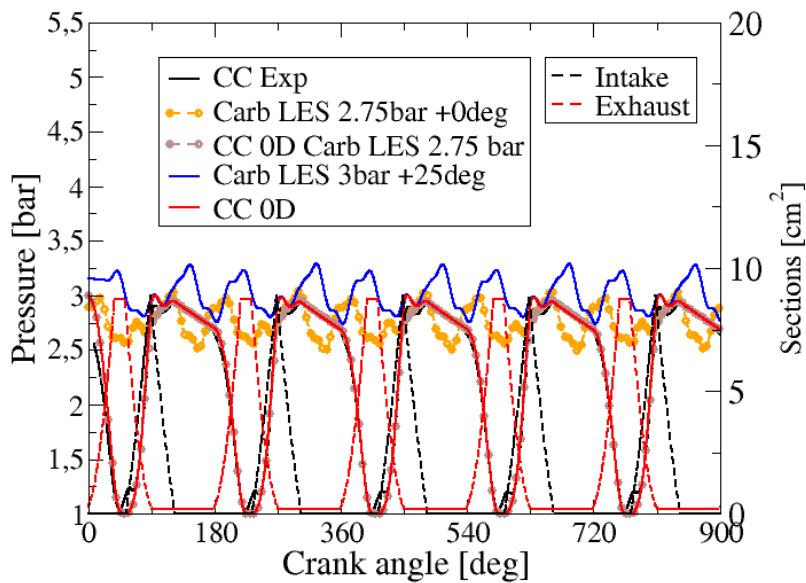


Figure 6.39: O.P.2 targeted pressure and final LES carburation chamber pressure adaptation

In the O.P.2 presented in Fig. 6.39, only the experimental combustion pressure is known. Consequently, the pressure of the combustion chamber plotted in the grey line with circle, has to be compared with the reference response of the 0D model, plotted here in the red line. In this figure, the measured LES carburation chamber pressure used to defined the targeted combustion pressure is plotted in yellow line with circle.

Like the previous analysis, the carburation chamber pressure from an averaged intake tank pressure set to 3 bar, has to be shifted by 25 degrees to meet the searched combustion chamber pressure which is the same as the experiment.

=====
Conclusion:
=====

The 0D simulations, performed by using the commercial software AMESim, allow the realization of a lot of test cases in a very short time. Here, the calibration of the section laws is realised by scaling them and introducing some residual sections during the constant volume phase, which permits to have a good accordance with the experimental filling-emptying rates and the pressure loss during the constant volume phase.

With these parameters, reference combustion chamber pressure are generated using the experimental carburation chamber pressure for the O.P.1 and the LES carburation chamber pressure of the O.P.2 when the pressure at the inlet is set to 2.75 bar. By assuming that an increase of the intake tank pressure by 0.25 bar only raises the carburation combustion pressure by 0.25 bar, two time shiftings are presented, namely +15 and +25 CAD. The last time shifting has a very good compatibilities between the modified LES carburation chamber pressure of the O.P.1 and the experimental one, and both operating points have a good accordance with the reference pressures.

Consequently, this study points out:

- The LES carburation pressure set to 3 bar is in advance compared with the experimental pressure, namely the fluctuations around the average value. Therefore, the pressure in the combustion chamber, at the closing time of the intake system, is significantly overestimated due to a higher pressure in the carburation chamber than in the experiment. In the LES, since the shape and the evolution of the carburation pressure are the result of the acoustics through the intake pipe and its interactions with the LIB and their closing times, the pressure at the inlet was decreased from 3 down to 2.75 bar, which allows the prediction of the experimental pressure in the combustion chamber at the beginning of the constant volume phase.
- With an inlet pressure set to 3 bar, the carburation chamber pressure must be delayed by +25 CAD to be consistent with the experiment. Therefore, some effort are required to analyse the causes of this functioning and find out if this problem comes from the LIB model.

Finally, this study shows that the pressure in the carburation chamber is in advance compared with the experiment. However the inlet pressure of the LES can be adjusted to get the right pressure in the combustion chamber at the beginning of the constant volume phase and allows the evaluation and the understanding of 2 non-reactive and one reactive operating points.

Chapter 7

Reactive case

Contents

7.1	Operating point	132
7.2	Computational parameters	133
7.3	Results	135
7.3.1	Velocity field analysis	135
7.3.2	Combustion chamber pressure evolution	142
7.4	Cycle-to-cycle variability analysis	146
7.4.1	Slow and fast cycles analysis	146
7.4.2	Peak pressure of consecutive cycles	153
7.4.3	Single regression analysis	154
7.4.4	Multidimensional data analysis	164
7.4.5	Conclusion on the different levers to improve the combustion process	168
7.4.6	Correlation of previous cycle variables with the cycle-to-cycle variability	169
7.5	Reactive case conclusion	180

This chapter presents results on one reactive operation point. This operating point, called in the following paragraph "O.P.3", is the same operating point as the O.P.2 presented in the previous chapter, where the fuel carburation and the combustion are activated. The experimental diagnostics are the same, namely the velocity fields and the pressure in the combustion chamber. Firstly, the analysis focuses on the velocity fields inside the combustion chamber where velocity profiles at the same positions as in section 6.6.2 are compared with the experiment. Then the pressure evolution in the combustion chamber is plotted, showing significant cycle-to-cycle variability. Last but not least, this variability is analysed and the possible causes of it are deduced from the LES result analysis and discussed hereafter.

7.1 Operating point

As introduced above, the considered operating point in this study is the following experiment of the O.P.2, where the combustion is studied. Therefore, this case has the same inlet conditions and the same crank angle shift between the intake and the exhaust systems as the O.P.2, with in addition the fuel carburation and the combustion. The

liquid injection of isooctane is realised by eight Bosch automotive injectors and the flame is initiated by one automotive spark plug on the bottom left position walls at 55 mm from the rotation centre of the intake cams as shown in Figs. 5.7 and 5.8. The targeted fuel air equivalence ratio is of 1.28 in the chamber, therefore 0.106 g are injected in the carburation chamber at each cycle. The fuel injection is realised by consecutive injections of injector pairs at 130, 140, 150 and 160 CAD.

The reactive mixture is ignited at 140 CAD and the flame propagates till the exhaust system opens. The maximum pressure reached in this configuration significantly depends on the flow at the spark plug during the ignition and on the flow properties encountered by the flame during its propagation.

Main parameters of the operating point O.P.3 and the two used experimental diagnostics are presented in the following Tabs 7.1, 7.2 and 7.3.

Operating points	Inlet pressure [bar]	Inlet temperature [k]	Shift crank angle [deg]
O.P.3	3.0	420	45.5

Table 7.1: Reactive operating point main parameters

Operating points	Averaged experimental mass of air per cycle [g]	Injected liquid mass [g]	FA eq. ratio [-]
O.P.3	1.25 g	0.106 g	1.28

Table 7.2: Following reactive operating point main parameters

Operating points	Diagnostics
O.P.3	CC pressure and velocity fields

Table 7.3: Experimental diagnostics

7.2 Computational parameters

The simulation of this operating point is performed with Lax-Wendroff numerical scheme [74] and the Sigma SGS model [26]. Conform walls in the chamber are modeled with an isothermal wall law-of-the-law boundary condition and a no-slip isothermal boundary condition is applied on LIB walls. In the simulation these temperatures are set to the inlet temperature since the apparatus is heated up with some pressurized and heated air, which goes through the device. Then, less than 3 seconds are analysed experimentally, which hardly changes the temperature of the apparatus.

The crank angle shift between the upper and the lower cams of the intake system, set in section 6.6.2, is decreased down to 1.5 degrees in order to decrease the time delay between the lower and the upper vortices. This adjustment improves the motion of the center of both vortex, which fits the measurements better.

With the LIB dimensions determined using the non reactive cases, namely the gaps between cams and walls, the preliminary reactive simulations show that the maximum pressure is overestimated while the mass loss is underestimated during the constant volume phase. Indeed, a higher mass flow rate through bearings was observed in the O.P.3 than in the non reactive case O.P.2. To account for this effect in the simulation, the gaps at the exhaust system are therefore increased. With this new LIB dimensions, the pressure at the end of the intake is underestimated, which is then improved by setting the pressure in the buffer tank from 2.75 bar to 2.95 bar.

The liquid fuel injection is realised through the four pair of injectors using the Lagrangian approach and the secondary breakup model SAB [46] is activated.

The combustion model used here is the ECFM-LES model [30] coupled to the ignition model ISSIM-LES [39], models respectively presented in paragraphs 2.4.2 and 2.4.3. The burnt gases deposit is supposed to be spherical in the ISSIM-LES model and the constant α_{cfm} of ECFM-LES combustion model, presented in the equation of the unresolved strain Eq. 2.88, is set to 1.0, where values from 0.6 to 1.8 can be chosen depending on the mesh refinement. As advised in SI engine simulations for which these models were developed, the ignition phase is calculated on the mesh where the spark plug is refined from a characteristic length scale of 0.5 mm down to 0.25 mm as presented in Fig. 7.1.

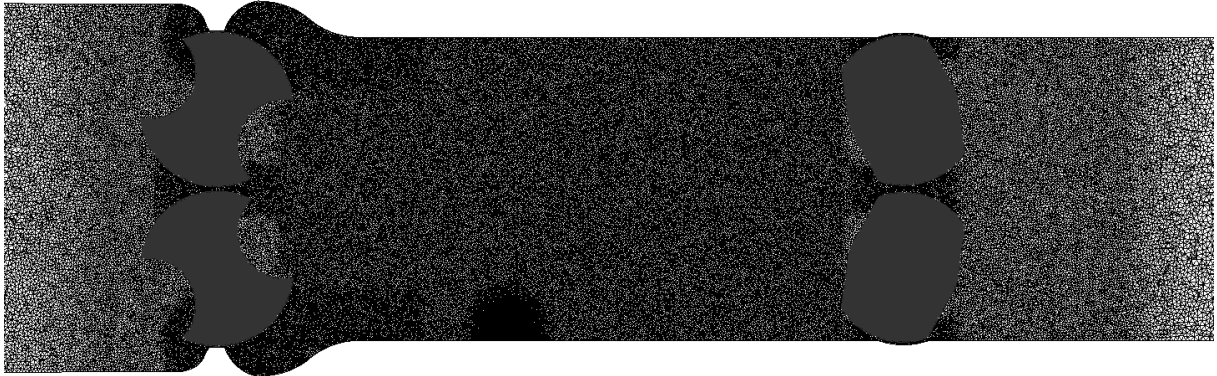


Figure 7.1: Mesh refinement at the spark plug position for the ignition phase

When the transition from the ignition model ISSIM to the propagation model ECFM-LES is completed, the flow is interpolated on the main mesh where the spark plug is not refined. This method permits the raising of the resolution of the first kernel and then continues the calculation of the flame propagation on a mesh less expensive in terms of CPU cost. Lastly, the combustion model is deactivated during the exhaust and the intake phases till the ignition CAD of 140 degrees.

In this configuration, the mixture is realised in the carburation chamber of cycle N by 4 injections at 140, 150, 160 and 170 located at different positions, shown in Fig. 7.2. In this figure, the carburation of cycle N creates a cloud of liquid particles in the chamber upstream of the combustion chamber, which then feeds the following cycle N+1. In

our simulations, the mixture of the second cycle leads to a misfire since the mixture in the vicinity of the spark plug and in the combustor was not favourable to the flame propagation. Then, from the third cycle after the first carburation, the combustion occurs in the chamber.

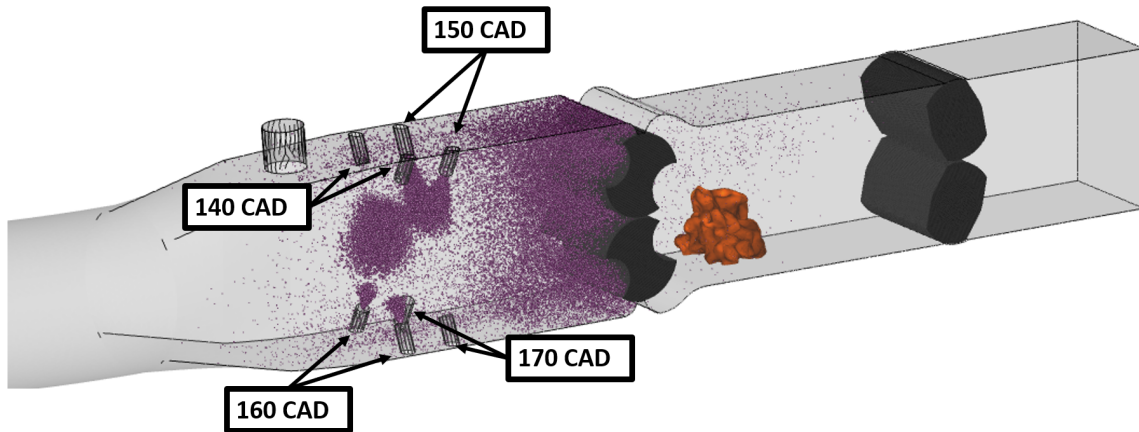


Figure 7.2: O.P.2 different pairs injection times

7.3 Results

The phase averaged velocity fields are realised on 13 LES cycles and compared with the experimental velocity field averaged on 80 cycles. Then, the combustion chamber pressure evolution is analysed. Like in the experiment, the combustion chamber pressure shows high cycle to cycle variability. Therefore, the reasons of this cycle-to-cycle variability are then investigated.

7.3.1 Velocity field analysis

Like in the O.P.2, PIV measurements are realised on this case. The comparisons between the experiment and the simulations are done during the intake phase where the vortices generated by the intake system are observed through the analysis window. The considered times are the same as in O.P.2, namely at 72.0, 75.6 and 79.2 CAD. The axial and the tangential velocity profiles are plotted at the six positions located between 5 mm and 55 mm separated with a spatial step of 10 mm.

Fig. 7.3 shows the first considered moment at 72.0 degrees. In this figure, the experimental phase averaged velocity fields are presented on the left and compared with the results of the LES, shown on the right. According to this figure, the experimental velocity fields are more noisy than in the previous non-reactive cases. This might be due to the strong cycle-to-cycle variability encountered in this operation point. The LES signal predicts the experimental trend but the lack of statistical convergence is visible.

In Fig. 7.3, the predicted upper vortex is more flattened than in the experiment and the

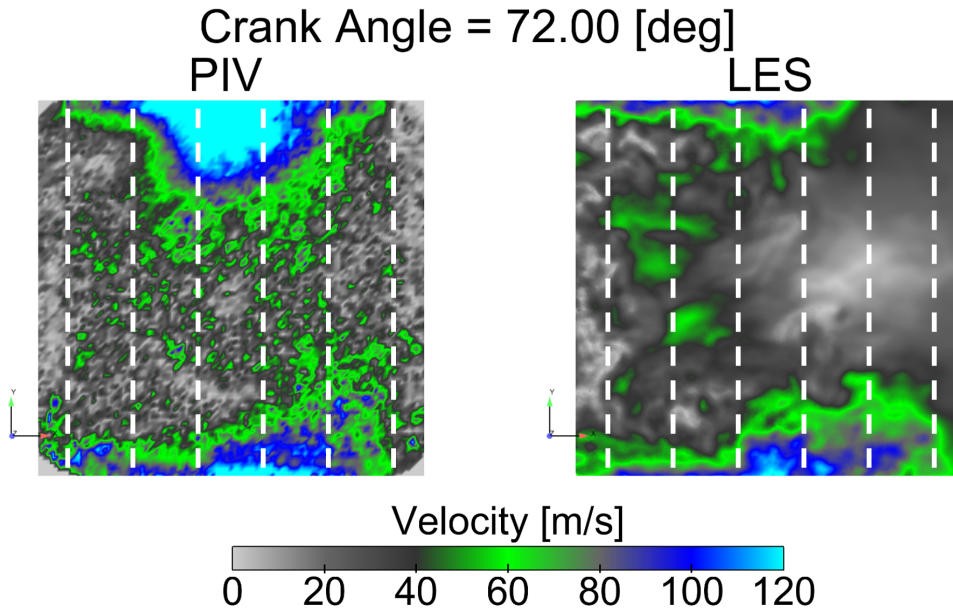


Figure 7.3: PIV and LES average velocity field at 72.00 CAD

velocity magnitude is slightly underestimated. At this time, the LES rotation centre of the upper vortex is not clearly identified and seems located in between 10 and 20 mm whereas the experimental measurement clearly shows a rotation centre at 10 mm.

The recirculation zone in the centre of the chamber is correctly captured.

The lower vortex shape is predicted by the LES but the rotation centre is less convected than in the experiment. The centre is measured at 17 mm where the experimental measurement gives a rotation centre in between close to 25 mm.

As expected and visualised in Fig. 7.4, the experimental results are noisy but the trend of both the axial and the tangential velocities are quite well predicted by the LES. The axial and the tangential velocities of the lower vortex presented in the lower part of graphics, match correctly the experimental result except at 25 mm where the LES predicts a tangential velocity of 30 m/s instead of zero. Indeed, the measurements show at 25 mm that the flow is mainly axial since its rotation centre is close to this position. In the simulation, the lower vortex is not completely flattened and is spinning around its rotation center located at 18 mm. Therefore, a positive tangential velocity is measured at 25 mm. Moreover, the LES upper vortex velocity magnitude is lower than the experiment, that is why both axial and tangential velocities are smaller than the experimental ones in the upper parts of graphics.

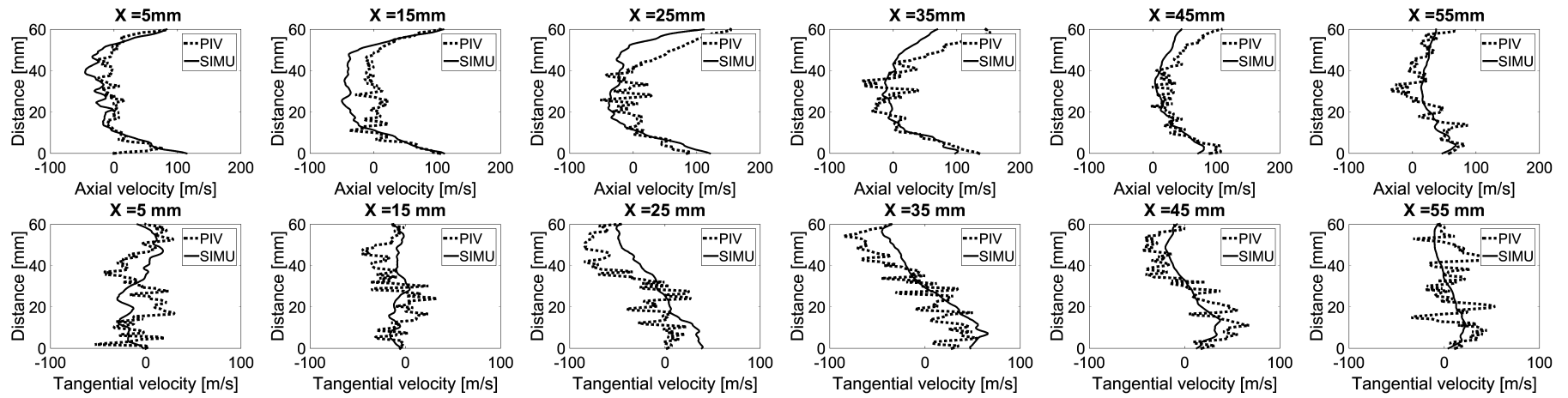


Figure 7.4: Axial (on top) and tangential (on bottom) velocity profiles at 72.00 CAD

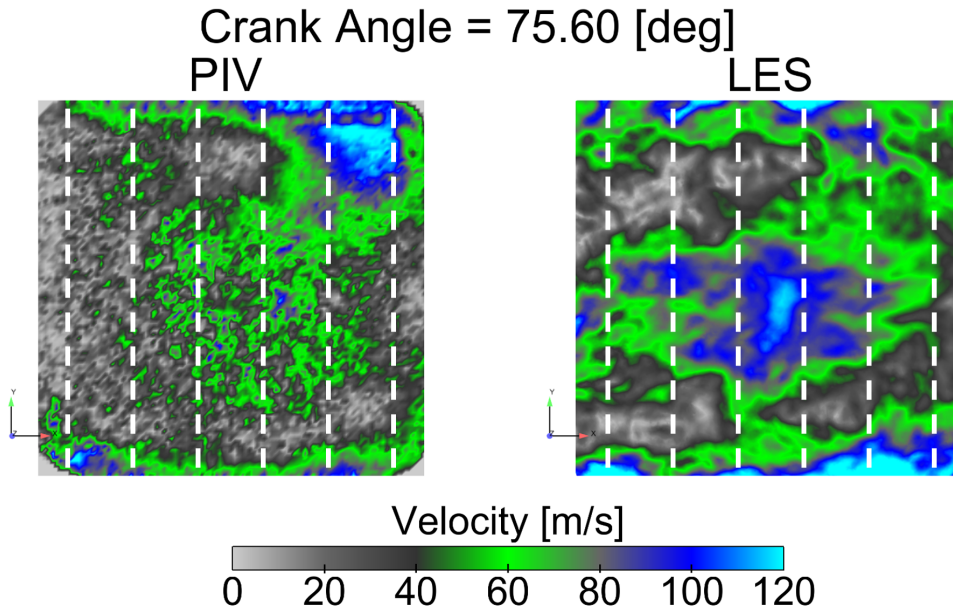


Figure 7.5: PIV and LES average velocity field at 75.60 CAD

Fig. 7.5 presents the second velocity fields at 75.6 CAD. At this time, the lower vortex is almost entirely flattened, which is correctly captured by the LES. The velocity magnitude at the bottom of the visualisation window of the LES is higher than in the experiment. The upper vortex center propagates faster than the previous non reactive O.P.2 and corresponds better to the experimental measurements. This motion is improved in the simulation thanks to the decrease of the CAD shift between the upper and the lower intake cams, which is now set to 1.5 degrees. The velocity magnitude and the spinning motion is qualitatively well captured by the LES. Some discrepancies appear in the recirculation zone in the center of the visualisation window where the LES seems to overestimate the velocity by 20 m/s.

The good accordance in the visualisation window is confirmed by the quantitative comparison of the axial and the tangential velocity profiles in Fig. 7.6. The tendency is correctly captured but discrepancies mentioned above are clearly exposed. Firstly, the lower vortex is completely flattened in the experiment since all tangential velocities are close to zero near the bottom of the experimental window. In the simulation, a positive component of the tangential velocity is observed at 45 and 55 mm, which highlights that the vortex is spinning at the end of the visualisation window. In this zone, the magnitude and the axial velocity are also slightly overestimated.

The upper vortex is also very well predicted by the LES. The main discrepancies are located at the end of the visualisation window where a strong recirculation zone is measured in the experiment. The spinning motion of the upper vortex is captured by the simulation since both axial and tangential velocities profiles have the same shapes and the same signs but the tangential velocity magnitude is almost two times lower.

Lastly, the recirculation zone in the centre of the chamber is stronger in the LES, which is mainly visible on axial velocity profiles at 5 and 15 mm.

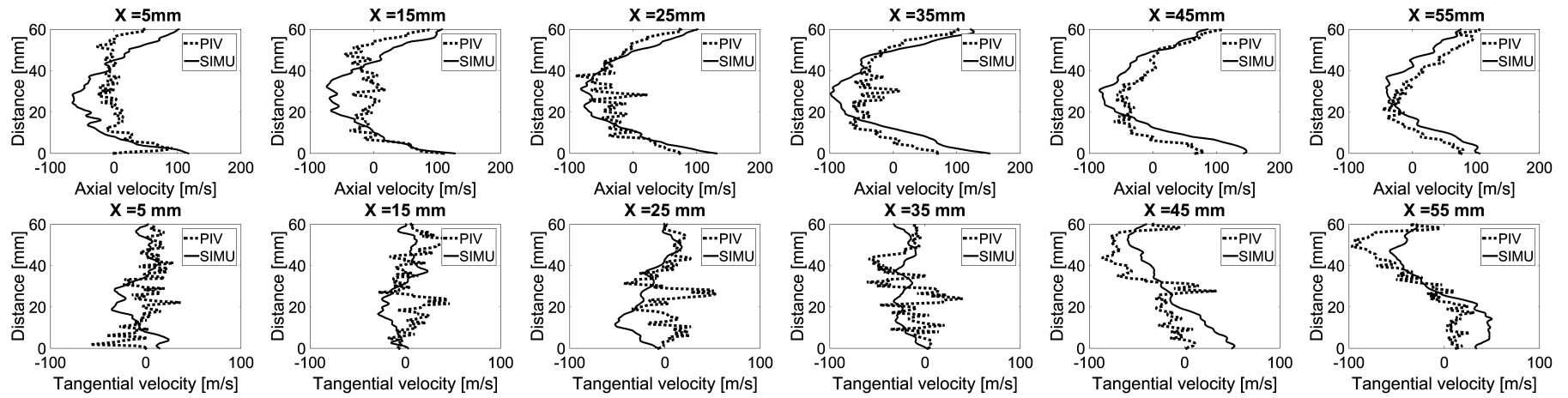


Figure 7.6: Axial (on top) and tangential (on bottom) velocity profiles at 75.60 CAD

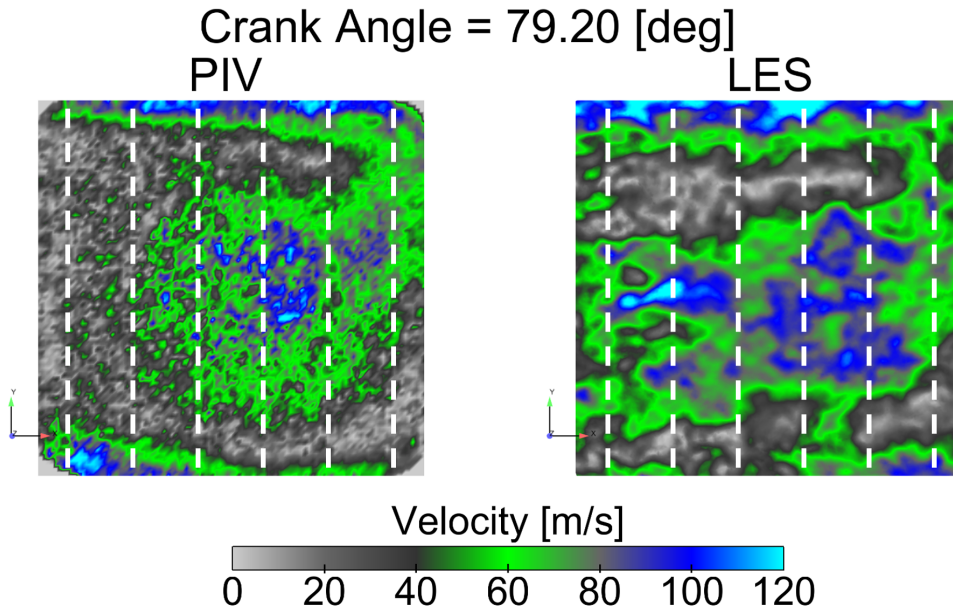


Figure 7.7: PIV and LES average velocity field at 79.20 CAD

The last considered CAD is at 79.2 degrees and Fig. 7.7 presents the velocity fields. At this time, the crank angle shift between upper and lower intake systems generates the velocity fields like in the experiment. Indeed, the lower vortex almost disappears from the visualisation window and the recirculation motion is created by the upper vortex. According to this figure, the simulation accurately predicts the position of the upper vortex centre and the recirculation zone. However, the simulations overestimate the recirculation zone close to the intake system.

At this CAD, the profiles shown in Fig. 7.8 highlight that the LES captures the shape and the magnitude of the experimental velocity fields. The main discrepancy is identified on first axial profiles where no velocity is measured in the experiment while the LES clearly predicts the recirculation zone along the whole middle part of the visualisation window. This overestimation might be due to an underestimation of the simulated leakage in-between both cams of the intake system, which could diminish the recirculation motion downstream of the intake system.

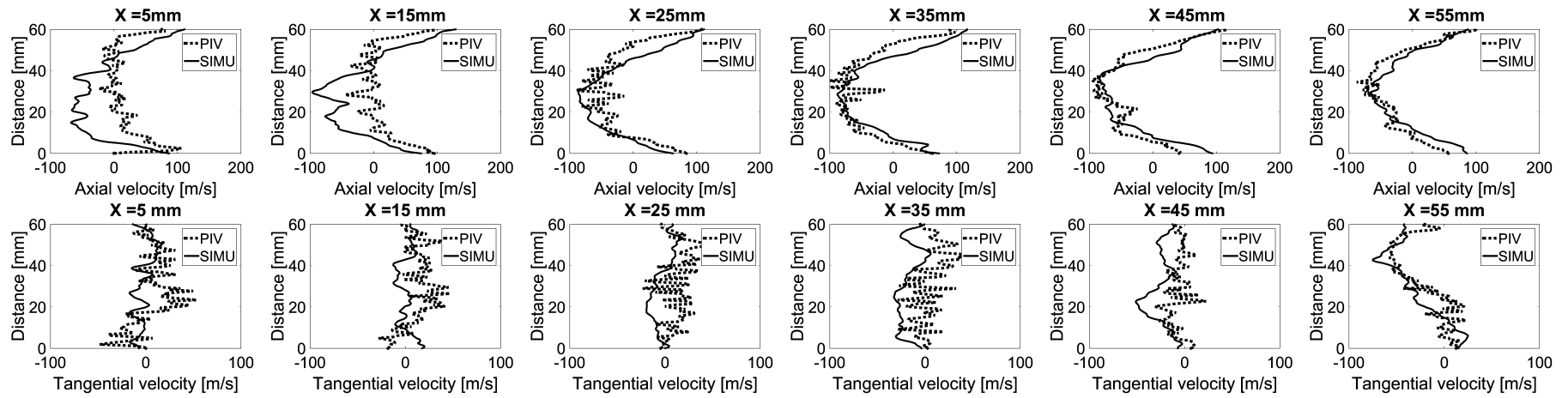


Figure 7.8: Axial (on top) and tangential (on bottom) velocity profiles at 79.20 CAD

=====
Conclusion:
=====

The experimental velocity fields action is correctly predicted by the LES, even if some exceptions are notable in some velocity profiles. According to this velocity fields analysis, this kind of complex experiment can be modeled with the LIB approach.

7.3.2 Combustion chamber pressure evolution

The second diagnostic used here is the combustion chamber pressure evolution. Fig. 7.9 and the following pressure graphics focus on the combustion process which starts at the ignition timing, namely at 140 CAD. Therefore, all following graphics begin at this CAD and finish at 330 CAD. Consequently, the beginning of the graph represents the end of the constant volume, then the exhaust takes place between 172 and 235 CAD, followed by the scavenging phase which ends at 277 CAD. Finally the intake occurs from 277 to 305 CAD. The last part of the graph, on the right of the figure is the beginning of the constant volume phase.

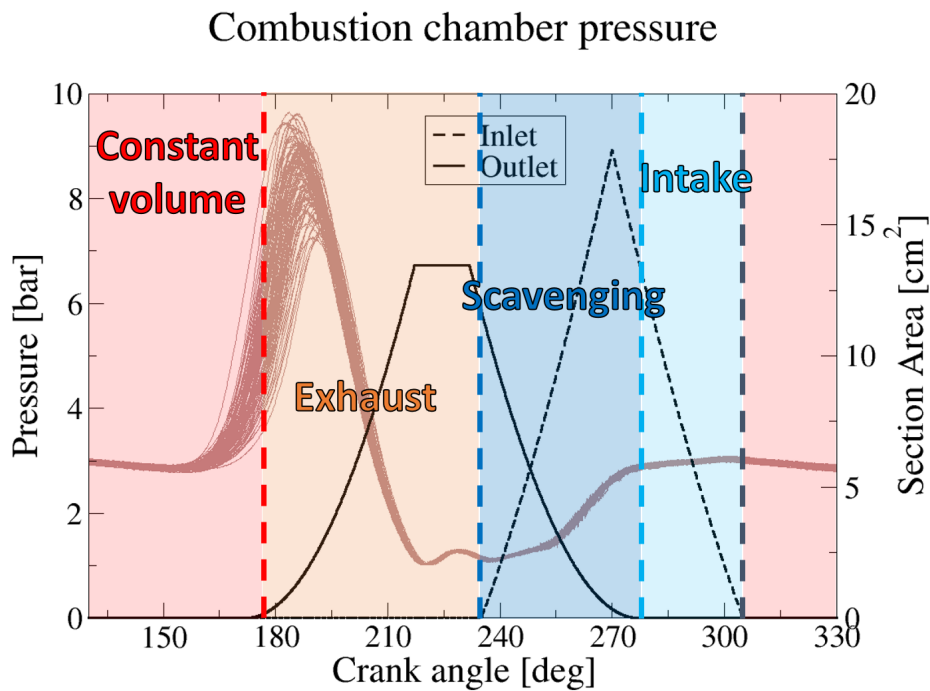


Figure 7.9: Different phases shown on the reactive experimental pressure results

Combustion chamber pressure

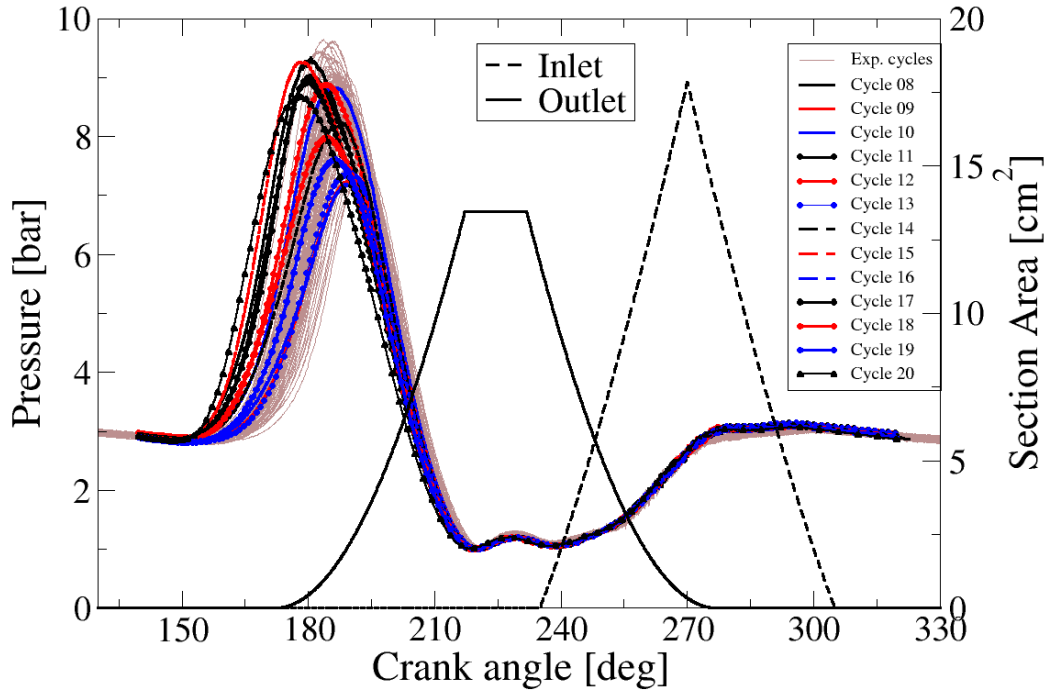


Figure 7.10: Individual combustion chamber pressure evolutions

Fig. 7.10 superimposes the predicted 13 LES cycles and experimental findings resulting from 80 engine cycles. Despite the limited number of simulated cycles, LES qualitatively yields a level of pressure variability comparable with the experimental observations. The maximum pressure of 9.25 bar is reached at around 178.7 CAD where the experiment gives 9.64 bar at 183.7 CAD. The minimum LES peak pressure of 7.16 bar is achieved at 189.8 CAD where minimum experimental peak pressure reaches 7.26 bar at 190.1 CAD. Consequently, the global envelope is captured, although it is shifted to lower CAD, especially for higher maximum pressure.

During the exhaust, the scavenging and the intake phases, the LES accurately captures the pressure evolution inside the combustion chamber.

Right after the spark breakdown CAD, the LES pressures tend to increase faster than in the experiment. The ignition process is very sensitive to the velocity near the spark plug. A small over-prediction of this velocity might lead to a faster flame kernel propagation. In these simulations, the spark plug geometry is not resolved which may generate higher velocity magnitude in this zone and thus explains partially this faster pressure increase right after the spark timing.

Combustion chamber pressure

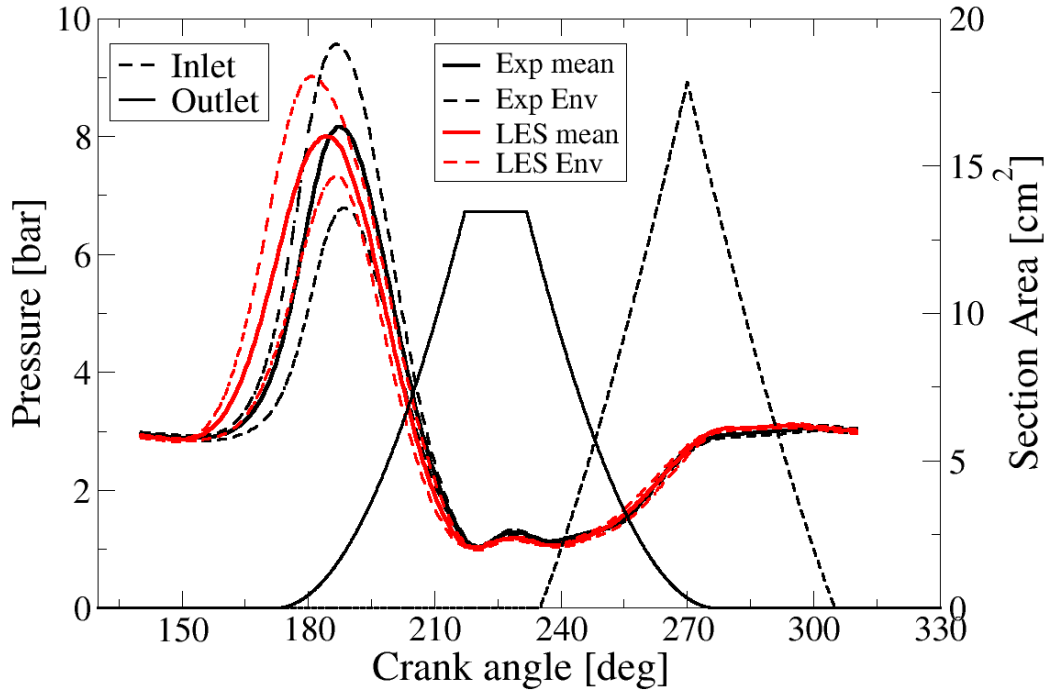


Figure 7.11: Comparison of the experimental and the LES mean pressures and their envelope

Fig. 7.11 shows for both the LES and the experiment the phase-averaged mean pressures in the combustion chamber and their envelope evolution Env defined as the mean pressure plus or minus the standard deviation ($Env(t) = P(t) \pm \sigma_P(t)$). They are respectively plotted in red and black lines and in red and black broken lines. Like in individual cycles, the global trend is correctly predicted by the simulation. In both cases, the maximum mean pressure is around 8.1 bar but this maximum is reached at 184 and 188 CAD respectively for the LES and the experiment. Furthermore, the flame propagation speed at the beginning of the combustion is significantly over-predicted which leads to a higher pressure increase than the measurements between 155 and 170 CAD. In other phases, the pressure evolution is correctly predicted.

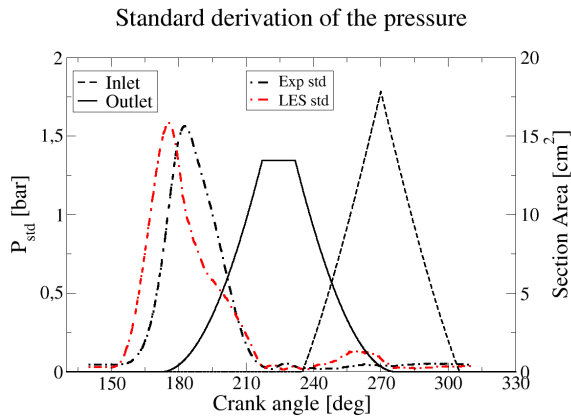


Figure 7.12: Standard deviation of the pressure function of CAD

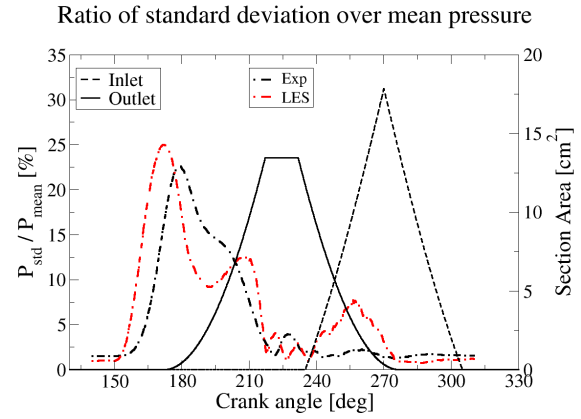


Figure 7.13: Percentage of the standard deviation over mean pressure

Figs. 7.12 and 7.13 focus on the standard deviation of the pressure and the percentage of the standard deviation over the mean pressure. In these figures, the two variable evolutions are accurately predicted by the LES even if the maximum values of the simulation are reached at around 175 CAD instead of 183 CAD. The good compatibility of the standard deviation confirms that the experimental cycle-to-cycle variability is captured by the LES. Consequently, the comprehension of this phenomena can be realised through the analysis of the LES results.

=====
Conclusion:
 =====

The LES predicts the experimental phase-averaged mean combustion chamber pressure and the right order of variability magnitude. In order to complete this analysis, several cycles might be calculated where the spark plug geometry is considered, which may change the velocity magnitude in this zone and then modify the very first kernel propagation. However, the cycle-to-cycle variability and its magnitude are captured by the LES. Therefore, the comprehension of such phenomenon can be analysed on these results. This analysis will allow the understanding of the combustion process in CVC chambers and will identify the levers to control the variability in these configurations better.

7.4 Cycle-to-cycle variability analysis

In this paragraph, the cycle-to-cycle variability captured by the LES is analysed in order to find the main causes of this phenomenon. The first step proposed here is to analyse the slow and fast cycles and visualise the flame propagation 1.30 ms after the spark timing which corresponds to 149.40 crank angle degrees. The responses like the peak pressure or the CA 02, which is the crank angle when 2% of the fuel mass is consumed, the CA 10, the CA 50 and the mean pressure of the cycle are correlated to local and global thermodynamic variables such as the velocity at the spark plug or the averaged residual burnt gases mass fraction in the combustion chamber at spark timing. These quantities are also correlated to averaged thermodynamic variables seen by the flame front like the subgrid scale velocity at the combustion filter size. In this kind of combustor, several parameters act simultaneously which can limit the single regression analysis. Therefore, a multidimensional data analysis proposed by Truffin *et al.* [53] is studied on the previous variables to find out the quantities strongly correlated to the responses. Finally, some quantities like the pressure difference on both sides of the intake system, which can generate the variability of the thermodynamic variables, are analysed.

7.4.1 Slow and fast cycles analysis

The aim of this paragraph is to measure the trend of consecutive cycles in terms of combustion speed and thus efficiency. The analysed quantities are averaged on the volume of the chamber at spark timing, they are the resolved kinetic energy, the equivalence ratio and the residual burnt gases. Tab. 7.4 presents the minimums, the maximums, the averages and the standard deviations of these quantities calculated on the 13 simulated cycles. Moreover, the peak pressure and its corresponding angle are added on the bottom of this table.

Variables	Minimum	Maximum	Averaged	Standard deviation
Kinetic energy [$\text{m}^2 \cdot \text{s}^{-2}$]	52.07	96.75	73.06	15.14
Equivalence Ratio [-]	1.17	1.32	1.24	0.024
Resid. GB mass fraction [-]	0.103	0.164	0.130	0.017
Peak pressure [bar]	7.16	9.25	8.32	0.68
Peak pressure angle [deg]	177.02	190.85	184.41	3.77

Table 7.4: Statistics of the mean resolved kinetic energy, the mean equivalence ratio, the mean residual burnt gases mass fraction, all being at spark timing, the peak pressure and its corresponding angle

Tab. 7.4 puts in the foreground the strong variability encounter in the configuration. Indeed, the mean resolved kinetic energy, the mean equivalence ratio and the mean residual burnt gases mass fraction fluctuate respectively by 85.8 %, 12.8 % and 59.2 % compared with the minimum values. These variations involve a considerable fluctuation of the peak pressure and its corresponding angle, which respectively evolve within a range of 29.1 % and 31.1 % compared with the minimum peak pressure of the 13 cycles and the average combustion time of 44.41 degrees. This mean combustion time is estimated between the ignition crank angle of 140 CAD and the average peak pressure angle of the 13 cycles.

The following analysis consists in identifying the slowest and fastest cycles which are respectively defined by a peak pressure lower than 7.50 bar at crank angle higher than 185 degrees, and a peak pressure close to 9 bar at crank angle lower than 185 degrees. These two criteria, only based on the pressure measurements, are used since its allows the identification of slow and fast cycles but also moderate ones.

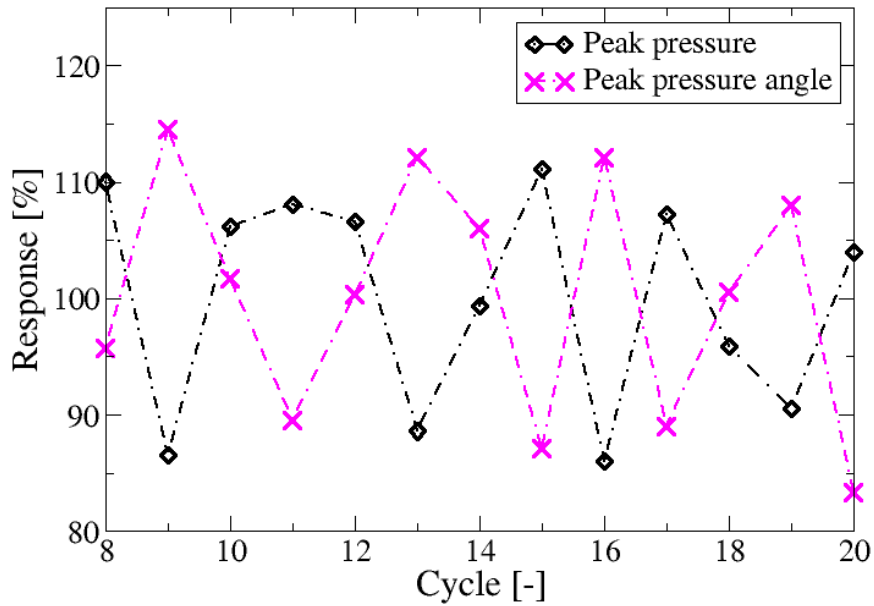


Figure 7.14: Peak pressure and its corresponding angle variations normalised by the averaged values

Fig. 7.14 presents the evolution of these two criteria during all cycles. The peak pressure in percentage, compared to its mean value, is plotted in dashed black line with diamonds and its corresponding angle in percentage, also compared to its mean peak pressure angle, is presented with the magenta dashed line with crosses. This figure points out that the probability to meet two consecutive slow or fast cycles is almost equal to zero. Indeed, the trend is to alternate slow and fast cycles, where a moderate cycle can be found in between these extreme cycles. The moderate cycles identified are, the cycle C13 which could have been identified as a fast cycle if the analysis were only based on the peak pressure, C14 and C18 which both have a peak pressure close to the average peak pressure.

Vars . / Cycle [-]	C09	C10	C11	C12	C13	C14	C15	C16	C17	C18
Peak pressure [bar]	7.20	8.84	8.99	8.87	7.73	8.27	9.25	7.16	8.93	7.89
Mean burnt gases mass fraction of cycle N+1 [-]	0.103	0.147	0.123	0.140	0.104	0.126	0.154	0.124	0.155	0.133

Table 7.5: Peak pressure and residual burnt gases mass fraction met in the following cycle

Tab. 7.5 shows that a high peak pressure comes with a high residual burnt gases mass fraction in the following cycle. Indeed, burnt gases have to be exhausted during the scavenging phase, which is not as efficient as expected. Consequently, it is observed in this operating point that the higher peak pressure of the previous cycle, the larger the residual burnt gases mass fraction is.

Cycle [-]	Peak pressure [bar]	Peak pressure angle [deg]	Mean kinetic energy [$\text{m}^2 \cdot \text{s}^{-2}$]	Mean equivalence ratio [-]	Mean burnt gases mass fraction [-]
08	9.16	182.51	96.26	1.18	0.151
11	8.99	179.78	96.76	1.25	0.147
12	8.87	184.55	86.66	1.24	0.123
15	9.25	178.68	84.77	1.21	0.126
17	8.93	179.61	89.74	1.23	0.124
20	8.65	177.02	82.60	1.24	0.107

Table 7.6: Fastest cycles peak pressure, its corresponding angle and the considered averaged variables on the combustion chamber volume at spark timing

Tabs 7.6 and 7.7 presents all the fastest and the slowest cycles and the variables averaged within the combustion chamber at spark timing, which are the resolved kinetic energy, the equivalence ratio and the residual burnt gases mass fraction. According to these tables, the resolved kinetic energy seems to be the main variable which drives the speed of the combustion, while the mean equivalence ratio and the residual burnt gases mass fraction seems to have a lesser effect.

Cycle [-]	Peak pressure [bar]	Peak pressure angle [deg]	Mean kinetic energy [$\text{m}^2 \cdot \text{s}^{-2}$]	Mean equivalence ratio [-]	Mean burnt gases mass fraction [-]
09	7.20	190.85	58.53	1.32	0.164
13	7.73	189.78	52.07	1.20	0.140
16	7.16	189.61	56.55	1.26	0.154
19	7.53	187.95	59.59	1.23	0.133

Table 7.7: Slowest cycle peak pressure, its corresponding angle and the considered averaged variables on the combustion chamber volume at spark timing

In order to visualise this trend, three consecutive cycles, namely the cycle C16, C17 and C18 are analysed. Tab. 7.8 summarizes the quantities evaluated here on these 3 cycles and also the previous cycle C15 and the following cycle C19. Consequently, the studied cycles set is made of one fast cycle C15, the first cycle analysed here, namely the C16 which is slow, the cycle C17 which is fast, the cycle C18 which is moderate and the last one, C19 which is slow and not analysed.

Cycle [-]	Peak pressure [bar]	Peak pressure angle [deg]	Mean kinetic energy [$\text{m}^2 \cdot \text{s}^{-2}$]	Mean equivalence ratio [-]	Mean burnt gases mass fraction [-]
15	9.25	178.68	84.77	1.21	0.126
16	7.16	189.61	56.55	1.26	0.154
17	8.93	179.53	89.74	1.23	0.124
18	7.98	184.64	61.06	1.24	0.155
19	7.53	187.95	59.59	1.23	0.133

Table 7.8: Analysis on the three consecutive cycles C16, C17 and C18

The visualisation of the flame propagation on several consecutive cycles illustrates the cyclic variability encountered in the combustor. In Figs. 7.15 to 7.17, the flame front is represented by the black line on the medium cut plane of the chamber and by an iso-surface of the progress variable on the fresh gases side ($c = 0.10$) in the 3D view. The following figures present:

- On the upper left corner, the velocity fields in the vicinity of the spark plug on the medium cut plane,
- On the lower left corner, the equivalence ratio on the same cut plane,
- On the lower right corner, the laminar flame speed, again on the same cut plane,
- On the upper right corner, the 3D visualisation of the flame propagation, the intake and exhaust systems and the carburation chamber upstream the combustor (here on the left).

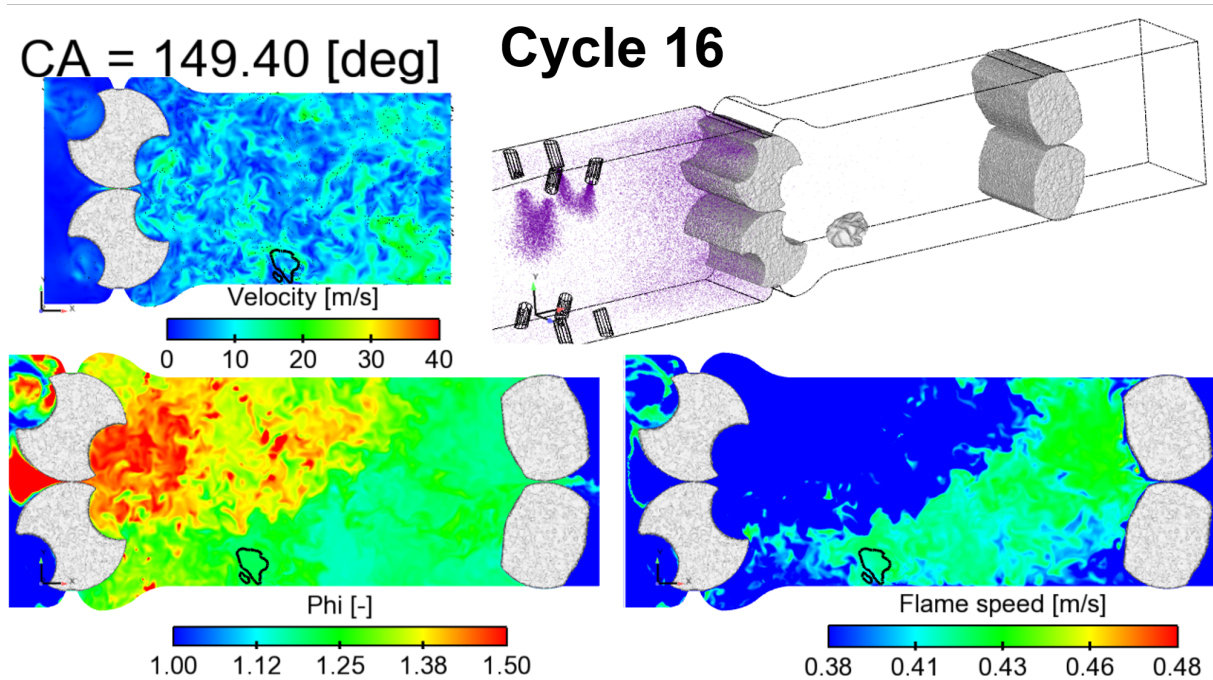


Figure 7.15: Cycle 16 flame propagation 9.40 CAD after the spark timing

Fig. 7.15 presents a very slow flame propagation. According to Tab. 7.8 the resolved kinetic energy of $56.55 \text{ m}^2 \cdot \text{s}^{-2}$ is significantly lower than the average of $73.06 \text{ m}^2 \cdot \text{s}^{-2}$, which is visible on the velocity field on the top left corner. In this cycle, the velocity meets values close to 20 m/s in some zones but the global trend is that this velocity is significantly lower than 10 m/s. The mean equivalence ratio of 1.26 is close to the average of 1.24. The heterogeneities in the median cut plane are quite significant since the equivalence ratio near the intake system reaches values up to 1.50 whereas at the exhaust, this quantity is close to 1.18. These disparities on the equivalence ratio significantly change the laminar flame speed, especially in very rich zones, where it decreases by 11.6 % compared with the mean value of 0.43 m/s. In addition, the mean residual burnt gases mass fraction of 0.154 is quite higher than the mean value of 0.130. In this cycle, these quantities near the spark plug seem better than in the remainder of the chamber which leads to a moderate flame kernel expansion. However, the analysis realised in the combustor shows that the flame will meet gases properties far from being favourable to a fast combustion.

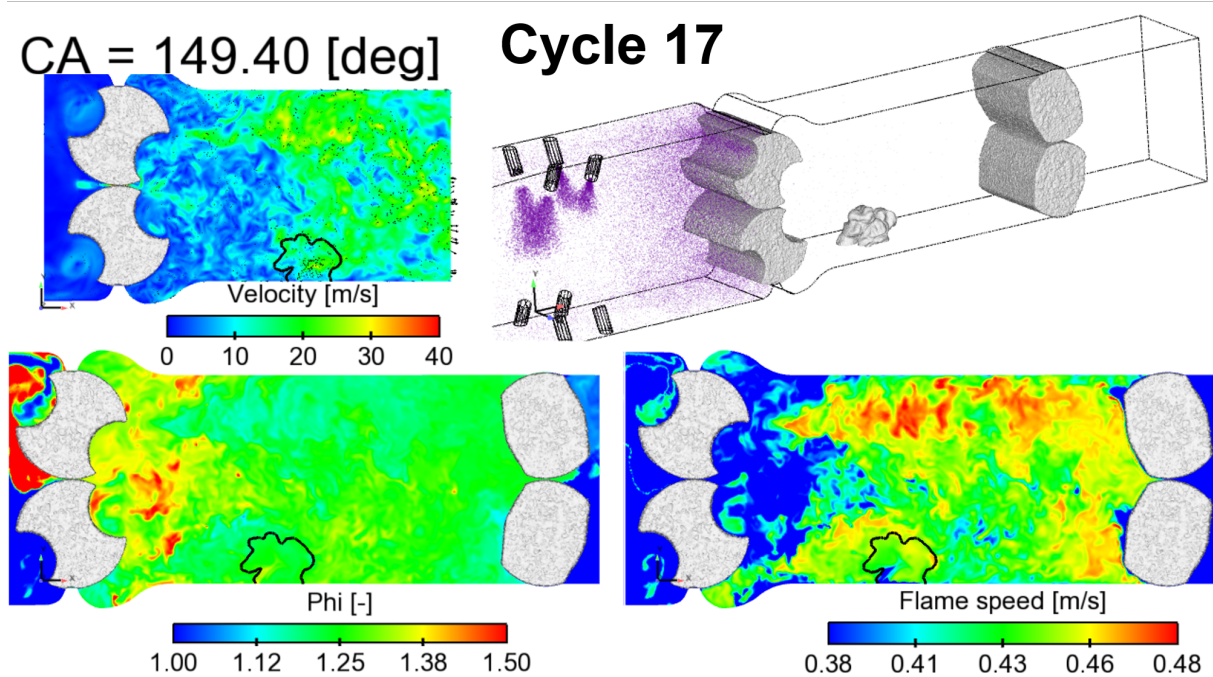


Figure 7.16: Cycle 17 flame propagation 9.40 CAD after the spark timing

The cycle 17 presented in Fig. 7.16 is a fast cycle. Tab. 7.8 shows that the peak pressure of 8.93 bar is reached at 179.53 CAD. Contrary to the previous cycle, the mean resolved kinetic energy of $89.74 \text{ m}^2 \cdot \text{s}^{-2}$ is far higher than the average of $73.06 \text{ m}^2 \cdot \text{s}^{-2}$, which is easily seen on the velocity fields where values up to 30 m/s are encountered. The heterogeneities on the equivalence ratio visible near the intake system are lower than the previous cycle even if a rich zone between 1.35 and 1.5 is clearly identified. The mean equivalence ratio in the chamber is 1.23 which is just below the average value of all the cycles. Last but not least, the mean residual burnt gases mass fraction is 0.124 since the previous cycle does not reach a high peak pressure (Tab. 7.5). Therefore, the laminar flame speed near the spark plug and in almost the whole of the domain is higher than 0.43 and close to 0.48 in some zones.

As a result, the flame kernel expands in a flow with higher velocity and therefore higher turbulent intensity than in the previous cycle, which is prone to fast propagation. Moreover, the flame will meet favourable conditions during its growth. These conditions lead to a fast cycle.

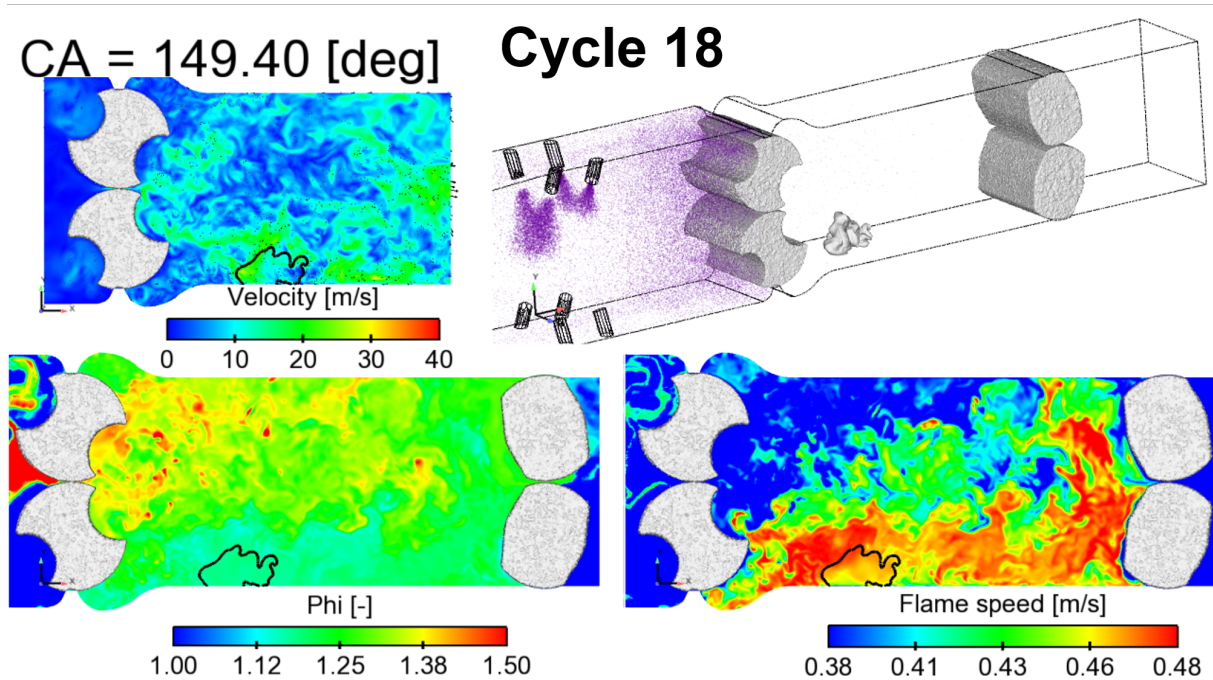


Figure 7.17: Cycle 18 flame propagation 9.40 CAD after the spark timing

Cycle 18 is a moderate cycle and is presented in Fig. 7.17. According to Tab. 7.8 the weakness of this cycle is due to the lack of kinetic energy. Indeed, the mean resolved kinetic energy is of $61.06 \text{ m}^2 \cdot \text{s}^{-2}$ and thus below the average value of $73.06 \text{ m}^2 \cdot \text{s}^{-2}$. This lower value of the resolved kinetic energy between cycles C17 and C18 is clearly visible on the velocity field where large zones below 10 m/s are visible. The equivalence ratio field is strongly stratified. In the bottom of the chamber, the equivalence ratio evolves in the range between 1.12 and 1.25. In the upper part of the chamber and close to the intake system, the equivalent ratio is slightly higher and ranges between 1.25 and 1.38. In this part of the chamber, some spots reach values up to 1.50. The residual burnt gases mass fraction of 0.155 is quite high. The heterogeneities of the equivalence ratio added to the high residual burnt gases mass fraction lead to a large range of laminar flame speed, which goes from 0.38 m/s in rich zones up to 0.48 in the lower part of the chamber. The spark ignition occurs in a region where previous variables seems favourable to the flame kernel expansion, that is why the flame expansion looks like the fast cycle C17 after 9.40 CAD. However, both the velocity and the laminar flame speed will soon meet gases conditions closer to the slow cycle C16. Consequently, this cycle reaches peak pressure of 7.89 bar, which is moderately lower than the average peak pressure of 8.32 bar at a crank angle of 184.64 CAD, which is also close to the average value of 184.41.

=====

Conclusion:

=====

This part shows that the kinetic energy strongly drives the peak pressure and its corresponding angle. Moreover, heterogeneities of the equivalence ratio and thus the laminar flame speed also impact the efficiency of the combustion but with a lower effect. According to the visualisation of the different fields, the combustion in this chamber is alternating between slow and fast cycles. In fact, a considered cycle is clearly impacted by the previous one. The high peak pressure seems to generate a large residual burnt gases mass fraction in the following cycle.

7.4.2 Peak pressure of consecutive cycles

In this paragraph the maximum pressure of cycle N+1 is plotted as a function of the previous maximum pressure.

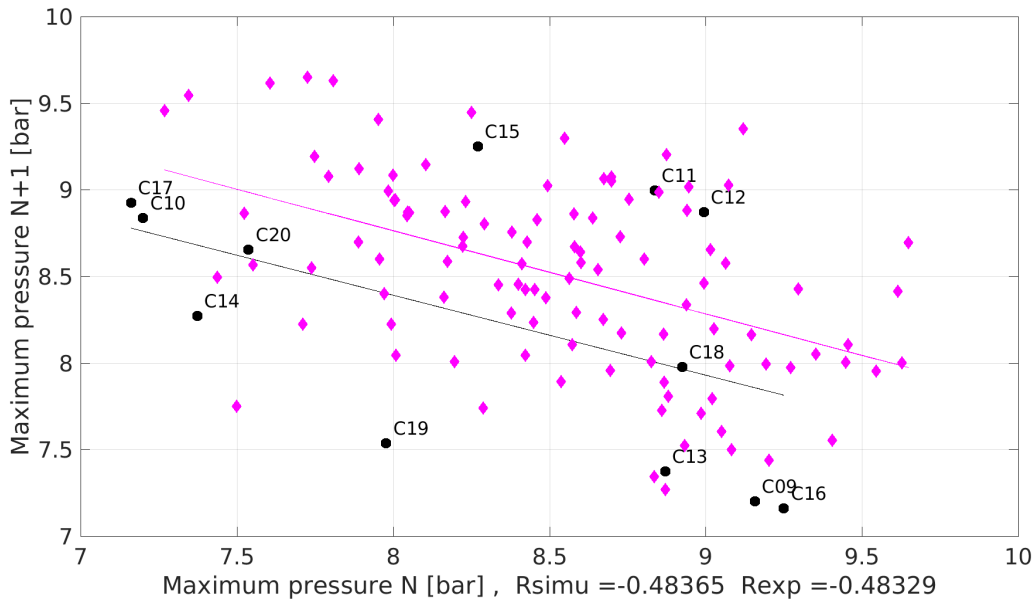


Figure 7.18: Peak pressure correlation between a cycle N+1 and the previous cycle N

Fig.7.18 shows both experimental and LES results. In this graph, the LES seems to mainly cover all the experimental findings but the numerical study lacks cycles to predict moderate consecutive cycles with a maximum pressure of 8.5 bar. The Bravais-Pearson correlation coefficient between the cycle N+1 and cycle N is in both experiment and simulation close to $R = -0.48$. However, the peak pressure of the simulation is mainly 0.35 bar lower than the experiment which was previously exposed in section 7.3.2.

7.4.3 Single regression analysis

The 2D and 3D visualisations of the thermodynamic variables can help to link them with each other. But to distinguish the main variables responsible for this variability accurately, the correlation between these variables and the main responses of the combustion process are all studied here. The considered responses are:

- The maximum pressure encountered during the combustion process called "P max" and its corresponding angle "Angle P max",
- The crank angle at which the mass fraction of the burnt fuel reaches values of 2%, 10% and 50%. They are called in the following paragraph: "CA 02", "CA 10" and "CA 50" or CA XX for all crank angles. CA 02 is representative of the ignition phase while CA 50 corresponds to the fully turbulent propagation.
- The mean pressure of the cycle integrated during the whole cycle and called "P mean" and calculated as in Eq. (7.1).

$$P_{mean} = \frac{\int^{cycle} P dt}{\int dt} \quad (7.1)$$

The quantification of the correlation uses the Bravais-Pearson correlation coefficient R defined by:

$$R = \frac{\sigma_{xy}}{\sigma_x \sigma_y} \quad (7.2)$$

Where σ_{xy} is the covariance of variables x and y , and σ_x and σ_y their standard deviations. A value of $|R|$ close to 1 indicates that x and y are perfectly linearly correlated, whereas a value of 0 implies that both variables are not correlated. Moreover the sign of R indicates the sign of slope of the regression line.

First of all the Bravais-Pearson correlation coefficient of all the responses are presented in Tab. 7.9. This table shows that all the responses are significantly correlated with each other. Moreover, this table presents the minimum, maximum, mean and the standard deviation of all responses and highlights the strong variability encountered in this combustor.

Resp. / Resp.	P max [bar]	Angle P max [deg]	CA 02 [deg]	CA 10 [deg]	CA 50 [deg]	P mean [bar]
Min(x)	7.16	177.02	151.13	155.23	163.53	3.90
Max(x)	9.26	190.85	158.03	164.64	177.08	4.85
Mean(x)	8.32	184.4	154.05	159.53	170.71	4.40
σ_x	0.68	3.77	1.63	2.37	3.66	0.30
P max	1.000	-0.846	-0.849	-0.854	-0.863	0.988
Angle P max	-0.846	1.000	0.925	0.945	0.976	-0.862
CA 02	-0.849	0.925	1.000	0.987	0.961	-0.882
CA 10	-0.854	0.945	0.987	1.000	0.987	-0.890
CA 50	-0.863	0.976	0.961	0.987	1.000	-0.896
P mean	0.988	-0.862	-0.882	-0.890	-0.896	1.000

Table 7.9: Bottom block of the table: correlation coefficients R between different considered response variables

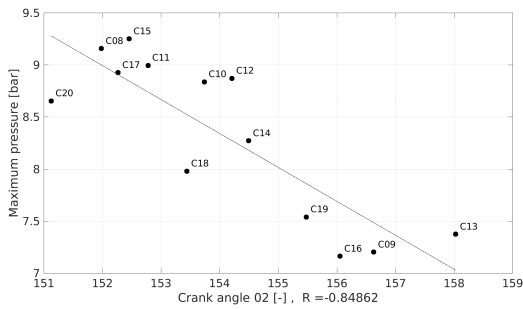


Figure 7.19: Correlation between the maximum pressure and the CA 02

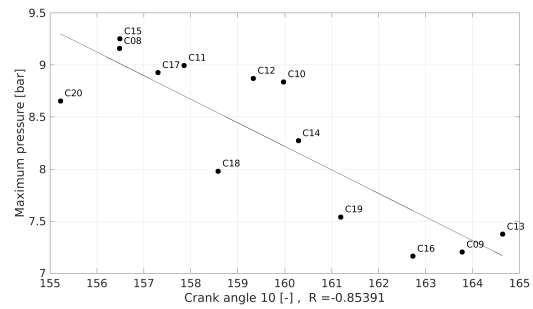


Figure 7.20: Correlation between the maximum pressure and the CA 10

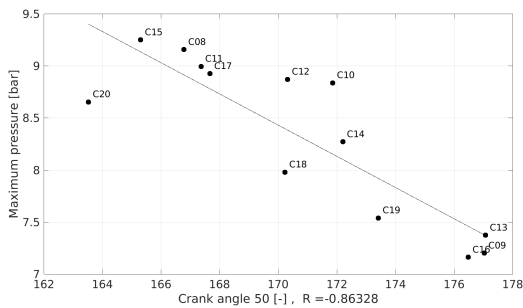


Figure 7.21: Correlation between the maximum pressure and the CA 50

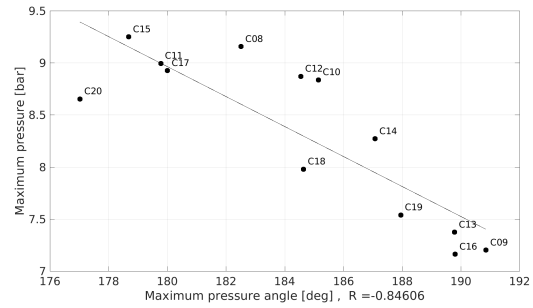


Figure 7.22: Correlation between the maximum pressure and the peak pressure angle

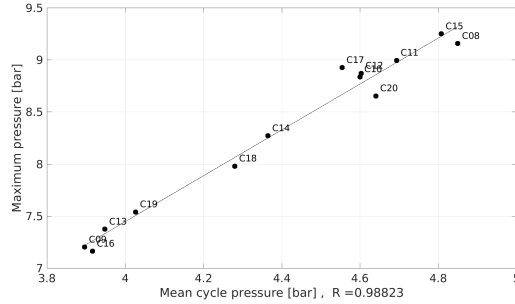


Figure 7.23: Correlation between the maximum pressure and the mean pressure of the cycle

According to Tab. 7.9, all responses are strongly correlated with each other. Therefore, only the single regression analysis on the maximum pressure is presented. The maximum pressure is then plotted as a function of all other responses separately, which results are presented in Figs. 7.19 to 7.23. In the following paragraphs, the Bravais-Pearson correlation coefficients between the different variables and the maximum pressure higher than 0.3 are presented.

The local and global variables correlated with the maximum pressure are studied. Then, variables averaged on the flame front are presented.

7.4.3.1 Local and global thermodynamic variables

Here only local and global variables with a Bravais-Pearson correlation coefficient higher than 0.3 are presented. These variables are:

- The mean kinetic energy in the combustion chamber at spark timing (Kinetic energy),
- The mean residual burnt gases mass fraction in the combustion chamber at spark timing (Y resid. BG),
- The mean equivalence ratio in the combustion chamber at spark timing (Mean EQ. RA.),
- The average velocity amplitude at the spark plug between 141 and 142 CAD (U norm SP 141-142),
- The velocity along the x-axis at the spark plug at spark timing. This velocity is positive if the flow field is oriented from the intake system to the exhaust system (U_x SP).

Resp. / Var.	Kinetic energy [m ² .s ⁻²]	Y resid. BG [-]	Mean EQ. RA. [-]	U norm SP 141-142 [m/s]	Ux SP [m/s]
Min(x)	52.073	0.103	1.177	5.631	-22.242
Max(x)	96.758	0.164	1.32	21.777	16.630
Mean(x)	73.065	0.130	1.24	13.250	-5.784
σ_x	15.143	0.017	0.024	4.693	10.681
P max	0.868	-0.399	-0.395	0.377	-0.315
Angle P max	-0.825	0.379	0.363	-0.348	0.137
CA 02	-0.799	0.418	0.303	-0.357	0.296
CA 10	-0.805	0.414	0.408	-0.411	0.313
CA 50	-0.822	0.398	0.429	-0.397	0.243
P mean	0.868	-0.381	-0.417	0.416	-0.362

Table 7.10: Bottom block of the table: correlation coefficients R of local and global variables

Tab. 7.10 presents the correlation coefficients of global variables averaged on the whole combustion chamber at spark timing which are the mean kinetic energy, the mean residual burnt gases mass fraction, the mean equivalence ratio and local variables near the spark plug position namely the velocity amplitude averaged between 141 and 142 CAD and the axial velocity at spark timing with all considered responses. For each variable, the absolute value of the correlation coefficients with all responses are significantly the same. That is why, only the results of the maximum pressure function of variables are presented here.

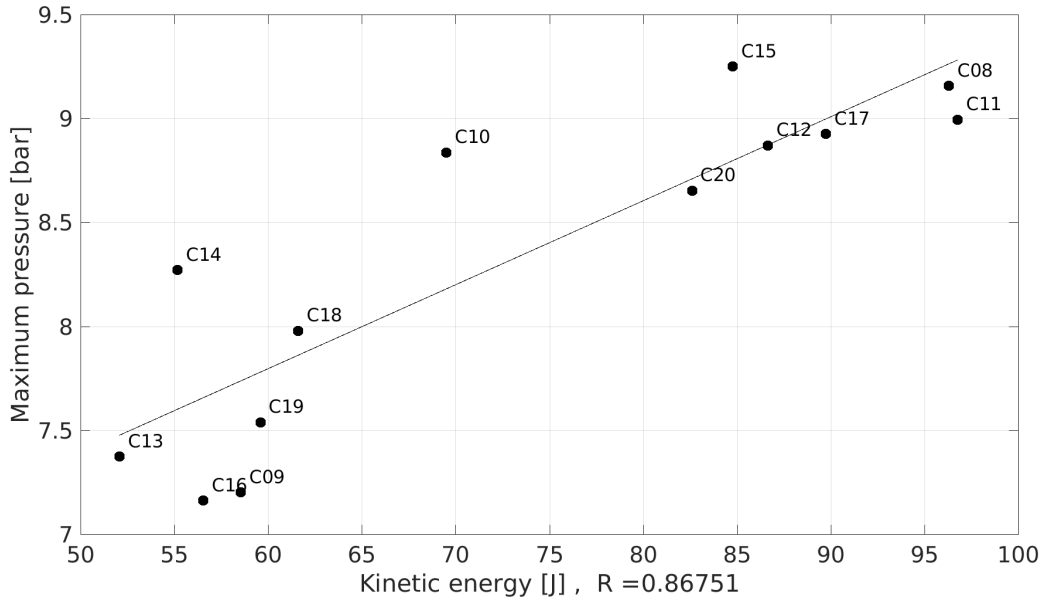


Figure 7.24: Correlation of the maximum pressure with the mean kinetic energy correlation at spark timing

According to Tab. 7.10 and Fig. 7.24, the maximum pressure and other responses are strongly correlated with the mean kinetic energy in the combustion chamber at spark timing since correlation coefficients are close to an absolute value of 0.8. Fig. 7.24 high-

lights two zones which correspond to slow and fast cycles. On the one hand, cycles with a mean kinetic energy lower than $65 \text{ m}^2/\text{s}^2$, on the left-bottom corner, do not reach a peak pressure higher than the average of 8.32 bar. On the other hand, cycles with a mean resolved kinetic energy higher than $80 \text{ m}^2/\text{s}^2$, on the right-top corner, reach a maximum pressure higher than 8.6 bar. In our simulations, values in between 60 and $80 \text{ m}^2/\text{s}^2$ seem rare since only cycle C10 is at $70 \text{ m}^2/\text{s}^2$. As presented in section 7.4.2, the simulations seem to lack cycles to be able to completely represent the experiment.

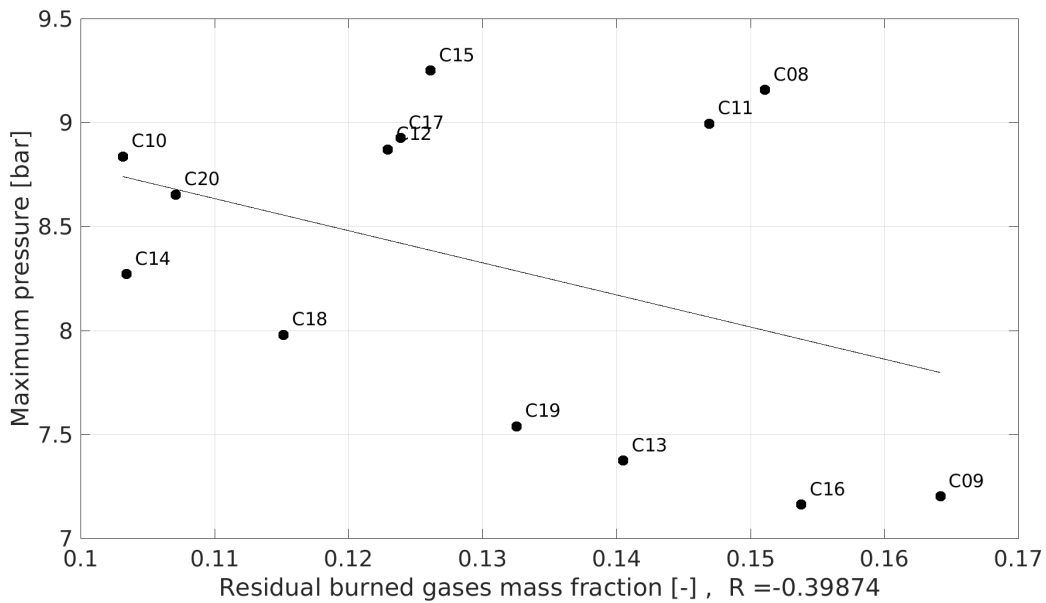


Figure 7.25: Correlation of the maximum pressure with the mean residual burnt gases mass fraction at spark timing

As shown in Tab. 7.10 the mean residual burnt gases mass fraction at spark timing is also one variable correlated to all responses. Indeed, all correlation coefficients are close to a value of $+/- 0.4$. As shown in Fig. 7.25, the global trend is that a high mean value of the residual burnt gases mass fraction at spark timing reduces the maximum pressure reached at the end of the combustion. However, specific cases like cycles C08 and C11 seem quite independent of the mean residual burnt gases mass fraction in the combustor, since they reach a peak pressure higher than 9 bar although their mass fractions are near 0.15. Consequently, the mean residual burnt gases in the combustion chamber at spark timing is an interesting way to control the combustion efficiency but it is not sufficient.

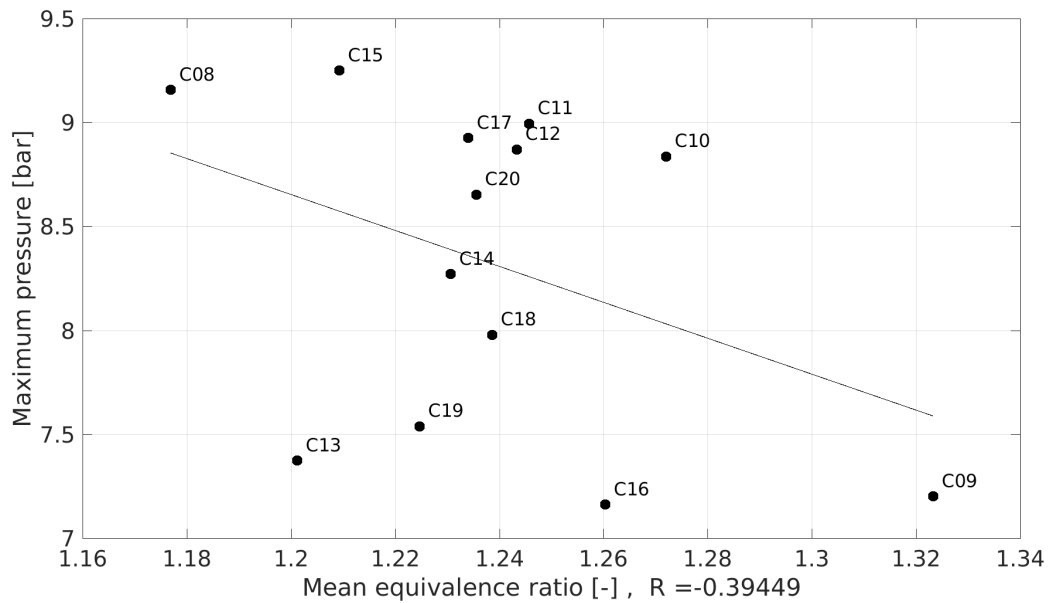


Figure 7.26: Correlation of the maximum pressure with the mean equivalence ratio at the spark plug at spark timing

Tab. 7.10 and Fig. 7.26 show that the mean equivalence ratio in the combustor at spark timing is also correlated with all considered responses, since Bravais-Pearson correlation coefficients are close to ± 0.4 . In this operating point a rich mixture is used, therefore a cycle which encounters a mean equivalence ratio lower than 1.24 can reach faster combustion and thus higher peak pressure. However, with a correlation coefficient close to -0.4 , the mean equivalence ratio is not the only variable correlated with the peak pressure. Around the average value of 1.24, slow, moderate and fast cycles could be encountered. As shown in Fig. 7.26 and specially highlighted by cycle C13 and C19, a mean equivalence ratio below the 1.24 does not necessary imply a fast combustion.

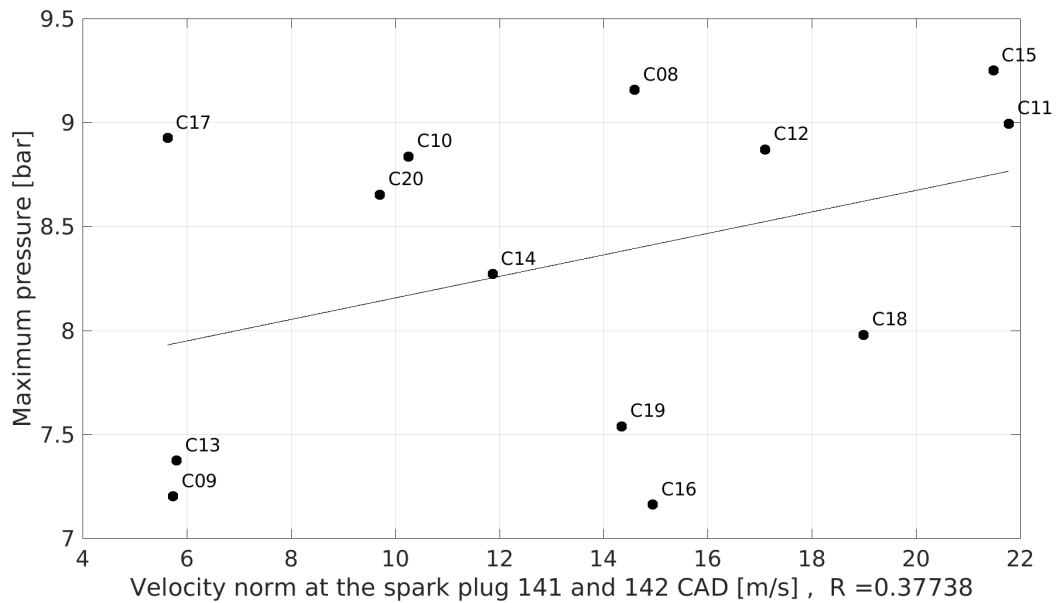


Figure 7.27: Correlation of the maximum pressure with the average velocity amplitude at the spark plug between 141 and 142 CAD

As highlighted in Tab. 7.10, the velocity amplitude at the spark plug at spark timing is also correlated to all responses. The velocity in the vicinity of the spark plug is known to be strongly linked to fast ignition, flame propagation or misfiring. Tab. 7.10 and Fig. 7.27 highlight that the velocity amplitude at the spark plug varies significantly between 5.6 up to 21.7 m/s, where this variability seems to contribute to either a slow or a fast combustion cycle. Here, with a reasonably high velocity magnitude at the spark plug at spark timing, the combustion seems faster but there are some exceptions in our simulations. Indeed, cycle C17, where the velocity amplitude is lower than 6 m/s, reaches a peak pressure close to 9 bar. On the contrary, in cycles C19 and C16 where the velocity amplitude at the spark plug at spark timing are higher than 14 m/s, reach a maximum pressure lower than 7.6 bar.

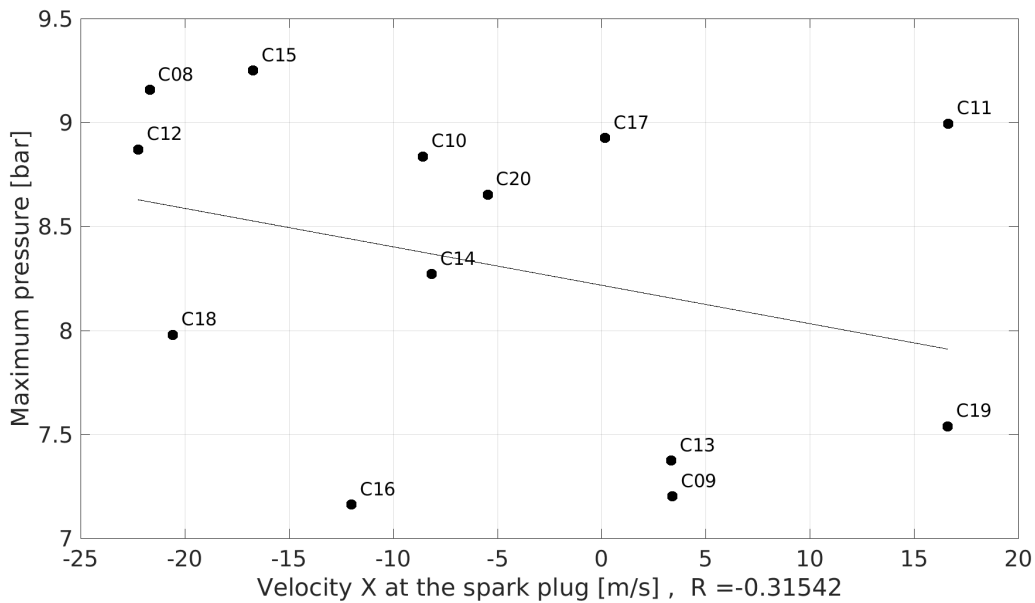


Figure 7.28: Correlation of the maximum pressure with the velocity along the x-axis at the spark plug at spark timing

Finally, the last local variable considered here is the axial velocity at the spark plug at spark timing. According to Tab. 7.10 and Fig. 7.28 the axial component of the velocity can also play a role in the efficiency of combustion. Indeed, the main information in Fig. 7.28 is that a negative value of the axial velocity could lead to faster combustion. In other words, this negative value of the axial velocity at the spark plug, which indicates that a flow field is oriented from the exhaust to the intake, slightly increases the peak pressure.

=====
Conclusion:
 =====

The study of local and global thermodynamic variables correlation shows that the efficiency of combustion in this configuration is mainly driven by the mean kinetic energy in the combustor at spark timing. However, other variables like the mean residual burnt gases mass fraction, the mean equivalence ratio and the velocity in the vicinity of the spark plug are also correlated to all responses. This first analysis brings up that a lot of variables have to be controlled so as to decrease the cycle-to-cycle variability.

7.4.3.2 Variable averaged on the flame front during the very first moments

The same kind of analysis is proposed here but this time on variables averaged on the flame front at a progress variable of 0.10. The variables which are correlated with all responses, with a correlation coefficient higher than 0.3 are the following:

- The subgrid scale velocity at the combustion filter size, as defined in Eq. (2.51), averaged on the flame front, between 140 and 145 CAD (u' F 140-145),
- The subgrid scale velocity at the combustion filter size, averaged on the flame front between 145 and 150 CAD (u' F 145-150),
- The subgrid scale velocity at the combustion filter size, averaged on the flame front between 140 and 150 CAD (u' F 140-150).

Resp. / Var.	u' F 140-145 [m/s]	u' F 145-150 [m/s]	u' F 140-150 [m/s]
Min(x)	0.371	1.225	0.878
Max(x)	1.521	2.834	2.210
Mean(x)	1.032	2.171	1.670
σ_x	0.234	0.375	0.309
P max	0.640	0.665	0.671
Angle P max	-0.703	-0.839	-0.838
CA 02	-0.759	-0.877	-0.863
CA 10	-0.759	-0.857	-0.852
CA 50	-0.712	-0.831	-0.828
P mean	0.669	0.723	0.721

Table 7.11: Bottom block of the table: correlation coefficients R of averaged variables

According to Tab. 7.11, the subgrid scale velocity at the combustion filter size, which modeling is based on the resolved velocity gradient tensor, is strongly correlated to all responses. Here, only the regression of the maximum pressure function of this subgrid scale velocity seen by the flame front averaged between 145 and 150 CAD is presented.

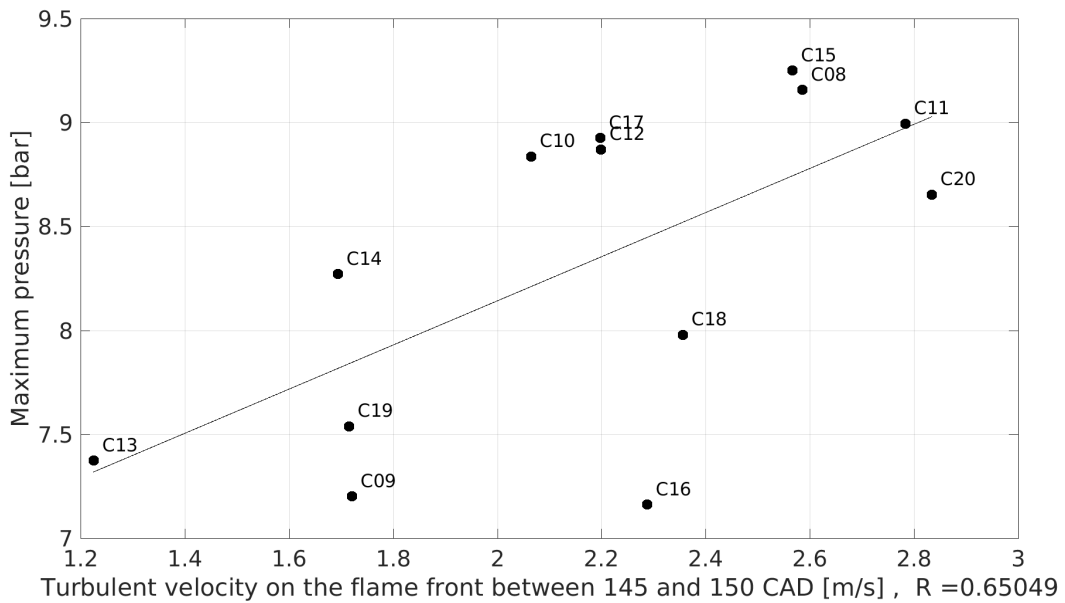


Figure 7.29: Correlation of the maximum pressure with the subgrid scale velocity seen by the flame front averaged between 145 and 150 CAD

Fig. 7.29 shows that the maximum pressure is strongly correlated to mean subgrid scale velocity at the combustion filter size, seen by the flame front and averaged between 145 and 150 CAD. Indeed, the higher the subgrid scale velocity at the combustion filter size, the quicker the flame surface will increase and the combustion will become faster due to the unresolved strain presented in Eq. 2.88.

=====

Conclusion:

=====

The single regression analysis realised on variables seen by the flame front shows that the main variable correlated to the peak pressure, is the subgrid-scale velocity at the combustion filter size, which has a correlation coefficient with the peak pressure higher than 0.65.

7.4.4 Multidimensional data analysis

The single correlation is able to find out the key variables here correlated to the peak pressure, its corresponding angle, the different CA degrees and the mean pressure of the cycle. However, this method reaches its limits when several variables act simultaneously as in this configuration. Even if some variables are strongly correlated to the chosen responses, the complexity of the configuration makes it difficult to clearly identify the most important factor and obtain relevant correlation coefficients. In order to improve the analysis, a multivariate regression model presented by Truffin *et al.* [53] is used. In this approach, a relationship between the dependant responses $RESP(n)$, where n is the number of cycles, is explicitly estimated using a set of independent parameters or variables $X_i(n)$. The creation of the responses $RESP(n)$ model follows these different steps:

1. First the necessary condition for selecting the X_i among all the possible parameters is that the X_i vectors are non collinear, and that $n > p + 1$, where p is the number of variables. These variables may be defined based on a correlation analysis between each available variables X_i in order to determine whether quantities are collinear or not.
2. The matrix equation system $RESP(n) = \sum_{i=1}^p \beta_i X_i(n) + \epsilon(n)$ is solved using a least-squares fit which provides the constant slopes β_i and the residuals of the equation. They are normalised by their mean value to avoid that any variable has a larger impact due to its scale.
3. The degree of correlation between X_i and the response $RESP$ is examined by calculating the coefficient of correlation between X_i and $RESP - \sum_{k \neq i}^p \beta_k X_k$, thus discarding the contribution of the other variables.
4. The degree of correlation between $RESP$ and the resulting model $\sum_{i=1}^p \beta_i X_i(n) + \epsilon(n)$ is examined. A correlation coefficient $|R|$ greater than 0.7 is usually considered as a strong correlation.
5. If the contribution of variable X_i is not significant in the resulting model (typically $|R_{XY}| < 0.4$), then it is suppressed from the equation and step (2) is repeated. If several sets of variables can be identified, steps (1) to (3) are performed with each of them to find the most relevant one, providing the final, best fitting model.

According to section 7.4.3, all responses are strongly correlated with each other, therefore only the models for the peak pressure, its corresponding angle are presented here. The analysis proposed here consists in comparing the single regression correlation coefficients of different variables to the correlation coefficients obtained with the multivariate regression proposed by Truffin *et al.* [53] and analysing whether or not some new variables seem correlated to the considered responses.

7.4.4.1 Maximum pressure

The first response studied here is the maximum pressure which must be as high as possible to improve the efficiency of the propulsive system. The multivariate regression provides the four main independent variables which have a non negligible influence on the variation of the peak pressure:

- The mean resolved kinetic energy in the combustor at spark timing (Kinetic energy),
- The mean laminar flame speed on the flame front between 140 and 141 CAD (SI F 140-141),
- The resolved velocity amplitude at the spark plug at spark timing (U norm SP)
- The resolved velocity along the z-axis at the spark plug at spark timing. This velocity is positive if the flow field is oriented from the right to the left side of the chamber while looking from the exhaust of it. In previous velocity fields analysis, this velocity is normal to the visualisation window and point toward the reader (Uz SP).

Variables	Min(x)	Max(x)	Mean(x)	σ_x	R single reg.	R multivar. reg.
Kinetic energy [m ² .s ⁻²]	52.073	96.758	73.065	15.143	0.868	0.951
SI F 141-142 [m/s]	0.456	0.664	0.542	0.046	0.199	0.884
U norm SP [m/s]	6.83	23.49	14.72	5.66	0.262	0.540
Uz SP [m/s]	-12.82	6.70	-1.19	2.64	0.236	0.369

Table 7.12: Statistics of the variables correlated to the maximum pressure and the corresponding correlation coefficients R of both the single regression and the multivariate regression approaches

Tab. 7.12 summarizes the main statistics of the 4 independent variables chosen to create the model of the maximum pressure. Only the resolved kinetic energy was clearly pointed out with the single regression analysis. The laminar flame speed of fresh gases, the velocity amplitude and the velocity along the z-axis were not considered in the previous analysis since their correlation coefficients are lower than 0.3. In this model, all correlation coefficients are significantly higher than with the single regression analysis.

Fig. 7.30 presents the increase of the correlation coefficients obtained with the multivariate regression compared with the single regression analysis. This figure clearly emphasises that if variables are discarded from other variable contributions, the correlations with the maximum pressure are very strong. With this approach, the kinetic energy, the laminar flame speed in fresh gases and the velocity amplitude and the velocity along the z-axis at the spark plug position at spark timing are the key variables to increase so as to reach a higher maximum combustion pressure. According to this graph, the mean resolved kinetic energy which can increase the flame wrinkling by the large scales and the velocity near the spark plug, which can improve the first flame kernel. This observation highlights that the "number one" key in this type of configuration is to control the aerodynamics within the combustor by optimising the scavenging and the spark plug position. However the flame quenching is not considered here. Previous studies on this subject, among them the analysis of Labarrere *et al.* [84], which highlights that the velocity in the vicinity of the spark plug may not exceed a magnitude of 25-30 m/s in order to avoid the quenching

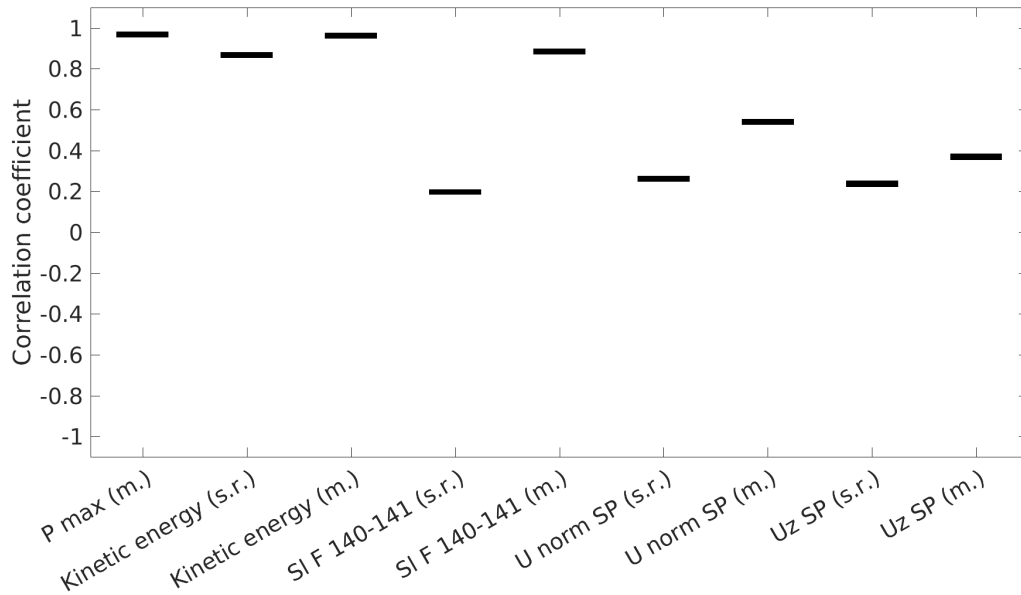


Figure 7.30: Maximum pressure correlation coefficients of the single regression (s.r.) and the multivariate regression model (m.)

of the first kernel. Here, the average velocity amplitude at the spark plug is 13 m/s (Tab. 7.10). This average velocity seems slightly overestimated as shown in section 7.3.2, probably because the spark plug geometry is not considered. The second strong lever is to increase the laminar flame speed computed as presented in section 2.4.2.5, which can be realised by the control of the fresh gases properties, namely the temperature, the pressure, the equivalence ratio and also the dilution gases. The multivariate regression analysis allows the identification of low dependent variables, which are strongly correlated with the peak pressure. These variables give an axis for improvement to reach higher maximum pressure at the end of combustion, which is mainly driven by the aerodynamics within the combustor and the efficiency of the scavenging phase. The control of both the aerodynamics and the scavenging phase leads to good repeatability of the velocity fields and the mixture composition encountered at spark timing.

7.4.4.2 Angle of the peak pressure

The same approach is realised on the angle of the peak pressure where the goal is to decrease as much as possible this value in order to shorten the combustion phase. According to the Tab. 7.10, the simulations give an averaged angle of 184.4 degrees and a standard deviation of 3.77 degrees. In order to improve this parameter the target is to reduce this angle. The multivariate analysis generates a model where 5 independent variables are found, they are:

- The subgrid scale velocity at the combustion filter size averaged on the flame front between 140 and 150 CAD ($u' F 140-150$),

- The mean residual burnt gases mass fraction in the combustion chamber at spark timing (Y resid. BG),
- The velocity along the x-axis at the spark at spark timing. This velocity is positive if the flow field is oriented from the intake system to the exhaust system (Ux SP),
- The resolved velocity along the z-axis at the spark plug at spark timing. This velocity is positive if the flow field is oriented from the right to the left side of the chamber while looking from the exhaust of it. In previous velocity fields analysis, this velocity is normal to the visualisation window and point toward the reader (Uz SP),
- The averaged equivalence ratio in a sphere of 1.5 mm radius around the spark plug between 140 and 141 CAD (VAR 2).

Variables	Min(x)	Max(x)	Mean(x)	σ_x	R single reg.	R model
u' F 140-150 [m/s]	0.877	2.210	1.671	0.309	-0.803	-0.954
Y resid. BG [-]	0.103	0.164	0.130	0.016	0.379	0.765
Ux SP [m/s]	-22.24	16.63	-5.78	10.68	0.137	0.742
Uz SP [m/s]	-12.82	6.70	-1.19	2.64	-0.139	-0.696
VAR 2 [-]	0.103	0.164	0.130	0.016	0.228	0.665

Table 7.13: Statistics of the variables correlated to the peak pressure angle and the corresponding correlation coefficients R of both the single regression and the multivariate regression approaches

Tab. 7.13 summarizes the main statistics of the 5 independent variables chosen to create the model of the maximum pressure angle. In the single regression analysis proposed in section 7.4.3, only variables with a Bravais-Pearson correlation coefficient higher than 0.3 are considered, thus only the subgrid scale velocity at the combustion filter size seen by the flame front and the mean residual burnt gases in the combustion chamber at spark timing could be identified. The multivariate regression analysis proposed here, allows to figure out the velocity components and the averaged equivalence ratio in a sphere of 1.5 mm radius around the spark plug between 140 and 141 CAD as variables strongly correlated to the peak pressure angle.

Fig. 7.31 shows the multivariate regression approach capability to separate variables from each other and point out its correlation with the peak pressure angle. Since the target here is to shorten the combustion phase, the negative correlation coefficients have to be as large as possible and positive correlation coefficients have to be as low as possible. The average subgrid scale velocity at the combustion filter size seen by the flame front between 140 and 150 CAD is the strongest variable to lower the peak pressure angle which can be raised by increasing the mean kinetic energy. The second variable pointed out by the model is the mean residual burnt gases mass fraction in the combustor at spark timing where the reduction of this quantity will lead to a lower peak pressure angle. The most efficient way to reach a residual burnt gases mass fraction is to improve the scavenging phase by firstly changing the shift crank angle between the intake and the exhaust systems or working on the aerodynamics of the combustor. The axial velocity is the first variable which was hardly identified by the single regression analysis. According to this figure, this velocity has to be as low as possible or clearly negative to improve the maximum pressure

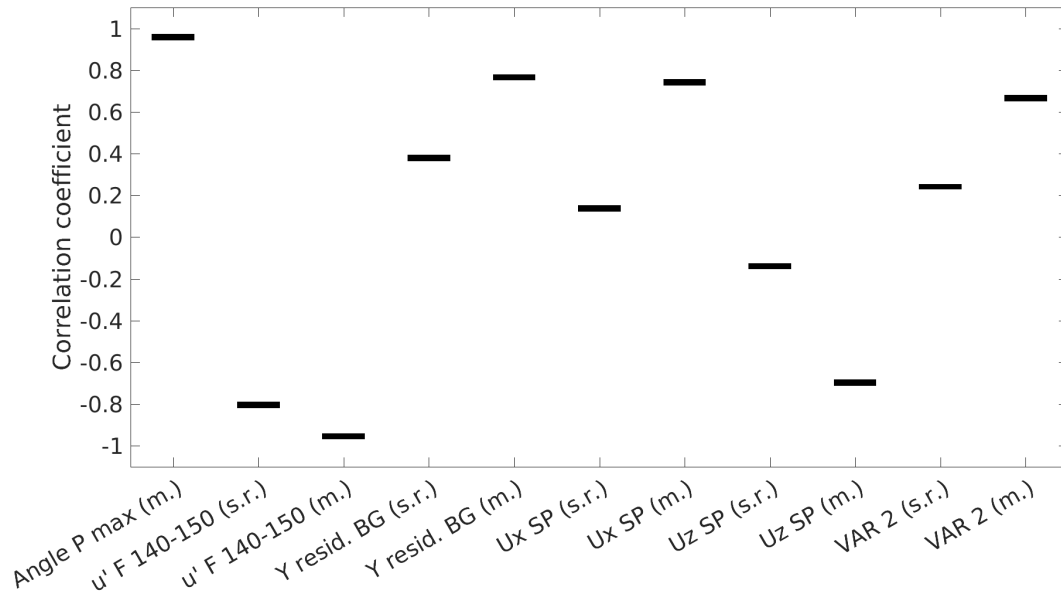


Figure 7.31: Peak pressure angle correlation coefficients of the single regression (s.r.) and the multivariate regression model (m.)

angle. The second component of the velocity at the spark plug position is the velocity on the z-axis. Here, this component has to be as strong as possible to move the initial flame kernel from the wall to the center of the combustion chamber and consequently decrease the peak pressure angle. The last but not the least variable figured out here is the averaged equivalence ratio in a sphere of 1.5 mm radius around the spark plug right after the spark timing. The average equivalence ratio is of 1.3, thus a reduction of this quantity down to the stoichiometric value, leads to better conditions for the flame kernel sustainability and its propagation.

7.4.5 Conclusion on the different levers to improve the combustion process

In order to analyse the cycle-to-cycle variability, both the single and multivariate regressions are proposed here. The single regression gives relevant local and global variables as much as averaged variables calculated on the flame front, where the absolute regression coefficients is above 0.3-0.8. In this kind of complex configuration, this type of analysis meets its limits since lots of parameters are acting simultaneously. Consequently, the multidimensional analysis is used to better identify the key variables, which might improve the performances of the combustor, control and reduce the cycle-to-cycle variability better. To conclude, the main parameters which require all the attention in the conception of CVC chambers are:

- The mean kinetic energy in the combustion chamber at spark timing which is one parameter to control the speed of the flame propagation,
- The velocity magnitude and its components which need to be as high as possible as long as the quenching of the flame kernel is avoided,

- The equivalence ratio around the spark plug and the chamber which needs to be as close as possible to the stoichiometric value,
- A low residual burnt gases mass fraction driven by an efficient scavenging phase.

Last but not least, the potential causes of the variability on these variables are analysed in the following paragraph.

7.4.6 Correlation of previous cycle variables with the cycle-to-cycle variability

The goal of this paragraph is to identify the variables of the previous cycle, which are correlated with the variables identified to be responsible for cycle-to-cycle variability. As presented in the previous paragraph, the scavenging phase needs to be optimised. This phase seems strongly influenced by the previous cycle, namely by the previous peak and mean pressure met in the combustor. The scavenging phase is preceded by the exhaust which is driven by the pressure difference of both sides of the exhaust system and thus has to be analysed. Moreover, the scavenging starts at the opening of the intake system where the flow is driven by the pressure difference on both sides of the intake system, whose impact is analysed here. To measure the influence of the previous cycle on the present cycle, the single regression correlation between the previous identified variables responsible for cycle-to-cycle variability and the following variables are examined:

- The maximum pressure of the previous cycle N-1 ($P_{\max} N-1$),
- The mean pressure of the previous cycle N-1 ($P_{\text{mean}} N-1$),
- The pressure difference between the combustion chamber and the exhaust pipe right after the opening of the exhaust system. The pressure difference is then calculated during the exhaust phase of the previous cycle at 20 CAD ($DP_{CC-EXH} 20$),
- The pressure difference between the carburation chamber and the combustion chamber at the opening time of the intake system, namely at 55 CAD ($DP_{IN-CC} 55$),
- The same kind of pressure difference between the carburation chamber and the combustion chamber at the beginning of the intake phase, namely at 65 CAD ($DP_{IN-CC} 65$).

Tab. 7.14 presents the statistics of the variables of the previous cycle which could influence the main variables responsible for a cycle-to-cycle variability and shows their single regression correlation coefficients with each other on the bottom right part of the table. According to this table, the maximum pressure of the previous cycle is strongly correlated with the mean pressure of the previous cycle ($R = 0.911$), therefore only the analysis on the mean pressure of the previous cycle is presented in the following paragraph. The pressure difference between the combustion chamber and the exhaust is not correlated with other quantities, that is why this pressure difference is analysed. Finally, the two pressure differences between the carburation chamber and the combustion chamber are significantly correlated with each other ($R = 0.890$), consequently only the analysis on the pressure difference at 55 CAD is shared here.

Resp. / Resp.	P max N-1[bar]	P mean N-1 [bar]	DP CC-EXH 20 CAD [bar]	DP IN-CC 55 CAD [bar]	DP IN-CC 65 CAD [bar]
Min(x)	7.16	3.90	1.14	1.53	1.60
Max(x)	9.26	4.85	2.15	1.65	1.80
Mean(x)	8.32	4.40	1.61	1.60	1.71
σ_x	0.68	0.30	0.25	0.15	0.16
P max N-1	1.000	0.991	-0.101	-0.295	-0.479
P mean N-1	0.991	1.000	-0.084	-0.340	-0.528
DP CC-EXH 20	-0.101	-0.084	1.000	-0.454	-0.192
DP IN-CC 55	-0.295	-0.340	-0.454	1.000	0.890
DP IN-CC 65	-0.479	-0.528	-0.192	0.890	1.000

Table 7.14: Bottom block of the table: correlation coefficients R between different variables

7.4.6.1 Correlation with the mean pressure of the previous cycle

In this paragraph, the aim is to measure how the mean pressure of the previous cycle influences the variables identified in sections 7.4.3 and 7.4.4. Like in section 7.4.3, only variables with a Bravais-Pearson correlation coefficient higher than 0.3 are presented which are:

- The mass in the combustion chamber at spark timing (Mass CC),
- The mean residual burnt gases mass fraction in the combustion chamber at spark timing (Y resid. BG),
- The average equivalence ratio on the flame front at 144 CAD (EQ.RA. F 144),
- The equivalence ratio at the spark plug at spark timing (EQ.RA. SP),
- The average equivalence ratio in a sphere of 1 mm around the spark plug at spark timing (Mean EQ.RA Sph 1 mm),
- The velocity amplitude at the spark plug at both the spark timing and between 140 and 141 CAD (U norm SP and U norm SP 140-141),
- The velocity along the y-axis at the spark between 142 and 143 CAD (U_y SP 142-143)

The correlation coefficient of the previous cycle mean pressure to these identified variables are presented in the following Tab. 7.15:

Tab. 7.15 points out that the residual burnt gases mass fraction and the mass in the combustion chamber are strongly driven by the mean pressure of the previous cycle since correlation coefficients obtained here are respectively $R = 0.800$ and $R = -0.609$.

Variables	Min(x)	Max(x)	Mean(x)	σ_x	R single reg.
Y resid. BG [-]	0.103	0.164	0.130	0.016	0.800
Mass CC [g]	3.89	4.85	4.39	0.301	-0.609
EQ. RA. F 144 [-]	1.116	1.356	1.204	0.039	0.301
EQ.RA SP [-]	1.119	1.361	1.204	0.041	0.341
Mean EQ.RA Sph 1mm [-]	1.119	1.361	1.206	0.045	0.319
U norm SP [m/s]	6.83	23.49	14.72	5.66	0.401
U norm SP 140-141 [m/s]	6.71	22.41	14.55	5.20	0.354
Uy SP 142-143 [m/s]	-5.87	6.27	-0.41	3.21	-0.429

Table 7.15: Statistics of the variables correlated with the previous mean pressure and the corresponding correlation coefficients R with a single regression approach

Vars. / Vars.	Y resid. BG [-]	Mass CC [g]	EQ. RA F 144 [-]	EQ.RA SP [-]	Mean EQ.RA Sph 1mm [-]
Y resid. BG [-]	1.000	-0.841	0.592	0.601	0.594
Mass CC [g]	-0.841	1.000	-0.510	-0.561	-0.589
EQ. RA. F 144 [-]	0.592	-0.510	1.000	0.978	0.967
EQ.RA SP [-]	0.601	-0.561	0.978	1.000	0.995
Mean EQ.RA Sph 1mm [-]	0.594	-0.589	0.967	0.995	1.000
U norm SP [m/s]	-0.011	0.091	-0.141	-0.136	-0.150
U norm SP 140-141 [m/s]	-0.054	0.112	-0.126	-0.117	-0.131
Uy SP 142-143 [m/s]	-0.440	0.148	-0.401	-0.448	-0.434

Table 7.16: Bottom block of the table: correlation coefficients R between different variables

Vars. / Vars.	U norm SP [m/s]	U norm SP 140-141 [m/s]	Uy SP 142-143 [m/s]
Y resid. BG [-]	-0.011	-0.054	-0.440
Mass CC [g]	0.091	0.112	0.148
EQ. RA. F 144 [-]	-0.141	-0.126	-0.401
EQ.RA SP [-]	-0.136	-0.117	-0.448
Mean EQ.RA Sph 1mm [-]	-0.150	-0.131	-0.434
U norm SP [m/s]	1.000	0.989	-0.384
U norm SP 140-141 [m/s]	0.989	1.000	-0.364
Uy SP 142-143 [m/s]	-0.384	-0.364	1.000

Table 7.17: Bottom block of the table: correlation coefficients R between different variables (following)

Moreover Tabs. 7.16 and 7.17 show that the residual burnt gases mass fraction and the mass in the combustion chamber are strongly correlated since their correlation coefficient is $R = -0.841$. The negative value of R specifies that a high residual burnt gases mass fraction leads to a low mass in the combustion chamber. In addition, these two variables are also correlated with different measured equivalence ratios since all absolute values of the correlation coefficient are in between 0.5 and 0.6. According to these tables, a strong previous cycle does not facilitate the exhaust of the high amount of burnt gases and thus, the filling of the combustion chamber with fresh air. Consequently, residual burnt gases are still trapped in the combustion chamber which results in a low mass in the combustion chamber. Last but not least, the liquid fuel which partially enters into the

chamber, evaporates more rapidly in a warmer flow which leads to a higher equivalence ratio at spark timing. In order to analyse these variables correlated with the previous mean pressure, only the study on the residual burnt gases mass fraction is presented here. According to Tabs. 7.15 and 7.17 the velocity amplitude at the spark plug and the velocity along the y-axis are correlated with both the previous cycle mean pressure and with each other, consequently only the analysis on the velocity amplitude at the spark plug position is presented here.

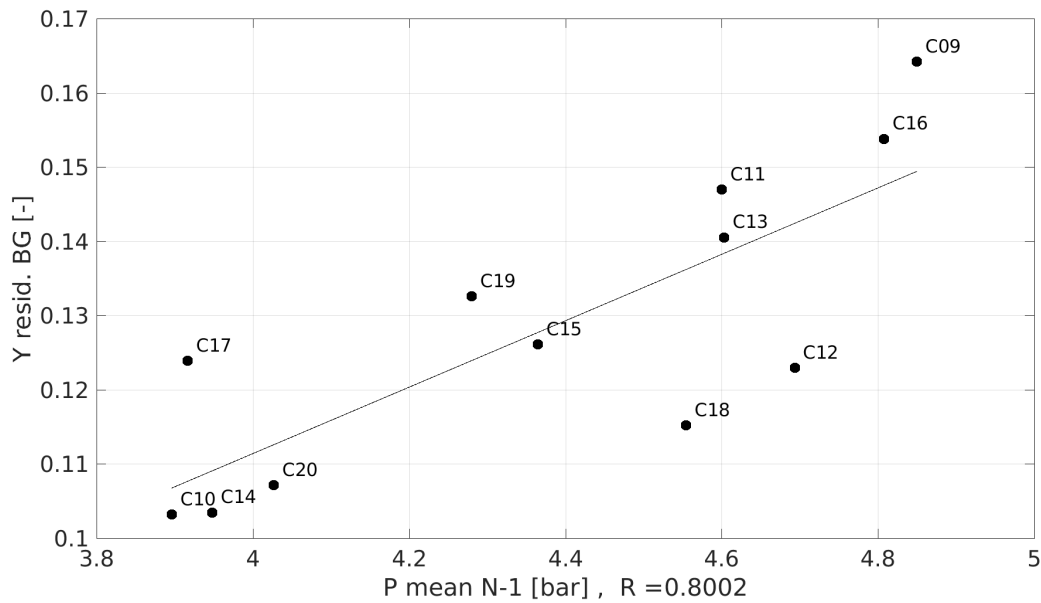


Figure 7.32: Correlation between the average residual burnt gases mass fraction in the combustion chamber at spark timing and the previous cycle mean pressure

The first variable analysed here is the average residual burnt gases mass fraction as a function of the previous cycle mean pressure and is presented in Fig. 7.32. This graph highlights the strong correlation between these two variables with a correlation coefficient of $R = 0.800$. According to Fig. 7.32 a strong previous mean pressure leads to the large residual burnt gases mass fraction, which in turn, decreases the probability of meeting a fast cycle as presented in sections 7.4.3 and 7.4.4. On the opposite, a slow previous cycle with a low mean pressure generates a low residual burnt gases mass fraction and consequently increases the probability of having a fast cycle. The variation is quite significant since, a fluctuation of 20 % of the previous cycle mean pressure results in a variation of around 35 % in the residual burnt gases mass fraction compared with the lower value.

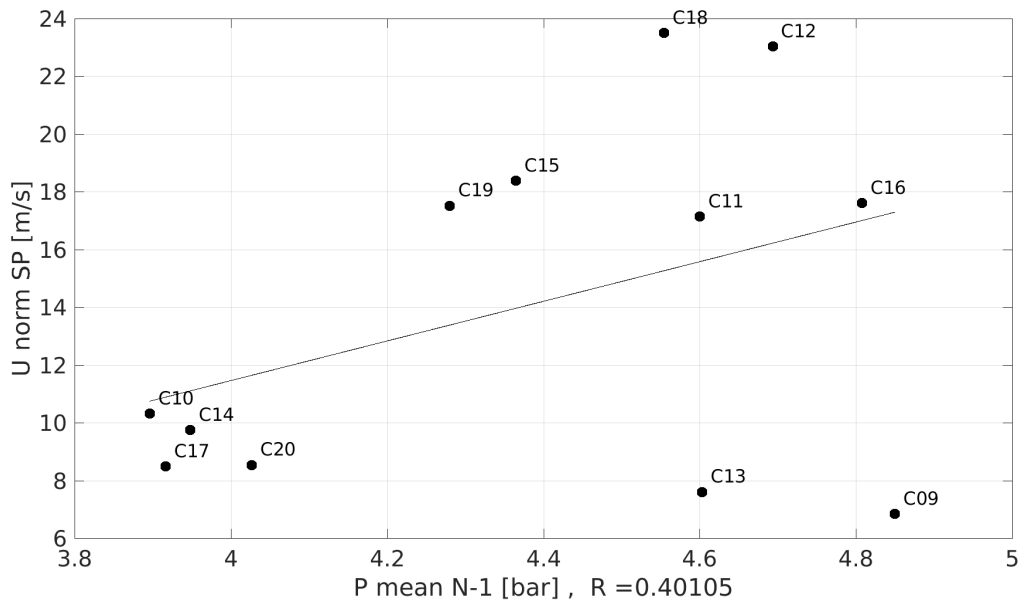


Figure 7.33: Correlation between the velocity amplitude at the spark plug at spark timing and the previous cycle mean pressure

The second variable correlated with the previous cycle mean pressure and presented in Fig. 7.33 is the velocity amplitude at the spark plug at spark timing. According to Tab. 7.17, the analysis made here can be extrapolated to the velocity amplitude at the spark plug between 140 and 141 CAD ($R = 0.989$) and to the velocity along the y-axis at the spark plug position between 142 and 143 CAD ($R = -0.384$).

The correlation between the velocity amplitude and the previous cycle mean pressure is lower than with the residual burnt gases mass fraction since the correlation coefficient is $R = 0.401$. Fig. 7.33 illustrates on the one hand, that a slow previous cycle with a mean pressure close to 4 bar leads to a velocity amplitude at the spark plug between 8 and 12 m/s. On the other hand, a fast previous cycle with a mean pressure higher than 4.6 bar might lead to the velocity amplitude at the spark plug higher than 16 m/s. In the studied simulated cycle, this correlation is not all the time verified since cycle C09 and C13 clearly show the opposite. The mean pressure of the previous cycle might be linked with the velocity amplitude generated by both the exhaust and the scavenging. These two steps are completed with the following analysis on the pressure difference on both sides of the exhaust and the intake systems presented in sections 7.4.6.2 and 7.4.6.3.

7.4.6.2 Correlation with the pressure difference at the exhaust system at 20 CAD

The second cause which can increase the variability in this apparatus, is the pressure difference on both sides of the exhaust system at 20 CAD, which starts to open at 157 CAD. The aim here is to identify how this pressure difference can influence the cycle-to-cycle variability. Like in section 7.4.3, only variables with a Bravais-Pearson correlation coefficient higher than 0.3 are presented, which are:

- The mass in the combustion chamber at spark timing (Mass CC),
- The mean resolved kinetic energy in the combustion chamber at spark timing (Kinetic energy),
- The velocity amplitude at the spark plug at spark timing (U norm SP),
- The velocity along the x-axis at the spark plug at spark timing (Ux SP),
- The velocity along the z-axis at the spark plug at spark timing (Uz SP),
- The velocity along the x-axis at the spark plug between 142 and 143 CAD (Ux SP 141-142),
- The velocity along the x-axis at the spark plug between 142 and 143 CAD (Ux SP 142-143).

The statistics of these identified variables and their correlation coefficients with the pressure difference on both sides of the exhaust system at 20 CAD are presented in the following Tab. 7.18:

Variables	Min(x)	Max(x)	Mean(x)	σ_x	R single reg.
Mass CC [g]	3.89	4.85	4.39	0.301	-0.415
Kinetic energy [m ² .s ⁻²]	52.073	96.758	73.065	15.143	0.314
U norm SP [m/s]	6.83	23.49	14.72	5.66	-0.323
Ux SP [m/s]	-22.24	16.63	-5.78	10.68	0.383
Uz SP [m/s]	-12.82	6.70	-1.19	2.64	0.413
Ux SP 141-142 [m/s]	-19.84	20.71	-4.30	9.91	0.405
Ux SP 142-143 [m/s]	-5.87	6.27	-0.41	3.20	0.489

Table 7.18: Statistics of the variables correlated with the pressure difference at the exhaust system at 20 CAD and the corresponding correlation coefficients R with a single regression approach

Tab. 7.18 identifies three main classes of variables, which are the mass in the combustion chamber, the mean kinetic energy in the combustion chamber at spark timing and different velocities at the spark plug position. All these variables are correlated with the pressure difference on both sides of the exhaust system at 20 CAD and the absolute values of different correlation coefficients are in between 0.3 and 0.5. In order to focus on the main variable in each class, the correlations between all analysed variables are proposed in Tab. 7.19.

Vars. / Vars.	Mass CC [g]	Kinetic energy [m ² .s ⁻²]	U norm SP [m/s]	Uz SP [m/s]	Ux SP [m/s]	Ux SP 141-142 [m/s]	Ux SP 142-143 [m/s]
Mass CC [g]	1.000	-0.063	0.091	-0.501	-0.263	-0.483	-0.515
Kinetic energy [m ² .s ⁻²]	-0.063	1.000	0.203	0.004	0.156	0.094	0.085
U norm SP [m/s]	0.091	0.203	1.000	-0.401	-0.294	-0.336	-0.308
Uz SP [m/s]	-0.263	0.156	-0.294	1.000	0.012	-0.070	-0.020
Ux SP [m/s]	-0.501	0.004	-0.401	0.012	1.000	0.975	0.972
Ux SP 141-142 [m/s]	-0.483	0.094	-0.336	0.975	-0.070	1.000	0.984
Ux SP 142-143 [m/s]	-0.515	0.085	-0.308	0.972	-0.020	0.984	1.000

Table 7.19: Bottom block of the table: correlation coefficients R between different variables

Tab. 7.19 confirms the previous subdivision into three classes, which are the mass in the combustion chamber, the mean kinetic energy in the combustion chamber at spark timing and different velocities at the spark plug position. Indeed, all considered velocities are correlated with each other except the velocity along the x-axis and the velocity along the z-axis but both of them correlated with the velocity amplitude called "U norm SP". Moreover, the mass in the combustion chamber is also correlated with almost all velocities which allows the presentation of only one variable to analyse the trend of all of them. Here, the mass in the combustion chamber is chosen. An increase of the mass in the combustion chamber goes hand in hand with an increase of the negative component of the velocities along the x-axis and the z-axis. Lastly, the mean kinetic energy in the combustion chamber at spark timing is not strongly correlated with all the other variables, even if it is slightly correlated with the velocity amplitude at the spark plug at spark timing ($R = 0.203$). Here, the increase of the mean kinetic energy leads to a increase of the velocity amplitude at the spark plug at spark timing.

The first correlation presented here is between the mass in the combustion chamber and the pressure difference on both sides of the exhaust system. As presented in Fig. 7.34, the higher the pressure difference on both sides of the exhaust system, the lower the mass in the combustion chamber is. Indeed, a high value of the pressure difference on both sides of the exhaust system might be interpreted as a difficulty to empty the burnt gases from the combustor which then leads to a higher residual burnt gases mass fraction at spark timing. As presented above, the presence of some burnt gases at a higher temperature result in a lower density, and unavoidably in a lower mass in the combustion chamber.

Slightly less correlated than the mass in the combustion chamber, the kinetic energy is also correlated with the pressure difference on both sides of the exhaust system. An increase of the pressure difference at 20 CAD during the opening of the exhaust system leads to an increase of the mean kinetic energy in the combustor. Indeed, the pressure difference on both sides of the exhaust system generates the mass flow through this system. The higher velocity during this phase, the lower pressure is met at the beginning of the scavenging phase and the higher the burnt gases expansion is. Then, the velocity magnitude encountered during the scavenging and the intake phases reaches high levels, and thus leads to a significant mean resolved kinetic energy in the combustion chamber.

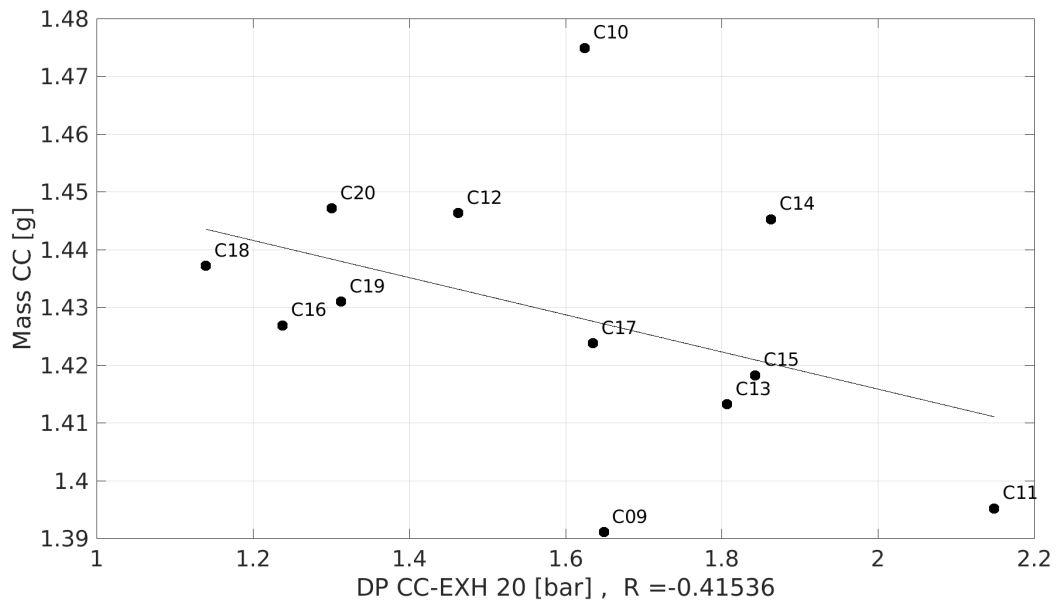


Figure 7.34: Correlation between the mass in the combustion chamber and the pressure difference on both sides of the exhaust system at 20 CAD

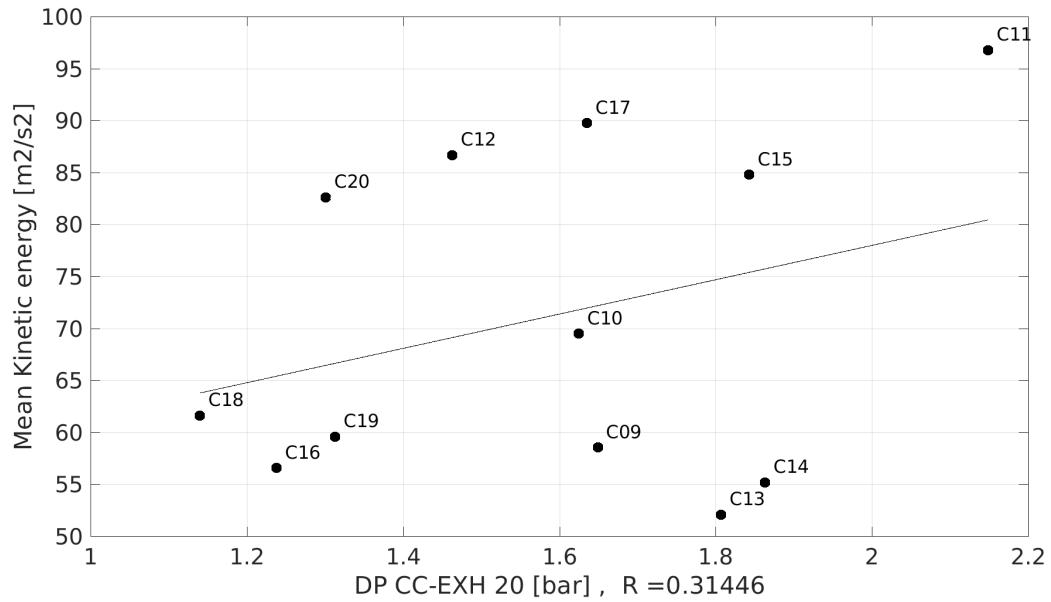


Figure 7.35: Correlation between the mean kinetic energy in the combustion chamber and the pressure difference on both sides of the exhaust system at 20 CAD

7.4.6.3 Correlation with the pressure difference at the intake system at 55 CAD

Last but not least, the influence of the pressure difference on both sides of the intake system at 55 CAD, which is at the opening of the intake system, on the different variables is presented here. Like in section 7.4.3, only variables with a Bravais-Pearson correlation coefficient higher than 0.3 are presented, which are:

Variables	Min(x)	Max(x)	Mean(x)	σ_x	R single reg.
Mass CC [g]	3.89	4.85	4.39	0.301	0.822
Y resid. BG [-]	0.103	0.164	0.130	0.016	-0.605
EQ. RA. F 144 [-]	1.116	1.356	1.204	0.039	-0.616
Mean EQ.RA [-]	1.119	1.361	1.204	0.041	-0.425
EQ.RA SP [-]	1.119	1.361	1.204	0.041	-0.685
Mean EQ.RA Sph 1 mm [-]	1.119	1.361	1.206	0.045	-0.705
Mean EQ.RA Sph 1.5 mm [-]	1.119	1.361	1.206	0.045	-0.714
U norm SP [m/s]	6.83	23.49	14.72	5.66	0.472
U norm SP 140-141 [m/s]	6.71	22.41	14.55	5.20	0.465
U norm SP 142-143 [m/s]	3.00	16.63	12.09	3.52	0.337
Ux SP [m/s]	-22.24	16.63	-5.78	10.68	-0.461
Uz SP [m/s]	-12.82	6.70	-1.19	2.64	-0.358
Ux SP 141-142 [m/s]	-19.84	20.71	-4.30	9.91	-0.446
Ux SP 142-143 [m/s]	-5.87	6.27	-0.41	3.20	-0.448

Table 7.20: Statistics of the variables correlated with the pressure difference at the intake system at 55 CAD and the corresponding correlation coefficients R with a single regression approach

Tab. 7.20 presents all variables correlated with the pressure difference on both sides of the intake system at 55 CAD. According to Tab. 7.14 the variation of this pressure difference evolves between 1.53 and 1.65 bar which is quite a low variation, however these fluctuations clearly drive all previous analysed variables. Indeed, The mass in the combustion chamber, the mean residual burnt gases mass fraction and the different measured equivalence ratios are all linked with each other as presented in Tab. 7.16 and are strongly driven by the pressure difference on both sides of the intake system, since absolute value of the correlation coefficients are larger than 0.685. Moreover, the pressure difference also plays a role in the velocity near the spark plug since all coefficient $|R|$ are in between 0.337 and 0.472. Like in sections 7.4.6.1 and 7.4.6.3, only the mass in the combustion chamber and the velocity amplitude at the spark plug at spark timing are presented here.

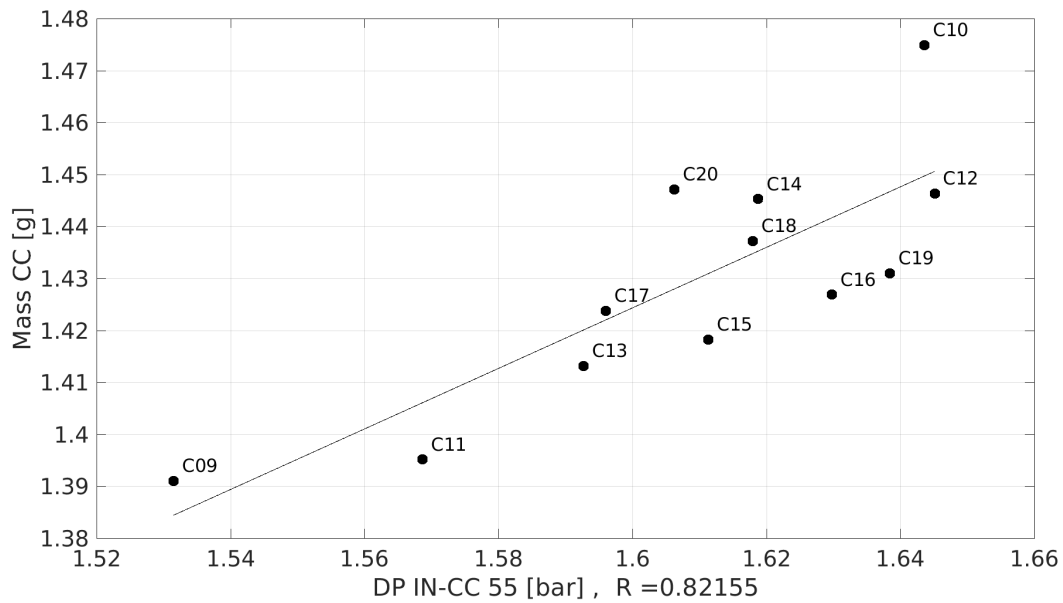


Figure 7.36: Correlation between the mass in the combustion chamber and the pressure difference on both sides of the intake system at 55 CAD

Fig. 7.36 presents the mass in the combustion chamber as a function of the pressure difference at the intake system at the opening crank angle. According to this graph, the increase of the pressure difference results in an improvement of the combustion chamber filling. Here a variation of 6.5 % in the pressure difference compared with the minimum value, leads to a variation of 5.0 % of the mass in the combustor. This curve highlights the importance of the control of this pressure difference on both sides of the intake system to avoid the fluctuation on the mass in the combustion chamber and thus the cycle-to-cycle variability.

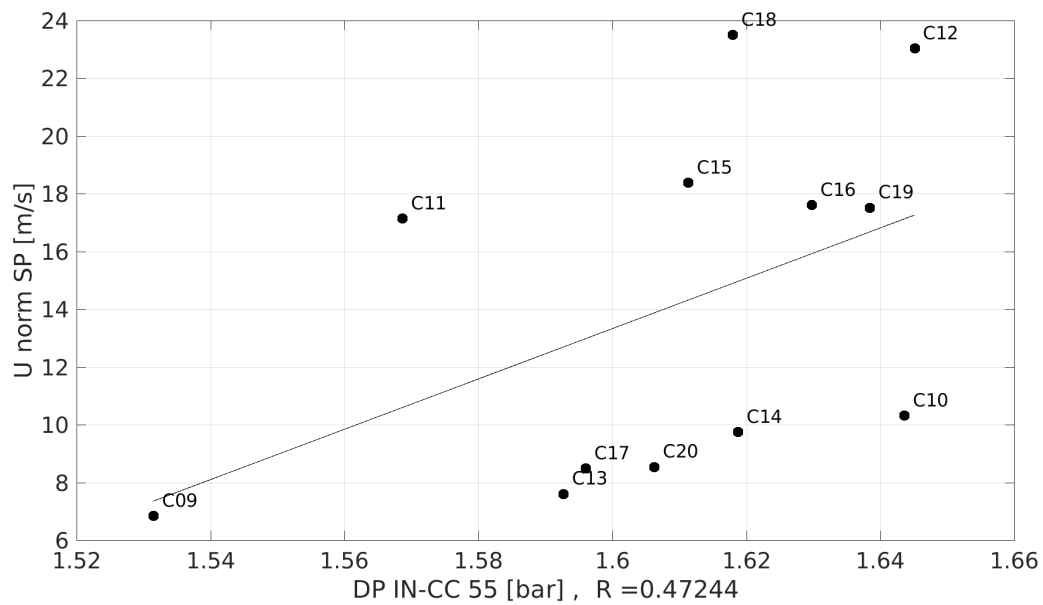


Figure 7.37: Correlation between the velocity amplitude at the spark plug at spark timing and the pressure difference on both sides of the intake system at 55 CAD

The velocity amplitude at the spark plug at spark timing is moderately correlated with the pressure difference on both sides of the intake system at the opening crank angle of 55 degrees. Like the mass in the combustion chamber, the increase of the pressure difference results in a higher velocity amplitude near the spark plug. Consequently, the ignition phase and the very first kernel growth and propagation might be improved by raising this velocity which has to be as high as possible till quenching is avoided. Moreover, this graph shows that the pressure difference tends to oscillate around the mean value of 1.61 bar which highlights the difficulty to control this gradient.

7.5 Reactive case conclusion

This chapter was dedicated to the validation of the developed LIB model and the analysis of one reactive case. The LES shows its capability to correctly capture the experimental functioning and variability after having done some adjustments on the immersed boundary dimensions and angular phasing. First of all, the velocity fields have a good accordance with the experiment even if some slight discrepancies are mentioned. The pressure evolution highlights that some improvement might be made on the dimensions of the LIB and adding the resolution of the spark plug geometry could allow the prediction of the beginning of the ignition and the flame propagation better. However, the global trend and the cycle-to-cycle variability are globally predicted by the LES. Last but not least, the analysis of these variabilities allows the identification of the main variables which have to be controlled to reduce these phenomena, among which the aerodynamics and more precisely the pressure difference on both sides of the intake system. Indeed, this pressure difference drives the mass, the residual burnt gases, the equivalence ratio and the velocity in the combustion chamber and thus controls the combustion process.

Chapter 8

Conclusions and perspectives

8.1 Conclusions of the present work

The main objective of the present PhD thesis was to develop a LES methodology that allows the evaluation of CVC chambers. These chambers are theoretically very interesting for reducing the fuel consumption and thus, diminishing the emission of CO_2 , as encouraged by a more stringent regulation. At the beginning of this work, several methods seemed capable of handling the moving parts required in CVC chambers. The "Arbitrary Lagrangian Eulerian" method which is commonly used in spark ignition engines, is suitable for parts in linear motion like the valves or the pistons but is not adapted for rotating parts. The "Multi Instance Solver Coupled through Overlapping Grids" was developed to evaluate compressor stages, is adapted for rotating parts like the cams in CVC chambers. However, the main disadvantage is that the gaps between the cams and the walls have to be resolved with several cells, which leads to very refined meshes and thus to a high CPU cost. The third method uses immersed boundaries to model moving parts. Despite the lack of maturity of this method with the numerical formalism of the LES solver AVBP and the use of it in such a configuration, the "Lagrangian Immersed Boundary" was chosen in this work. In fact, this method enables to have lighter meshes than the two other methods and seems easier to use.

The first part of this work was to evaluate the method on very simple cases, which leads to the development of a new formulation of the source terms slightly different from the original one. With the implementation of linear or rotation motions, the new formulation allows the modeling of the moving parts without using any parametrisation of the model, but the airtightness of the immersed boundaries was not acceptable for the study of CVC chambers. Consequently, some work was realised on the application of the source terms into the Navier-Stokes equations, in order to improve the capability of immersed boundary to hold back the fluid from a high pressure zone. Supplementary source terms based on the previous ones were added into the second order derivative of the numerical scheme. With these additional source terms, the numerical method reaches very acceptable mass leakages in gaps between the LIB and the walls, and through immersed objects while a high pressure gradient on both sides of the immersed walls was applied. Moreover, a special treatment in wall cells was developed to decrease the mass flow rate through these cells. In addition, an isothermal boundary condition in LIB was implemented to allow the user to choose the temperature inside the moving parts. These developments were

realised during the evaluation of the method on several test cases from very simple ones to cases more representative of CVC chambers. Then, the Lagrangian liquid injection used for fuel sprays was adapted to work with LIB. Indeed, the localisation algorithm was modified to find out if there was an immersed boundary in the in-coming cells and then to activate a rebound on them. Last but not least, the combustion model ECFM-LES was also modified to take into account the liquid phase evaporation and also the interaction of the flame with LIB, like the quenching of it.

The second part of the manuscript was dedicated to the evaluation of the developed method on the semi-industrial CVC chamber studied experimentally in the PPRIME laboratory in Poitiers. This complex configuration used two pairs of cams for both the intake and the exhaust systems. The carburation was realised with four pairs of automotive injectors and the mixture in the combustion chamber was ignited with an automotive spark plug.

The first step of this work was to analyse two non-reactive operating points. The first one gave the evolution of the pressure in both the carburation and the combustion chambers, while in the second one, the pressure and the velocity fields were measured in the combustion chamber.

Thanks to these three measurements, the dimensions of cams were reduced by around 1.5-2.0 % to correctly fit the experimental pressure loss during the constant volume phase.

According to the experimental velocity fields, the air-flow during the intake phase was non symmetrical, which might be the consequence of different mechanical slacks between cams and walls of the upper and the lower cams of the intake system. In the simulation, these gaps were far from the dimensions of the real ones, therefore, this non symmetrical air-flow was generated by introducing a shift crank angle between the upper and the lower cams of the intake system. In fact, the aim was to open the lower cam earlier than the upper one, to create the recirculation zone observed in the experiment. In the simulation, a time shifting of 0.15 ms was realised by adding a crank angle shift of 2 degrees. If these gaps will be resolved, the angular shift introduced in our simulation will have to be taken into account to generate the non symmetrical flow encountered in the experiment but with a more realistic value of a few tenths of a degree.

Finally, the pressure at the intake tank upstream of the combustion chamber, was decreased from 3 down to 2.75 bar to avoid the overestimation of the combustion chamber pressure at the beginning of the constant volume phase. Indeed, the acoustic mode in the simulation was slightly different from the experiment, but the reason was not clearly identified and requires more investigations. With these adjustments, both the pressure and the velocity fields in the combustion chamber fitted the measurements reasonably.

The second step of this work was to activate the carburation and the combustion in the second non-reactive case. In this case, the pressure and the velocity fields in the combustion chamber were available. According to the experiment, the pressure loss during the constant volume phase was higher than in non-reactive cases. Therefore, the dimensions of the exhaust cams were slightly downsized to reach the correct pressure loss. With this modification of the intake cams, the intake pressure in the buffer tank was increased back up to 2.95 bar to reach the correct pressure at the beginning of the constant volume phase. Lastly, the shift crank angle between the upper and the lower cams of the intake system was decreased down to 1.5 degrees to shorten the time delay between the two openings. The velocity fields obtained with the simulations in this complex case are representative

of the experiment even if additional cycles shall improve the phase average velocity fields. The LES predicted correctly the pressure increase during the combustion even if the first kernel growth seemed overestimated. Indeed, the ignition model is strongly impacted by an overestimation of the velocity at the spark plug, which might occur in our simulation, since this part was completely removed. However, the cycle-to-cycle variability encountered in the experiment was predicted by the LES all the same. This phenomenon was analysed with a simple regression, which highlighted that the key variable correlated with the peak pressure was the mean resolved kinetic energy. This approach also identified other variables slightly correlated with the peak pressure. These were the mean residual burnt gases mass fraction, the mean equivalence ratio, the velocity in the vicinity of the spark plug, all of these being at the spark timing and also the subgrid-scale velocity at the combustion filter size met by the flame front during the propagation. The cycle-to-cycle variability was then analysed with a multidimensional approach which enabled the clear identification of independent variables correlated with the peak pressure and its corresponding angle. These variables were the mean residual kinetic energy, all velocity components at the spark plug position, the mean residual burnt gases and the mean equivalence ratio, all of these being at the spark timing and the laminar flame speed met by the flame front. According to these two approaches, these variables were acting simultaneously and directly influenced the measured responses like the peak pressure. Last but not least, the analysis of the origin of the fluctuation of variables like the kinetic energy, the residual burnt gases mass fraction and the velocity field are correlated with quantities of the previous cycle like the pressure gradient on both sides of the intake system. This last analysis confirmed that, in this configuration, a very fast previous cycle leads then to a slow cycle which does not burn well. The LIB method shows its capability to model this CVC chamber and allows the comprehension of the fluctuations observed experimentally.

The cycle-to-cycle variability that might be encountered in other CVC chambers should be decreased by optimising the scavenging phase. The aim is to diminish the variability of the kinetic energy, the residual burnt mass fraction and the velocity near the spark plug. In fact, a better control of the aerodynamics in the combustor leads to a better control of both the velocity near the spark plug and the mixture encountered by the flame. The developed LIB method is an attractive approach to evaluate these main parameters on several configurations in a short period of time, which then allows the determination of the most promising one. Lastly, an optimisation of the intake and exhaust systems might be realised with the LIB method but a very accurate approach, which allows a better description of the influence of leakage and flow dynamics at walls on the proposed configuration, like the "Multi Instance Solver Coupled through Overlapping Grids", could be done before manufacturing the first prototype.

8.2 Perspectives

The developed LIB method is capable of evaluating CVC chambers, but some misunderstanding must be clarified. Indeed, the acoustic is slightly different in the simulation which should be investigated with another approach like the Multi Instance Solver Coupled through Overlapping Grids or with a better experimental characterisation of the boundaries. First the accuracy of the LIB method could be assessed and improved by

comparing the results with these obtained with MISCOG on a simplified geometry with only two rotating objects and the whole experimental apparatus.

The second action should be to take into account the liquid phase in the cycle-to-cycle variability and to check if there are some fluctuations of the trapped liquid phase fuel and its evaporation, which can also lead to variabilities on the peak pressure.

Then, the spark plug geometry could be considered to examine its impact on the velocity fields near this part, which might improve the beginning of the first kernel growth and thus the whole pressure evolution in the combustor. Last but not least, the method developed in this PhD thesis could be used to improve the spark plug position of the studied reactive case. This method could also give access to the details of the flow for different operating points realised in the PPRIME laboratory. Indeed, the experimental database covers a variation of the geometries of the cams, different crank angle shift between the intake and the exhaust systems and different types of fuel injections, namely the injection of liquid fuel in the carburation chamber or the injection of gaseous fuel directly in the combustion chamber.

Bibliography

- [1] International Civil Aviation Organization, *Environmental Report*. 2010.
- [2] G. Hao and W. Zhan-xue, “Effects of intercooling and recuperation on turbofan engine performance,” in *Mechanical Engineering and Information Technology (EMEIT)*, pp. 2482–2485, 2011.
- [3] K. G. Kyprianidis, T. Grönstedt, S. O. T. Ogaji, P. Pilidis, and R. Singh, “Assessment of future aero-engine designs with intercooled and intercooled recuperated cores,” *Journal of Engineering for Gas Turbines and Power*, vol. 133, no. 1, p. 011701, 2011.
- [4] L. Xu, K. G. Kyprianidis, and T. U. J. Grönstedt, “Optimization study of an intercooled recuperated aero-engine,” *Journal of Propulsion and Power*, vol. 29, no. 2, pp. 424–432, 2013.
- [5] W. Camilleri, E. Anselmi, V. Sethi, P. Laskaridis, A. Rolt, and P. Cobas, “Performance characteristics and optimisation of a geared intercooled reversed flow core engine,” *Proceedings of the Institution of Mechanical Engineers, Part G: Journal of Aerospace Engineering*, vol. 229, no. 2, pp. 269–279, 2015.
- [6] E. Wintenberger and J. E. Shepherd, “Thermodynamic cycle analysis for propagating detonations,” *Journal of Propulsion and Power*, vol. 22, no. 3, pp. 694–698, 2006.
- [7] P. Wolański, “Detonative propulsion,” *Proceedings of the Combustion Institute*, vol. 34, no. 1, pp. 125–158, 2013.
- [8] T. C. Adamson Jr. and G. R. Olsson, “Performance analysis of a rotating detonation wave rocket engine,” *Astronautica Acta*, vol. 13, no. 4, pp. 405–415, 1967.
- [9] F. A. Bykovskii and E. F. Vedernikov, “Continuous detonation of a subsonic flow of a propellant,” *Combustion, Explosion and Shock Waves*, vol. 39, no. 3, pp. 323–334, 2003.
- [10] F. A. Bykovskii, S. A. Zhdan, and E. F. Vedernikov, “Continuous spin detonation of fuel-air mixtures,” *Combustion, Explosion, and Shock Waves*, vol. 42, no. 4, pp. 463–471, 2006.
- [11] F. A. Bykovskii, S. A. Zhdan, and E. F. Vedernikov, “Continuous spin detonations,” *Journal of Propulsion and Power*, vol. 22, no. 6, pp. 1204–1216, 2006.
- [12] M. Hishida, T. Fujiwara, and P. Wolanski, “Fundamentals of rotating detonations,” *Shock Waves*, vol. 19, no. 1, pp. 1–10, 2009.

- [13] D. Davidenko, I. Gökalp, and A. Kudryavtsev, “Numerical study of the continuous detonation wave rocket engine,” in *15th AIAA International Space Planes and Hypersonic Systems and Technologies Conference*, International Space Planes and Hypersonic Systems and Technologies Conferences, American Institute of Aeronautics and Astronautics, 2008.
- [14] P. Kalina, “Turbine engine with detonation combustion chamber in institute of aviation,” *Journal of KONES. Powertrain and Transport*, vol. 21, no. 1, pp. 119–124, 2014.
- [15] B. C. Bobusch, P. Berndt, C. O. Paschereit, and R. Klein, “Shockless explosion combustion: An innovative way of efficient constant volume combustion in gas turbines,” *Combustion Science and Technology*, vol. 186, no. 10-11, pp. 1680–1689, 2014.
- [16] M. Bellenoue, B. Boust, P. Vidal, R. Zitoun, T. Gaillard, D. Davidenko, M. Leyko, and B. Le Naour, “New combustion concepts to enhance the thermodynamic efficiency of propulsion engines.”
- [17] B. Boust, Q. Michalski, and M. Bellenoue, “Experimental investigation of ignition and combustion processes in a constant-volume combustion chamber for air-breathing propulsion,” in *52nd AIAA/SAE/ASEE Joint Propulsion Conference*, AIAA Propulsion and Energy Forum, American Institute of Aeronautics and Astronautics, 2016.
- [18] L. Labarrere, T. Poinso, A. Dauplain, F. Duchaine, M. Bellenoue, and B. Boust, “Experimental and numerical study of cyclic variations in a constant volume combustion chamber,” *Combustion and Flame*, vol. 172, pp. 49–61, 2016.
- [19] T. Poinso and D. Veynante, *Theoretical and numerical Combustion*. R.T. Edwards, 3rd edition, 2012.
- [20] F. M. White, *Fluid Mechanics*. McGraw-Hill, 4th edition, 1999.
- [21] Hirschfelder, Curtis, and Bird, *Molecular Theory of Gases and Liquids*. New York: John Wiley & Sons, 1954 ed., 1954.
- [22] R. B. Bird, W. E. Stewart, and E. N. Lighfoot, *Transport phenomena*. New York: John Wiley & Sons, 1960.
- [23] J. Smagorinsky, “General circulation experiments with the primitive equations. i: The basic experiment,” *Monthly Weather Review*, vol. 91(3), pp. 99–165, 1963.
- [24] F. Nicoud and F. Ducros, “Subgrid-scale stress modelling based on the square of the velocity gradient tensor,” *Flow, Turbulence and Combustion*, vol. 62, no. 3, pp. 183–200, 1999.
- [25] P. Sagaut, *Large eddy simulation for incompressible flows*. Springer, 2002.
- [26] H. Baya, O. Cabrit, G. Balarac, S. Bose, J. Lee, H. Choi, and F. Nicoud, “A subgrid-scale model base on singular values for les in complex geometries,” *Center for Turbulence Research Proceeding of the Summer Program*, pp. 193–202, 2010.
- [27] N. Peters, “The turbulent burning velocity for large-scale and small-scale turbulence,” *Journal of Fluid Mechanics*, vol. 384, pp. 107–132, 1999.

- [28] A. R. Kerstein, W. T. Ashurst, and F. A. Williams, “Field equation for interface propagation in an unsteady homogeneous flow field,” *Physical Review A*, vol. 37, no. 7, pp. 2728–2731, 1988.
- [29] O. Colin, F. Ducros, D. Veynante, and T. Poinso, “A thickened flame model for large eddy simulations of turbulent premixed combustion,” *Physics of Fluids*, vol. 12, pp. 1843–1863, 2000.
- [30] S. Richard, O. Colin, O. Vermorel, A. Benkenida, C. Angelberger, and D. Veynante, “Towards large eddy simulation of combustion in spark ignition engines,” *Proceedings of the Combustion Institute*, vol. 31, no. 2, pp. 3059 – 3066, 2007.
- [31] O. Colin, A. Benkenida, and C. Angelberger, “3d modeling of mixing, ignition and combustion phenomena in highly stratified gasoline engines,” *Oil & Gas Science and Technology*, vol. 58, no. 1, pp. 47–62, 2003.
- [32] Colin, O., Benkenida, A., and Angelberger, C., “3d modeling of mixing, ignition and combustion phenomena in highly stratified gasoline engines,” *Oil & Gas Science and Technology - Rev. IFP*, vol. 58, no. 1, pp. 47–62, 2003.
- [33] K. K. Kuo, *Principles of Combustion*. New York: John Wiley, 1986.
- [34] M. Metghalchi and J. C. Keck, “Laminar burning velocity of propane-air mixtures at high temperature and pressure,” *Combustion and Flame*, vol. 38, pp. 143–154, 1980.
- [35] S. Candel and T. Poinso, “Flame stretch and the balance equation for the flame area,” *Combustion Science and Technology*, vol. 70, no. 1-3, pp. 1–15, 1990.
- [36] F. Charlette, C. Meneveau, and D. Veynante, “A power-law flame wrinkling model for les of premixed turbulent combustion part ii: dynamic formulation,” *Combustion and Flame*, vol. 131, no. 1–2, pp. 181–197, 2002.
- [37] S. Richard, *Simulation aux grandes échelles de la combustion dans les moteurs à allumage commandé*. Phd thesis, Ecole Centrale Paris, 2005.
- [38] R. J. BLINT, “The relationship of the laminar flame width to flame speed,” *Combustion Science and Technology*, vol. 49, no. 1-2, pp. 79–92, 1986.
- [39] O. Colin and K. Truffin, “A spark ignition model for large eddy simulation based on an fsd transport equation (issim-les),” *Proceedings of the Combustion Institute*, vol. 33, no. 2, pp. 3097–3104, 2011.
- [40] M. García, *Développement et validation du formalisme Euler-Lagrange dans un solveur parallèle et non-structuré pour la simulation aux grandes échelles*. PhD thesis, Université de Toulouse - Ecole doctorale : Mécanique, Energétique, Génie civil, Procédés, 2009.
- [41] P. Fede, P. Février, and O. Simonin, “Numerical study of the effect of the fluid turbulence microscales on particle segregation and collision in gas-solid turbulent flows,” in *5th International Conference on Multiphase Flow*, (Yokohama, Japan), 2004.

- [42] L. Schiller and A. Nauman, “A drag coefficient correlation,” *VDI Zeitung*, vol. 77, pp. 318–320, 1935.
- [43] D. B. Spalding, “The combustion of liquid fuels,” in *Proceedings of the Fourth Symposium (international) on Combustion*, (Baltimore), pp. 847–864, The Combustion Institute, 1953.
- [44] W. A. Sirignano, *Fluid dynamics and transport of droplets and sprays*. Cambridge University Press, 1999.
- [45] M. Boileau, *Simulation aux grandes échelles de l’allumage diphasique des foyers aéronautiques*. PhD thesis, INP Toulouse, 01/01/2007.
- [46] C. Habchi, “The energy spectrum analogy breakup (sab) model for the numerical simulation of sprays,” *Atomization and Sprays*, vol. 21, no. 12, pp. 1033–1057, 2011.
- [47] M. Pilch and C. Erdman, “Use of breakup time data and velocity history data to predict the maximum size of stable fragments for acceleration-induced breakup of a liquid drop,” *International Journal of Multiphase Flow*, vol. 13, no. 6, pp. 741 – 757, 1987.
- [48] C. W. Hirt, A. A. Amsden, J. L. Cook, “An arbitrary lagrangian-eulerian computing method for all flow speeds,” *Journal of Computational Physics*, vol. 14, pp. 227–253, 1974.
- [49] V. Moureau, G. Lartigue, Y. Sommerer, C. Angelberger, O. Colin, and T. Poinsot, “High-order methods for dns and les of compressible multi-component reacting flows on fixed and moving grids,” *\jcp*, vol. 202, no. 2, pp. 710–736, 2005.
- [50] A. Robert, S. Richard, O. Colin, L. Martinez, and L. de Francqueville, “Les prediction and analysis of knocking combustion in a spark ignition engine,” *Proceedings of the Combustion Institute*, vol. 35, no. 3, pp. 2941–2948, 2015.
- [51] A. Robert, S. Richard, O. Colin, and T. Poinsot, “Les study of deflagration to detonation mechanisms in a downsized spark ignition engine,” *Combustion and Flame*, vol. 162, no. 7, pp. 2788–2807, 2015.
- [52] G. Lecocq, S. Richard, J.-B. Michel, and L. Vervisch, “A new les model coupling flame surface density and tabulated kinetics approaches to investigate knock and pre-ignition in piston engines,” *Proceedings of the Combustion Institute*, vol. 33, no. 2, pp. 3105–3114, 2011.
- [53] K. Truffin, C. Angelberger, S. Richard, and C. Pera, “Using large-eddy simulation and multivariate analysis to understand the sources of combustion cyclic variability in a spark-ignition engine,” *Combustion and Flame*, vol. 162, no. 12, pp. 4371–4390, 2015.
- [54] J. Legier, T. Poinsot, and D. Veynante, “Dynamically thickened flame les model for premixed and non-premixed turbulent combustion,” *Center for Turbulence Research Proceeding of the Summer Program*, pp. 157–168, 2000.

- [55] A. Misdariis, O. Vermorel, and T. Poinso, “Les of knocking in engines using dual heat transfer and two-step reduced schemes,” *Combustion and Flame*, vol. 162, no. 11, pp. 4304–4312, 2015.
- [56] A. Piacentini, T. Morel, A. Thevenin, and F. Duchaine, “O-palm: an open source dynamic parallel coupler,” *Coupled problem 2011*, 2011.
- [57] B. Raverdy, I. Mary, P. Sagaut, and N. Liamis, “High-resolution large-eddy simulation of flow around low-pressure turbine blade,” *AIAA Journal*, vol. 41, no. 3, pp. 390–397, 2003.
- [58] V. Michelassi, J. G. Wissink, J. Fr-ograve, hlich, and W. Rodi, “Large-eddy simulation of flow around low-pressure turbine blade with incoming wakes,” *AIAA Journal*, vol. 41, no. 11, pp. 2143–2156, 2003.
- [59] J. U. Schlüter, X. Wu, S. Kim, S. Shankaran, J. J. Alonso, and H. Pitsch, “A framework for coupling reynolds-averaged with large-eddy simulations for gas turbine applications,” *Journal of Fluids Engineering*, vol. 127, no. 4, p. 806, 2005.
- [60] G. Wang, F. Duchaine, D. Papadogiannis, I. Duran, S. Moreau, and L. Y. Gicquel, “An overset grid method for large eddy simulation of turbomachinery stages,” *Journal of Computational Physics*, vol. 274, pp. 333–355, 2014.
- [61] C. S. Peskin, “Flow patterns around heart valves: A numerical method,” *Journal of Computational Physics*, vol. 10, no. 2, pp. 252–271, 1972.
- [62] D. Goldstein, R. Handler, and L. Sirovich, “Modeling a no-slip flow boundary with an external force field,” *Journal of Computational Physics*, vol. 105, no. 2, pp. 354–366, 1993.
- [63] E. M. Saiki and S. Biringen, “Numerical simulation of a cylinder in uniform flow: Application of a virtual boundary method,” *Journal of Computational Physics*, vol. 123, no. 2, pp. 450–465, 1996.
- [64] J. Mohd-Yusof, “Combined immersed-boundary / b-spline methods for simulations of flow in complex geometries,” *Center for Turbulent Research, Annual Research Briefs*, 1997.
- [65] E. A. Fadlun, R. Verzicco, P. Orlandi, and J. Mohd-Yusof, “Combined immersed-boundary finite-difference methods for three-dimensional complex flow simulations,” *Journal of Computational Physics*, vol. 161, no. 1, pp. 35–60, 2000.
- [66] T. Ye, R. Mittal, H. S. Udaykumar, and W. Shyy, “An accurate cartesian grid method for viscous incompressible flows with complex immersed boundaries,” *Journal of Computational Physics*, vol. 156, no. 2, pp. 209–240, 1999.
- [67] T. Nguyen, P. Janas, T. Lucchini, G. D’Errico, S. Kaiser, and A. Kempf, “Les of flow processes in an si engine using two approaches: Openfoam and psiphi,” in *SAE 2014 World Congress & Exhibition*, SAE Technical Paper Series, SAE International400 Commonwealth Drive, Warrendale, PA, United States, 2014.

- [68] T. M. Nguyen, F. Proch, I. Wlokas, and A. M. Kempf, “Large eddy simulation of an internal combustion engine using an efficient immersed boundary technique,” *Flow, Turbulence and Combustion*, vol. 97, no. 1, pp. 191–230, 2016.
- [69] H. Forrer and M. Berger, *Flow Simulations on Cartesian Grids Involving Complex Moving Geometries*, pp. 315–324. Basel: Birkhäuser Basel, 1999.
- [70] A. Bonhomme, F. Duchaine, G. Wang, L. Selle, and T. Poinsot, “A parallel multidomain strategy to compute turbulent flows in fan-stirred closed vessels,” *Computers & Fluids*, vol. 101, pp. 183–193, 2014.
- [71] Y. Zhang and B. Tabarrok, “Modifications to the lax-wendroff scheme for hyperbolic systems with source terms,” *International Journal for Numerical Methods in Engineering*, vol. 44, no. 1, pp. 27–40, 1999.
- [72] P. Schmitt, *Simulation aux grandes échelles de la combustion étagée dans les turbines à gaz et son interaction stabilité - polluants-thermique - TH/CFD/05/45*. PhD thesis, Institut National Polytechnique de Toulouse, 01/01/2005.
- [73] J. Smagorinsky, “General circulation experiments with the primitive equations,” *Monthly Weather Review*, vol. 91, no. 3, pp. 99–164, 1963.
- [74] P. D. Lax and B. Wendroff, “Difference schemes for hyperbolic equations with high order of accuracy,” *Communications on pure and applied mathematics*, no. 17, pp. 381–391, 1964.
- [75] O. Colin and M. Rudgyard, “Development of high-order taylor-galerkin schemes for les,” *J. Comput. Phys.*, vol. 162, no. 2, pp. 338–371, 2000.
- [76] L. Thobois, G. Rymer, T. Soulères, and T. Poinsot, “Large-eddy simulation in ic engine geometries,” in *2004 SAE Fuels & Lubricants Meeting & Exhibition*, SAE Technical Paper Series, SAE International400 Commonwealth Drive, Warrendale, PA, United States, 2004.
- [77] F. Piscaglia, A. Montorfano, and A. Onorati, “Towards the les simulation of ic engines with parallel topologically changing meshes,” *SAE Int. J. Engines*, vol. 6, no. 2, pp. 926–940, 2013.
- [78] F. Piscaglia, A. Montorfano, and A. Onorati, “A scale adaptive filtering technique for turbulence modeling of unsteady flows in ic engines,” *SAE International Journal of Engines*, vol. 8, no. 2, pp. 426–436, 2015.
- [79] E. Nicoud, *Quantifying combustion stability in GDI engines by Large-Eddy Simulation*. Phd thesis, CentraleSupélec, 24/09/2018.
- [80] B. Robic, “Constant-volume combustion (cvc) chamber for an aircraft turbine engine including an intake/exhaust valve having a spherical plug.” <https://patents.google.com/patent/US20150204240A1/en?q=US20150204240A1>, Aug. 3 2012. Patent App. US20150204240A1.
- [81] C. Taliercio, Guillaume ;Viguier, “Constant-volume combustion system for a turbine engine of an aircraft engine.” <https://patents.google.com/patent/US20180038278A1/ko>, Feb. 17 2015. Patent App. US20180038278A1.

- [82] M. Leyko, “Module de combustion a volume constant pour une turbomachine.” url=<https://patents.google.com/patent/US20180010517A1/en>, Aug. 4 2016. Patent App. WO2016120551A1.
- [83] M. Aguilar, “Jet engine, in particular a jet engine for an aircraft.” url=<https://patents.google.com/patent/US8925296>, Jan. 1 2009. Patent App. US8925296B2.
- [84] Laure Labarrere, Thierry Poinsot, Antoine Dauplain, Florent Duchaine, Marc Belenoue, and Bastien Boust, “Experimental and numerical study of cyclic variations in a constant volume combustion chamber,” *Combustion and flame*, 2016.